UNIVERSITY OF SOUTHAMPTON

FACULTY OF ENGINEERING, SCIENCE AND MATHEMATICS

INSTITUTE OF SOUND AND VIBRATION RESEARCH

Joint Identification in Structural Waveguides Using Wave Reflection and Transmission Coefficients

By

Bing ZHANG

A thesis submitted for the degree of

Doctor of Philosophy

September 2007

University of Southampton

Abstract

Faculty of Engineering, Science and Mathematics
Institute of Sound and Vibration Research

Doctor of Philosophy

Joint Identification in Structural Waveguides Using Wave Reflection and Transmission Coefficients

By Bing Zhang

The dynamic modelling of one-dimensional jointed structures is relevant to many engineering applications, such as pipe systems and beam networks in constructions. Currently available techniques are undermined by inadequate ability to model the joints and other discontinuities due to uncertainty in their properties. Measured modal data can be used to update joint models, but often with limited success. In this thesis a wave approach is employed to investigate the reflection and transmission coefficients of various joint models in structural waveguides. The reflection and transmission coefficients are potentially more sensitive to the parameters of the joint models. Numerical simulations and experiments have been performed on three types of jointed waveguides. Appropriate models have been identified for these cases and sensitivities of the scattering coefficients to joint parameters have been investigated.

Accurate measurement of the reflection and transmission coefficients is desired in order to estimate joint parameters. A noise model is developed and a perturbation method is used to study the influence of measurement noise on the estimated reflection and transmission coefficients.

An iterative method is examined to solve the non-linear problem of estimating the parameters of a joint from measured reflection and transmission coefficients, in a least-squares sense. Issues concerning the iteration process, such as the selection of objective functions and frequency ranges, are examined in accordance with the sensitivity of the objective function to unknown parameters. The parameter identification method is validated by numerical simulation case studies and then verified by using measured data for mass discontinuities on beams, a supported straight pipe and a right-angled pipe bend. The case studies demonstrate that parameter identification of discontinuities in waveguides by using the wave approach is a success where modal methods are inappropriate.

Acknowledgements

I would like to express my gratitude to Dr. Tim Waters and Prof. Brian Mace, whose advice and encouragement were invaluable throughout this project.

Many suggestions from Prof. David Thompson and Dr. Neil Ferguson to improve the quality of my work are gratefully acknowledged.

I would like to thank my family and new married wife for their support and tolerance to me whilst I have been engaged in this endeavour.

I would also like to express my gratitude to Dr. Jen Muggleton for her encouragement and friends Yuyou Liu, Yan Gaon, Jian Cheng, Tianshu Zhao, Lin Ji, Jianguo Han, Shan Lin, Xiaolin Zhang, Zhenyu Huang, Jin Wang, Lili Zhao, Jun Sun, Bo Yan, Tingting Wu, Yan Hou, Jing Lv, Yoshiyuki Waki, Simon Shone, David Herron, and others for their support and care during the time I spent in the university.

Declaration of Authorship

I, Bing ZHANG, declare that the thesis entitled Joint Identification in Structural Waveguides Using Wave Reflection and Transmission Coefficients and the work presented in it are my own. I confirm that :

- this work was done wholly or mainly while in candidature for a research degree at this University;
- no part of this thesis has previously been submitted for a degree or any other qualification at this University or any other institution;
- where I have consulted the published work of others, this is always clearly attributed;
- where I have quoted from the work of others, the source is always given. With the exception of such quotations, this thesis is entirely my own work;
- I have acknowledged all main sources of help;
- where the thesis is based on work done by myself jointly with others, I have made clear exactly what wad done by others and what I have contributed myself;
- parts of this work have been published as:

    - B. Zhang, T.P. Waters and B.R. Mace 2006 The influence of measurement noise on the estimation of reflection and transmission coefficients in waveguides. Proceedings of the 9th International Conference on Recent Advances in Structural Dynamics, Southampton, UK
    - J.M. Muggleton, T.P. Waters, B.R. Mace and B. Zhang 2007 Approaches to estimating the reflection and transmission coefficients of discontinuities in waveguides from measured data. Journal of Sound and Vibration **307** (1-2): 280-294.

Signed: .....

Date: .....

Table of Contents

Abstract…… ii
Acknowledgements iii
Declaration of Authorship iv
List of Figures.. ix
List of Tables.. xiii
Glossary of Symbols xiv

Chapter 1 Introduction 1
1.1 Background 1
1.2 Modelling Methodologies 2
1.3 Wave Propagation Approach 3
1.4 Uncertainties of Joints and Discontinuities 4
1.5 Brief Introduction to Joint Identification 5
1.6 Objectives 9
1.7 Contributions of the Thesis 9
1.8 Overview of the Thesis 10

Chapter 2 Wave Propagation, Reflection and Transmission in Waveguides 12
2.1 Introduction 12
2.2 Longitudinal Wave Propagation in Rods 13
2.3 Flexural Wave Propagation in Beams 14
2.4 Damping Effects of Waveguides 16
2.5 Reflection and Transmission coefficients 17
2.6 A General Wave Approach 19
2.6.1 Wave Amplitude, Displacement and Internal Force Vectors 19
2.6.2 Displacement and Internal Force Matrices 20
2.6.3 Wave Propagation, Reflection and Transmission Matrices 20
2.7 Reflection and Transmission Coefficients in Terms of Parameters of Discontinuities 22
2.7.1 Reflection at Boundaries 22
2.7.2 Reflection and Transmission at Discontinuities in Waveguides 23
2.8 Case Study: Reflection and Transmission Coefficients of Two Identical Semi-infinite Beams Connected by a Discontinuity 25
2.9 Summary 30

Chapter 3 Measurement of Reflection and Transmission Coefficients 31
3.1 Introduction 31
3.2 A Wave Amplitude Decomposition Approach 32
3.3 Estimating Reflection and Transmission Coefficients by Wave Amplitude Decomposition 34
3.4 Analysis of Influence of Measurement Noise 37
3.4.1 Noise Model 37
3.4.2 Statistical Estimates of the Noisy Power Reflection Coefficient 38

3.4.3 Statistical Estimates of the Noisy Power Transmission Coefficient 40
3.5 Effects of Nearfields 41
3.6 Numerical Simulations 42
3.6.1 Parametric Model for the Discontinuity 43
3.6.2 Simulation Results for the Power Reflection Coefficient 43
3.6.3 Statistical Distribution of the Simulated Noisy Power Reflection Coefficient 46
3.7 Wavenumber Measurements 49
3.8 Experiments on Mass Discontinuities 51
3.8.1 Experimental Setup 51
3.8.2 Wavenumber Measurements 53
3.8.3 Reflection and Transmission Coefficients 54
3.9 Summary 60

Chapter 4 Wave Reflection and Transmission at Pipe Supports 62
4.1 Introduction 62
4.2 Wave Modes in In-vacuo Piping Systems 63
4.3 Dependence of Reflection and Transmission Coefficients on Parametric model of a Support 64
4.3.1 Model of a Support 65
4.3.2 Parametric Reflection and Transmission Coefficients 65
4.3.3 Numerical Examples 67
4.4 Experiments on Pipe Supports 71
4.4.1 Experimental Setup 71
4.4.2 Wavenumber Measurement and n=2 Cut-on Frequency 72
4.4.3 Direct Measurements of the Translational Dynamic Stiffness of the Supports 73
4.4.4 Direct Measurement of the Rotational Dynamic Stiffness of the Supports 76
4.4.5 Parameter Fitting of the Directly Measured Rotational Dynamic Stiffness of the Supports 78
4.4.6 Reflection and Transmission Coefficients 81
4.5 Summary 85

Chapter 5 Wave Reflection and Transmission at Angled Bends 87
5.1 Introduction 87
5.2 Wave Fields in Some Joint Networks 88
5.3 Reflection and Transmission Coefficients in terms of the Parameters of an Angled Bend 89
5.3.1 Reflection and Transmission Coefficient Matrices 89
5.3.2 Parametrical Model of the Angled Bend 90
5.3.3 Reflection and Transmission Coefficients 92
5.3.4 Power Reflection and Transmission Coefficients 95
5.3.5 Rigid Massless Right-angled Connection 96
5.3.6 Mass-like Joint 97
5.3.7 Spring-like Joint 102
5.3.8 Damping of the Joint 104
5.4 Reflection and Transmission Coefficients in terms of Wave Amplitudes 105
5.5 Experiments on a Right-angled Pipe Bend 107
5.5.1 Experimental Setup 107

5.5.2 Cut-on Frequency for n =2 wave mode 108
5.5.3 Wavenumber Measurements 109
5.5.4 Measured Reflection and Transmission Coefficients 111
5.6 Summary 117

Chapter 6 Parameter Identification 119
6.1 Introduction 119
6.2 Generic Problem 120
6.3 Parameter Estimation Methods 122
6.3.1 Direct Method 122
6.3.2 Iterative Method 123
6.3.2.1 Nonlinear Least-squares Problem 123
6.3.2.2 Gauss-Newton Method 123
6.4 Application of Parameter Estimation Methods to Joints 125
6.4.1 Direct Method for a Mass-like Discontinuity 127
6.4.2 Iterative Method for a Mass-like Discontinuity 128
6.4.3 Iterative Method for a Right-angled Joint 130
6.5 Some Issues Concerning the Iteration Process 132
6.5.1 Choice of Objective Function 132
6.5.2 Selection of Frequency Range 133
6.5.3 Initial Estimate of Parameters 133
6.5.4 Termination of Iteration 134
6.5.5 Evaluating the Goodness of the Estimates 135
6.6 Numerical Simulations on a Mass-like Discontinuity 136
6.6.1 Effect of Selected Frequency Range 137
6.6.2 Sensitivity of the Objective Function to Parameters 139
6.6.3 Effect of Initial Parameter Values 141
6.7 Summary 142

Chapter 7 Experimental Validation of the Parameter Identification Method 144
7.1 Introduction 144
7.2 Parameter Identification of the Mass/Moment of Inertia Discontinuity on a Beam 144
7.2.1 Results over Different Frequency Ranges 145
7.2.2 Results from Measured Transmission Coefficients 147
7.2.3 Results from Normalised Reflection or Transmission Coefficient 149
7.2.4 Accuracy of the Identified Results 150
7.2.5 Results for Blocks 2 and 3 151
7.3 Parameter Identification of Pipe Supports 152
7.4 Parameter Identification of a Right-angled Pipe Bend 155
7.5 Summary 158

Chapter 8 Conclusions 160
8.1 Introduction 160
8.2 Modelling of Joints and Discontinuities 160
8.3 Measurement Considerations 161
8.4 Parameter Identification 161
8.5 Validation of Parameter Identification Approach 162
8.6 Future Work 163

References…… 164

Appendix 1 Longitudinal Wave Propagation in Rods 168
Appendix 2 Bending Wave Propagation in Beams 171
Appendix 3 Simplification of the general equation for the reflection and transmission coefficients of a mass and moment of inertia discontinuity 176
Appendix 4 Some definitions of Symbols 178
Appendix 5 Mean Values and Variances of Noisy Reflection and Transmission Coefficients 181
Appendix 6 Conditions for Euler-Bernoulli beam theory and cut-on frequency for n=2 wave mode in terms of non-dimensional frequency ξ^2 187
Appendix 7 Direct Measurements of the Translational Dynamic Stiffnesses of Pipe Supports 189
Appendix 8 Mass-loading Effect of the Force Transducer 191
Appendix 9 Direct Measurements of the Rotational Dynamic Stiffnesses of Pipe Supports 193
Appendix 10 Derivative of a Matrix to a Variable 195
Appendix 11 Stiffnesses of Several Pipe Support Models 196

List of Figures

Figure 2.1 A rod lying along x-axis 13
Figure 2.2 Wave field of an infinite beam 15
Figure 2.3 Wave field at a discontinuity 18
Figure 2.4 Wave vectors at two points of a waveguide lying along x-axis 21
Figure 2.5 Waves at a discontinuity at $x = x_j$ 22
Figure 2.6 Wave reflection at a boundary 23
Figure 2.7 Element j with input and output forces and displacements 24
Figure 2.8 A beam with a mass discontinuity at $x = 0$ 26
Figure 2.9 Magnitudes (squared) and phases of the flexural reflection and transmission coefficients for the mass discontinuity 29
Figure 2.10 Regions of $\rho = 0$ and $\tau = 0$ for the mass discontinuity 29
Figure 3.1 Local coordinate of transducers 34
Figure 3.2 Waves in two semi-infinite waveguides connected by a joint 34
Figure 3.4 Monte Carlo simulations of the power reflection coefficient 44
Figure 3.5 First order approximations and MC simulations of (a) the mean value and (b) the variance of $\hat{\rho}$ 45
Figure 3.6 Closed form solutions for the upper bound normalised standard deviation of $\hat{\rho}$ 46
Figure 3.7 Normalised probability density of $\hat{\rho}$ with zero mean and unit variance for various values of $k_b\Delta$ 48
Figure 3.8 Skew and Kurtosis of the MC simulations on $\hat{\rho}$ 48
Figure 3.9 Transducer array for wavenumber measurements 50
Figure 3.10 Experimental setup for measurements on a beam with a mass and moment of inertia discontinuity 52
Figure 3.11 Steel blocks attached to the beam as discontinuities 52
Figure 3.12 Algebraic average of the acceleration ratios for wavenumber measurements of a beam 53
Figure 3.13 Wavenumber of the beam 54
Figure 3.14 Magnitudes of the measured accelerances for block 1 56
Figure 3.15 Decomposed wave amplitudes of at the centres of the transducer pairs for block 1 56
Figure 3.16 Decomposed power reflection and transmission coefficients of block 1 57
Figure 3.17 Sum of measured power reflection and transmission coefficients 57
Figure 3.18 Power reflection coefficients of block 1 58
Figure 3.19 Power transmission coefficients of block 1 59
Figure 3.20 Sum of the estimated power reflection and transmission coefficients 59
Figure 3.21 Power reflection and transmission coefficients for blocks 2 and 3 60
Figure 4.1 Cylindrical shell coordinates and wavenumbers 63
Figure 4.2 Cross-sectional mode shapes of a cylindrical shell 64
Figure 4.3 The model of a support of an infinite one-dimensional waveguide 65
Figure 4.4 Model of a support featured with mass, moment of inertia and stiffnesses 67

Figure 4.5 Magnitudes (squared) and phases of the propagating wave reflection and transmission coefficients for the support 68
Figure 4.6 Power reflection and transmission coefficients of a support 69
Figure 4.7 The influence of damping on the power reflection coefficient ρ 70
Figure 4.8 Experimental rig for measuring the reflection and transmission coefficients of a pipe support 72
Figure 4.9 Wavenumber of the pipe 73
Figure 4.10 Experimental rig for direct measurements of the translational dynamic stiffness of the pipe supports 74
Figure 4.11 Translational dynamic stiffness of the long aluminium pipe support 75
Figure 4.12 Experimental rig for direct measurements of the rotational dynamic stiffness of the pipe supports 76
Figure 4.13 Measured accelerances of the long aluminium support 77
Figure 4.15 Free body diagram of the experimental rig for directly measuring the rotational dynamic stiffness 78
Figure 4.16 Directly measured rotational dynamic stiffness of the long aluminium pipe support 80
Figure 4.17 Power reflection coefficient of the long aluminium support 82
Figure 4.18 Power transmission coefficient of the long aluminium support 83
Figure 4.19 Sum of power reflection and transmission coefficients of the long aluminium support 83
Figure 4.20 Power reflection and transmission coefficients of the short aluminium support 84
Figure 4.21 Power reflection and transmission coefficients of the long steel support 84
Figure 4.22 Power reflection and transmission coefficients of the short steel support 85
Figure 5.1 Typical structures in pipe networks 88
Figure 5.2 Wave fields in a right angled structure 89
Figure 5.3 Wave amplitudes at an arbitrary-angled bend 90
Figure 5.4 Model of an angled bend 91
Figure 5.5 Free body diagram of the angled bend and each waveguide 92
Figure 5.6 Power reflection and transmission coefficients of the rigid massless joint 97
Figure 5.7 Power reflection and transmission coefficients of the mass-like joint 100
Figure 5.8 Power reflection and transmission coefficients of the mass-like joint 100
Figure 5.9 First order approximations for the power reflection and transmission coefficients of the mass-like joint 101
Figure 5.10 First order approximations for the power reflection and transmission coefficients of the mass-like joint 101
Figure 5.11 Power reflection and transmission coefficients of the spring-like joint 103
Figure 5.12 Power reflection and transmission coefficients of the spring-like joint 104
Figure 5.13 Power reflection and transmission coefficients of the right-angled bend 105
Figure 5.14 Wave field in the right-angled pipes 106
Figure 5.15 Experimental rig for measurements of the reflection and transmission coefficients of a right-angled pipe bend 108
Figure 5.16 Placement of the accelerometers to measure the cut-on frequency for the $n = 2$ wave mode 109
Figure 5.17 Measured transmissibility, a_2/a_1 between the two accelerometers shown in Figure 5.16 109
Figure 5.18 Magnitude of $(W_1 + W_3)/2W_2$ for wavenumber measurements of the right-angled pipe 110

Figure 5.19 $\cos k_b \Delta$ for the pipes ……..110
Figure 5.20 Measurement method of the axial wave motion. 111
Figure 5.21 Flexural wave amplitudes in each pipe 112
Figure 5.22 Axial wave amplitudes in each pipe 112
Figure 5.23 Power reflection and transmission coefficients of the pipe bend 113
Figure 5.24 Power reflection coefficient ρ_{PP} of the pipe bend 115
Figure 5.25 Power transmission coefficient τ_{PP} of the pipe bend 115
Figure 5.26 Power reflection coefficient ρ_{PL} of the pipe bend 116
Figure 5.27 Power transmission coefficient τ_{PL} of the pipe bend 116
Figure 5.28 Sum of the power reflection and transmission coefficients of the pipe bend 117
Figure 6.1 Joint with three coplanar waveguides 120
Figure 6.2 A mass-like discontinuity attached to a uniform beam 126
Figure 6.3 Flow chart of joint parameter identification based on simulated response data 126
Figure 6.4 Flow chart of Gauss-Newton solution procedure on a simple mass-like discontinuity 130
Figure 6.5 Grid of the range of estimated μ and ϑ for the simple mass-like discontinuity 134
Figure 6.6 Numerical simulations of noisy power reflection coefficient 137
Figure 6.7 Identified power reflection coefficient in the frequency range 139
Figure 6.8 Objective function in the four frequency ranges 140
Figure 6.9 Contour plot of the objective function in the frequency range of case 4 with starting parameters 141
Figure 6.10 Contour plot of the objective function in the frequency range of case 4 with starting parameters 142
Figure 7.1 Power reflection coefficient of block 1 146
Figure 7.2 Objective function based on power reflection coefficient for block 1 146
Figure 7.3 Power transmission coefficient of block 1 148
Figure 7.4 Normalised power reflection and transmission coefficients of block 1 149
Figure 7.5 Power reflection and transmission coefficients for blocks 2 and 3 151
Figure 7.6 Power reflection and transmission coefficients of the long aluminium support 153
Figure 7.7 Power reflection and transmission coefficients of the short aluminium support 153
Figure 7.8 Power reflection and transmission coefficients of the long steel support 154
Figure 7.9 Power reflection and transmission coefficients of the short steel support 154
Figure 7.10 Results for the power reflection and transmission coefficients of the right-angled bend when iterating on the rotational stiffness using 157
Figure 7.11 Results for the power reflection and transmission coefficients of the right-angled bend when iterating on the rotational stiffness using 158
Figure A7.1 Translational dynamic stiffness of the short aluminium support 189
Figure A7.2 Translational dynamic stiffness of the long steel support 190
Figure A7.3 Translational dynamic stiffness of the short steel support 190
Figure A8.1 Experimental Setup for measuring the mass-loading effect of the force transducer 191
Figure A8.2 Measured dynamic mass of the transducer for the two positions 192
Figure A9.1 Rotational dynamic stiffness of the short aluminium support 193

Figure A9.2 Rotational dynamic stiffness of the long steel support 194
Figure A9.3 Rotational dynamic stiffness of the short steel support 194
Figure A11.1 Translational stiffness of two clamped parallel bars 196
Figure A11.2 Translational stiffness at the middle point of a bar with simply-supported ends 197
Figure A11.3 Translational stiffness at the middle point of a bar with clamped ends .. 197
Figure A11.4 Torsional stiffness at the middle point of a bar with clamped ends 198

List of Tables

Table 2.1 Wave amplitude reduction due to damping of waveguide for bending waves 17
Table 3.1 Amplitude reduction of nearfield waves with distance 42
Table 3.2 Properties of the beam and discontinuity 43
Table 3.3 Dimension of the beam and steel blocks 54
Table 4.1 Properties of the pipe 72
Table 4.2 Estimated translational parameters of the supports 75
Table 4.3 Rotational parameter fit of the supports 80
Table 4.4 Modified values of the directly measured parameters of the supports 82
Table 6.1 The estimated values of μ and ϑ in different frequency ranges 138
Table 6.2 Step changes of μ and ϑ relative to true values and the condition number of $\mathbf{S}$ in the last iteration 140
Table 7.1 Estimates of the parameters of block 1 from measured power reflection coefficient 147
Table 7.2 Estimation of the parameters of block 1 from measured power transmission coefficient 148
Table 7.3 Estimates of the parameters of block 1 from normalised power reflection or transmission coefficient 150
Table 7.4 Goodness of the estimation for block 1 in terms of R^2 150
Table 7.5 Estimates of the parameters of blocks 2 and 3 from normalised measured reflection and transmission coefficients 152
Table 7.6 Estimates of the parameters of the pipe supports from $\hat{\rho}/(\hat{\rho}+\hat{\tau})$ 155
Table 7.7 Relative change of parameters and condition number of the Jacobean matrix 155
Table A11.1 Stiffnesses of pipe supports based on several boundary condition assumptions. 198

Glossary of Symbols

Abbreviations

FEM	Finite Element Method
FRF	Frequency Response Function
MC	Monte Carlo
RMSE	Root Mean Square Error
SEA	Statistical Energy Analysis
SVD	Singular Value Decomposition
SSE	the sum of squares due to errors
SSR	the total sum of squares
SST	the sum of squares about the mean
TMM	Transfer Matrix Method

Symbols

$\| \ \|_2$	p_2 (Euclidean) norm
$[\ ]$	Matrix
$[\ ]^+$	pseudo-inverse of a matrix
$\{\ \}$	Vector
$\hat{}$	noisy or measured reflection coefficient or transmission coefficient

Roman Letters

A	cross-section area
$\mathbf{A}$	wave amplitude vector; vector
$\mathbf{B}$, $\mathbf{C}$	vector or matrix
D	dynamic stiffness
$\mathbf{D}$	dynamic stiffness matrix; mass matrix
E	Young's modulus; expectation of a variable
F	force; objective function

F	internal force vector
K	stiffness
I	second moment of area
J	moment of inertia
M	moment
N	noise in the measured displacement
P	power; axial force; probability density function
Q	transverse force
R	reflection coefficient matrix; residual
S	propagation matrix; Jacobean matrix
T	transmission coefficient matrix
U	amplitude of longitudinal displacement
V	velocity
W	amplitude of transverse displacement
W	displacement vector; weighting matrix
X	displacement
X	vector of unknown parameters
Y	measured or predicted response
Z	impedance
a	wave amplitude; acceleration
a	wave amplitude vector
b	wave amplitude; width
b	wave amplitude vector; vector
c	wave speed
c	wave amplitude vector
d	wave amplitude vector
e	eccentricity
f	frequency; force
h	thickness
k	wavenumber
l	length
m	mass
n	circumferential mode number

r	wave amplitude reflection coefficient
t	time; wave amplitude transmission coefficient
u	longitudinal displacement
w	transverse displacement
x	Cartesian coordinate x variable
y	Cartesian coordinate y variable
$\mathbf{z}$	vector

Greek Letters

β	wavenumber constant of proportionality
β_2	kurtosis
χ	dimensionless translational stiffness
δ	norm of difference between the parameter vector
ε	perturbation on a noise free value of wave amplitude; small values
γ	distance of exciting point to the central axis; impedance ratio
γ_1	skew
η	damping loss factor
κ	radius of gyration
λ	wavelength
μ	dimensionless mass; mean value
ν	wavenumber ratio
θ	angle in the polar system
ϑ	dimensionless moment of inertia
ρ	density; power reflection coefficient
σ	standard deviation; impedance ratio
σ^2	variance
τ	power transmission coefficient
ω	angular frequency
ξ^2	dimensionless frequency
ψ	dimensionless rotational stiffness
Δ	transducer spacing

φ	vector with elements given by $\sqrt{f_i}$
ω	vector with elements given by $\arccos\left[\left(W_1+W_3\right)/2W_2\right]_i$
Φ	internal force matrix
Λ	matrix
Ω	element of transfer matrix
Ψ	displacement matrix

Subscript/superscript

+	positive-going
–	negative-going
0	location of discontinuity
D	dynamic stiffness
H	complex conjugate
R	rotational
T	transverse of a matrix
T	transverse direction
N	nearfield wave
P	propagating flexural wave
a	waveguide *a*
b	flexural wave; waveguide *b*
c	complex
cs	helical wave
g	group velocity
i	incident
j	number
l	longitudinal wave
m	measured
q	dimension of a vector
r	reflected; ring frequency
s	circumferential wave; segment
t	transmitted

Chapter 1 Introduction

1.1 Background

Beams, bars and pipes are widely used in many fields of engineering such as construction of buildings, power generation facilities, oil refineries, ships and exhaust systems for internal combustion engines. Unintentionally, they also act as waveguides, conveying vibrational energy away from the source of excitation via wave propagation through the structure [1-4]. The transmission of structure-borne sound from built-up structures and, more generally, to the infrastructure to which the waveguides are connected is an annoyance and can become a health and safety issue, or compromise stealth of military vehicles. Dynamic modelling of these structures is often required to determine typical in-operation stress cycles for fatigue predictions, to assess structural integrity and to monitor the condition of the systems by comparison with vibration measurements. Currently available prediction techniques for vibration involve compromises between the conflicting demands of accuracy and complexity. Improved techniques are required to model built-up structures while retaining a physical insight into vibration behaviour.

Built-up piping systems often comprise many joints or discontinuities in the form of flanges, hangers, supports, valves, pumps and changes in section. Dynamically, these joints contribute stiffness, inertia and damping and can dramatically alter the response of the system. A robust technique for parametric joint identification would benefit many areas of dynamic modelling, such as improved narrowband prediction of vibration response, quantification of Statistical Energy Analysis (SEA) parameters (coupling and damping loss factors), for energy flow predictions, condition monitoring of structures and quantification of statistical variation in jointed structures due to manufacturing processes and installation. In this thesis, an integrated, systematic procedure to estimate joint parameters reliably from vibration measurements is presented which makes use of

wave models of the systems.

1.2 Modelling Methodologies

Among currently available prediction techniques for vibration in built-up systems, the Finite Element Method (FEM), SEA, the Transfer Matrix Method (TMM) and the wave propagation approach are frequently used.

The FEM has become commonplace in recent decades and earned itself a good reputation in structural dynamic modelling [5-7]. The fundamental principle of the FEM is to discretise a complicated structure into many small elements (finite elements). The local mass and stiffness matrices for each element are established by assuming that the displacements over the element obey a known prescribed function. The dynamic response characteristics of the structure, such as natural frequencies and mode shapes, can be derived by relating the global mass and stiffness matrices to local ones via continuity and equilibrium conditions. The damping properties of the structure are usually modelled by introducing a proportional damping matrix. Numerical solutions to even very complicated geometries can now be obtained routinely using the FEM. The geometries of beams, bars and piping systems, however, are relatively simple and do not call for the versatility of the FEM with its associated disadvantages. The underlying premise of the FEM is that the response at any position in an element can be approximated by a prescribed function of the responses at the nodes of the element. At high frequencies, when wavelengths become short, to achieve an accurate result, the mesh of the FEM must be further refined. FE models may become very large and the program will be expensive to run. Consequently, it may fail to predict the dynamics of structures with confidence and reasonable computational cost. Furthermore, the numerical solution does not help to understand the physical essence of the problem.

SEA has been applied with some success to power flow in one-dimensional systems [8-10]. The basic premise of SEA is that the energetic exchange can be modelled in a way which is similar to heat diffusion between the hotter subsystem and the cooler one. SEA is particularly suited to systems with a large modal density and modal overlap, i.e. for

high frequencies, where a deterministic analysis of all the resonant modes of vibration is not practical. The weakness of the SEA stems from its heuristic and constrained hypothesis: the subsystems are weakly coupled and only an energy level for each subsystem can be estimated. This can undermine the confidence in the results from the conventional SEA models.

The TMM has been an attractive approach in recent years [11-13]. The coupled response of individual elements that support axial, torsional, bending and fluid waves can be predicted easily by applying appropriate continuity and equilibrium conditions. Each typical element can be described by a transfer matrix and the system transfer matrix can be assembled by successive multiplication of the transfer matrices of the components. However, the transfer matrices can become ill conditioned or even singular at some frequencies. The TMM is discussed in detail in Chapter 2.

1.3 Wave Propagation Approach

Beams, bars and piping systems can be considered as one-dimensional waveguides. The wave propagation approach [1-4], therefore, has been widely used in the analysis of the response of these systems. This approach deals with vibration of elastic structures such as strings, beams, and plates in terms of waves propagating and attenuating in waveguides. The wave amplitudes are chosen as the degrees of freedom by which the displacements and internal forces of the waveguides can be fully expressed. This method can accommodate branches and can be used to analyse complex structures such as multi-span beams and trusses. The physical characteristics associated with the vibration of the structure can be revealed easily by the wave propagation approach. In this thesis, this approach is employed to analyse wave propagation in one-dimensional waveguides and wave reflection and transmission at discontinuities or joints. The reflection and transmission coefficients of the discontinuities, which are introduced in detail in Chapter 2, are derived for some typical structures and used to estimate the parameters of the discontinuities.

In this thesis, several chapters are concerned with wave propagation, reflection and transmission in *in-vacuo* piping systems. The dynamic response of a pipe varies largely according to the pipe length, diameter and wall thickness. At high frequencies, the distortion of the cross section must be considered. However, it is negligible at low frequencies for long, slender and thick-walled pipes. In general, only the axial, torsional and transverse flexural (bending) wave modes are of practical interest at low frequencies in these structures. In this thesis, only *in-vacuo* piping systems are of concern and only the axial, torsional and transverse flexural waves are considered. The wave modes associated with cylindrical shells are briefly discussed in Chapter 4.

1.4 Uncertainties of Joints and Discontinuities

The properties of discontinuities depend on the boundary conditions. Joints of built-up systems are affected by the friction, elasticity and the relative dimensions of all interacting parts. Each factor varies from joint to joint because of manufacturing tolerances. As a result, all joints and jointed structures have parametric uncertainty. Structural joints can be regarded as sources of energy dissipation due to contacting surfaces undergoing relative motions. Energy dissipation through joints in built-up structures has been studied [14-16] and it was found that the joint friction exhibited viscous-like damping characteristics when the normal force was allowed to vary with the relative slip amplitude. The energy dissipation in mechanical joints depends on the clamping pressure. Beards and Williams [17] showed in their experiments on a frame structure that a useful increase in damping could be achieved by fastening joints tightly enough to prohibit translational slip, but not tightly enough to prevent rotational slip. Dowell [18] and Tang and Dowell [19, 20] investigated the non-linear response of beams and plates to sinusoidal and random excitations at a point close to one end, and with dry friction damping due to slippage at the support boundaries. The response statistics in terms of the normal load at the support joints by using a statistical linearisation method, numerical solution and experimental tests revealed that the stick-slip and stick phenomena take place as the normal load increases. Esteban and Rogers [21] examined an analytical approach to determine the energy dissipation through joints at high frequency and its relation to the localised actuation-sensing region surrounding

an integrated piezoceramic actuator.

In real applications, most of the boundary conditions are not ideal, for example, infinite stiffness for clamped ends can not be obtained. Wang and Chen [22] represented the unknown boundaries of a slender beam by a boundary stiffness matrix in their FE model and determined the stiffness matrix from measured structural modal parameters. Lee and Kim [23] used frequency-dependent transverse and torsional springs to represent the non-ideal boundary conditions on a beam. The effective boundary stiffness constants were estimated from the measured Frequency Response Functions (FRFs) by the spectral element method. The spectral element method relates the vector of forces and moments at the boundaries to the vector of degrees of freedom at the boundaries through the spectral element matrix.

Doyle and Kamle [24] studied the a parametric model of a T-joint experimentally and found that the dynamic response was not sensitive to the particular values of the joint model but depended mainly on the member arrangement and only secondarily on the particular shape and mass of the joint.

Damping in joints and fasteners is mainly generated by friction in the screw thread, gas pumping, asperities of contact surfaces and plastic deformation. The stiffness is affected by the hardness and roughness of contact surfaces. The mass and inertia depend mostly on the dimensions and material of the structure. In most cases, these parameters cannot be accurately modelled due to uncertainties in the manufacture and assembly, variability of material properties and dimensions. Parameter uncertainties of joints have been qualified by fuzzy parameters [25, 26], which uses fuzzy logic to investigate the possible distribution of the parameters. However, for a practical structure, this method can not help to predict the response precisely, which undermines its superiority in practical engineering applications.

1.5 Brief Introduction to Joint Identification

Identification of joint parameters is required in predicting the dynamic characteristics of

mechanical systems. The main purpose of joint identification is to estimate the joint parameters that minimise the difference between the measured assembly response, such as FRFs and that predicted analytically or numerically [27-31]. There is no doubt that due to the problems of inaccuracy in theoretical models and limitations in measurements, significant discrepancies are often found to exist between analytical predictions and experimental results [32]. In this situation, system identification techniques have been popular in the structural dynamics area. They aim to develop a model of a system based on experimental measurements. The model to be identified may be parametric or non-parametric (black-box problem), and sometimes may be nonlinear. The problem of identifying the parameters of a structure involves two main steps: the first is to establish an appropriate parametric model for the structure; the second is to estimate the corresponding parameters by experimental observation.

Over recent decades, modal testing has developed quickly for the experimental evaluation of the dynamic properties [33]. This method extracts the modal data (natural frequencies, damping loss factors and mode shapes) from measurement data first and then uses these data to obtain the mass, stiffness and damping properties of the model. It is supposed to identify the 'true' vibration characteristics of a structure from the 'correct' assumptions regarding mass, stiffness and damping properties.

In structural dynamics, modal testing may be considered as a special area of system identification. It became an extremely active research topic with the rapid development of digital computers since the 1960s [33]. However, the number of coordinates is limited and number of modes is incomplete due to various practical restrictions in measurements, such as a limited number of measurement locations, limited frequency range, measurement noise, and so on. The consequence is that the information acquired is primarily available as modal parameters, rather than spatial properties [28]. In order to correct the inaccurate spatial properties of the structure, a new technique, model updating was proposed [6, 27, 29, 30, 34-36]. It aims at adjusting the mass, stiffness and damping parameters of an existing FE model in the light of a measured vibration test. After adjustment, the updated model is expected to represent the dynamic behaviour of the structure more accurately. More mathematical and comprehensive surveys about model updating method were presented by Natke [34], Natke *et al* [36] and Imregun and Visser [35]. Natke [37] seems to be the first to use direct system identification for the

identification of a system without updating a reference model. He referred to model updating as indirect system identification. Berman [38, 39] made strong contributions to structural system identification. He pointed out that it is usually the result of improper actuator or sensor location or limited frequency range involved in the experimental tests. Coordinate incompleteness (too few sensor locations) can give rise to problems of ill-conditioning and non-uniqueness. This can be overcome by extracting the information from an *a priori* model rather than purely from the experimental records.

Model updating involves data post-processing, which may introduce processing errors. Accurate modal parameters are not easily obtained for structures containing closely spaced modes or large modal damping [40] and sometimes it is impossible to measure all possible modes of interest. In order to overcome these shortcomings, rather than convert the measurement data into modal data, researchers try to use them directly. The data can be FRFs [41-45] or time responses [46]. The substructure synthesis method has been widely applied to joint identification from direct use of measured data. Tsai and Chou [41] extracted the properties of a single bolt joint directly from the measured FRFs of the substructures and the assembled structure. Then the results were checked by a synthesis method based on the receptance method. Wang and Liou [42] synthesised the FRFs of a two-beam structure by using diagonal matrices for the linear joint springs and dampers. They introduced a simple method based on statistical criteria to reduce the effect of measurement noise. Ren and Beards [43, 47-49] generalised the FRF joint identification technique for systems involving rigid and flexible joints. Mottershead and Stanway [44] proposed an algorithm for obtaining structural parameters from FRF measurements. However, the algorithm may not be practical for cases where measurements are not possible for certain locations. Hong and Lee [45] proposed a method to identify the linearised joint parameters of a structure using the measured FRFs of a structure and the computed FRFs of an auxiliary model. Thus inverting the measured FRF matrices is avoided. Hwang [50] determined the damping and spring constants of a joint by measuring the FRFs of a structure with and without connections. Yang and Park [40] treated the joint model as a coupled stiffness matrix, and identified the translational and rotational stiffness of the joint by the substructure synthesis method. The damping properties were not considered. Rong and Tzou [51] developed a theoretical model of elastic joints considering the joint friction and clearance effects. A time-domain system identification method was presented to estimate the dynamic

contact parameters of elastic joints and the eigenvalues of jointed structures. Ma *et al*. [46] constructed a non-parametric model for a joint from the comparison of the overall dynamics of two bolted beams to that of a similar but unbolted beam. Then a numerical algorithm was developed to identify the joint force. The approach is not expected to be applied to more complex models. Frikha *et al*. [52] developed a method to estimate in a least squares sense the physical joint parameters that most closely replicate measured response. However, this approach is ineffective in "bands of critical frequencies", which makes robust implementation tenuous.

This thesis develops a similar parameter identification approach to reference [52] but applied to wave-based models. Modal analysis is good at solving systems with single-degree-of-freedom and multi-degree-of-freedom. But wave approach is good at analysing continuous systems, especially at high frequency. Wave models can be written in a well-conditioned way at all frequencies, which is superior to methods based on modal analysis, such as FEM and SEA. In fact, models have been developed for a change in section of a two-rod system with longitudinal waves [53]. But the theory has not been verified by practical measurement. Frequently, inertia is modelled explicitly but the joint is assumed to be perfectly rigid [24, 54, 55]. Stiffness can be introduced by using discrete elements [56, 57]. Damping can be incorporated for reasons of convenience by complex Young's moduli [58], the use of discrete elements [59, 60], or omitted altogether [56]. Reflection and transmission coefficients have been derived in terms of the parameters of the discontinuities [54, 61] and measured in a single discontinuity [24, 62, 63]. However, the related problem of estimating the parameters from measured output has not been considered. This thesis discusses the parameter identification of discontinuities from reflection and transmission coefficient measurements and in particular the estimation of joint properties in structural waveguides such as beams. Identifying physical parameters in this way can yield a better conditioned inverse problem and also greatly facilitate simultaneous identification of more than one joint of a piping system *in situ*.

1.6 Objectives

The aim of this research is to develop a systematic procedure for accurate modelling of joints in structural waveguides and parameter identification of the joint models. The specific objectives are to:

1) develop a theoretical and computational framework for the assembly of wave models for joints in structural waveguides using continuous elements supporting flexural, longitudinal etc. wave modes;
2) adapt model updating techniques to joint identification of wave models;
3) investigate the robustness of wave model joint identification to wave amplitude measurement techniques;
4) examine the applicability of joint identification techniques to the developed wave models with measured wave response.

1.7 Contributions of the Thesis

The research has demonstrated that parameters of joints can be successfully identified from measured reflection and transmission coefficients. The reflection and transmission coefficients are used since they have several advantages over modal information. First, these coefficients characterise the joint and adjacent waveguides but are independent of the rest of the built-up system; second, they are potentially more sensitive to the joint parameters in question. The main contributions of the thesis are summarised as follows:

1) Depending on the contribution of the properties of the discontinuities, such as mass/inertia, stiffness and damping, appropriate dynamic models are selected for three types of joints, mass discontinuities on beams, a supported straight pipe and a right-angled pipe bend. The effect of joint parameters on wave reflection and transmission coefficients has been investigated through closed form solutions and numerical simulations.
2) A measurement noise model of individual transducers is developed to simulate the influence of measurement noise on the estimated reflection and transmission coefficients. Closed form solutions are derived for the mean values and variances of

the noisy reflection and transmission coefficients. Monte Carlo simulation results agree well with the derived statistical results.

3) The Gauss-Newton method is first applied to the parameter identification of discontinuities through iteration on reflection and transmission coefficients. Issues concerning the iteration process, such as the selection of frequency range, objective function and initial parameter values and assessment of goodness of identification are examined. Numerical case studies indicate the sensitivity of the objective function to the unknown parameters is significant to the identification accuracy.
4) Applicability of the Gauss-Newton method to the parameter identification of discontinuities in waveguides is demonstrated using experimentally measured data on various structures. The parameters of the discontinuity models are successfully estimated.

1.8 Overview of the Thesis

Owing to the uncertainties of the joints and discontinuities in built-up systems, there is no ideal technique and there is a strong case to develop continuous models to accommodate more complex configurations. Parameter identification of joints and discontinuities in built-up structures has been widely discussed by using modal updating or direct FRF measurements. In this thesis, a novel approach is developed through which the parameters of joint and discontinuity models can be estimated from measured reflection and transmission coefficients.

Chapter 2 reviews a general approach for analysing wave propagation, reflection and transmission in waveguides carrying various wave modes. A technique is described to derive the reflection and transmission coefficients of the discontinuities when only one particular wave mode is of interest. As an example, this method is applied to a mass/inertia discontinuity in a straight beam.

Chapter 3 investigates the influence of the measurement noise on the estimated reflection and transmission coefficients from FRF measurements. A Gaussian-like noise model is introduced to the transducer array measurements as a perturbation and the

statistics of the estimated reflection and transmission coefficients by a wave amplitude decomposition method are discussed. Measurements on the reflection and transmission coefficients of a mass/inertia discontinuity in a steel beam are performed.

The general approach given in Chapter 2 is applied to other typical discontinuities, namely one-dimensional waveguide supports and angled bends in waveguides in Chapters 4 and 5 respectively. Experiments are performed to obtain the reflection and transmission coefficients from FRF measurements. The parameters of the pipe supports are also measured directly.

Chapter 6 examines an iterative method to solve the non-linear problem of parameter identification of the discontinuities from the measured reflection and transmission coefficients. This method is then successfully applied to the three typical discontinuities in Chapter 7 to estimate the parameters. Finally Chapter 8 summarises the results of this research in the parameter identification of discontinuities in waveguides and recommends key issues for further research.

Chapter 2 Wave Propagation, Reflection and Transmission in Waveguides

2.1 Introduction

The wave propagation approach has been widely used to analyse the dynamic response of waveguides [1-4]. When there are discontinuities in the waveguides, it is very convenient to use the reflection and transmission coefficients to describe the characteristics of the discontinuities. The basic intention of this thesis is to identify the parameters of a discontinuity in a waveguide from measured reflection and transmission coefficients. This chapter reviews a general approach [64] which aims to relate the reflection and transmission coefficients of discontinuities to the parameters of the waveguides and discontinuities. The reflection and transmission coefficients of all the structures considered in this thesis can be easily derived by this approach.

The next two sections introduce the equations of longitudinal and flexural waves briefly. The torsional wave equation is omitted here since it is similar to the longitudinal one. The damping of the waveguide can be considered by adopting the complex Young's modulus. Its effect is also discussed briefly. The concepts of reflection and transmission coefficients are given subsequently. Then a general wave approach is reviewed. Together with the dynamic stiffness and transfer matrix methods, this approach can be used to analyse the dynamic response of waveguides in which various wave modes are accommodated. Most usefully, the reflection and transmission coefficients can be easily related to the parameters of the waveguides and discontinuities by this approach. As an example, numerical results are presented for the reflection and transmission coefficients of a beam with a mass discontinuity. Then the sensitivity of the reflection and transmission coefficients to the parameters of the discontinuity is discussed. The general approach will also be used in Chapters 4 and 5 to obtain the reflection and transmission coefficients of joint models for pipe supports and a pipe bend.

2.2 Longitudinal Wave Propagation in Rods

Longitudinal waves in rods are compressional/extensional waves, in which the primary motion of the rod and the wave propagation both occur in the longitudinal direction [1-3]. There is also transverse motion perpendicular to the wave propagation direction. However, this motion is negligible if the wavelength in the rod is large compared to the rod's radial dimension. This thesis only considers longitudinal waves under this condition. This section briefly introduces the equation of longitudinal waves in homogeneous, slender rods and its solutions.

The longitudinal wave equation of a slender rod can be derived directly based on the fundamental relationship between stress and strain for a differential mass element. The detailed derivation procedure is omitted here for brevity and only the equation of motion is given. For a homogeneous, slender rod lying along the *x*-axis as shown in Figure 2.1, it can be obtained that [1-3]

$$c_l^2 \frac{\partial^2 u}{\partial x^2} = \frac{\partial^2 u}{\partial t^2} \tag{2.1}$$

where u is the longitudinal displacement and $c_l = \sqrt{E/\rho}$ is the longitudinal wave speed. E and ρ are the Young's modulus and density of the material respectively. The subscript l indicates the longitudinal character of this wave mode. The wave speed increases with increasing stiffness and decreases with increasing density. Since it is independent of frequency, this kind of wave propagates without dispersion. This is not the case for bending waves, which will be discussed later. The wave equation (2.1) is valid for slender rods of arbitrary cross-section.

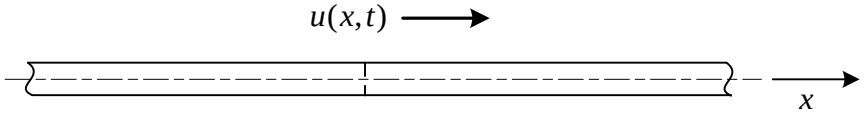

Figure 2.1 A rod lying along x-axis.

By assuming time-harmonic motion and applying the method of separation of variables, the solution to equation (2.1) is assumed to be of the form $u(x,t) = U(x)e^{i\omega t}$. In the

following analysis, the time dependence $e^{i\omega t}$ is suppressed if not explicitly indicated. $U(x)$ is given by

$$U(x) = U^{+}e^{-ik_l x} + U^{-}e^{ik_l x} \tag{2.2}$$

where U^{+} and U^{-} are complex amplitudes, which can be determined from the excitation and boundary conditions. $U^{+}e^{-ik_l x}$ represents a positive-going wave and $U^{-}e^{ik_l x}$ a negative-going wave. The variable

$$k_l = \omega\sqrt{\frac{\rho}{E}} \tag{2.3}$$

is the longitudinal wavenumber, where ω is the frequency in rad/s. It is related to the wave speed c_l by

$$k_l = \frac{\omega}{c_l}. \tag{2.4}$$

Since frequency $f = \omega/2\pi = c_l/\lambda_l$, where λ_l is the longitudinal wavelength, the wavenumber can also be expressed as

$$k_l = \frac{2\pi}{\lambda_l}. \tag{2.5}$$

k_l is inversely proportional to the spatial period λ_l, therefore, the wavenumber k_l can be considered as the spatial analogue of the angular frequency ω. It indicates the phase change of the wave motion per unit length in the direction of propagation.

2.3 Flexural Wave Propagation in Beams

Bending or flexural waves are widely found in wave propagation in solid structures, such as beams and plates. This type of wave is characterised by the particle motion being perpendicular to the direction of propagation. In this section the bending wave equation and its solutions are briefly introduced.

Consider a beam of constant section lying along the *x*-axis shown in Figure 2.2. If an external distributed force $f(x,t)$ is applied to the beam, the partial differential equation for bending waves is given by Euler-Bernoulli beam bending theory [1-3] as

$$EI\frac{\partial^4 w}{\partial x^4}+\rho A\frac{\partial^2 w}{\partial t^2}=f\left(x,t\right). \tag{2.6}$$

where $w\left(x,t\right)$ is the transverse displacement of the beam. The equation gives a good description of the motion in a bending wave field if the wavelength is larger than about six times the thickness of the beam [1].

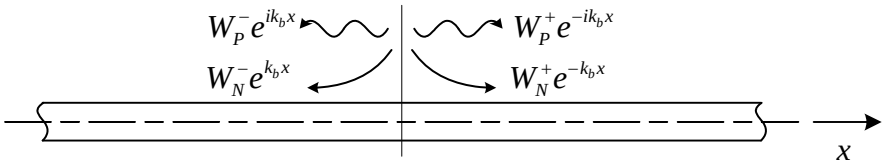

Figure 2.2 Wave field of an infinite beam.

For time harmonic waves in beams, the transverse displacement can be written as

$$w(x,t)=W(x)e^{i\omega t}. \tag{2.7}$$

Substituting the above equation into equation (2.6), for free response ($f=0$), one gets

$$EI\frac{d^4 W}{dx^4}-\omega^2\rho AW=0. \tag{2.8}$$

The general solution to equation (2.8) can be written as

$$W(x)=W_P^+e^{-ik_b x}+W_P^-e^{ik_b x}+W_N^+e^{-k_b x}+W_N^-e^{k_b x} \tag{2.9}$$

where

$$k_b=\sqrt{\omega}\sqrt[4]{\frac{\rho A}{EI}} \tag{2.10}$$

is the bending wavenumber of the beam. It is real and positive unless structural damping is incorporated into the Young's modulus when it will have a negative imaginary part. I is the second moment of area of the cross-section. The first and second terms in equation (2.9) represent waves that propagate in the positive and negative *x*-direction respectively. The third and fourth are the nearfield terms. They have constant phase but decay exponentially with distance in the positive and negative *x*-direction respectively. The near-field terms are of importance only close to excitation points, discontinuities or terminations. The subscripts *P* and *N* denote the propagating and nearfield waves respectively and the superscripts + and − indicate positive- and negative-going waves respectively.

The phase velocity of bending waves $c_b=\omega/k_b$ is

$$c_b = \sqrt{\omega}\sqrt[4]{\frac{EI}{\rho A}}, \tag{2.11}$$

which is frequency dependent. Waveforms composed of various sinusoidal components distort with time, because the higher-frequency components will propagate with a higher velocity than the lower-frequency ones. This is called dispersion [3]. The group velocity is defined by

$$c_g = \frac{d\omega}{dk}, \tag{2.12}$$

which is $2k_b\sqrt{EI/\rho A}$ for bending waves. It determines the velocity of energy propagation along the beam. For bending waves, the group velocity is twice the phase velocity, $c_g = 2c_b$, but they are equal for longitudinal waves.

2.4 Damping Effects of Waveguides

The above analysis does not consider the influence of damping of the structure, which is valid only for ideal situations. In practice the energy contained in a given oscillation will convert into other forms and therefore every oscillation decays with space and time because of the damping. The damping can be simply represented by introducing a complex Young's modulus for the material $E(1+i\eta)$ where η is the damping loss factor. Thus all the parameters associated with Young's modulus will become complex, such as the stiffness, wave velocity and wavenumber. For example, the flexural wavenumber becomes

$$k_b^c = \sqrt{\omega}\sqrt[4]{\frac{\rho A}{EI(1+i\eta)}} \approx k_b\left(1-i\frac{\eta}{4}\right) \tag{2.13}$$

where the first order approximation is valid for small damping, i.e. $\eta < 0.05$. Similarly the complex longitudinal wavenumber can be expressed as $k_l^c \approx k_l(1-i\eta/2)$.

The loss factors of metals are usually considerably smaller than 10^{-3} except some soft ones, such as lead, tin, silver and copper. However, the actual damping of practical structures is determined not only by the loss in the materials but also by friction at supports, interfaces, connections, etc. Loss factors of other materials, sandwich

structures and metal interfaces can be seen in reference [1].

Table 2.1 gives the wave amplitude reduction when propagating along the waveguide due to the damping of waveguides for two kinds of materials, steel and copper. The value given is the amplitude at distance x as a percentage of the amplitude at distance 0. The typical values of the loss factors in the table are quoted from reference [1]. Except for soft metals, the wave amplitude attenuation is very small even over a long distance, say less than 5% in 100 wavelengths.

Table 2.1 Wave amplitude reduction due to damping of waveguide for bending waves. (λ denotes wavelength)

	amplitude, $e^{-k_b x\eta/4}$	
	distance, $x=10\lambda$	distance, $x=100\lambda$
steel: $\eta=2\times10^{-4}$	99.7%	96.9%
copper: $\eta=2\times10^{-3}$	96.9%	73.0%

The damping effects of the discontinuities considered in this thesis will be discussed in later chapters.

2.5 Reflection and Transmission coefficients

This section introduces the concept of reflection and transmission coefficients. Figure 2.3 shows two waveguides connected by a discontinuity. A positive-going wave propagating along waveguide a is incident upon the discontinuity, where a reflected wave and a transmitted wave are generated. At the discontinuity, the amplitudes of the incident, reflected and transmitted waves can be written as a^+, a^- and b^+. Then the wave amplitude reflection and transmission coefficients are defined respectively by

$$r=\frac{a^-}{a^+} \text{ and } t=\frac{b^+}{a^+}. \tag{2.14}$$

Since wave amplitudes are complex, these two coefficients are also complex. They are determined by the characteristics of the waveguide and the discontinuity.

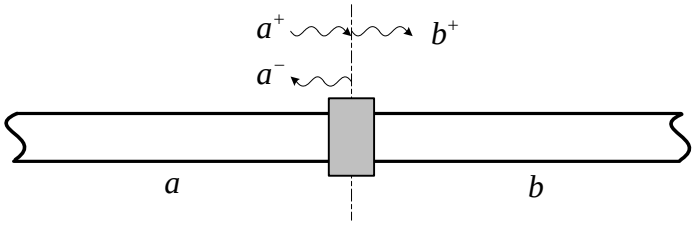

Figure 2.3 Wave field at a discontinuity.

Wave reflection and transmission is actually the redistribution of the energy in the incident wave to the reflected and transmitted waves. The power in a longitudinal wave and a bending wave is given by [1]

$$P = \frac{1}{2}\rho A c_l |V|^2 \text{ and } P = \rho A c_b |V|^2 \tag{2.15}$$

where V is the particle velocity. The power reflection and transmission coefficients can be defined in a similar fashion to the wave amplitude ones as

$$\rho = \frac{P_r}{P_i} \text{ and } \tau = \frac{P_t}{P_i} \tag{2.16}$$

where the subscripts i, r and t represent incident, reflected and transmitted waves respectively. Referring to equation (2.15) and recalling the definition of amplitude reflection and transmission coefficients given in equation (2.14), if there is no wave mode conversion, equation (2.16) becomes

$$\rho = |r|^2 \text{ and } \tau = \frac{Z_b}{Z_a}|t|^2 \tag{2.17}$$

where Z_a and Z_b are the characteristic impedances of the waveguides carrying the incident and transmitted waves. If there is no energy dissipation, the energy involved in the reflected and transmitted waves should equal to that in the incident waves. Thus

$$\rho + \tau = 1. \tag{2.18}$$

In practice owing to the existence of damping, the sum of power reflection and transmission coefficients should be less than unity.

Appendices 1 and 2 summarise the reflection and transmission coefficients of some simple structures in rods and beams.

2.6 A General Wave Approach

This section reviews the general approach developed in reference [64] which relates the displacements and internal forces to the wave amplitudes in a waveguide which might contain various wave modes.

2.6.1 Wave Amplitude, Displacement and Internal Force Vectors

Generally speaking, there might be several different wave modes in a waveguide. At any cross-section the waves can be separated into two groups in terms of the two directions they are travelling, positive and negative. Accordingly, the amplitudes of waves can then be grouped into two vectors

$$\mathbf{a}^{+}=\begin{Bmatrix} a_1^{+} \\ a_2^{+} \\ \vdots \\ a_n^{+} \end{Bmatrix} \text{ and } \mathbf{a}^{-}=\begin{Bmatrix} a_1^{-} \\ a_2^{-} \\ \vdots \\ a_n^{-} \end{Bmatrix}, \tag{2.19}$$

where the superscripts + and − indicate the positive and negative wave travelling directions respectively. For the special case where there are both longitudinal and flexural waves, the wave amplitude vectors are considered to have the form

$$\mathbf{a}^{\pm}=\begin{Bmatrix} U^{\pm} \\ W_P^{\pm} \\ W_N^{\pm} \end{Bmatrix}. \tag{2.20}$$

The displacements and internal forces describe the state of a cross-section at any point in a waveguide. The displacements can also be grouped into a so-called *displacement vector*, $\mathbf{W}$. Similarly, the internal forces moments can be grouped into the *internal force vector,* $\mathbf{F}$. For waveguides only including longitudinal and flexural waves

$$\mathbf{W}=\begin{Bmatrix} U \\ W \\ \partial W/\partial x \end{Bmatrix} \tag{2.21}$$

and

$$\mathbf{F}=\begin{Bmatrix} P \\ Q \\ M \end{Bmatrix}. \tag{2.22}$$

where

$$P = EA\frac{\partial U}{\partial x},\quad Q = -EI\frac{\partial^3 W}{\partial x^3},\quad M = EI\frac{\partial^2 W}{\partial x^2}. \tag{2.23}$$

P, Q and M correspond to axial force, transverse force and moment respectively.

2.6.2 Displacement and Internal Force Matrices

The general displacements and internal forces can be related to the wave amplitudes simply by the displacement and internal force matrices respectively. Thus

$$\mathbf{W} = \begin{bmatrix}\boldsymbol{\Psi}^+ & \boldsymbol{\Psi}^-\end{bmatrix}\begin{Bmatrix}\mathbf{a}^+\\ \mathbf{a}^-\end{Bmatrix} \text{ and } \mathbf{F} = \begin{bmatrix}\boldsymbol{\Phi}^+ & \boldsymbol{\Phi}^-\end{bmatrix}\begin{Bmatrix}\mathbf{a}^+\\ \mathbf{a}^-\end{Bmatrix} \tag{2.24}$$

where $\boldsymbol{\Psi}^+$ and $\boldsymbol{\Psi}^-$ are the displacement matrices, and $\boldsymbol{\Phi}^+$ and $\boldsymbol{\Phi}^-$ are the internal force matrices. For waveguides which involve longitudinal and flexural waves

$$\boldsymbol{\Psi}^+ = \begin{bmatrix}1 & 0 & 0\\ 0 & 1 & 1\\ 0 & -ik_b & -k_b\end{bmatrix},\ \boldsymbol{\Psi}^- = \begin{bmatrix}1 & 0 & 0\\ 0 & 1 & 1\\ 0 & ik_b & k_b\end{bmatrix} \tag{2.25}$$

and

$$\boldsymbol{\Phi}^+ = \begin{bmatrix}-iEAk_l & 0 & 0\\ 0 & -iEIk_b^3 & EIk_b^3\\ 0 & -EIk_b^2 & EIk_b^2\end{bmatrix},\ \boldsymbol{\Phi}^- = \begin{bmatrix}iEAk_l & 0 & 0\\ 0 & iEIk_b^3 & -EIk_b^3\\ 0 & -EIk_b^2 & EIk_b^2\end{bmatrix}. \tag{2.26}$$

These matrices denote the contribution of the wave components to the waveguide deformations and internal forces.

2.6.3 Wave Propagation, Reflection and Transmission Matrices

Waveguides of finite length have boundaries and may have discontinuities along their length. The amplitude of a wave changes with distance while travelling along a waveguide. When a wave impinges on a boundary it is reflected and when it is incident upon a discontinuity then it will be reflected and transmitted. The amplitudes of the reflected and transmitted waves are related to the incident waves by the reflection and transmission coefficients. A particular wave mode may be scattered into other wave modes depending on the particular structure. Therefore, reflection and transmission coefficients may involve wave mode conversion. Reflection and transmission matrices

are composed of these coefficients and are determined by applying the continuity and equilibrium conditions for the particular structure.

Consider two points, $x = x_1$ and $x = x_2$ of a one-dimensional waveguide lying along the x-axis shown in Figure 2.4. The amplitudes of the waves at the two points can be related by

$$\begin{Bmatrix} \mathbf{a}_2^+ \\ \mathbf{a}_1^- \end{Bmatrix} = \begin{bmatrix} \mathbf{S}^+ & \mathbf{0} \\ \mathbf{0} & \mathbf{S}^- \end{bmatrix} \begin{Bmatrix} \mathbf{a}_1^+ \\ \mathbf{a}_2^- \end{Bmatrix}, \tag{2.27}$$

where the subscripts 1 and 2 indicate the positions of the waveguide; $\mathbf{S}^{\pm}$ are the propagation matrices relating the wave propagation of the two points and usually $\mathbf{S}^- = \mathbf{S}^+$. For waveguides which involve longitudinal and flexural waves

$$\mathbf{S}^{\pm} = \begin{bmatrix} e^{-ik_l(x_2-x_1)} & 0 & 0 \\ 0 & e^{-ik_b(x_2-x_1)} & 0 \\ 0 & 0 & e^{-k_b(x_2-x_1)} \end{bmatrix} \tag{2.28}$$

The propagation matrices describe the phase and amplitude changes of the waves as they propagate along the waveguide.

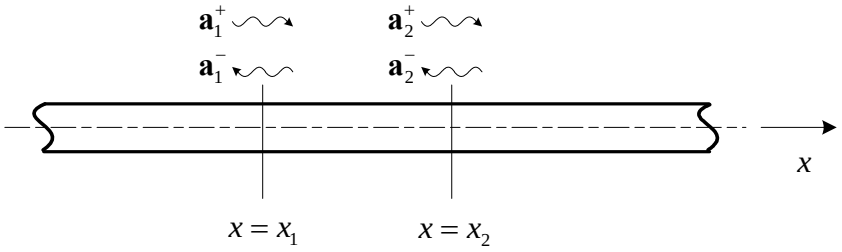

Figure 2.4 Wave vectors at two points of a waveguide lying along x-axis.

Consider a discontinuity connecting two waveguides at junction $x = x_j$ (Figure 2.5). A wave is incident upon the discontinuity, where it is partly reflected and partly transmitted. In general, wave mode conversion occurs, which means an incident wave of one mode might be scattered into waves of all modes. Incident waves of amplitudes $\mathbf{a}_j^+$ and $\mathbf{b}_j^-$ at the junction are scattered into waves $\mathbf{a}_j^-$ and $\mathbf{b}_j^+$. The wave vectors can be related by the reflection and transmission matrix as

$$\begin{Bmatrix} \mathbf{a}_j^- \\ \mathbf{b}_j^+ \end{Bmatrix} = \begin{bmatrix} \mathbf{R}_j^{aa} & \mathbf{T}_j^{ba} \\ \mathbf{T}_j^{ab} & \mathbf{R}_j^{bb} \end{bmatrix} \begin{Bmatrix} \mathbf{a}_j^+ \\ \mathbf{b}_j^- \end{Bmatrix}, \tag{2.29}$$

where **R** and **T** are the reflection and transmission matrices composed of reflection and transmission coefficients. Subscript '*j*' denotes the position of the discontinuity $x = x_j$. Superscript '*ab*' indicates from waveguide a to waveguide b. The rest can be deduced by analogy. For symmetric discontinuities, $\mathbf{R}^{aa} = \mathbf{R}^{bb}$ and $\mathbf{T}^{ab} = \mathbf{T}^{ba}$. If the discontinuity is a boundary, for example, when there is no waveguide b in Figure 2.5, equation (2.29) can be simplified as $\mathbf{a}_j^- = \mathbf{R}_j^{aa}\mathbf{a}_j^+$.

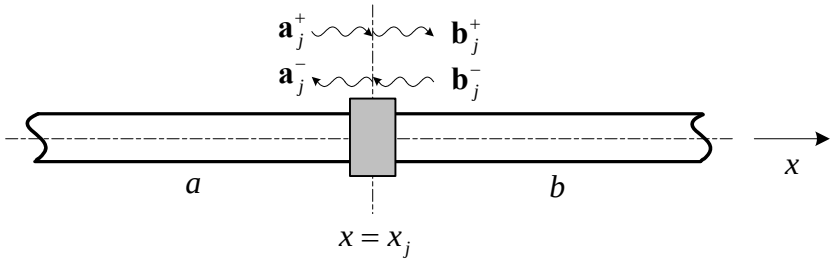

Figure 2.5 Waves at a discontinuity at $x = x_j$.

2.7 Reflection and Transmission Coefficients in Terms of Parameters of Discontinuities

This section introduces two methods to set up the continuity and equilibrium equations of discontinuities in waveguides. One is the dynamic stiffness matrix for the reflection of boundaries and the other is the transfer matrix method for discontinuities between waveguides. These methods, especially the latter, will be used in the following chapters to derive the reflection and transmission coefficients of different structures.

2.7.1 Reflection at Boundaries

This section discusses setting up equilibrium equations at boundaries of waveguides by the dynamic stiffness matrix. Figure 2.6 shows a waveguide with a boundary at $x = 0$. In most cases the equilibrium condition can be given by a dynamic stiffness matrix, which relates the displacements and internal forces at the boundary,

$$\mathbf{F} = \mathbf{D}\mathbf{W} \tag{2.30}$$

where **D** is the dynamic stiffness matrix. It is usually composed of the parameters of

the boundary.

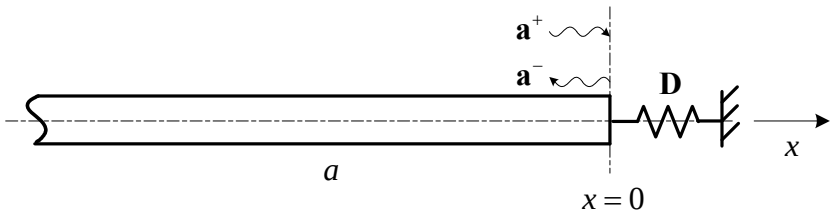

Figure 2.6 Wave reflection at a boundary.

Substituting the displacement and internal force vectors given by equation (2.24) into equation (2.30) and rearranging yields

$$\left(\mathbf{\Phi}^- - \mathbf{D}\mathbf{\Psi}^-\right)\mathbf{a}^- = \left(\mathbf{D}\mathbf{\Psi}^+ - \mathbf{\Phi}^+\right)\mathbf{a}^+ . \tag{2.31}$$

Assuming the matrix on the left-hand side is invertible, then

$$\mathbf{a}^- = \left(\mathbf{\Phi}^- - \mathbf{D}\mathbf{\Psi}^-\right)^{-1}\left(\mathbf{D}\mathbf{\Psi}^+ - \mathbf{\Phi}^+\right)\mathbf{a}^+ . \tag{2.32}$$

The wave amplitude vectors are related by the reflection coefficient matrix as

$$\mathbf{a}^- = \mathbf{R}\mathbf{a}^+ . \tag{2.33}$$

Comparing equations (2.33) and (2.32), the reflection matrix is given by

$$\mathbf{R} = \left(\mathbf{\Phi}^- - \mathbf{D}\mathbf{\Psi}^-\right)^{-1}\left(\mathbf{D}\mathbf{\Psi}^+ - \mathbf{\Phi}^+\right). \tag{2.34}$$

The reflection coefficients include the parameters of the waveguide and discontinuity.

2.7.2 Reflection and Transmission at Discontinuities in Waveguides

This section discusses the reflection and transmission matrices derived by the transfer matrix method. Figure 2.7 represents a linear element with input and output. For a linear mechanical system, it can be a combination of many linear subsystems, such as masses, springs, dampers, or linear continuous systems, such as bars, beams, plates and so on. Assuming that **F** and **W** are the internal force and displacement vectors with subscripts '*a*' and '*b*' indicating the input and output positions, they can be related by

$$\begin{Bmatrix} \mathbf{W}_a \\ \mathbf{F}_a \end{Bmatrix} = \begin{bmatrix} \mathbf{\Omega}_{11} & \mathbf{\Omega}_{12} \\ \mathbf{\Omega}_{21} & \mathbf{\Omega}_{22} \end{bmatrix} \begin{Bmatrix} \mathbf{W}_b \\ \mathbf{F}_b \end{Bmatrix} \tag{2.35}$$

where $\mathbf{\Omega}_{ij}$, $i, j = 1, 2$ are the elements of the transfer matrix. They can be obtained by applying appropriate continuity and equilibrium conditions. The transfer matrix method

is limited for some systems, in which cases, the internal force and displacement vectors can be related by other methods, such as the spectral element method [2]. All the systems discussed in this thesis can be analysed by the transfer matrix method.

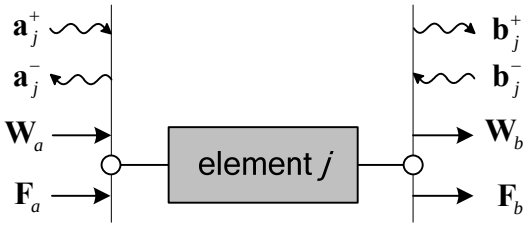

Figure 2.7 Element j with input and output forces and displacements.

If the element is a discontinuity connecting two waveguides a and b as shown in Figure 2.5, referring to equation (2.24), the displacements and internal forces on both sides can be related to waves amplitudes by

$$\begin{Bmatrix}\mathbf{W}_a\\ \mathbf{F}_a\end{Bmatrix}=\begin{bmatrix}\boldsymbol{\Psi}_{ja}^+ & \boldsymbol{\Psi}_{ja}^-\\ \boldsymbol{\Phi}_{ja}^+ & \boldsymbol{\Phi}_{ja}^-\end{bmatrix}\begin{Bmatrix}\mathbf{a}_j^+\\ \mathbf{a}_j^-\end{Bmatrix} \text{ and } \begin{Bmatrix}\mathbf{W}_b\\ \mathbf{F}_b\end{Bmatrix}=\begin{bmatrix}\boldsymbol{\Psi}_{jb}^+ & \boldsymbol{\Psi}_{jb}^-\\ \boldsymbol{\Phi}_{jb}^+ & \boldsymbol{\Phi}_{jb}^-\end{bmatrix}\begin{Bmatrix}\mathbf{b}_j^+\\ \mathbf{b}_j^-\end{Bmatrix}. \tag{2.36}$$

Substituting equation (2.36) into (2.35) and rearranging, after some lengthy manipulation, yield

$$\begin{bmatrix}\boldsymbol{\Psi}_{ja}^- & -\boldsymbol{\Omega}_{11}\boldsymbol{\Psi}_{jb}^+-\boldsymbol{\Omega}_{12}\boldsymbol{\Phi}_{jb}^+\\ \boldsymbol{\Phi}_{ja}^- & -\boldsymbol{\Omega}_{21}\boldsymbol{\Psi}_{jb}^+-\boldsymbol{\Omega}_{22}\boldsymbol{\Phi}_{jb}^+\end{bmatrix}\begin{Bmatrix}\mathbf{a}_j^-\\ \mathbf{b}_j^+\end{Bmatrix}=\begin{bmatrix}-\boldsymbol{\Psi}_{ja}^+ & \boldsymbol{\Omega}_{11}\boldsymbol{\Psi}_{jb}^-+\boldsymbol{\Omega}_{12}\boldsymbol{\Phi}_{jb}^-\\ -\boldsymbol{\Phi}_{ja}^+ & \boldsymbol{\Omega}_{21}\boldsymbol{\Psi}_{jb}^-+\boldsymbol{\Omega}_{22}\boldsymbol{\Phi}_{jb}^-\end{bmatrix}\begin{Bmatrix}\mathbf{a}_j^+\\ \mathbf{b}_j^-\end{Bmatrix}. \tag{2.37}$$

The following introduces the method to obtain the reflection and transmission coefficients.

Assuming that the matrix on the left-hand side is invertible, then

$$\begin{Bmatrix}\mathbf{a}_j^-\\ \mathbf{b}_j^+\end{Bmatrix}=\begin{bmatrix}\boldsymbol{\Psi}_{ja}^- & -\boldsymbol{\Omega}_{11}\boldsymbol{\Psi}_{jb}^+-\boldsymbol{\Omega}_{12}\boldsymbol{\Phi}_{jb}^+\\ \boldsymbol{\Phi}_{ja}^- & -\boldsymbol{\Omega}_{21}\boldsymbol{\Psi}_{jb}^+-\boldsymbol{\Omega}_{22}\boldsymbol{\Phi}_{jb}^+\end{bmatrix}^{-1}\begin{bmatrix}-\boldsymbol{\Psi}_{ja}^+ & \boldsymbol{\Omega}_{11}\boldsymbol{\Psi}_{jb}^-+\boldsymbol{\Omega}_{12}\boldsymbol{\Phi}_{jb}^-\\ -\boldsymbol{\Phi}_{ja}^+ & \boldsymbol{\Omega}_{21}\boldsymbol{\Psi}_{jb}^-+\boldsymbol{\Omega}_{22}\boldsymbol{\Phi}_{jb}^-\end{bmatrix}\begin{Bmatrix}\mathbf{a}_j^+\\ \mathbf{b}_j^-\end{Bmatrix}. \tag{2.38}$$

The first matrix on the right-hand side can be written as

$$\begin{bmatrix}\boldsymbol{\Psi}_{ja}^- & -\boldsymbol{\Omega}_{11}\boldsymbol{\Psi}_{jb}^+-\boldsymbol{\Omega}_{12}\boldsymbol{\Phi}_{jb}^+\\ \boldsymbol{\Phi}_{ja}^- & -\boldsymbol{\Omega}_{21}\boldsymbol{\Psi}_{jb}^+-\boldsymbol{\Omega}_{22}\boldsymbol{\Phi}_{jb}^+\end{bmatrix}=\begin{bmatrix}\mathbf{B}_{11} & \mathbf{B}_{12}\\ \mathbf{B}_{21} & \mathbf{B}_{22}\end{bmatrix}. \tag{2.39}$$

By using the partitioned inverse, it can be obtained that

$$\begin{bmatrix}\mathbf{C}_{11} & \mathbf{C}_{12}\\ \mathbf{C}_{21} & \mathbf{C}_{22}\end{bmatrix}=\begin{bmatrix}\mathbf{B}_{11} & \mathbf{B}_{12}\\ \mathbf{B}_{21} & \mathbf{B}_{22}\end{bmatrix}^{-1} \tag{2.40}$$

where

$$\begin{aligned}
\mathbf{C}_{11} &= \left(\mathbf{B}_{11} - \mathbf{B}_{12}\mathbf{B}_{22}^{-1}\mathbf{B}_{21}\right)^{-1}, \\
\mathbf{C}_{12} &= -\mathbf{C}_{11}\mathbf{B}_{12}\mathbf{B}_{22}^{-1}, \\
\mathbf{C}_{21} &= -\mathbf{B}_{22}^{-1}\mathbf{B}_{21}\mathbf{C}_{11}, \\
\mathbf{C}_{22} &= \mathbf{B}_{22}^{-1} + \mathbf{B}_{22}^{-1}\mathbf{B}_{21}\mathbf{C}_{11}\mathbf{B}_{12}\mathbf{B}_{22}^{-1}.
\end{aligned} \tag{2.41}$$

Substituting equation (2.40) into (2.38) and comparing the result with equation (2.29), the reflection and transmission matrices are given by

$$\begin{aligned}
\mathbf{R}_j^{aa} &= -\mathbf{C}_{11}\boldsymbol{\Psi}_{ja}^{+} - \mathbf{C}_{12}\boldsymbol{\Phi}_{ja}^{+}, \\
\mathbf{T}_j^{ba} &= \mathbf{C}_{11}\left(\boldsymbol{\Omega}_{11}\boldsymbol{\Psi}_{jb}^{-} + \boldsymbol{\Omega}_{12}\boldsymbol{\Phi}_{jb}^{-}\right) + \mathbf{C}_{12}\left(\boldsymbol{\Omega}_{21}\boldsymbol{\Psi}_{jb}^{-} + \boldsymbol{\Omega}_{22}\boldsymbol{\Phi}_{jb}^{-}\right), \\
\mathbf{T}_j^{ab} &= -\mathbf{C}_{21}\boldsymbol{\Psi}_{ja}^{+} - \mathbf{C}_{22}\boldsymbol{\Phi}_{ja}^{+}, \\
\mathbf{R}_j^{bb} &= \mathbf{C}_{21}\left(\boldsymbol{\Omega}_{11}\boldsymbol{\Psi}_{jb}^{-} + \boldsymbol{\Omega}_{12}\boldsymbol{\Phi}_{jb}^{-}\right) + \mathbf{C}_{22}\left(\boldsymbol{\Omega}_{21}\boldsymbol{\Psi}_{jb}^{-} + \boldsymbol{\Omega}_{22}\boldsymbol{\Phi}_{jb}^{-}\right).
\end{aligned} \tag{2.42}$$

The reflection matrix can also be obtained for a boundary by setting the terms with subscript b to zero.

Some techniques can be used to simplify the process when only reflection and transmission coefficients of a particular wave mode are of interest. Substituting equation (2.29) into (2.37) and rearranging gives

$$\left\{\begin{bmatrix} \boldsymbol{\Psi}_{ja}^{-} & -\boldsymbol{\Omega}_{11}\boldsymbol{\Psi}_{jb}^{+} - \boldsymbol{\Omega}_{12}\boldsymbol{\Phi}_{jb}^{+} \\ \boldsymbol{\Phi}_{ja}^{-} & -\boldsymbol{\Omega}_{21}\boldsymbol{\Psi}_{jb}^{+} - \boldsymbol{\Omega}_{22}\boldsymbol{\Phi}_{jb}^{+} \end{bmatrix}\begin{bmatrix} \mathbf{R}_j^{aa} & \mathbf{T}_j^{ba} \\ \mathbf{T}_j^{ab} & \mathbf{R}_j^{bb} \end{bmatrix} - \begin{bmatrix} -\boldsymbol{\Psi}_{ja}^{+} & \boldsymbol{\Omega}_{11}\boldsymbol{\Psi}_{jb}^{-} + \boldsymbol{\Omega}_{12}\boldsymbol{\Phi}_{jb}^{-} \\ -\boldsymbol{\Phi}_{ja}^{+} & \boldsymbol{\Omega}_{21}\boldsymbol{\Psi}_{jb}^{-} + \boldsymbol{\Omega}_{22}\boldsymbol{\Phi}_{jb}^{-} \end{bmatrix}\right\}\begin{Bmatrix} \mathbf{a}_j^{+} \\ \mathbf{b}_j^{-} \end{Bmatrix} = \mathbf{0}. \tag{2.43}$$

When only one wave mode is assumed to exist in $\mathbf{a}_j^{+}$, by substituting $\mathbf{a}_j^{+}$ and $\mathbf{b}_j^{-} = \mathbf{0}$ into the above equation, the corresponding reflection and transmission coefficients can be determined easily from the above equation. The next section discusses such an example. This method can also be used to obtain the reflection at boundaries.

2.8 Case Study: Reflection and Transmission Coefficients of Two Identical Semi-infinite Beams Connected by a Discontinuity

In this section the general approach introduced above is employed to derive the flexural wave amplitude reflection and transmission coefficients for a discontinuity in a waveguide. The structure comprises two semi-infinite uniform beams connected by a mass discontinuity at $x = 0$, as shown Figure 2.8. For simplicity beams *a* and *b* are

taken to have the same physical properties, such as density, Young's modulus and cross section. A time harmonic exciting source at $x=-\infty$ gives rise to a positive-going bending wave, $W_0 e^{-ik_b x}$, where W_0 is the wave amplitude at $x=0$. The incident wave impinges upon the discontinuity at $x=0$ where it is partly reflected and partly transmitted. Since there are only flexural waves in the system and there is only one propagating incident wave in beam a, the wave vectors are expressed as

$$\mathbf{a}_0^+ = \begin{Bmatrix} W_0 \\ 0 \end{Bmatrix} \text{ and } \mathbf{b}_0^- = \begin{Bmatrix} 0 \\ 0 \end{Bmatrix}. \tag{2.44}$$

Correspondingly the displacement and internal force vectors are

$$\mathbf{W}_{a,b} = \begin{Bmatrix} W_{a,b} \\ \partial W_{a,b}/\partial x \end{Bmatrix}, \ \mathbf{F}_{a,b} = \begin{Bmatrix} Q_{a,b} \\ M_{a,b} \end{Bmatrix}. \tag{2.45}$$

The beams on both sides of the discontinuity are identical, so the displacement and internal force matrices are

$$\boldsymbol{\Psi}_{0a}^+ = \boldsymbol{\Psi}_{0b}^+ = \begin{bmatrix} 1 & 1 \\ -ik_b & -k_b \end{bmatrix}, \ \boldsymbol{\Psi}_{0a}^- = \boldsymbol{\Psi}_{0b}^- = \begin{bmatrix} 1 & 1 \\ ik_b & k_b \end{bmatrix} \tag{2.46}$$

and

$$\boldsymbol{\Phi}_{0a}^+ = \boldsymbol{\Phi}_{0b}^+ = EIk_b^2 \begin{bmatrix} -ik_b & k_b \\ -1 & 1 \end{bmatrix}, \ \boldsymbol{\Phi}_{0a}^- = \boldsymbol{\Phi}_{0b}^- = EIk_b^2 \begin{bmatrix} ik_b & -k_b \\ -1 & 1 \end{bmatrix}. \tag{2.47}$$

The discontinuity is considered to be symmetric, thus

$$\mathbf{R}_0^{aa} = \mathbf{R}_0^{bb} = \begin{bmatrix} r_{PP} & r_{NP} \\ r_{PN} & r_{NN} \end{bmatrix} \text{ and } \mathbf{T}_0^{ba} = \mathbf{T}_0^{ab} = \begin{bmatrix} t_{PP} & t_{NP} \\ t_{PN} & t_{NN} \end{bmatrix}. \tag{2.48}$$

where the subscript '*PN*' indicates from propagating wave to nearfield wave. The rest can be deduced by analogy.

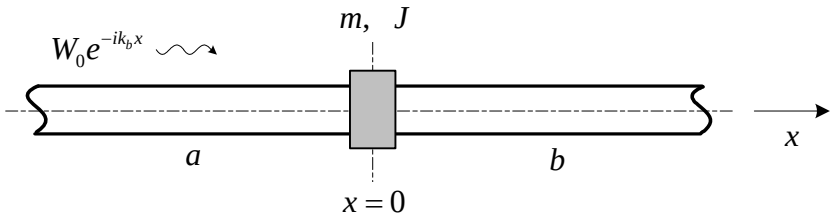

Figure 2.8 A beam with a mass discontinuity at $x=0$.

The discontinuity in the beam may feature inertia, stiffness and damping, and can dramatically alter the response of the structure. Depending on the specific situation, one

or more dynamic properties of the discontinuity may dominate the others. The discontinuity should be modelled appropriately according to the practical conditions. Here attention is focused on a mass discontinuity whose parameters are characterised by a point mass m and moment of inertia J.

By applying continuity and equilibrium conditions to the discontinuity, the transfer matrix in equation (2.35) can be obtained as

$$\mathbf{\Omega}_{11}=\begin{bmatrix}1 & 0\\ 0 & 1\end{bmatrix},\ \mathbf{\Omega}_{12}=\begin{bmatrix}0 & 0\\ 0 & 0\end{bmatrix},\ \mathbf{\Omega}_{21}=\begin{bmatrix}\omega^2 m & 0\\ 0 & \omega^2 J\end{bmatrix} \text{ and } \mathbf{\Omega}_{22}=\begin{bmatrix}1 & 0\\ 0 & 1\end{bmatrix}. \quad (2.49)$$

Substituting equations (2.44), (2.46) to (2.49) into (2.43), after some lengthy manipulation (see Appendix 3), yields

$$\begin{bmatrix}1 & -1 & 1 & -1\\ i & i & 1 & 1\\ i & -\mu\xi+i & -1 & -\mu\xi-1\\ -1 & i\vartheta\xi^3+1 & 1 & \vartheta\xi^3-1\end{bmatrix}\begin{Bmatrix}r_{PP}\\ t_{PP}\\ r_{PN}\\ t_{PN}\end{Bmatrix}=\begin{Bmatrix}-1\\ i\\ i\\ 1\end{Bmatrix}, \quad (2.50)$$

where

$$\mu=\frac{m}{\rho A\kappa},\quad \vartheta=\frac{J}{\rho A\kappa^3},\quad \xi=\sqrt{\frac{\omega\kappa}{c_l}}. \quad (2.51)$$

$\kappa=\sqrt{I/A}$ is the radius of gyration of the cross-section of the beam. μ is the ratio of the added mass to the beam mass in a length κ. ϑ is the ratio of the moment of inertia J to a moment of inertia equivalent to that of a mass $\rho A\kappa$ with a radius of gyration κ. Both parameters μ and ϑ are frequency independent. ξ^2 is the non-dimensional frequency and is equal to $\left(k_b\kappa\right)^2$. By inspection of equation (2.50), it is apparent that $\mu\xi$ and $\vartheta\xi^3$ influence the reflection and transmission coefficients. $i\mu\xi$ is the ratio of the translational impedance of the mass discontinuity to the translational characteristic impedance of bending waves (see Appendix 2). $i\vartheta\xi^3$ is the ratio of the rotational impedance of the mass discontinuity to the rotational characteristic impedance of bending waves (see Appendix 2). See Appendix 4 for detailed definitions. Parameters μ and ϑ are chosen for the task of parameter estimation in Chapters 6 and 7.

The reflection and transmission coefficients can be obtained directly by matrix inversion in equation (2.50). Alternatively, they can also be expressed in closed form as

$$
\begin{aligned}
r_{PP} &= -\frac{i\left[\left(\mu\xi\right)\left(\vartheta\xi^3\right)-2\mu\xi+2\vartheta\xi^3\right]}{\left(\mu\xi+2-2i\right)\left(\vartheta\xi^3-2-2i\right)},\\
t_{PP} &= -\frac{2\left(\mu\xi-\vartheta\xi^3+4\right)}{\left(\mu\xi+2-2i\right)\left(\vartheta\xi^3-2-2i\right)},\\
r_{PN} &= \frac{\left(i-1\right)\left(\mu\xi\right)\left(\vartheta\xi^3\right)+2\mu\xi+2i\vartheta\xi^3}{\left(\mu\xi+2-2i\right)\left(\vartheta\xi^3-2-2i\right)},\\
t_{PN} &= \frac{2\left(\mu\xi-i\vartheta\xi^3\right)}{\left(\mu\xi+2-2i\right)\left(\vartheta\xi^3-2-2i\right)}.
\end{aligned}
\tag{2.52}
$$

From these expressions it can be seen that the reflection and transmission coefficients are functions of the frequency dependent impedance ratios, $i\mu\xi$ and $i\vartheta\xi^3$.

Figure 2.9 shows the propagating reflection and transmission coefficients as functions of the magnitudes of the translational and rotational impedance ratios. The magnitudes of the scattering coefficients are presented by the power coefficients. The mass-discontinuity is considered to be rigidly connected to the beam and damping is neglected, so $\rho+\tau=1$. Small values of $\mu\xi$ signify small added mass and/or low frequency, while small values of $\vartheta\xi^3$ denote small added moment of inertia and/or low frequency. If both $\mu\xi$ and $\vartheta\xi^3$ are small, $\rho\to 0$ and $\tau\to 1$, so most energy is transmitted. For large modulus of impedance ratios, $\rho\to 1$ and $\tau\to 0$, which means most energy is reflected. Therefore, a mass discontinuity cannot significantly impede low frequency wave motion but can effectively reflect high-frequency wave motion. If either of the magnitudes of impedance ratios tends to zero and the other tends to infinity, both the power reflection and transmission coefficients approach one half. The reason behind this is that the mass prevents energy transmission by the internal shear force, while the moment of inertia by internal flexural moment [4]. At the regions where $\rho\to 0$, the phase of the reflection coefficient will have a sudden change of π (Figure 2.9(b)). At regions $\tau\to 0$, the phase of the transmission coefficient will have a sudden change of π (Figure 2.9(d)).

From equation (2.52), it is easy to find the regions where $\rho=0$ ($\tau=1$) and $\tau=0$ ($\rho=1$) in terms of parameters $\mu\xi$ and $\vartheta\xi^3$. Figure 2.10 shows these regions. They are actually the contour lines for $\rho=0$ and $\tau=0$ in Figure 2.9.

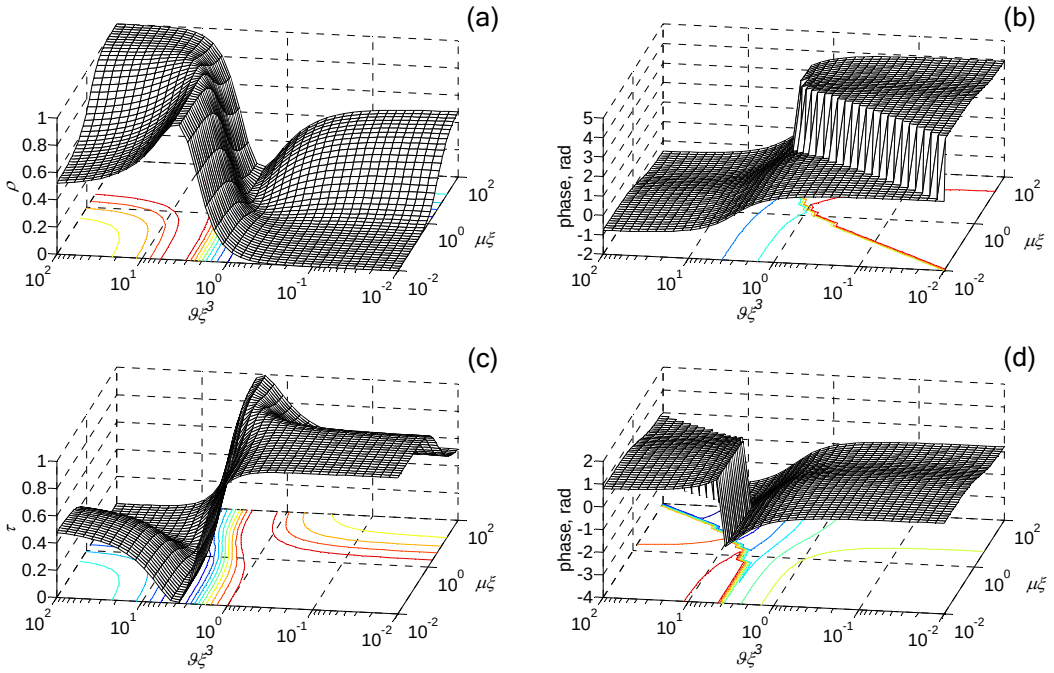

Figure 2.9 Magnitudes (squared) and phases of the flexural reflection and transmission coefficients for the mass discontinuity: $\mu\xi$, magnitude of translational impedance ratio; $\vartheta\xi^3$, magnitude of rotational impedance ratio: (a) ρ; (b) phase of r_{PP}; (c) τ; (d) phase of t_{PP}.

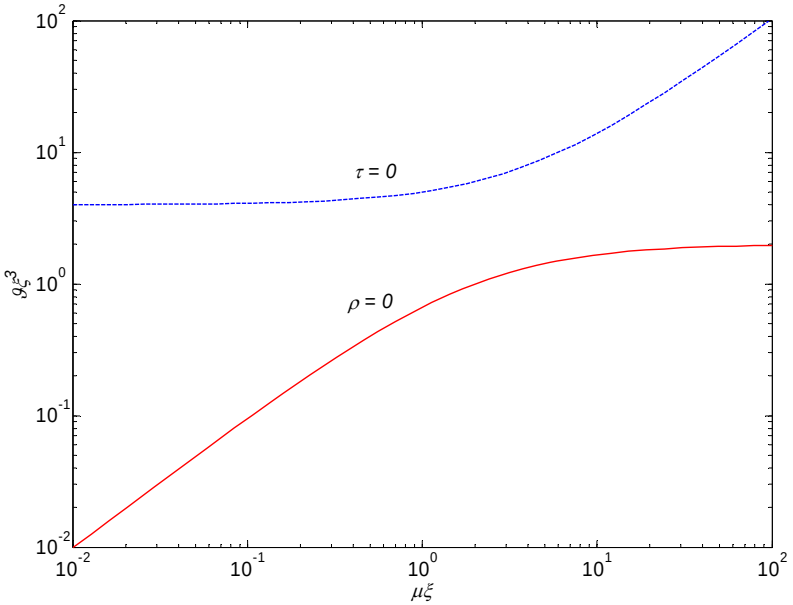

Figure 2.10 Regions of $\rho = 0$ and $\tau = 0$ for the mass discontinuity.

2.9 Summary

This chapter briefly introduced the longitudinal and flexural wave equations, their solutions and some fundamental concepts regarding wave speed and wavenumbers. The damping effect of metal waveguides is usually very small. When a wave propagating along the waveguide impinges on a discontinuity, a reflected wave and a transmitted wave (if there exists another waveguide on the other side of the discontinuity) will be generated. Thus the wave amplitude reflection and transmission coefficients were defined accordingly. From the view point of energy, the power reflection and transmission coefficients were also introduced. A general wave approach was reviewed and employed to derive the reflection and transmission coefficients in terms of the parameters of the boundaries and discontinuities in waveguides. This approach can be applied to complex structures in which various wave modes are accommodated. Finally a case study was demonstrated on the reflection and transmission coefficients of two identical semi-infinite beams connected by a mass discontinuity.

Chapter 3 Measurement of Reflection and Transmission Coefficients

3.1 Introduction

The final goal of this thesis is to estimate the parameters of a discontinuity in a waveguide from measured wave reflection and transmission coefficients. This can be achieved by two steps: the first is to obtain the reflection and transmission coefficients from transducer array measurements, and the second is to estimate the parameters of the joint from these measured coefficients. Clearly, the precision of the measured reflection and transmission coefficients is crucial to the accuracy of the parameter estimates of the discontinuity. This chapter considers the accuracy by which the flexural reflection and transmission coefficients of a discontinuity may be estimated from noisy transfer function measurements.

A Wave Amplitude Decomposition (WAD) approach can be used to estimate amplitudes of various waves from transducer array measurements [58, 65]. A series of transducers are attached at various points to the waveguide. The spectra of their outputs are post-processed to get the wave amplitudes in the frequency domain. In references [58, 65] the design of the transducer array was discussed with respect to how to achieve good numerical conditioning according to the number of effective waves in the waveguide. However, the quality of the estimated amplitudes depends not only on the conditioning of the problem, but also on the accuracy of the measured data. By measuring the responses of transducers on either side of the discontinuity, the wave amplitudes on each side can be estimated and in turn the reflection and transmission coefficients of the discontinuity can be obtained from equation (2.14). In practice, measurement noise contaminates the measured data (transfer functions), and consequently affects the estimated reflection and transmission coefficients. Here a Gaussian noise model is introduced to the simulated measured data in the frequency

domain to examine the effects of measurement noise on the estimated reflection and transmission coefficients. Closed form solutions for the mean values and variances of the noisy reflection and transmission coefficients are given. Then Monte Carlo (MC) simulations and experiments are performed to illustrate the applicability of the closed form solutions.

In the next section the WAD method is reviewed. Then this method is applied to a discontinuity connecting two semi-infinite waveguides in Section 3.3. The flexural reflection and transmission coefficients for the discontinuity are found from the decomposed amplitudes. In Section 3.4 a Gaussian noise model is applied to the transducer measurements to simulate the influence of measurement noise. Considering the noise as a perturbation on the ideal output of the measurement, expressions are derived for the mean and variance of the power reflection and transmission coefficients. The parameters that influence the variance of the power reflection and transmission coefficients are discussed. The statistical distribution of the power reflection coefficient is also investigated given that the noise on the transducer measurements is assumed to be Gaussian. Effects of nearfields are considered in Section 3.5. Section 3.6 gives the MC simulations for the reflection coefficient for a mass discontinuity and the mean and standard deviation of these simulations are compared with the closed form solutions. Section 3.7 reviews how the flexural wavenumber may be estimated using measurements taken by a transducer array. Section 3.8 presents the results of experiments on a beam with steel blocks attached. Flexural reflection and transmission coefficients are estimated based on the method introduced in the previous sections.

3.2 A Wave Amplitude Decomposition Approach

A brief outline of a WAD approach is reviewed in this section [58, 65]. This approach is used to identify the positive- and negative-going wave amplitudes at a point in a waveguide. The method is demonstrated on flexural waves here but it can be extended by analogy to various other waves.

Figure 3.1 shows a measurement system comprising n transducers at n locations on a

waveguide. The aim is to decompose the wave amplitudes at point $x = x_0$. The outputs (displacement, or velocity or acceleration) of the *n* transducers are given in terms of the wave components by

$$\mathbf{W} = \mathbf{\Lambda}\mathbf{A} \tag{3.1}$$

where

$$\mathbf{W} = \begin{Bmatrix} W(x_1) \\ W(x_2) \\ \vdots \\ W(x_n) \end{Bmatrix}, \quad \mathbf{\Lambda} = \begin{bmatrix} e^{-ik_b x_1} & e^{-k_b x_1} & e^{ik_b x_1} & e^{k_b x_1} \\ e^{-ik_b x_2} & e^{-k_b x_2} & e^{ik_b x_2} & e^{k_b x_2} \\ \vdots & \vdots & \vdots & \vdots \\ e^{-ik_b x_n} & e^{-k_b x_n} & e^{ik_b x_n} & e^{k_b x_n} \end{bmatrix}, \quad \mathbf{A} = \begin{Bmatrix} a_P^+ \\ a_N^+ \\ a_P^- \\ a_N^+ \end{Bmatrix}. \tag{3.2}$$

$a_P^{\pm}$ and $a_N^{\pm}$ are the propagating and nearfield wave amplitudes respectively. $W(x_i)$ is the measured output at point $x = x_i$ ($i = 1, 2, \cdots, n$). Measurements of flexural wavenumber k_b will be discussed in Section 3.7. If the number of measurements is less than the number of wave components, i.e. the system is underdetermined, additional conditions are required to yield a solution. More specifically, if the number of measurements is chosen to match the number of wave components, in which case $\mathbf{\Lambda}$ is square, then the wave components are given by

$$\mathbf{A} = \mathbf{\Lambda}^{-1}\mathbf{W} \tag{3.3}$$

In the case of an overdetermined system, the wave components may be found in a least-squares sense as

$$\mathbf{A} = \left(\mathbf{\Lambda}^{\mathrm{H}}\mathbf{\Lambda}\right)^{-1}\mathbf{\Lambda}^{\mathrm{H}}\mathbf{W} \tag{3.4}$$

The superscript H indicates the conjugate transpose of a matrix.

The estimation of wave amplitudes depends on the existence of the inverse of matrix $\mathbf{\Lambda}$, or $\mathbf{\Lambda}^{\mathrm{H}}\mathbf{\Lambda}$ in the case of an overdetermined system. Normally, if the transducer spacing is uniform and the same physical variable is measured at each location, the matrix is singular when the spacing is zero or an integer number of half-wavelengths. When the transducer spacings approach those which result in singularity, the matrix is ill-conditioned and may cause unacceptable errors in the calculated wave amplitudes. This imposes limits on the transducer spacings. It should be noted that wavenumber k_b must be known in equations (3.3) and (3.4).

A hybrid measurement system which includes a variety of transducer types, allowing

more than one vibrational quantity (e.g., acceleration and strain) to be measured can give better conditioning of this method [58]. In this thesis, equally spaced accelerometer arrays are employed.

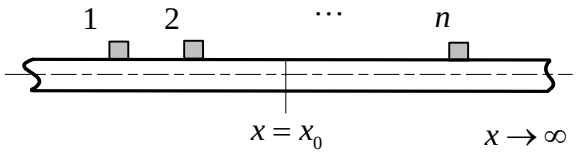

Figure 3.1 Local coordinate of transducers.

3.3 Estimating Reflection and Transmission Coefficients by Wave Amplitude Decomposition

In this section, the reflection and transmission coefficients of a discontinuity in an infinite beam are derived by using the WAD method introduced above.

Consider two identical semi-infinite waveguides lying along the x-axis which are connected by a joint at $x = 0$, as shown in Figure 3.2. Two (positive- and negative-going) flexural waves $\mathbf{a}^+$ and $\mathbf{b}^-$ are incident upon the discontinuity at $x = 0$, which give rise to propagating and nearfield reflected and transmitted waves on both sides. Two transducers are placed with spacing Δ on each side of the joint. The mid-point of each pair of transducers is chosen as the local coordinate origin, which is located at $x = -a$ and $x = b$ respectively in the global coordinate system. The intention here is to estimate the flexural reflection and transmission coefficients of the joint by applying WAD in the local coordinate systems.

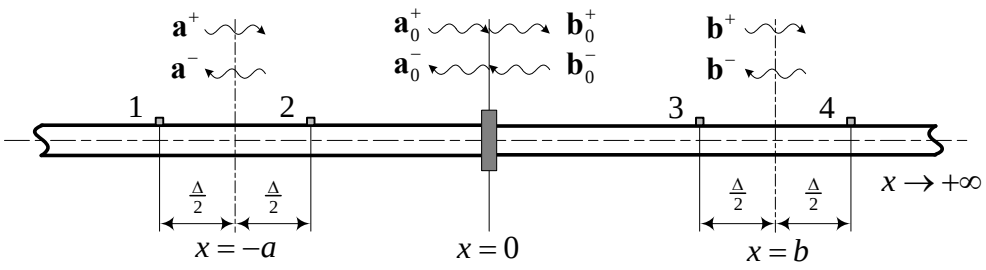

Figure 3.2 Waves in two semi-infinite waveguides connected by a joint.

As is known, the nearfield waves are only of significance around the discontinuities, such as the excitation point and the joint. The transducers are considered to be far enough away from these discontinuities that the influence of the nearfields on the accelerometer outputs can be neglected. Therefore, the two transducers on each side are only used to estimate the amplitudes of the propagating flexural waves. The vectors and matrix in equation (3.1) are then simplified as

$$\mathbf{W}=\begin{Bmatrix} W(x_1) \\ W(x_2) \end{Bmatrix},\ \mathbf{\Lambda}=\begin{bmatrix} e^{-ik_b x_1} & e^{ik_b x_1} \\ e^{-ik_b x_2} & e^{ik_b x_2} \end{bmatrix} \text{ and } \mathbf{A}=\begin{Bmatrix} a_P^+ \\ a_P^- \end{Bmatrix}. \tag{3.5}$$

Applying this equation to the left-hand-side the transducer pair where $x_1=-\Delta/2$, the outputs of the transducers can be written as

$$\begin{Bmatrix} W_1 \\ W_2 \end{Bmatrix}=\begin{bmatrix} e^{ik_b\Delta/2} & e^{-ik_b\Delta/2} \\ e^{-ik_b\Delta/2} & e^{ik_b\Delta/2} \end{bmatrix}\begin{Bmatrix} a_{Pa}^+ \\ a_{Pa}^- \end{Bmatrix} \text{ and } \begin{Bmatrix} W_3 \\ W_4 \end{Bmatrix}=\begin{bmatrix} e^{ik_b\Delta/2} & e^{-ik_b\Delta/2} \\ e^{-ik_b\Delta/2} & e^{ik_b\Delta/2} \end{bmatrix}\begin{Bmatrix} a_{Pb}^+ \\ a_{Pb}^- \end{Bmatrix} \tag{3.6}$$

where the subscripts 1, 2, 3, 4 indicate the positions of transducers; subscripts *a* and *b* denote waveguides. The wave amplitudes at the local origins can be obtained simply by solution of the above equation. For example,

$$\begin{Bmatrix} a_{Pa}^+ \\ a_{Pa}^- \end{Bmatrix}=\frac{1}{2i\sin k_b\Delta}\begin{bmatrix} e^{ik_b\Delta/2} & e^{-ik_b\Delta/2} \\ e^{-ik_b\Delta/2} & e^{ik_b\Delta/2} \end{bmatrix}\begin{Bmatrix} W_1 \\ W_2 \end{Bmatrix}. \tag{3.7}$$

Here the singularity of a matrix must be considered. When $k_b\Delta=n\pi$ ($n=0,1,2,\cdots$), the matrices in equation (3.5) become singular. In this case, the transducer spacing is equal to either multiples of one wavelength in which case the transducers observe the same motion, or odd multiples of half a wavelength in which case the transducers move in anti-phase. This method fails to identify the positive- and negative-going waves. Therefore, there is a maximum separation for the transducers within a given frequency range. Since $k_b=2\pi/\lambda$ (λ is the wavelength), the transducer spacing must be less than half the shortest wavelength.

Referring to equation (2.29), at the discontinuity (indicated by subscript " 0 "), the propagating reflected and transmitted waves are related to the incident waves by

$$\begin{Bmatrix} a_{0a}^- \\ a_{0b}^+ \end{Bmatrix}=\begin{bmatrix} r^{aa} & t^{ba} \\ t^{ab} & r^{bb} \end{bmatrix}\begin{Bmatrix} a_{0a}^+ \\ a_{0b}^- \end{Bmatrix}, \tag{3.8}$$

where r^{aa} is the propagating reflection coefficient and t^{ab} is the transmission coefficient.

If the discontinuity is considered to be physically symmetric, the reflection and transmission coefficients are such that

$$r^{aa} = r^{bb} = r \text{ and } t^{ab} = t^{ba} = t \tag{3.9}$$

In order to estimate the reflection and transmission coefficients from transducer array measurements, the local coordinate systems need to be related to the global coordinate system. Referring to equation (2.27), the wave amplitudes at the discontinuity and midpoints of the transducer pairs can be related by

$$\begin{Bmatrix} a_{0a}^{+} \\ a_{0a}^{-} \end{Bmatrix} = \begin{bmatrix} e^{-ik_b a} & 0 \\ 0 & e^{ik_b a} \end{bmatrix} \begin{Bmatrix} a_{Pa}^{+} \\ a_{Pa}^{-} \end{Bmatrix} \text{ and } \begin{Bmatrix} a_{0b}^{+} \\ a_{0b}^{-} \end{Bmatrix} = \begin{bmatrix} e^{ik_b b} & 0 \\ 0 & e^{-ik_b b} \end{bmatrix} \begin{Bmatrix} a_{Pb}^{+} \\ a_{Pb}^{-} \end{Bmatrix}. \tag{3.10}$$

Substituting equations (3.9) and (3.10) into equation (3.8), the reflection and transmission coefficients can be expressed in terms of the wave amplitudes defined in the local coordinate systems as

$$\begin{Bmatrix} r_P \\ t_P \end{Bmatrix} = \begin{bmatrix} a_{Pa}^{+} e^{-ik_b a} & a_{Pb}^{-} e^{-ik_b b} \\ a_{Pb}^{-} e^{-ik_b b} & a_{Pa}^{+} e^{-ik_b a} \end{bmatrix}^{-1} \begin{Bmatrix} a_{Pa}^{-} e^{ik_b a} \\ a_{Pb}^{+} e^{ik_b b} \end{Bmatrix}. \tag{3.11}$$

The wave amplitudes a_{Pa}^{+}, a_{Pa}^{-}, a_{Pb}^{+} and a_{Pb}^{-} can be expressed as functions of transducer outputs from equations (3.6) by matrix inversion. Then substituting these wave amplitudes into equation (3.11) gives the reflection and transmission coefficients in terms of transducer outputs.

For simplicity, from here on a simple case is considered where there is only one incident wave in the left-hand waveguide, i.e. $a_{Pb}^{-} = 0$. Then the reflection and transmission coefficients can be expressed in terms of the transducer outputs as

$$r = -\frac{W_1 e^{-ik_b \Delta/2} - W_2 e^{ik_b \Delta/2}}{W_1 e^{ik_b \Delta/2} - W_2 e^{-ik_b \Delta/2}} e^{2ik_b a},\ t = \frac{W_3 e^{ik_b \Delta/2} - W_4 e^{-ik_b \Delta/2}}{W_1 e^{ik_b \Delta/2} - W_2 e^{-ik_b \Delta/2}} e^{ik_b (a+b)}. \tag{3.12}$$

Whilst the reflection and transmission coefficients are in theory determined by the properties of the waveguides and the discontinuities, the estimated reflection and transmission coefficients given by equation (3.12) depend on the wavenumber, transducer spacing and locations as well as the transducer outputs. Again by substituting equation (3.6) into the denominators of the above expressions, it can be concluded that when $k_b \Delta = n\pi$ ($n = 0, 1, 2, \cdots$) the denominators will become zero, which should be avoided.

3.4 Analysis of Influence of Measurement Noise

The above discussion does not consider the influence of noise on the measurement of the reflection and transmission coefficients. However, in practice, measurement noise is unavoidable. In this section a noise model is introduced into the simulated measured transducer outputs. Then the effects of measurement noise on the estimated reflection and transmission coefficients are investigated. Since the terms $k_b a$ and $k_b b$ in equation (3.12) are typically very large and change rapidly with frequency, the phases of the reflection and transmission coefficients are sensitive to combinations of errors on wavenumber and transducer locations $x = -a$ and $x = b$, especially at high frequencies. Consequently, parameter identification methods for the discontinuity might judiciously use only the moduli of the estimated reflection and transmission coefficients. This chapter focuses on the influence of measurement noise on the moduli of the estimated reflection and transmission coefficients. For convenience, the statistical distribution of the squared moduli of these coefficients, i.e. the power reflection and transmission coefficients, will be analysed here.

3.4.1 Noise Model

The measured outputs are assumed to be contaminated by noise. This can be expressed as

$$\hat{W}_i = W_i + N_i \tag{3.13}$$

where $\hat{W}_i$ is the estimated quantity, W_i is the true quantity and N_i indicates the noise on the measured output of transducer i. The noise model can be selected in many ways, but here it is applied in the frequency domain and is represented as

$$N_i = m_i e^{i\phi_i} \tag{3.14}$$

where m_i is Gaussian distributed with zero mean and variance $\sigma_i^2 \left| a_{Pa}^{+} \right|^2$ and the phase ϕ_i is uniformly distributed between $-\pi/2$ and $\pi/2$. m_i is chosen to be Gaussian since the Gaussian distribution often provides an adequate approximation to the distribution of many measured quantities. Zero mean indicates the noise is purely random and

without systematic errors. a_{Pa}^{+} is included here so that the noise on the transducer readings is assumed to be multiplicative, i.e. proportional to the amplitude of the incident wave. σ_i^2 is assumed to be relatively small, i.e. much smaller than unity. Therefore, N_i can be considered as a perturbation on the output measurement. For simplicity, N_i are assumed to be uncorrelated. Since the noise is random, its phase is regarded as uniformly distributed between $-\pi$ and π. However, with the amplitude being Gaussian with zero mean, it is equivalent to saying that the phase component of the noise is uniformly distributed between $-\pi/2$ and $\pi/2$.

3.4.2 Statistical Estimates of the Noisy Power Reflection Coefficient

Given the noise model described above, the mean values and variances of the power reflection coefficient are estimated in this section by a perturbation method.

Substituting the noisy outputs defined by equation (3.13) into the first expression of equation (3.12), after some lengthy algebra, the noisy reflection coefficient is given by

$$\hat{r} = \frac{a_{Pa}^{-}\left(1+\varepsilon_1\right)}{a_{Pa}^{+}\left(1+\varepsilon_2\right)} e^{2ik_b a} = r\frac{1+\varepsilon_1}{1+\varepsilon_2} \tag{3.15}$$

where

$$\varepsilon_1 = \frac{-e^{-ik_b\Delta/2}N_1 + e^{ik_b\Delta/2}N_2}{2ira_{Pa}^{+}\sin k_b\Delta} e^{2ik_b a}, \quad \varepsilon_2 = \frac{e^{ik_b\Delta/2}N_1 - e^{-ik_b\Delta/2}N_2}{2ia_{Pa}^{+}\sin k_b\Delta} \tag{3.16}$$

can be considered as perturbations on the noise free values of wave amplitudes, which means that the noise levels of the "measured" transducer outputs are relatively small. Here it is assumed that $|\varepsilon_2| < 1$, then

$$\hat{r} = r\left(1+\varepsilon_1\right)\left(1-\varepsilon_2+\varepsilon_2^2+\cdots+\left(-1\right)^n\varepsilon_2^n+\cdots\right). \tag{3.17}$$

Recalling the definition of power reflection coefficient given in Chapter 2, multiplying each side of equation (3.17) by its own complex conjugate and neglecting the terms in which the summed indices of ε_1, ε_2, $\varepsilon_1^{\mathrm{H}}$ or $\varepsilon_2^{\mathrm{H}}$ are higher than the second order (the condition that $|\varepsilon_1| \ll 1$ and $|\varepsilon_2| \ll 1$ must be assumed), the estimated power reflection coefficient can be approximated by

$$\hat{\rho} \approx \rho \begin{bmatrix} 1+\varepsilon_1+\varepsilon_1^{\mathrm{H}}-\varepsilon_2-\varepsilon_2^{\mathrm{H}}+\varepsilon_2^2+\varepsilon_2^{\mathrm{H2}} \\ +\varepsilon_1\varepsilon_1^{\mathrm{H}}+\varepsilon_2\varepsilon_2^{\mathrm{H}}-\varepsilon_1\varepsilon_2-\varepsilon_1^{\mathrm{H}}\varepsilon_2^{\mathrm{H}}-\varepsilon_1^{\mathrm{H}}\varepsilon_2-\varepsilon_1\varepsilon_2^{\mathrm{H}} \end{bmatrix}. \tag{3.18}$$

Substituting for ε_1 and ε_2 from equation (3.16), taking the expectation of both sides and neglecting the terms with second and higher orders of σ_1^2 or σ_2^2 gives the mean value of the estimated power reflection coefficient (see Appendix 5 for the detailed derivation of this mean and other expressions below):

$$\mu_{\hat{\rho}} \doteq \rho + \frac{1}{4\sin^2 k_b\Delta}\left\{2\,\mathrm{Re}\left[re^{-2ik_ba}\left(e^{ik_b\Delta}\sigma_1^2+e^{-ik_b\Delta}\sigma_2^2\right)\right]+(1+\rho)\left(\sigma_1^2+\sigma_2^2\right)\right\}, \tag{3.19}$$

where Re indicates the real part of a complex number. Since k_ba is typically very large and changes rapidly with frequency, the exponential term e^{-2ik_ba} in equation (3.19) causes fluctuations to the mean value of $\hat{\rho}$. Considering that the magnitudes of r, ρ and the exponential terms are all bounded by unity, upper and lower bounds for the mean value can be approximated by

$$\rho \le \mu_{\hat{\rho}} \le \rho + \frac{\sigma_1^2+\sigma_2^2}{\sin^2 k_b\Delta}. \tag{3.20}$$

Therefore, the mean value is always no less than the noise free value, which means the expectation is biased.

The variance of a variable quantifies the error dispersion and is defined by $\sigma_X^2 = E\left[X^2\right]-E^2\left[X\right]$, where $E\left[X\right]$ indicates the expectation of a variable. Following similar analysis to the manipulation of the mean value of $\hat{\rho}$, the variance of $\hat{\rho}$ is given by

$$\sigma_{\hat{\rho}}^2 \doteq \frac{\rho}{2\sin^2 k_b\Delta}\left\{2\,\mathrm{Re}\left[re^{-2ik_ba}\left(e^{ik_b\Delta}\sigma_1^2+e^{-ik_b\Delta}\sigma_2^2\right)\right]+(1+\rho)\left(\sigma_1^2+\sigma_2^2\right)\right\}, \tag{3.21}$$

from which the following upper bound can be obtained:

$$\sigma_{\hat{\rho}}^2 \le \frac{2\rho\left(\sigma_1^2+\sigma_2^2\right)}{\sin^2 k_b\Delta}. \tag{3.22}$$

This upper bound can be seen to depend on:

1) the sum of the variances of the two transducers, $\sigma_1^2+\sigma_2^2$. The smaller the noise variances of the transducers, the lower of the variance of the estimation. It also can be seen that the sequence of the transducers does not affect the estimation.

2) the true value of the power reflection coefficient, ρ. This is a consequence of the noise model chosen.
3) the transducer spacing, Δ. The optimum transducer spacing is a quarter wavelength (where $\sin k_b\Delta = 1$). Poor estimates occur when the transducer spacing is close to multiples of one half wavelength.

The conditions for the validity of equations (3.17) to (3.22) will be discussed here. The moduli of the noise contaminations for output measurements are assumed to be Gaussian. For a Gaussian distribution, data with extremely large deviations still arise occasionally though they are relatively infrequent. So it is not guaranteed that the conditions $|\varepsilon_1| \ll 1$ and $|\varepsilon_2| \ll 1$ are definitely satisfied for every measurement even if the simulated noise level on the transducer measurement is assumed to be very small. However, if both the mean values of $|\varepsilon_1|$ and $|\varepsilon_2|$ are much less than unity, then the first order approximation is usually a good estimation. With reference to equation (3.16), the mean values of $|\varepsilon_1|$ and $|\varepsilon_2|$ are respectively

$$\mu_{|\varepsilon_1|} = \frac{\sqrt{\sigma_1^2 + \sigma_2^2}}{2\sqrt{\rho}\,|\sin k_b\Delta|}, \quad \mu_{|\varepsilon_2|} = \frac{\sqrt{\sigma_1^2 + \sigma_2^2}}{2|\sin k_b\Delta|}. \tag{3.23}$$

Since $\sqrt{\rho} \le 1$, it can be said that when

$$\frac{\sqrt{\sigma_1^2 + \sigma_2^2}}{2\sqrt{\rho}\,|\sin k_b\Delta|} \ll 1, \tag{3.24}$$

both $\mu_{|\varepsilon_1|}$ and $\mu_{|\varepsilon_2|}$ are much less than unity. Under this condition, equations (3.17) to (3.22) can be regarded as good approximations.

3.4.3 Statistical Estimates of the Noisy Power Transmission Coefficient

In this section the mean value and variance of the estimated power transmission coefficient are given.

Similarly to equation (3.15), the estimated transmission coefficient with simulated measurement noise is given by

$$\hat{t} = \frac{a_{Pb}^{+}\left(1+\varepsilon_3\right)}{a_{Pa}^{+}\left(1+\varepsilon_2\right)} e^{ik_b(a+b)} = t\frac{1+\varepsilon_3}{1+\varepsilon_2} \tag{3.25}$$

where

$$\varepsilon_2 = \frac{e^{ik_b\Delta/2}N_3 - e^{-ik_b\Delta/2}N_4}{2ita_{Pa}^{+}\sin k_b\Delta} e^{ik_b(a+b)} \tag{3.26}$$

is the perturbation on the transmitted wave amplitude. With the same manipulations as those of the reflection coefficient, the mean value and variance of the estimated power transmission coefficient $\hat{\tau}$ can be approximated respectively by

$$\mu_{\hat{\tau}} \doteq \tau + \frac{1}{4\sin^2 k_b\Delta}\left[\tau\left(\sigma_1^2+\sigma_2^2\right)+\sigma_3^2+\sigma_4^2\right] \tag{3.27}$$

and

$$\sigma_{\hat{\tau}}^2 \doteq \frac{\tau}{2\sin^2 k_b\Delta}\left[\tau\left(\sigma_1^2+\sigma_2^2\right)+\sigma_3^2+\sigma_4^2\right]. \tag{3.28}$$

The mean value of $\hat{\tau}$ is also biased. Since the waves on each side of the discontinuity are identified by a transducer pair, so the noise on all of the four transducers contributes to the variance of $\hat{\tau}$. The effect of the factor $\sin^2 k_b\Delta$ is the same as that of the reflection coefficient. The condition for good approximations of equations (3.27) to (3.28) are the same as those for the reflection coefficient.

3.5 Effects of Nearfields

The analysis presented in the above sections assumes that the nearfields are negligible. This section discusses the effect of the nearfield terms. For simplicity, the nearfields on the left-hand side of the discontinuity are considered here. The nearfields decay exponentially with distance, so they have more effect on the transducers closer to the discontinuity. In this case the nearfield at transducer 2 will be studied. The amplitude of the combined left-going nearfield at the joint can be expressed in an analogous way to the propagating wave (see equation (3.8)) as

$$a_{Na}^{-} = r_N^{aa}a_{0a}^{+} + t_N^{ba}a_{0b}^{-}. \tag{3.29}$$

Referring to equation (3.1), the total output at transducer 2 including nearfield effects becomes

$$W_2 = a_{Pa}^{+} e^{-ik_b \Delta/2} + a_{Pa}^{-} e^{ik_b \Delta/2} + a_{Na}^{-} e^{k_b(-a+\Delta/2)}. \tag{3.30}$$

Consider the case with only one incident wave (with $t_N^{ba} a_{b0}^{-}$ disappearing in equation (3.29)), and with reference to equations (3.10) and (3.8) (notice that $r_P^{aa} = r$), the above equation can be expressed as

$$W_2 = a_{Pa}^{+} e^{-ik_b \Delta/2} + r_P^{aa} a_{Pa}^{+} e^{ik_b(-2a+\Delta/2)} + r_N^{aa} a_{Pa}^{+} e^{k_b(-a+\Delta/2)}. \tag{3.31}$$

In the nearfield term $r_N^{aa} a_{Pa}^{+} e^{k_b(-a+\Delta/2)}$, the amplitude of $r_N^{aa} a_{Pa}^{+}$ is comparable to that of the propagating wave term. However, the component $e^{k_b(-a+\Delta/2)}$ decays exponentially. Table 3.1 lists the effect of this exponential component in the nearfield term in terms of wavelength. For example, if the distance $|-a+\Delta/2|$ is equal to one wavelength, the amplitude of the nearfield wave will be reduced to 0.2% of its original value; and less than 5% over a distance of half a wavelength. If the effect of the presence of the nearfield is much smaller than that of the noise, the nearfield can be neglected.

Table 3.1 Amplitude reduction of nearfield waves with distance.
(λ denotes wavelength)

	Distance, $\lvert -a+\Delta/2 \rvert$	$e^{k_b(-a+\Delta/2)}$
1	λ	0.2%
2	0.73λ	1%
3	0.47λ	5%

3.6 Numerical Simulations

In this section, MC simulations are performed for a thin, homogeneous, Euler-Bernoulli beam to which a mass discontinuity is attached. The intentions are to investigate the accuracy of the closed form solutions for the mean values and variances of the estimated power reflection and transmission coefficients, and also to investigate the statistical distribution of the estimated coefficients given a Gaussian noise model for the measured outputs. For simplicity, it is assumed in what follows that all the transducers have similar accuracy.

3.6.1 Parametric Model for the Discontinuity

The beam is assumed to be infinitely long. The mass/inertia discontinuity is considered to be rigidly attached to the beam. The parametric model introduced in section 2.8 will be employed here to simulate the mass discontinuity. Table 3.2 lists the properties of the beam and the discontinuity. Correspondingly, the non-dimensional parameters are $\mu = 74.019$ and $\vartheta = 1.645 \times 10^4$. These data relate to the experiments which will be discussed in the next section.

Table 3.2 Properties of the beam and discontinuity (SI units)

beam			discontinuity	
density, ρ	Young's modulus, E	width × thickness, $b \times h$	mass, m	moment of inertia, J
7800	194×10^9	0.050×0.006	0.300	2.0×10^{-4}

3.6.2 Simulation Results for the Power Reflection Coefficient

The results of MC simulations on the power reflection coefficient are given in this section. Conclusions below are all drawn regarding this set of MC simulations. Figure 3.4 shows the MC simulations for the case with noise level $\sigma_1 = \sigma_2 = 5\%$. The *x*-axis $k_b\Delta$ is proportional to the non-dimensional frequency ξ. In this case, $k_b\Delta = 29.412\xi$ when the transducer spacing $\Delta = 0.05$ m. MC simulations are performed at 100 frequencies at equally spaced wavenumbers in a range of $0 < k_b\Delta < 3.5$. At each frequency, 10,000 calculations are performed with random perturbations on "measured" transducer outputs. The mean value of MC simulation and the true value of the power reflection coefficient are also shown in the figure. The deviation and fluctuation of the simulated points can be seen from the "spread" of the data. For frequencies such that $k_b\Delta > 0.28$, the transducers are more than one wavelength from the discontinuity and the nearfields can be neglected.

When $\rho = 0$, the energy will be totally transmitted through the discontinuity. Referring to equation (2.52), $r_{PP} = 0$, i.e. $\mu\vartheta\xi^3 + 2\vartheta\xi^2 - 2\mu = 0$. Substituting the values of μ and

ϑ into the this equation, it gives $\xi = 0.042$, thus $k_b\Delta = 1.235$. Here it should be noticed that $\xi = k_b\kappa$, where $\kappa = h/\sqrt{12}$. When $\tau = 0$ and $t_{PP} = 0$, i.e. $\vartheta\xi^3 - \mu\xi + 4 = 0$. In this case $\xi = 0.086$ and $k_b\Delta = 2.529$. The energy will be totally reflected from the discontinuity.

Figure 3.5(a) shows the mean value of the estimated power reflection coefficient $\hat{\rho}$, obtained from MC simulations with a transducer spacing $\Delta = 0.05$ m and transducer noise standard deviation levels $\sigma_1 = \sigma_2 = 5\%$. Also shown is the noise free value, the approximate solution given by perturbation (equation (3.19)), and the resulting upper bound given by equation (3.20). The MC simulation is close to the approximate solution over the whole frequency range, and the upper bound of this is fairly conservative. The power reflection coefficient is estimated well except near zero frequency and $k_b\Delta = \pi$ where bias in the estimate is most apparent. Near these frequencies the sensor spacing is nearly 0 and 1 times half a wavelength respectively. This causes $\sin k_b\Delta \approx 0$ in equations (3.19) and (3.20).

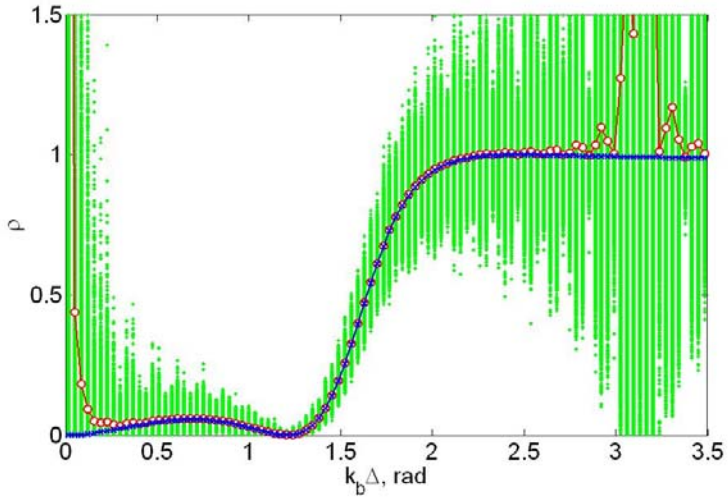

Figure 3.4 Monte Carlo simulations of the power reflection coefficient: $\sigma_1 = \sigma_2 = 5\%$, $a = 1.20$ m and $\Delta = 0.05$ m: ·, $\hat{\rho}$; —o—, $E[\hat{\rho}]$; —×—, $E[\rho]$.

Figure 3.5(b) gives the corresponding estimates for the variance of $\hat{\rho}$. The approximate solution given by equation (3.21) is again in close agreement with the MC simulations. The upper bound given by equation (3.22) appears fairly conservative except near zero

frequency and $k_b\Delta = \pi$. This is due in part to fluctuations in the approximate solution for $\hat{\rho}$ arising from the term $e^{-2ik_b a}$ in equation (3.21). The exponent, $k_b a$ can become very large, especially at high frequencies, so the variance changes rapidly with frequency. The estimate of the variance is smallest at about $k_b\Delta = 1.2$, where the power reflection coefficient is the smallest. This is due to the definition of the noise model.

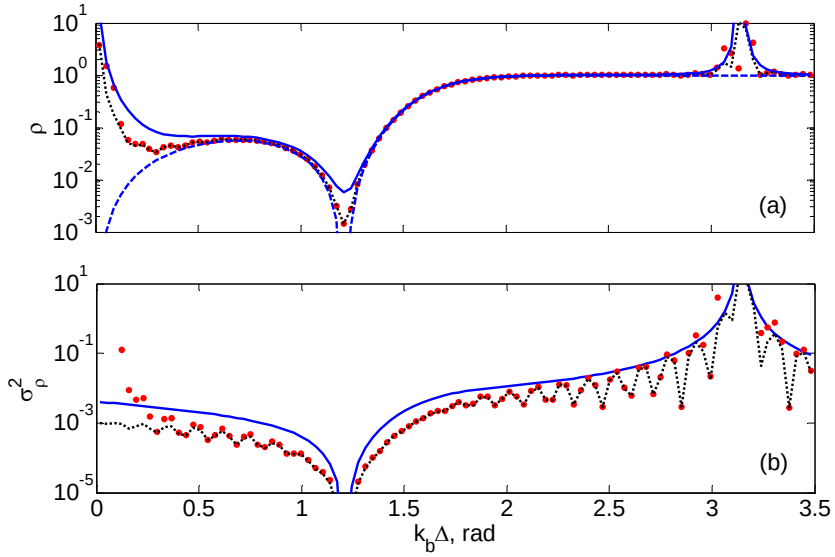

Figure 3.5 First order approximations and MC simulations of (a) the mean value and (b) the variance of $\hat{\rho}$: $\Delta = 0.05$ m and $\sigma_1 = \sigma_2 = 5\%$: ----- , ρ (noise free); ····· , perturbation solutions; • , Monte Carlo simulations; ——, upper bound of perturbation solutions.

The effect of noise level was similarly investigated using the approximate solution of equation (3.22). Figure 3.6 contrasts the effect of transducer noise levels of 1% and 5% for a fixed sensor spacing of $\Delta = 0.05$ m. The results are expressed in terms of the standard deviation normalised by the true value in order to assess the extent to which the wave decomposition process amplifies noise on the transducers. The first peak at about $k_b\Delta = 1.2$ is inevitable since there is no true reflection at this frequency to measure, and the second peak corresponds to a half-wavelength transducer spacing. At best (i.e. at frequencies for which the transducer spacing is a quarter wavelength) the noise on the power reflection coefficient is twice as large as that of the individual sensor measurements. The imperative for high fidelity measurements is clear if high precision of the reflection coefficients is desired.

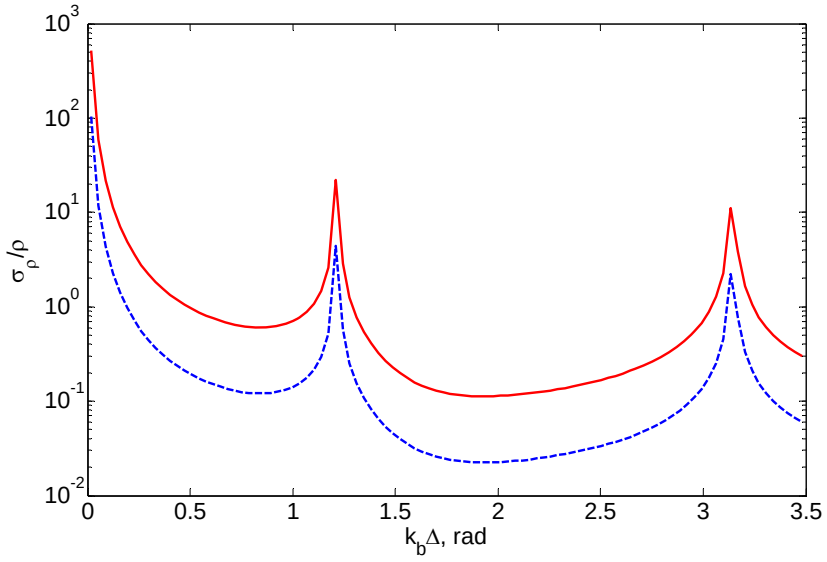

Figure 3.6 Closed form solutions for the upper bound normalised standard deviation of $\hat{\rho}$: ——, $\sigma_1 = \sigma_2 = 5\%$; ----, $\sigma_1 = \sigma_2 = 1\%$.

If the mass or moment of inertia changes, usually the frequencies where $\rho = 0$ and $\rho = 1$ will change correspondingly. If the discontinuity is a spring-like discontinuity, the trend of ρ is different from that of the mass and moment of inertia discontinuity. However, the noise on the power reflection coefficient keeps a similar trend (see Figure 3.4), i.e. when ρ is small, the noise is small; when ρ is large, the noise becomes large. Also at frequencies where $k_b\Delta = n\pi$, the variance of ρ is very large because of the ill-condition of the wave amplitude decomposition method.

3.6.3 Statistical Distribution of the Simulated Noisy Power Reflection Coefficient

This section investigates whether the MC simulation points obey a Gaussian distribution given the noise model on the output measurements. The following analysis is based on one MC simulation (one set of random noise seeds in the Matlab code) and conclusions are therefore limited.

The distribution range of 10,000 MC simulations of $\hat{\rho}$ at each frequency is divided into

100 intervals. Then the probability density of the distribution can be obtained by counting the number of samples at each interval. The concepts of skew and kurtosis are introduced first in order to describe the distribution characteristics of the MC simulations. Skew measures the degree of asymmetry of a distribution. It is defined by

$$\gamma_1 = \frac{E\left[\left(\hat{x}-\mu\right)^3\right]}{\sigma^3}, \tag{3.32}$$

where E indicates the expectation, $\hat{x}$ is a random variable, μ and σ are the mean and standard deviation of $\hat{x}$ respectively. Negative values for the skew indicate data that are skewed left and positive values indicate data that are skewed right. Any symmetric data should have a skew equal to zero. +1 or −1 will be very extreme examples of skew defined in equation (3.32) [66]. Kurtosis is defined by

$$\beta_2 = \frac{E\left[\left(\hat{x}-\mu\right)^4\right]}{\sigma^4}. \tag{3.33}$$

Kurtosis measures the data's peakedness relative to a normal distribution which has a kurtosis of 3. High kurtosis indicates a "peaked" distribution and low kurtosis indicates a "flat" distribution. Equation (3.33) for kurtosis will yield values around 4 for marked leptokurtic distributions with sharp middles and flattened tails. A value of around 2 will indicate platykurtic distributions with rounded middles and thin tails [66].

Figure 3.7 shows the probability densities of the distribution of $\hat{\rho}$ at three typical frequencies with $\sigma_1 = \sigma_2 = 5\%$. The probability densities are normalised so that the distributions have zero mean and unit variance. Figure 3.8 shows the skew and kurtosis of the distribution of the MC simulations on $\hat{\rho}$. From the whole trend, it can be seen that the distribution of the MC simulations of $\hat{\rho}$ with lower measurement noise appears more Gaussian. All the skews are positive, which means that all the data are skewed right. But with the lower noise level of "measurement", the skew of the distribution approaches zero. This is because the power reflection coefficient is defined as the squared modulus of the amplitude reflection coefficient. When $k_b\Delta$ is close to zero or π, the distribution of MC simulations are skewed significantly to the right. This is due to the data having lower bounds and the deviations of the data at these areas become very large.

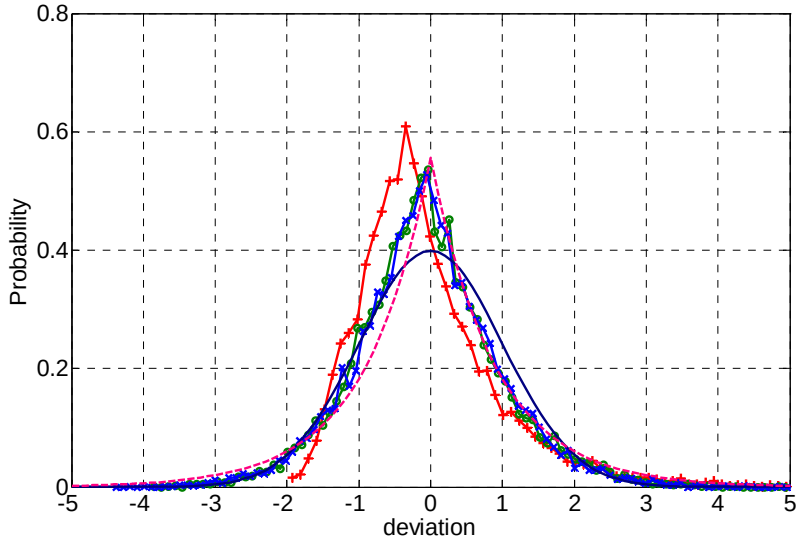

Figure 3.7 Normalised probability density of $\hat{\rho}$ with zero mean and unit variance for various values of $k_b\Delta$: $\sigma_1=\sigma_2=5\%$: —+—, $k_b\Delta=0.51$; —o—, $k_b\Delta=1.52$; —x—, $k_b\Delta=2.47$; - - - -, $Lap(0,0.9)$; ——, Gaussian.

The kurtosis shown in Figure 3.8 has a marked leptokurtic distribution, which means the

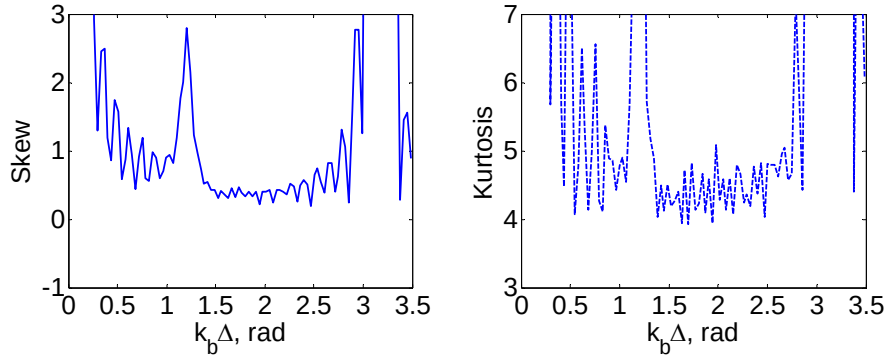

(a) $\sigma_1=\sigma_2=5\%$

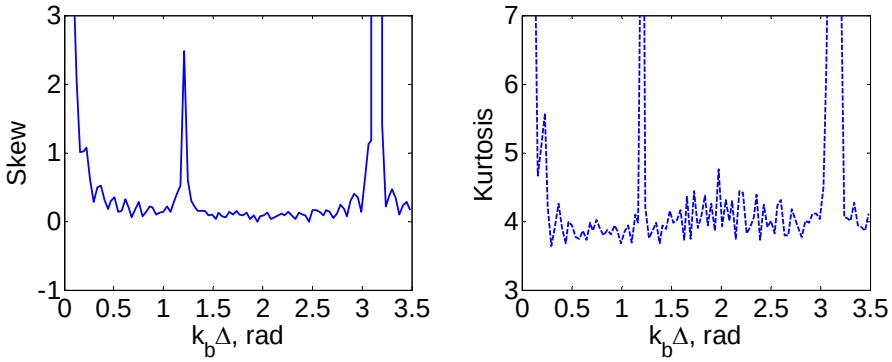

(b) $\sigma_1=\sigma_2=1\%$

Figure 3.8 Skew and Kurtosis of the MC simulations on $\hat{\rho}$.

distributions have a narrow middle and a great concentration in the tails. This can be seen from Figure 3.8: the sampled data have a narrow middle compared to Gaussian distribution. In this respect, the distribution of the sampled data except for the frequencies with remarkable skews shows a characteristic of a Laplace distribution. The probability density function of Laplace distribution is defined by

$$P(x) = \frac{1}{2\sigma} e^{-\frac{|x-\mu|}{\sigma}} \tag{3.34}$$

The parameters for the Laplace distribution in Figure 3.7 are $\mu = 0$ and $\sigma = 0.9$. The kurtosis for the Laplace distribution is 6.

3.7 Wavenumber Measurements

This section reviews a method for measuring the flexural wavenumber directly. In order to obtain the wave amplitudes and hence the reflection and transmission coefficients, the wavenumber of the waveguide needs to be known. The flexural wavenumber from Euler-Bernoulli beam theory can be expressed as

$$k_b = \sqrt[4]{\omega^2 \rho A / EI} \ . \tag{3.35}$$

Due to inaccuracies in the density, the Young's modulus and the dimensions of the waveguide, equation (3.35) is not a reliable estimate for the wavenumber of a practical waveguide. Alternatively, a method is presented to measure the wavenumber directly.

Consider the one-dimensional waveguide shown in Figure 3.9. Three points are linearly distributed along the neutral axis of the waveguide. All of them are considered to be far enough from the excitation point to neglect the nearfields. Location 2 is chosen as the origin of the coordinate system. By referring to equation (3.1) and neglecting the nearfields, the outputs at the three points can be obtained by

$$\begin{Bmatrix} W_1 \\ W_2 \\ W_3 \end{Bmatrix} = \begin{bmatrix} e^{ik_b\Delta} & e^{-ik_b\Delta} \\ 1 & 1 \\ e^{-ik_b\Delta} & e^{ik_b\Delta} \end{bmatrix} \begin{Bmatrix} a_P^+ \\ a_P^- \end{Bmatrix}. \tag{3.36}$$

Thus

$$\frac{W_1 + W_3}{W_2} = 2\cos k_b\Delta \, . \tag{3.37}$$

The wavenumber can be derived from the above equation as

$$k_b = \frac{1}{\Delta}\arccos\frac{W_1 + W_3}{2W_2} \tag{3.38}$$

The optimal transducer spacing, Δ can be determined after some pre-measurements based on several reasonable values of Δ. Note that the optimal value of Δ depends on which frequency is of most interest.

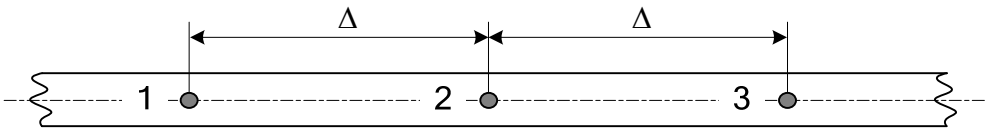

Figure 3.9 Transducer array for wavenumber measurements.

Any response quantity varying time harmonically under the passage of a wave, such as the displacement, velocity, acceleration, shear force and so on, can be used as the output of the transducers. Whichever is chosen is only a matter of convenience. In the experiments, three accelerometers were placed equidistantly on the centre line of the beams. The acceleration ratios W_1/W_2 and W_3/W_2 were measured in order to obtain the wavenumber in equation (3.38).

Referring to equation (3.35), the flexural wavenumber can also be written as

$$k_b = \beta\sqrt{f} \tag{3.39}$$

where $f = \omega/2\pi$ and $\beta = \sqrt[4]{4\pi^2\rho A/EI}$. Substituting equation (3.39) into (3.38) gives

$$\beta\Delta\sqrt{f} = \arccos\frac{W_1 + W_3}{2W_2}. \tag{3.40}$$

Then β can be obtained for each frequency. β can also be fitted over many frequencies by using the Moore-Penrose inverse, thus

$$\beta = \frac{1}{\Delta}\left(\boldsymbol{\varphi}^{\mathrm{T}}\boldsymbol{\varphi}\right)^{-1}\boldsymbol{\varphi}^{\mathrm{T}}\boldsymbol{\omega}. \tag{3.41}$$

where $\boldsymbol{\varphi}$ and $\boldsymbol{\omega}$ are vectors whose elements are given by $\sqrt{f_i}$ and $\arccos\left[\left(W_1 + W_3\right)/2W_2\right]_i$ respectively. Subscript 'i' indicates the ith frequency. Once β is known, the wavenumber can be obtained easily from equation (3.39).

Due to the damping of the waveguide and measurement noise, $(W_1 + W_3)/2W_2$ is complex instead of real. Since the damping of metal materials is typically very small, the imaginary part is usually very small so that it can be neglected. In the following the damping is set to zero.

3.8 Experiments on Mass Discontinuities

This section discusses the measurements of reflection and transmission coefficients of a beam with attached mass and moment of inertia discontinuities. The intention is to investigate the characteristics of measured reflection and transmission coefficients of mass and moment of inertia discontinuities on a beam.

3.8.1 Experimental Setup

The structure under test was a steel beam suspended by wire at three locations. Figure 3.10 shows the experimental rig. A sandbox was placed on each end of the beam to approximate anechoic conditions, although the system model developed here can be applied to waveguides of both infinite and finite length. The beam was excited in the transducer direction with a random signal by an electrodynamic shaker through a force gauge. The mass discontinuity was formed by gluing two steel blocks to either side of the beam, which is shown in Figure 3.11.

Only the flexural wave in the beam is of interest here. A stinger with relatively large axial but small bending stiffness was incorporated between the shaker and force gauge. The excitation point was chosen on the centre line of the beam. All of these precautions were taken to avoid torsional excitation as much as possible. Note that the resonance frequency of the force gauge and stinger system should be out of the frequency range of interest, otherwise the measured data will be contaminated.

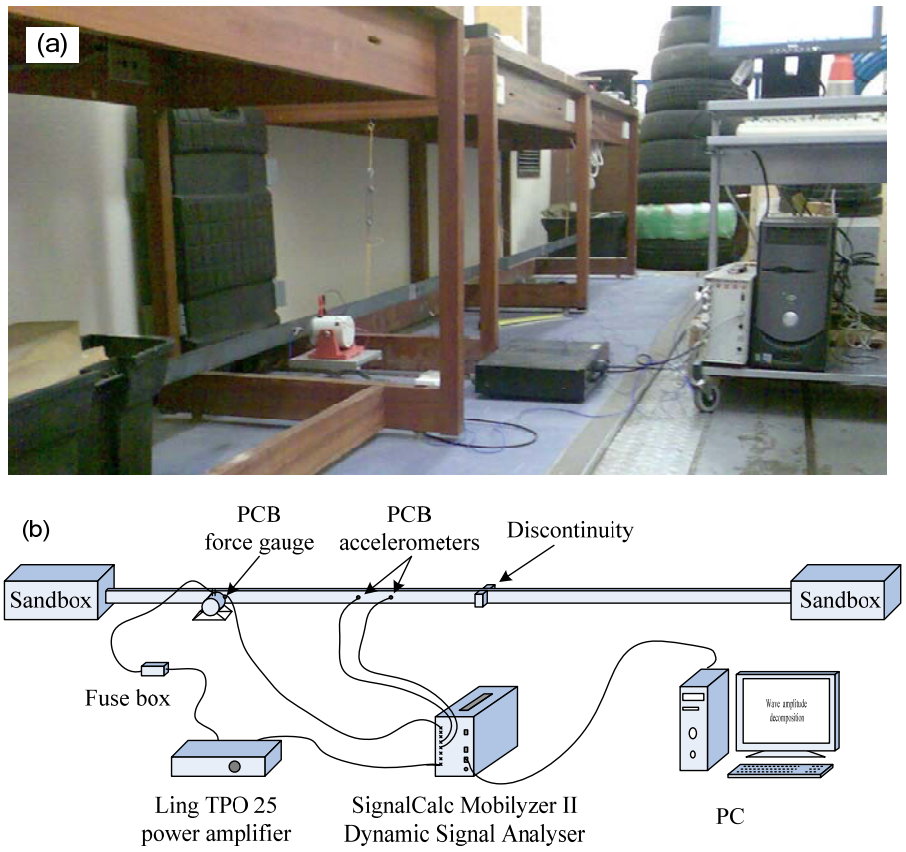

Figure 3.10 Experimental setup for measurements on a beam with a mass and moment of inertia discontinuity: (a) actual experimental rig; (b) block diagram.

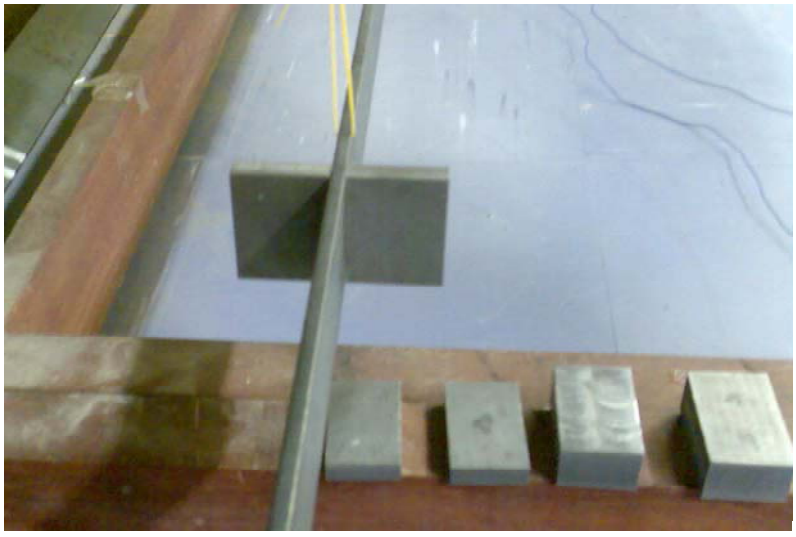

Figure 3.11 Steel blocks attached to the beam as discontinuities.

3.8.2 Wavenumber Measurements

Before measuring the reflection and transmission coefficients, the flexural wavenumber of the beam was measured using the method introduced in Section 3.7.

The algebraic average of the acceleration ratios between locations 1 to 2 and 3 to 2 (Figure 3.9) is shown in Figure 3.12. The imaginary part is nearly zero. The real part can be considered as the value of $(W_1 + W_3)/2W_2$ needed in equation (3.38). Letting the real part equal $\cos k_b \Delta$ gives the estimation of the wavenumber of the beam. By using equation (3.41), $\beta = 0.851$ is obtained in the frequency range 500-3000Hz.

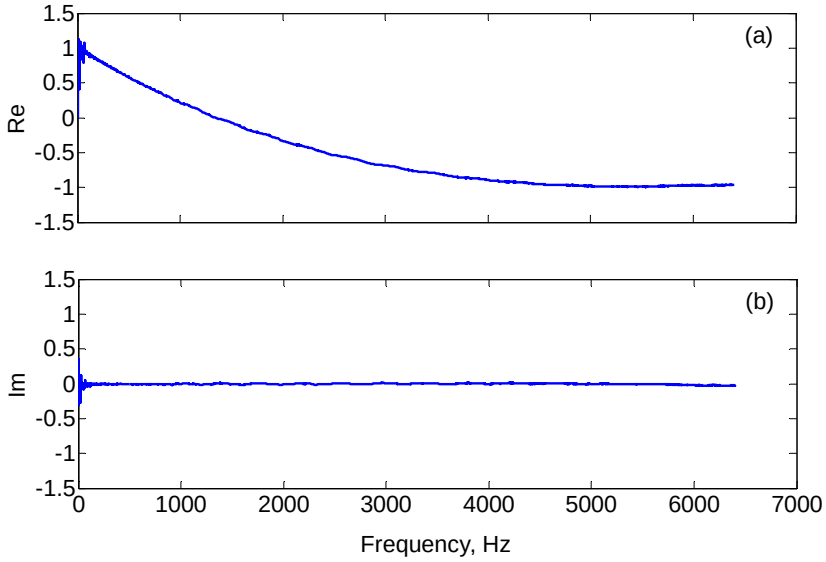

Figure 3.12 Algebraic average of the acceleration ratios for wavenumber measurements of a beam: (a) real part; (b) imaginary part.

Figure 3.13 shows the measured real part of $(W_1 + W_3)/2W_2$ compared to $\cos k_b \Delta$ based on $\beta = 0.851$. A very good agreement is obtained. In what follows $\beta = 0.851$ is used for the estimation of the reflection and transmission coefficients of a mass discontinuity in the beam.

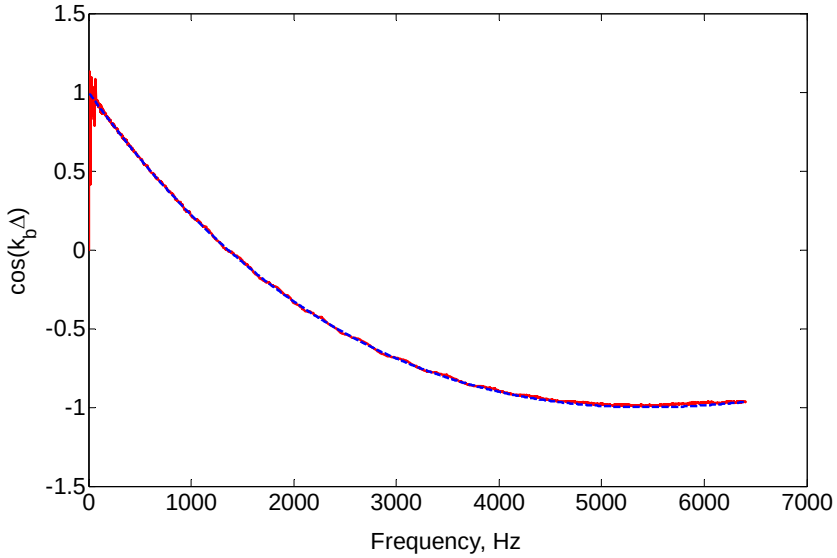

Figure 3.13 Wavenumber of the beam: ——, measured real part of $(W_1 + W_3)/2W_2$; -------, $\cos k_b\Delta$ with fitted wavenumber at frequency range 500-3000Hz ($\beta = 0.851$).

3.8.3 Reflection and Transmission Coefficients

This section discusses the measurements of the reflection and transmission coefficients of the steel blocks attached to the beam. The dimensions of the beam and the properties of the blocks are listed in Table 3.3. The beam is of same material as the blocks, for which the density is $\rho = 7.82\times10^3\,\mathrm{kg/m^3}$. The method introduced in Section 3.2 is employed here to decompose the wave amplitudes on both sides of the discontinuity

Table 3.3 Dimension of the beam and steel blocks (SI units).

	Beam	block 1 long-thin	block 2 short-thin	block 3 short-thick
Width, b	0.050	0.050	0.050	0.050
Thickness, h	0.006	0.010	0.010	0.020
Length, l	6.060	0.040×2	0.030×2	0.030×2
Mass, m	/	0.313	0.235	0.469
Moment of inertia, J	/	207×10^{-6}	93.6×10^{-6}	187×10^{-6}
μ	/	76.955	57.735	115.421
ϑ	/	1.699×10^4	7.679×10^3	1.535×10^4

from pairs of transducer measurements. The left-hand side local origin of the transducer pair was located at $x = -1.075$ m and the right-hand side was at $x = 1.000$ m. The transducer spacing is $\Delta = 0.050$ m for which the optimal frequency is about 1400Hz where the transducer spacing is equal to a quarter wavelength and the worst frequency is about 5500Hz where the transducer spacing is equal to half wavelength. Above 60Hz the nearfields can be neglected (influence on the wave amplitude less than 0.2%). The non-dimensional parameters $\xi = 0.066$ and $k_b\Delta = 1.903$ at 2000Hz, for example.

The FRFs of the accelerations of the four locations to the exciting force at each frequency were measured and their magnitudes are shown in Figure 3.14. Figure 3.15 illustrates the positive- and negative-going wave amplitudes at the local origins of the transducer pairs, which are decomposed from the measured FRFs. Figure 3.16 gives the power reflection and transmission coefficients, $\hat{\rho}$ and $\hat{\tau}$ of block 1 estimated from the decomposed wave amplitudes based on assumptions described in Section 3.3, which are that there is one incident wave from each side of the discontinuity and the discontinuity itself is symmetric. This actually assumes the presence of the end reflections of the beam. The decomposed wave amplitudes, and reflection and transmission coefficients can interpret the behaviour of the measured FRFs. For example, below 1000Hz, since the reflection from the discontinuity is small, the measured FRFs are of similar magnitudes. Above that frequency, the reflected wave (dashed line in Figure 3.15) becomes larger, and the transmitted wave (dotted line in Figure 3.15) becomes smaller. Therefore the FRFs on the left-hand-side get larger and correspondingly the FRFs on the right-hand-side become smaller. From about 2800Hz the transmitted wave begins to increase slowly, which causes the increase of the measured FRFs on the right-hand-side. The fluctuations of the measured left-hand side FRFs originate from the standing waves on the left-hand side beam. They are caused by the distance from the transducers to the mass.

From Figure 3.15 it can be seen that the influence of the reflected wave from the right-hand side end of the beam is relatively large below about 2200Hz, but above that it becomes nearly zero. The decomposition method fails at very low frequencies and 5400Hz where the transducer spacing is about half wavelength. This is consistent with the results of Section 3.6.

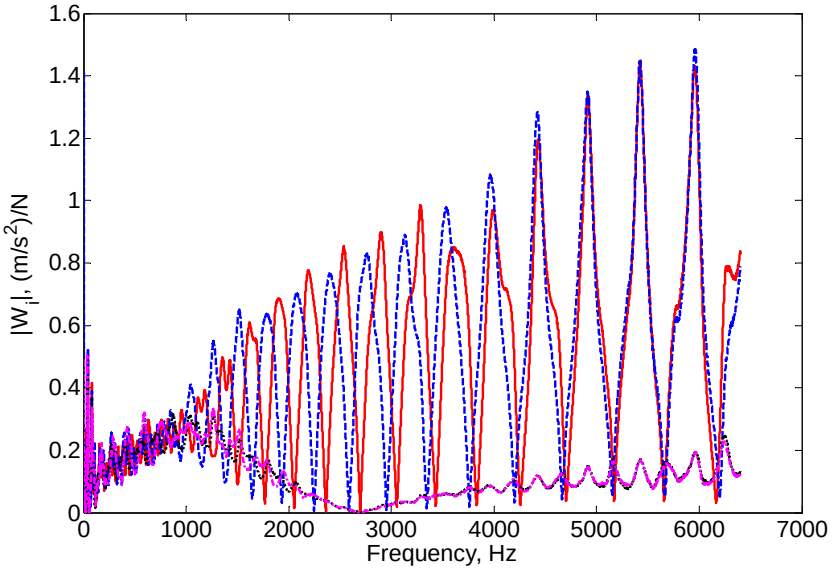

Figure 3.14 Magnitudes of the measured accelerances for block 1: ——, location 1 in Figure 3.2; - - - - -, location 2; ·····, location 3; – · – · –, location 4.

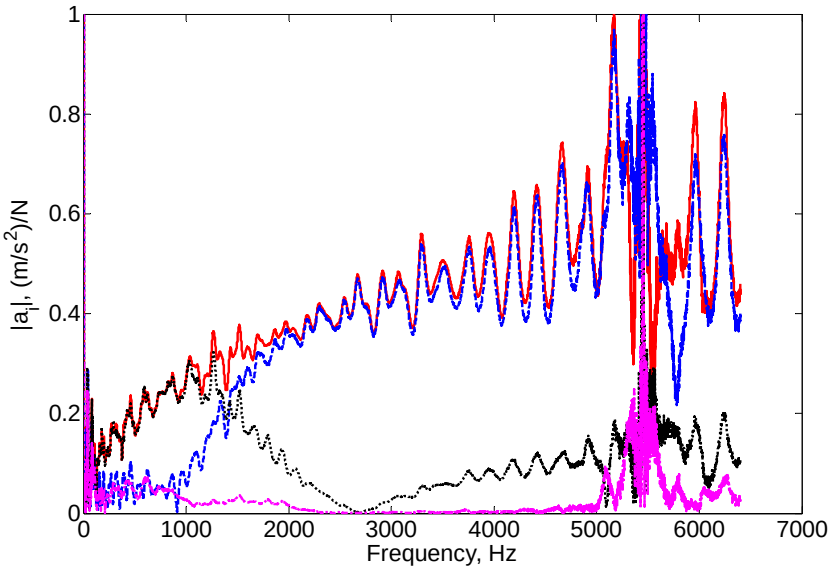

Figure 3.15 Decomposed wave amplitudes of at the centres of the transducer pairs for block 1: ——, positive-going, left-hand-side; - - - - -, negative-going left-hand-side; ·····, positive-going, right-hand-side; – · – · –, negative-going, right-hand-side.

In Figure 3.16 the estimated power reflection and transmission coefficients are poor around zero frequency and 5400 Hz where $k_b\Delta = \pi$. This is because of the ill-condition of the wave amplitude decomposition method. The estimated scattering coefficients are relatively noisy at frequencies where they are large. In this sense, the noise model chosen in section 3.4.1 is reasonable.

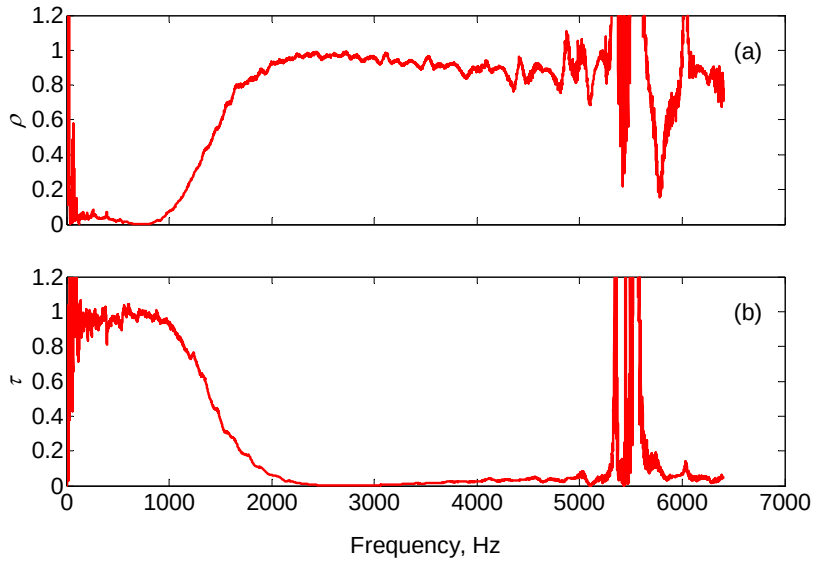

Figure 3.16 Decomposed power reflection and transmission coefficients of block 1.

Figure 3.17 gives the sum of the decomposed power reflection and transmission coefficients. Below 3000Hz it can be seen that they approximately sum up to unity. This means the damping effect of structure can be neglected below 3000Hz. The following analysis will focus on frequencies below 3000Hz.

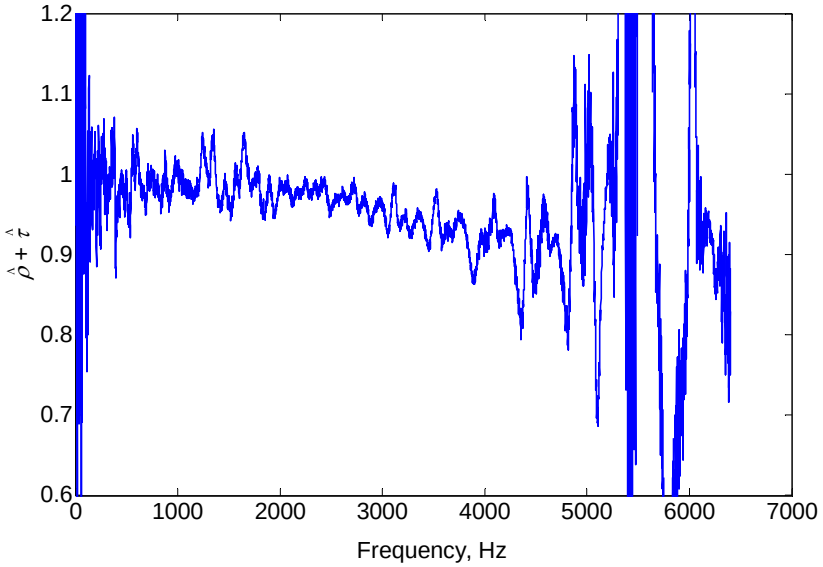

Figure 3.17 Sum of measured power reflection and transmission coefficients.

In section 3.4 it was seen that the decomposed power reflection and transmission coefficients are biased based on a Gaussian-like measurement noise model, therefore,

the discontinuity parameters estimated from these coefficients are also biased. However, if the measurement noise is very small, the estimates can be considered to be very close to the real values.

Figures 3.18 and 3.19 show the experimental estimates of the power reflection and transmission coefficients respectively compared with the theoretical predictions from the parametric model given in section 2.8. The curves are included for different sets of assumptions. The results from the non-reflecting end assumption are oscillatory. The oscillations are significant up to 2200Hz. This is consistent with the results shown in Figure 3.15, where the wave reflected from the beam end is relatively large below 2200Hz. The non-reflecting end assumption is only valid above this frequency since the reflections from the beam end are nearly zero from there on (dash-dot line in Figure 3.15). Large errors occur at low frequencies, as a result of the poor conditioning of the WAD method. The assumption of reflecting ends (one incident wave from each side) produces smoother results. For both the reflection and transmission coefficients, the overall trends have been produced for the frequency range considered here and good agreement with the theoretical predictions is achieved. This indicates that the blocks match the lumped mass theory well.

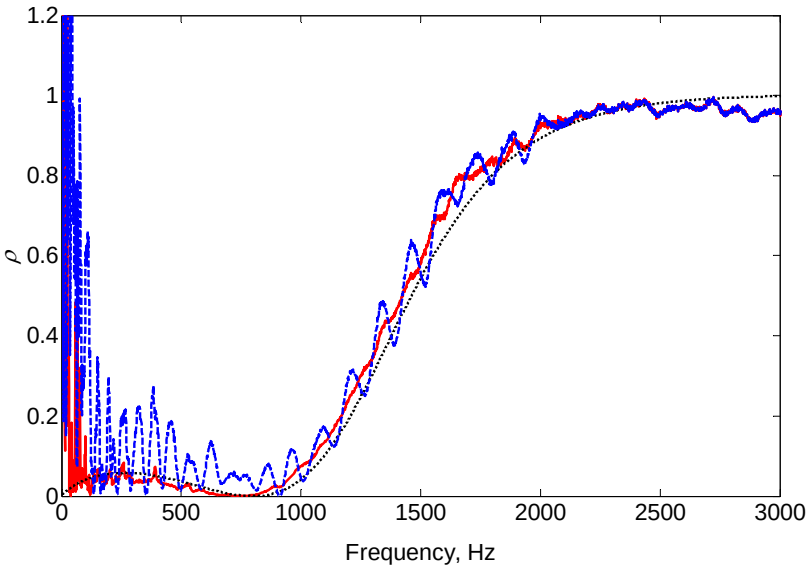

Figure 3.18 Power reflection coefficients of block 1: ——, experimental estimate assuming reflecting ends; - - - - - - -, experimental estimate assuming non-reflecting ends; ·····, predicted based on directly measured mass and moment of inertia (non-reflecting ends): (a) reflection coefficient; (b) transmission coefficient.

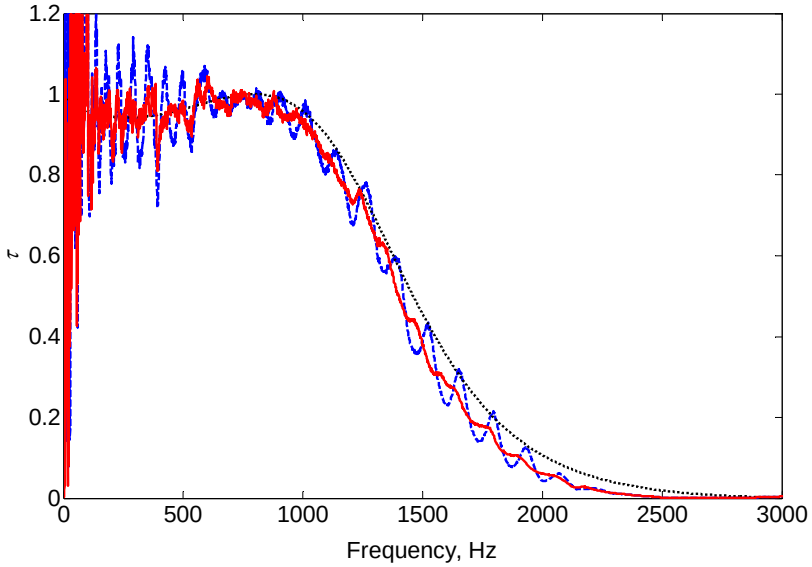

Figure 3.19 Power transmission coefficients of block 1: ——, experimental estimate assuming reflecting ends; - - - - - - -, experimental estimate assuming non-reflecting ends; ..... , predicted based on directly measured mass and moment of inertia (non-reflecting ends): (a) reflection coefficient; (b) transmission coefficient.

Figures 3.20(a), (b) show the sums of the measured power reflection and transmission coefficients for blocks 2 and 3 respectively. In the range 200-3000Hz the sums are close to unity, which means the damping is very small.

Figure 3.21 shows the experimentally estimated power reflection and transmission coefficients of blocks 2 and 3 along with the theoretical predictions. The overall trends of the predictions can also be obtained in the frequency range shown in the figures. With increasing frequency, the differences become larger. The model presented here is less accurate.

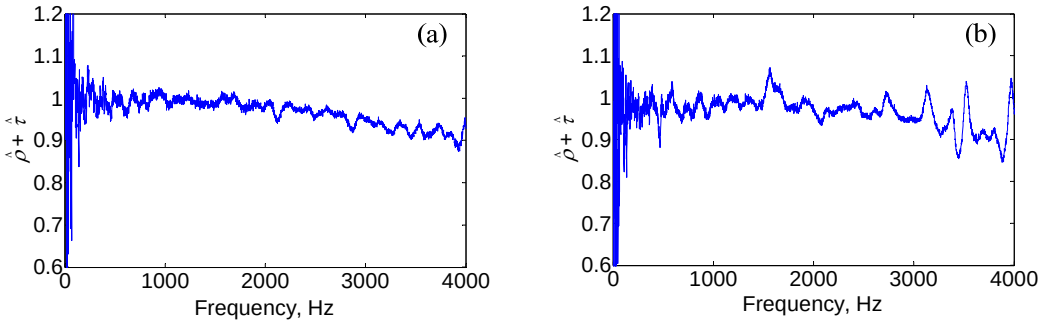

Figure 3.20 Sum of the estimated power reflection and transmission coefficients for (a) block 2 and (b) block 3.

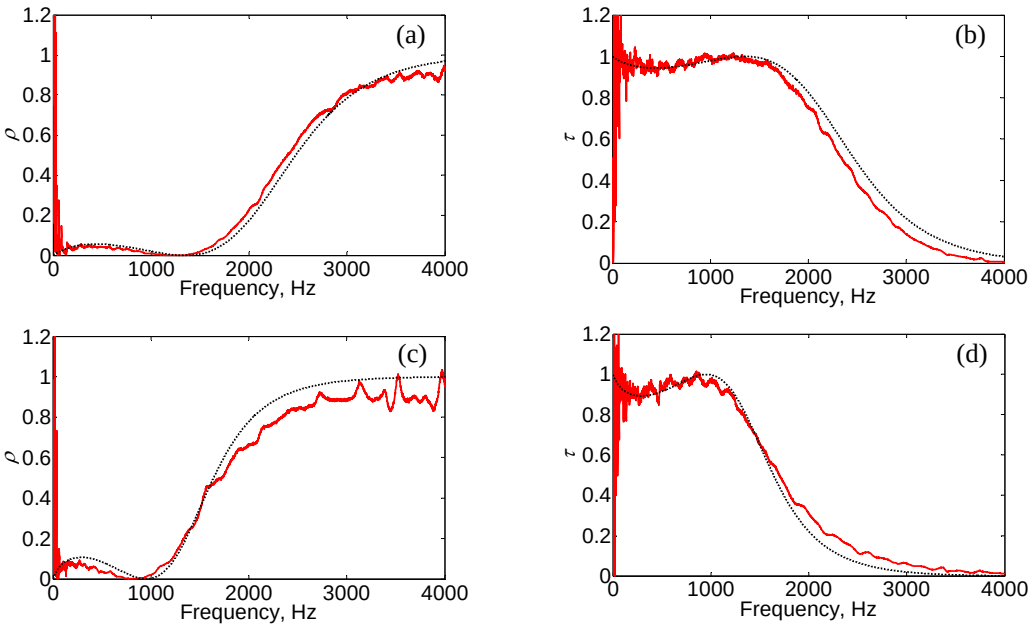

Figure 3.21 Power reflection and transmission coefficients for blocks 2 and 3: ——, experimental estimate assuming reflecting ends; ·····, predicted based on directly measured mass and inertia (non-reflecting ends): (a) ρ of block 2; (b) τ of block 2; (c) ρ of block 3; (d) τ of block 3.

3.9 Summary

A wave amplitude decomposition approach has been reviewed and employed to calculate the reflection and transmission coefficients of discontinuities from the measurements of arrays of transducers. Considering noise contamination as a perturbation on the ideal measurements, expressions for the mean and standard deviation of the power reflection and transmission coefficients were derived and a first order approximation was developed. The results of Monte Carlo simulations on a discontinuity which involves a mass and a moment of inertia agree well with the first order approximations. To minimise the standard deviation of the power reflection and transmission coefficients, the optimal transducer spacing is a quarter wavelength and poor situations occur at small spacings and those approaching a multiple of half a wavelength. The statistical distribution of the Monte Carlo simulations for the power reflection coefficient was also investigated and found to be fairly similar to a Laplace distribution under some particular conditions.

Experiments were performed on a beam with attached steel blocks. The flexural reflection and transmission coefficients were estimated by the wave amplitude decomposition approach. The results were consistent with the theoretical analysis given in the previous sections. The anechoic assumption caused large errors if the reflection from the beam end is large. For the long-thin block, the measured power reflection and transmission coefficients agree well with the predictions based on the theoretical model given in Chapter 2. The agreement for the short-thin and short-thick blocks is less consistent, especially with increasing frequency, which means the discontinuity model is less valid for blocks of larger dimensions.

Chapter 4 Wave Reflection and Transmission at Pipe Supports

4.1 Introduction

Built-up systems comprise many discontinuities in the form of joints, hangers, supports, flanges and so on. Dynamically these discontinuities contribute stiffness, inertia and damping and can dramatically alter the response of the system. In Chapters 2 and 3, wave reflection and transmission through a mass discontinuity on a beam has been investigated. This chapter discusses wave reflection and transmission at a support of an *in-vacuo* piping system. This support features not only mass and moment of inertia, but also translational and rotational stiffnesses, and damping.

Mace [61] modelled a point support of a beam by translational and rotational dynamic stiffnesses, and derived the reflection and transmission coefficients of such a model in terms of the support dynamic stiffnesses. Here the pipe support is modelled in the same way and then the dynamic stiffnesses are decomposed into mass, inertia and stiffness terms, which help the parameter identification of the support in Chapter 7. Damping is incorporated into the dynamic stiffnesses by loss factors.

In the next section, wave modes in *in-vacuo* piping systems are discussed briefly. In this thesis, attention is only focused on the axial and transverse waves. Section 4.3 gives the parametric model for a pipe support. The reflection and transmission coefficients are derived using the general method presented in Chapter 2. Then numerical simulations of the reflection and transmission coefficients are performed in terms of the non-dimensional joint dynamic stiffnesses. Section 4.4 presents the experiments on a pipe support. The propagating flexural reflection and transmission coefficients of the support are measured by using the wave amplitude decomposition method. In order to be able to compare the measured and simulated reflection and transmission coefficients, methods

are also developed to measure the translational and rotational dynamic stiffnesses of the support directly. The stiffnesses, mass and moment of inertia of the support are estimated from the directly measured translational and rotational dynamic stiffnesses.

4.2 Wave Modes in *In-vacuo* Piping Systems

Piping systems can be considered as an example of thin-walled cylindrical shells. A thin-walled cylindrical shell can be considered as a three dimensional structure. Structural waves in a thin-walled cylinder propagate in a helical pattern and can be described by the wavenumber k_{cs}, shown in Figure 4.1 (Fahy [3]). The wavenumber of the helical wave, k_{cs} is given by

$$k_{cs}^2 = k_l^2 + k_s^2 \tag{4.1}$$

where k_l is the longitudinal wavenumber and k_s is the circumferential wavenumber. The longitudinal wavenumber is hence

$$k_l = \sqrt{k_{cs}^2 - k_s^2} \tag{4.2}$$

Therefore the longitudinal wave can propagate only when $k_{cs}^2 \geq k_s^2$. Otherwise, the wave is evanescent.

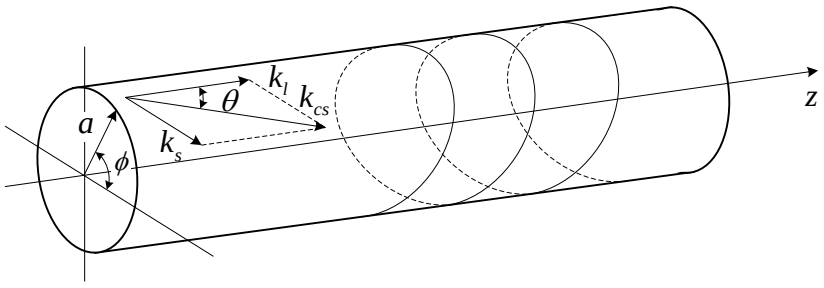

Figure 4.1 Cylindrical shell coordinates and wavenumbers.

The radial wave variables must be continuous in the circumferential direction due to the closure of the pipe in this direction. Thus the radial displacement takes the form of sine or cosine functions of $k_s a\theta$, where a is the mean radius of the pipe, θ is the angle in the polar coordinate system of the cross-section and $k_s = n/a$ ($n = 0,1,2,\cdots$), n is the wave mode number. The $n = 0$ mode behaves as a line monopole with only stretching

and contracting of the wall. The $n=1$ mode, also called the bending wave mode, propagates as a line dipole. There is no cross-sectional deformation with this mode. The $n=2$ mode, ovalling mode, moves as a line quadrupole, and so on (Figure 4.2).

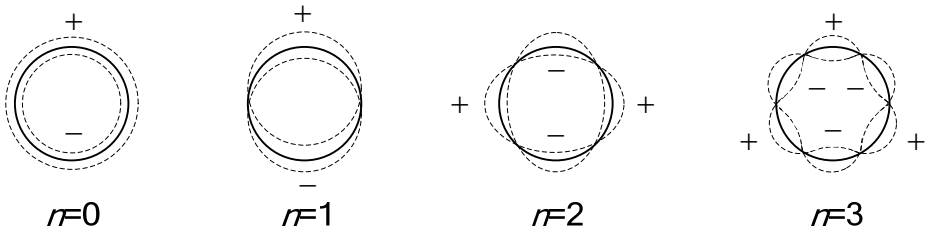

Figure 4.2 Cross-sectional mode shapes of a cylindrical shell.

Longitudinal, torsional and flexural (bending) waves can always propagate at all frequencies. For longitudinal and torsional waves $n=0$ and for flexural waves $n=1$. However, the $n=0$ breathing wave mode can only exist above the ring frequency [3]

$$\omega_r = \frac{c_l}{a} \tag{4.3}$$

where c_l is the longitudinal wavespeed in a plate of the shell material. The longitudinal wavelength in the shell wall is equal to the shell circumference at the ring frequency. $n=2$ and higher modes can only exist above their cut-on frequencies. The cut-on frequencies are given approximately by

$$\frac{\omega_{cut-on}}{\omega_r} \approx \frac{h}{\sqrt{12}a}\left(n^2 - \frac{3}{2}\right),\ n \geq 2, \tag{4.4}$$

where h is the wall thickness. In this thesis, only the longitudinal and flexural wave modes are of interest. An estimate for the cut-on frequency for the $n=2$ wave mode can be obtained from the above equation and this is an upper bound frequency that should be considered in the numerical simulations and experimental measurements, above which the simple models break down.

4.3 Dependence of Reflection and Transmission Coefficients on Parametric model of a Support

The infrastructure to which the waveguide is connected acts as a discontinuity when

structural waves propagate along the waveguide. Supports or hangers of pipes can be considered as such discontinuities. This section discusses the modelling of a support of a one-dimensional waveguide carrying flexural waves and the reflection and transmission coefficients in terms of the parameters of such a model.

4.3.1 Model of a Support

This section gives the model of a support of a one-dimensional waveguide. Figure 4.3 shows a waveguide of infinite length lying along the *x*-axis supported at $x = 0$. For simplicity the waveguides on both sides of the support are considered to have the same physical properties, such as material and dimension. The support exerts both translational and rotational constraints, which are modelled by translational dynamic stiffness D_T and rotational dynamic stiffness D_R. Here the flexural reflection and transmission coefficients of this support will be derived by using the general approach presented in Chapter 2.

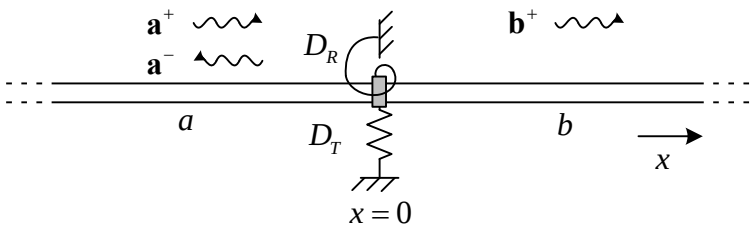

Figure 4.3 The model of a support of an infinite one-dimensional waveguide.

4.3.2 Parametric Reflection and Transmission Coefficients

The reflection and transmission coefficients of the support described above are derived in this section. Now consider the case that a set of flexural incident waves $\mathbf{a}^+$ propagates along waveguide *a* and impinges upon the support, which gives rise to reflected $\mathbf{a}^-$ and transmitted $\mathbf{b}^+$ waves. The excitation source that generates the incident wave is considered to be far enough away from the support, therefore the nearfield component in the incident wave is neglected. Thus the wave vectors, displacement and internal force vectors and matrices, and the reflection and transmission coefficients matrices are the same as the case discussed in Section 2.8, which are given by equations

(2.44) to (2.48). Note that the support is also considered to be symmetric.

By applying continuity and equilibrium conditions to the support, the transfer matrices in equation (2.35) can be obtained as

$$\mathbf{\Omega}_{11}=\begin{bmatrix}1 & 0\\ 0 & 1\end{bmatrix},\ \mathbf{\Omega}_{12}=\begin{bmatrix}0 & 0\\ 0 & 0\end{bmatrix},\ \mathbf{\Omega}_{21}=\begin{bmatrix}-D_T & 0\\ 0 & -D_R\end{bmatrix}\text{ and }\mathbf{\Omega}_{22}=\begin{bmatrix}1 & 0\\ 0 & 1\end{bmatrix}. \tag{4.5}$$

Substituting equations (2.44), (2.46) to (2.48) and (4.1) into (2.43), after some lengthy manipulation (referring to Appendix 3), yields

$$\begin{bmatrix} 1 & -1 & 1 & -1 \\ i & i & 1 & 1 \\ i & \dfrac{\chi_D}{\xi^3}+i & -1 & \dfrac{\chi_D}{\xi^3}-1 \\ -1 & -i\dfrac{\psi_D}{\xi}+1 & 1 & -\dfrac{\psi_D}{\xi}-1 \end{bmatrix}\begin{Bmatrix} r_{PP} \\ t_{PP} \\ r_{PN} \\ t_{PN} \end{Bmatrix}=\begin{Bmatrix} -1 \\ i \\ i \\ 1 \end{Bmatrix} \tag{4.6}$$

where

$$\chi_D=\frac{D_T}{EA/\kappa},\ \ \psi_D=\frac{D_R}{EI/\kappa},\ \ \xi=\sqrt{\frac{\omega\kappa}{c_l}}\,. \tag{4.7}$$

$\kappa=\sqrt{I/A}$ is the radius of gyration of the pipe. The parameters in equation (4.7) are all non-dimensional. Parameter χ_D is the ratio of the translational dynamic stiffness of the support to the axial stiffness of a length κ of the pipe. Parameter ψ_D is the ratio of the rotational dynamic stiffness of the support to the rotational stiffness of a cantilever of length κ. By inspection of equation (4.6), it is apparent that χ_D/ξ^3 and ψ_D/ξ determine the reflection and transmission coefficients. $-i\chi_D/\xi^3$ is the ratio of the translational impedance of the support to the translational characteristic impedance of the waveguide, and $-i\psi_D/\xi$ is the ratio of rotational impedance of the support to the rotational characteristic impedance of the waveguide (see Appendix 4).

The reflection and transmission coefficients can be obtained numerically by matrix inversion in equation (4.6). Alternatively, they can also be expressed in closed form as

$$
\begin{aligned}
r_{PP} &= -\frac{i\left[\left(\chi_D/\xi^3\right)\left(\psi_D/\xi\right)+2\chi_D/\xi^3-2\psi_D/\xi\right]}{\left(\chi_D/\xi^3-2+2i\right)\left(\psi_D/\xi+2+2i\right)},\\
t_{PP} &= \frac{2\left(\chi_D/\xi^3-\psi_D/\xi-4\right)}{\left(\chi_D/\xi^3-2+2i\right)\left(\psi_D/\xi+2+2i\right)},\\
r_{PN} &= -\frac{(1-i)\left(\chi_D/\xi^3\right)\left(\psi_D/\xi\right)+2\chi_D/\xi^3+2i\psi_D/\xi}{\left(\chi_D/\xi^3-2+2i\right)\left(\psi_D/\xi+2+2i\right)},\\
t_{PN} &= -\frac{2\left(\chi_D/\xi^3-i\psi_D/\xi\right)}{\left(\chi_D/\xi^3-2+2i\right)\left(\psi_D/\xi+2+2i\right)}.
\end{aligned}
\tag{4.8}
$$

If the support is modelled as a structure characterised by translational stiffness K_T, rotational stiffnesses K_R, mass m and moment of inertia J, shown in Figure 4.4, and assuming that there is no eccentricity, then the dynamic stiffnesses can be expressed as

$$D_T = K_T - m\omega^2,\ D_R = K_R - J\omega^2. \tag{4.9a,b}$$

Then the parameters in equation (4.7) can be written as

$$\chi_D = \chi - \mu\xi^4,\ \psi_D = \psi - \vartheta\xi^4 \tag{4.10}$$

where

$$\chi = \frac{K_T}{EA/\kappa},\ \ \psi = \frac{K_R}{EI/\kappa},\ \ \mu = \frac{m}{\rho A\kappa},\ \ \vartheta = \frac{J}{\rho A\kappa^3}. \tag{4.11}$$

The physical meanings of these parameters can be interpreted similarly to those in equation (4.7). Damping in the support can be included by introducing loss factors to the dynamic stiffnesses. Letting $\chi = 0$ and $\psi = 0$, and substituting equation (4.10) into (4.8), the same expressions can be obtained as those of the mass-like discontinuity given in equation (2.52).

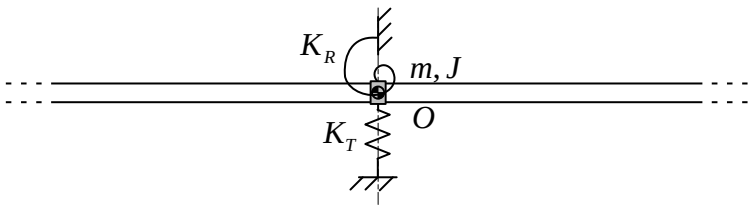

Figure 4.4 Model of a support featured with mass, moment of inertia and stiffnesses.

4.3.3 Numerical Examples

Some numerical simulations of the propagating wave reflection and transmission

coefficients of the support are given in this section. The magnitudes (squared) and phases are shown as functions of the magnitudes of impedance ratios in Figures 4.5 (a) to (d). Damping is not considered in the parameters here, so the rest parts, χ_D / ξ^3 and ψ_D / ξ are real, and the power reflection and transmission coefficients sum to unity. Positive χ_D / ξ^3 and ψ_D / ξ indicate stiffness dominated regions and negative ones signify mass and moment of inertia dominated regions. When the magnitudes of both χ_D / ξ^3 and ψ_D / ξ become large, whether positively or negatively, $\rho \to 1$ and $\tau \to 0$, i.e. the energy in the incident waves is totally reflected. At the regions where $\chi_D / \xi^3 = 2$ and ψ_D / ξ is large, or $\psi_D / \xi = -2$ and χ_D / ξ^3 is large, the energy is totally transmitted through the support. Note that $\chi_D / \xi^3 = 2$ means that the magnitude of translational impedance of the support is twice that of the translational characteristic impedance of bending waves in the waveguide, and $\psi_D / \xi = -2$ signifies that the magnitude of rotational impedance of the support is minus twice that of the rotational characteristic impedance of bending waves in the waveguide. The phases of r_{PP} and t_{PP} have a sudden change of π when the magnitudes approach zero.

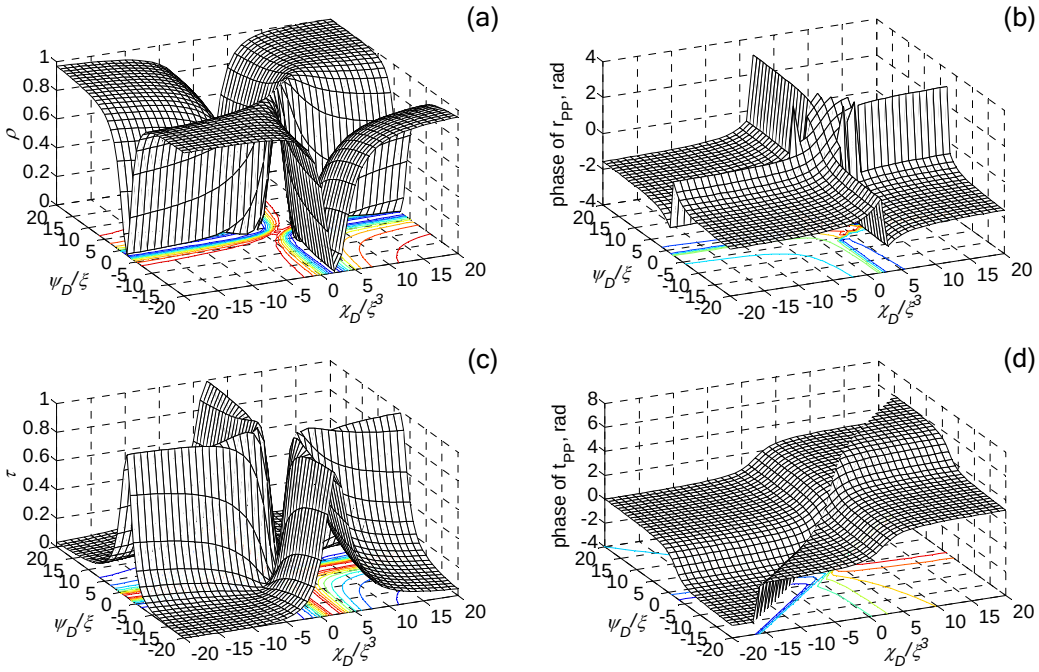

Figure 4.5 Magnitudes (squared) and phases of the propagating wave reflection and transmission coefficients for the support.

In order to study the influence of frequency, in the following examples the power reflection and transmission coefficients are plotted against the non-dimensional frequency, $\xi^2 = \omega\kappa / c_l$. A frequency range of $\omega\kappa / c_l < 0.1$ is selected to ensure that, firstly, Euler-Bernoulli beam theory is valid and, secondly, the $n = 2$ wave mode has not yet cut-on for a typical thin-walled cylindrical pipe. Detailed analysis of these two conditions is given in Appendix 6.

Figure 4.6 shows the power reflection and transmission coefficients as functions of the non-dimensional frequency based on specific values for the parameters of the support, which are $\chi = 10^{-2}$, $\psi = 10^{-1}$, $\mu = 10$ and $\vartheta = 10$. Recalling the physical meanings of the parameters, these values are not unrealisable. For example, for $\chi = 10^{-2}$, the translational stiffness of the support is equivalent to that of the axial stiffness of a pipe of length 100κ, which is roughly 70 times the pipe radius. Values of the other parameters can be interpreted similarly. From the expression of r_{PP} in equation (4.8) it can be seen that when frequency $\xi \to 0$, $|r_{PP}| \to 1$, i.e. $\rho \to 1$. This means most of the energy will be reflected at low frequencies. For the particular values of the parameters given above, $\rho = 1$ also occurs when $\omega\kappa / c_l = 0.014$ and $\rho = 0$ occurs when $\omega\kappa / c_l = 0.028$.

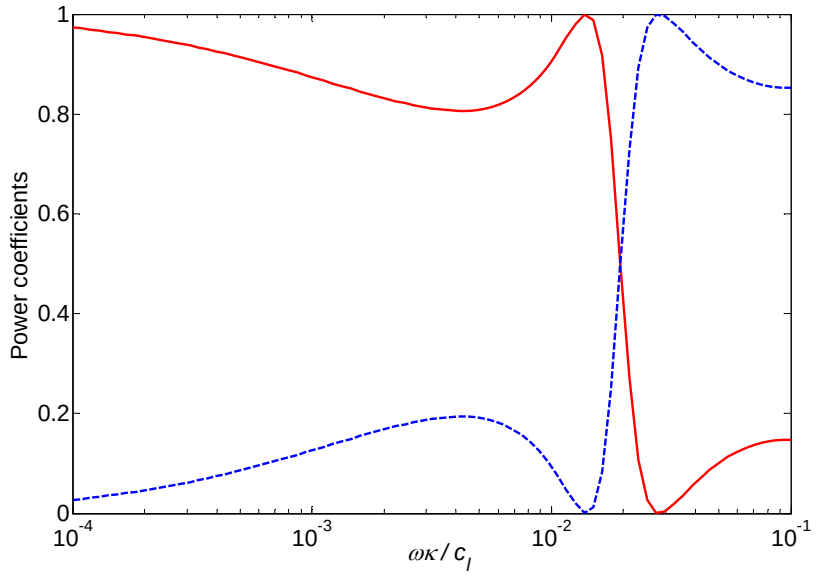

Figure 4.6 Power reflection and transmission coefficients of a support: $\chi = 10^{-2}$, $\psi = 10^{-1}$, $\mu = 10$ and $\vartheta = 10$: ——, ρ; - - - -, τ.

The above simulations do not consider damping in the support, so $\rho+\tau=1$. As mentioned previously the damping of the joint can be included as a complex stiffness. Therefore the translational damping loss factor, η_T and rotational loss factor, η_R are incorporated into the translational and rotational stiffnesses, χ and ψ which can be written as $\chi(1+i\eta_T)$ and $\psi(1+i\eta_R)$ respectively. Figure 4.7 shows the influence of damping of the translational and rotational springs on the power reflection and transmission coefficients. The loss factors of riveted or bolted thin sheet-metal structures are typically about 0.02 . For welded structures of thick plates $\eta\approx 0.001$ [1].

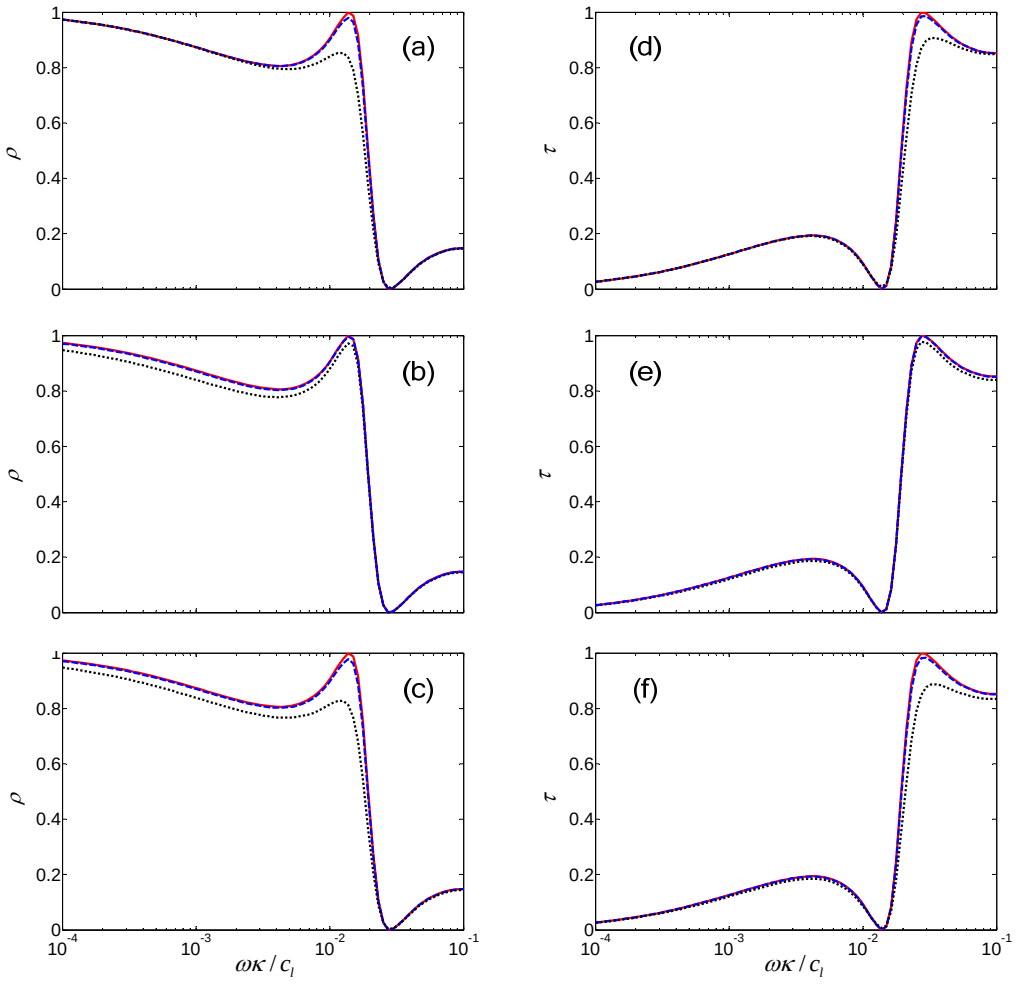

Figure 4.7 The influence of damping on the power reflection coefficient ρ: $\chi=10^{-2}$, $\psi=10^{-1}$, $\mu=10$ and $\vartheta=10$: ——, $\eta=0$; - - - -, $\eta=0.01$; ·····, $\eta=0.1$. (a), (d) damping in translational spring; (b), (e) damping in rotational spring; (c), (f) damping in both translational and rotational springs.

It can be seen that for this order of magnitude, the effect of damping is negligible. Only when the loss factor is very large, does the damping effect become obvious. The effects of damping in the translational and rotational directions are different, which is related to the sensitivity of the power reflection coefficient to the translational and rotational dynamic stiffnesses. For the case considered here, damping in the translational direction only dominates the regions where $\rho = 1$ and $\tau = 1$. And the effect of the damping in the rotational direction becomes apparent when ρ or τ is of large magnitude. When considering the damping in both directions, the effect is the combination of the two separate cases. It also should be noted that due to the existence of damping, $\rho + \tau < 1$.

4.4 Experiments on Pipe Supports

This section presents measurements of the reflection and transmission coefficients of a pipe support by the method discussed in Chapter 3. The translational and rotational stiffnesses of the support are also measured directly. The intention is to verify the applicability of the reflection and transmission coefficients in determining the parameters of the support.

4.4.1 Experimental Setup

Figure 4.8 shows the experimental rig featuring a 6m straight thin-walled copper pipe held at its mid-point by an adjustable support. A steel block is mounted by three long bolts to a massive concrete block which can be considered as a grounded support. A clamp which holds the pipe is connected by screws to a supporting bar at each end. The pipe support is idealised. The length of the supporting bars is adjustable in order to accommodate more positions, i.e. more supports with each pair of supporting bars. The rig is designed to be symmetrical in order to avoid torsional motion of the pipe (here only flexural waves are considered). A sandbox is placed at each end of the pipe to approximate anechoic conditions. On each side of the support, two accelerometers are attached to the pipe. The pipe is excited by a shaker in the direction perpendicular to the pipe in the horizontal plane. The method introduced in Chapter 3 is employed to measure the reflection and transmission coefficients of the support. Attention was paid

to the position of the accelerometers to ensure that the motions measured were in the same direction as the excitation.

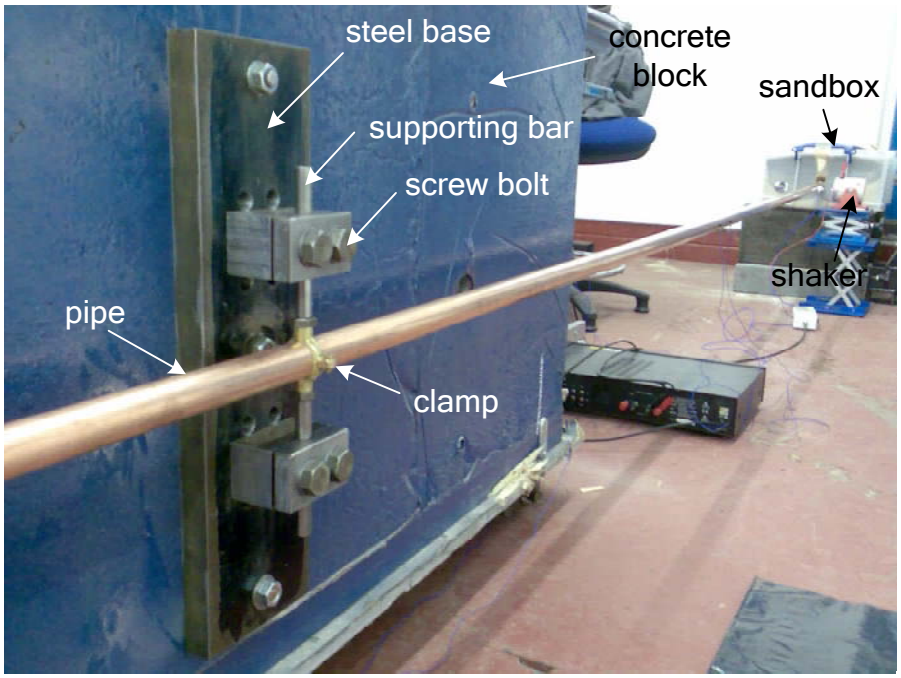

Figure 4.8 Experimental rig for measuring the reflection and transmission coefficients of a pipe support.

Two kinds of materials, aluminium and steel, were used for the supporting bars and the bars were designed to be fixed at one of two lengths. Therefore, in total 4 support configurations were investigated. The properties of the copper pipe are listed in Table 4.1.

Table 4.1 Properties of the pipe (SI units).

Density	Outer radius	Wall thickness	Length
8900	0.014	0.9×10^{-3}	6.060

4.4.2 Wavenumber Measurement and *n*=2 Cut-on Frequency

In order to obtain the wave amplitudes and further the reflection and transmission coefficients, the wavenumber of the waveguide needs to be measured. The flexural wavenumber of the pipe was measured first by the method discussed in Chapter 3. Figure 4.9 shows the measured real part of $\left(W_1+W_3\right)/2W_2$ (see equation (3.35)). The

transducer spacing was $\Delta = 0.10$ m which is a quarter wavelength at 1250Hz. At frequency 2200Hz, the $n = 2$ wave mode cuts on. The wavenumber constant of proportionality $\beta = k_b / \sqrt{f}$ was estimated in a least-squares sense, and $\beta = 0.428$ and $\beta = 0.427$ were obtained in the ranges 200-2000Hz and 200-1400Hz respectively. They are quite close to each other. The fitted estimate of $\cos(k_b \Delta)$ with $\beta = 0.427$ is also plotted in the figure. A good agreement is obtained in the frequency range considered. In what follows, the analysis is focus on the frequency range 200-1400Hz.

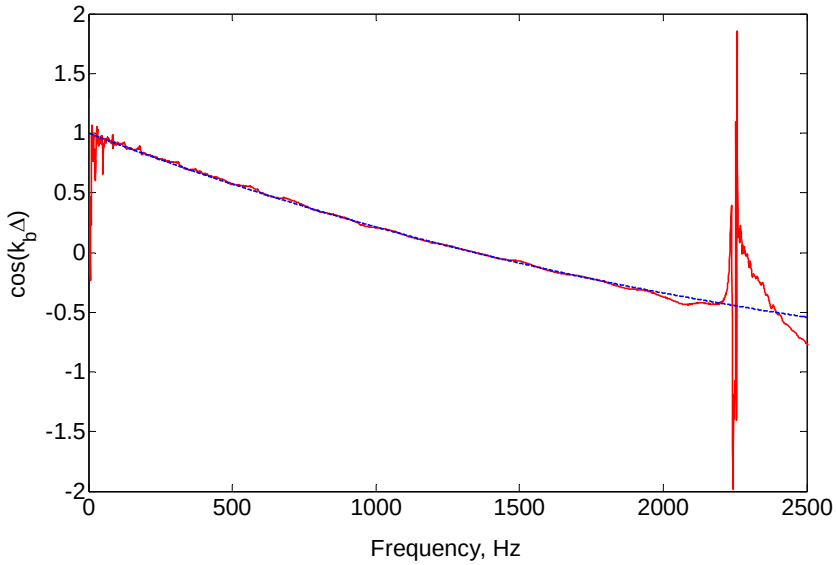

Figure 4.9 Wavenumber of the pipe: ——, measured real part of $(W_1 + W_3)/2W_2$; ------, $\cos k_b \Delta$ using fitted wavenumber over frequency range 200-1400Hz ($\beta = 0.427$).

4.4.3 Direct Measurements of the Translational Dynamic Stiffness of the Supports

The translational and rotational dynamic stiffnesses of the pipe support were measured directly. The intention is to find the mass and stiffness parameters of the support, verify the applicability of the support model in predicting the reflection and transmission coefficients, and later to compare these values with the parameter values estimated by inverse means in Chapter 7. This section discusses the measurements of the translational dynamic stiffness.

The translational dynamic stiffness is defined by

$$D_T = \frac{F}{X} \tag{4.12}$$

where F is the exciting force and X is the displacement output. Referring to equation (4.9a) and considering the damping effect of the structure give

$$D_T = K_T\left(1+i\eta_T\right) - m'\omega^2 . \tag{4.13}$$

The stiffness, K_T and mass, m' of the support can be estimated from the measured dynamic stiffnesses at two frequencies, or in a frequency range containing more than two frequencies by fitting the real part of the measured dynamic stiffness using the least-squares method. The damping loss factor can be found from the imaginary part of the measured dynamic stiffness.

Figure 4.10 shows the experimental rig used to measure the translational dynamic stiffness of the support. A short length of the pipe was placed in the clamp in order to replicate the local stiffness present when measuring the reflection and transmission coefficients in practice. The clamp was excited directly by a shaker through a force transducer. The force transducer was connected to the shaker by a stinger. An accelerometer was attached to the other side of the clamp.

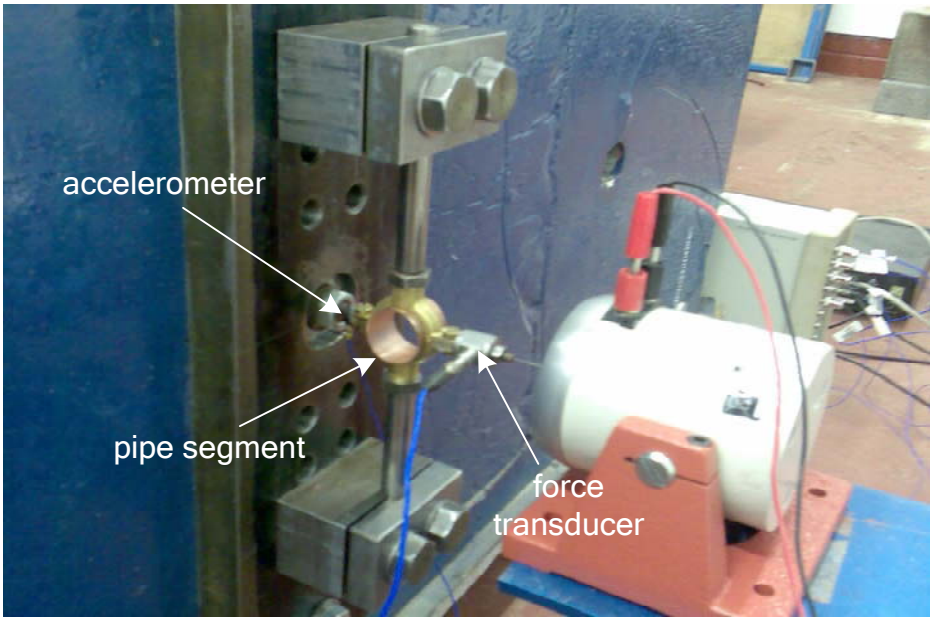

Figure 4.10 Experimental rig for direct measurements of the translational dynamic stiffness of the pipe supports.

Figure 4.11 shows the real and imaginary parts of the measured dynamic stiffness for the aluminium pipe support fixed at its larger length. Also shown in the figure is the fitted result of the mass-spring-damping model by the least-squares method in the range 200-1400Hz. A good agreement is obtained in this frequency range.

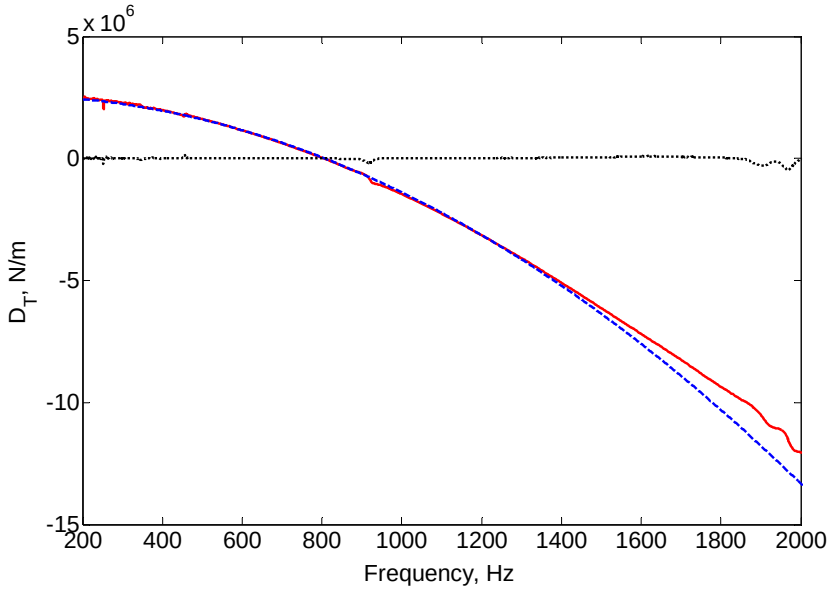

Figure 4.11 Translational dynamic stiffness of the long aluminium pipe support: ——, real part of measured D_T; - - - - - -, fitted real part of D_T over the frequency range 200-1400Hz; ·····, imaginary part of measured D_T.

The measured translational dynamic stiffnesses for the other three support conditions are given in Appendix 7. The estimated parameters for the four supports are presented in Table 4.2. Different frequency ranges are chosen based on the behaviour of the measured dynamic stiffnesses (translational and rotational).

Table 4.2 Estimated translational parameters of the supports (SI).

Support		Frequency range	K_T	m'	η_T
aluminium	long	200-1400	2.595×10^6	0.101	0.003
	short	400-1400	9.019×10^6	0.100	0.003
steel	long	200-1400	5.127×10^6	0.130	0.002
	short	400-1400	1.464×10^7	0.115	0.009

Note: 1. the pipe segment ($m_s = 0.015$) is included in the above mass.

2. the mass-loading effect of the force transducer: 38% of the total mass of the force transducer ($m_a = 0.0235$), is considered to be added to the support (see Appendix 8).

4.4.4 Direct Measurement of the Rotational Dynamic Stiffness of the Supports

The direct measurements of the rotational dynamic stiffnesses of the pipe supports are described in this section. In general, the rotational dynamic stiffness of a structure is much more difficult to measure. Here an approach is developed. Figure 4.12 shows the experimental rig to measure the rotational dynamic stiffness (in the direction of the torsional motion of the supporting bars) of the support. Owing to the close proximity of the clamp to the seismic mass, the clamp could only be excited on the side far away from the concrete block. Accelerometers were placed on either side of the clamp to measure the side to side motions. The structure becomes asymmetric because of the mass-loading effect of the force transducer.

Figure 4.13 shows the measured accelerances of the two accelerometers when the force was applied as shown in Figure 4.12. The first resonance is principally in the translational direction because the phases of the two accelerances are the same. The second resonance around 1180Hz is predominantly rotational since the phase difference is π. At frequencies above 1400Hz, more resonances occur and the situation becomes more complicated. Here, attention is focused only on the frequency range 200-1400Hz.

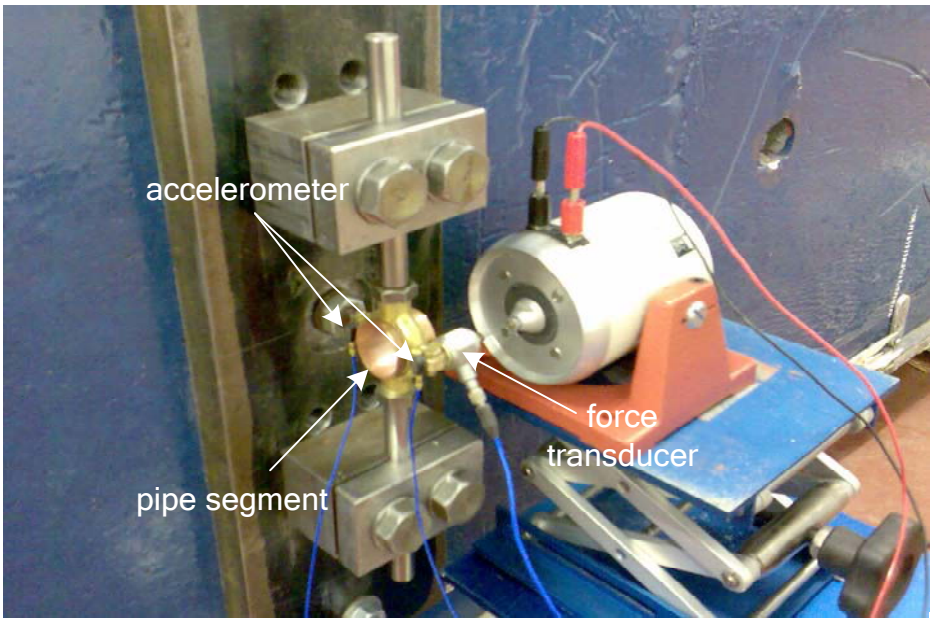

Figure 4.12 Experimental rig for direct measurements of the rotational dynamic stiffness of the pipe supports.

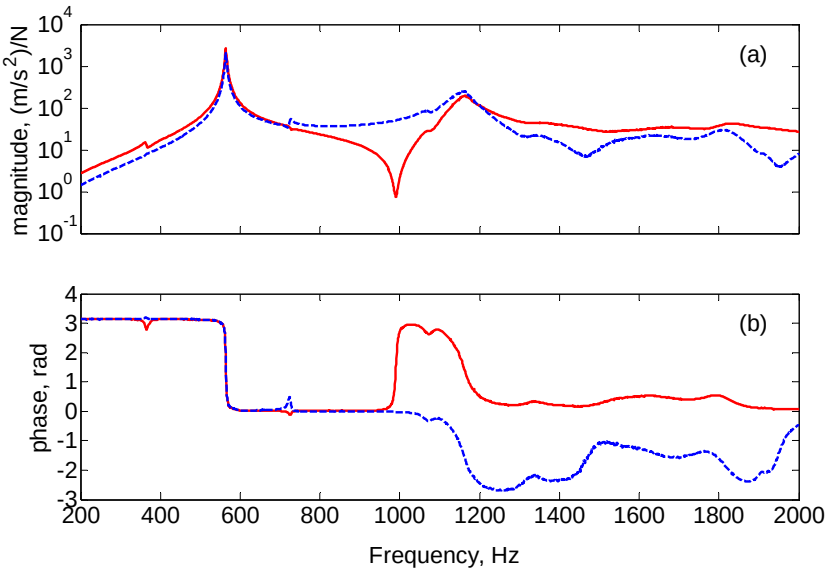

Figure 4.13 Measured accelerances of the long aluminium support: (a) magnitude; (b) phase: ——, $\ddot{X}_1 / F$; ------, $\ddot{X}_2 / F$.

The rotational dynamic stiffness is defined by

$$D_R = \frac{M}{\theta_C} = \frac{\gamma}{\theta_C / F} \tag{4.14}$$

where the moment $M = F\gamma$, F is the force, θ_C is the rotational displacement of the support about its geometric central axis and γ is the distance of the excitation point to the central axis.

The rotational displacement can be estimated from the accelerances at the two points in Figure 4.12 by (assuming the two points are symmetrically located with respect to the central axis)

$$\theta_C / F = -\frac{\ddot{X}_1 / F - \ddot{X}_2 / F}{2\gamma\omega^2}. \tag{4.15}$$

Substituting the above equation into equation (4.14), the rotational dynamic stiffness can be obtained from the FRF measurements by

$$D_R = -\frac{2\gamma^2\omega^2}{\ddot{X}_1 / F - \ddot{X}_2 / F}. \tag{4.16}$$

A parametric model is also needed to fit the estimated rotational dynamic stiffness. This is discussed in the following section.

4.4.5 Parameter Fitting of the Directly Measured Rotational Dynamic Stiffness of the Supports

In the experimental rig, one force transducer was attached to the clamp to excite the support, which gives rise to the presence of eccentricity of the structure. Due to this, the rotational dynamic stiffness can not be written in a simple form analogously to the translational dynamic stiffness given in equation (4.13). A more complicated model needs to be developed for the system. Figure 4.15 illustrates the free body diagram of a suitable model. The rotational stiffness, K_R and translational stiffness, K_T'' (different from K_T discussed in the above section) are defined at the geometric centre of the system. The moment of inertia J'' is defined at the centre of gravity. The eccentricity is indicated by e. Considering equilibrium of forces in the x direction and equilibrium of moments about the geometric central axis yields

$$\begin{bmatrix} m'' & m''e \\ m''e & J''+m''e^2 \end{bmatrix}\begin{Bmatrix} \ddot{X}_C \\ \ddot{\theta}_C \end{Bmatrix}+\begin{bmatrix} K_T'' & 0 \\ 0 & K_R \end{bmatrix}\begin{Bmatrix} X_C \\ \theta_C \end{Bmatrix}=\begin{Bmatrix} F \\ M \end{Bmatrix}. \tag{4.17}$$

For time harmonic excitation, the above equation can be expressed as

$$\begin{bmatrix} K_T''-m''\omega^2 & -m''e\omega^2 \\ -m''e\omega^2 & K_R-\left(J''+m''e^2\right)\omega^2 \end{bmatrix}\begin{Bmatrix} X_C/F \\ \theta_C/F \end{Bmatrix}=\begin{Bmatrix} 1 \\ \gamma \end{Bmatrix}. \tag{4.18}$$

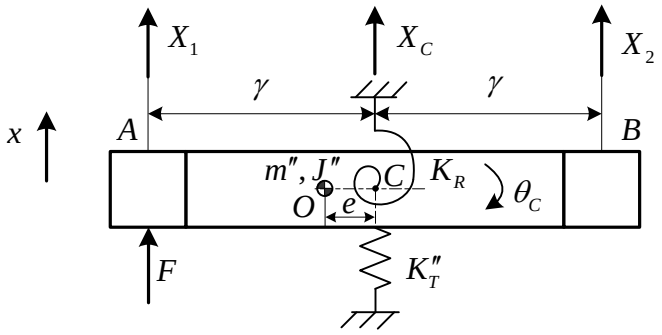

Figure 4.15 Free body diagram of the experimental rig for directly measuring the rotational dynamic stiffness.

By introducing the following symbols

$$\mathbf{D}=\begin{bmatrix} K_T''-m''\omega^2 & -m''e\omega^2 \\ -m''e\omega^2 & K_R-\left(J''+m''e^2\right)\omega^2 \end{bmatrix},\ \mathbf{b}=\begin{Bmatrix} 1 \\ \gamma \end{Bmatrix} \text{ and } \mathbf{z}=\begin{Bmatrix} 0 & 1 \end{Bmatrix}, \tag{4.19}$$

and assuming that $\mathbf{D}$ is invertible, the rotational displacement FRF can be obtained by

$$\theta_C / F = \mathbf{z}\mathbf{D}^{-1}\mathbf{b}\,. \tag{4.20}$$

Substituting equation (4.20) into the equation (4.14) gives the rotational dynamic stiffness in terms of the mass and stiffness parameters of the support,

$$D_R = \frac{\gamma}{\mathbf{z}\mathbf{D}^{-1}\mathbf{b}}\,. \tag{4.21}$$

Updating the parameters of the support to fit the rotational dynamic stiffness given by equation (4.21) to the measured one given by equation (4.16) is a non-linear problem. The Gauss-Newton iterative method (detailed later in Chapter 6) is employed here. The objective function is defined in terms of the rotational dynamic stiffness and the iteration process is performed on the five parameters, K_T'', m'', K_R, J'' and e. Considering the conditioning of the iteration process, the damping effect (typically small and only significant around the resonance and anti-resonance frequencies) is neglected here. So only the real part of the measured rotational dynamic stiffness is discussed here.

In Figure 4.16, the rotational dynamic stiffness of the long aluminium support is plotted against frequency. The small fluctuations in the measured FRFs around 700Hz (Figure 4.13) can cause large and rapid changes in the rotational dynamic stiffness. These frequencies were excluded in the iteration process. The initial values of the mass, moment of inertia and stiffnesses for the iteration process were estimated from the simple model given by equation (4.13). The parameters were then identified and are given in Table 4.3. Figure 4.16 also shows the rotational stiffness as predicted by the method given the estimated parameters of the support. Except for the frequency ranges deliberately excluded from the fit for reasons stated previously, the estimated dynamic stiffness agrees well with the measured result.

The measured FRFs for the other three support conditions are given in Appendix 9 alongside the rotational dynamic stiffnesses and fitted counterparts. Table 4.3 also gives the estimated parameters for the other three supports. Considering the dimension of the structure and the masses of the clamp (0.042kg) and the force transducer, the values for the eccentricity are reasonable. The asymmetry of the support is considered to be caused by the mass-loading effect of the force transducer.

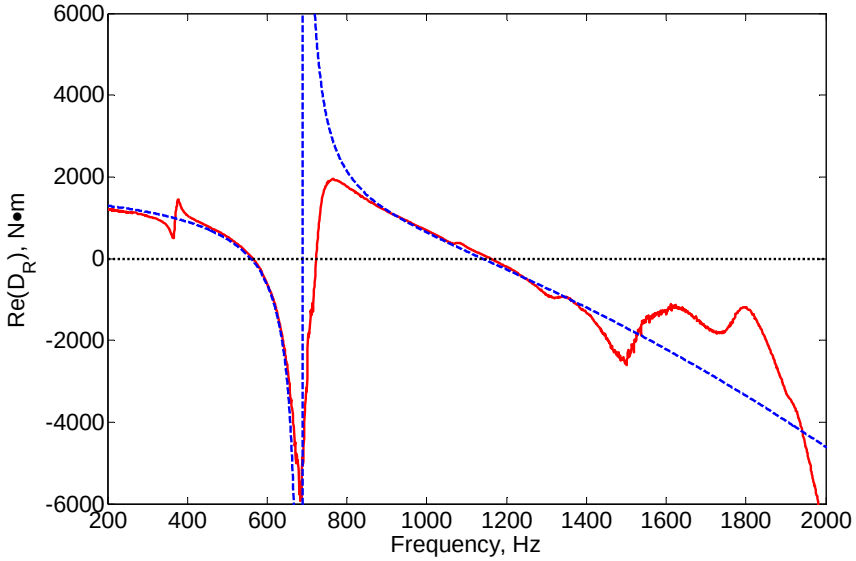

Figure 4.16 Directly measured rotational dynamic stiffness of the long aluminium pipe support: ——, real part of measured D_R; ------, fitted real part of D_R.

Table 4.3 Rotational parameter fit of the supports (SI units).

support		frequency	K_T''	m''	K_R	J''	e
aluminium	long	$[200,300]$ $[420,600]$ $[900,1400]$	8.811×10^5	0.069	1.398×10^3	2.833×10^{-5}	0.007
	short	$[200,300]$ $[450,1100]$ $[1400,1700]$	2.328×10^6	0.061	1.840×10^3	1.918×10^{-5}	0.009
steel	long	$[200,300]$ $[460,840]$ $[1000,1400]$	3.941×10^6	0.161	2.713×10^3	3.575×10^{-5}	0.006
	short	$[200,300]$ $[460,1200]$ $[1280,1400]$ $[1900,2100]$	4.923×10^6	0.079	2.997×10^3	1.808×10^{-5}	0.009

Note: 1. the pipe segment ($m_s = 0.015$) is included in the above mass.

2. the mass-loading effect of the force transducer: 38% of the total mass of the force transducer ($m_a = 0.0235$), is considered to be added to the support (see Appendix 8).

4.4.6 Reflection and Transmission Coefficients

In this section, the power reflection and transmission coefficients measured by the WAD method are presented. Based on the estimated support parameters from direct measurements, the reflection and transmission coefficients are also predicted by the parametric model for the waveguide support described in Section 4.2. Here the transducer spacing is $\Delta = 0.10\,\mathrm{m}$.

When directly measuring the parameters of the support, the directly measured mass m' and moment of inertia J'' were influenced by the added pipe segment and the mass-loading effect of the force transducer. In order to revert to the status of the support for measurements of the reflection and transmission coefficients by the WAD method, they need to be modified when used to predict the reflection and transmission coefficients.

In Table 4.2, the damping loss factors are typically very small in the translational direction and can be neglected in the frequency range discussed. The mass m' includes the added pipe segment and the loaded mass of the force transducer, which should be reduced. The modified mass is given by

$$m = m' - m_s - 0.41 m_a \tag{4.22}$$

where $m_s = 0.015$ is the mass of the pipe segment held by the clamp, and m_a is the mass of the force transducer.

When measuring the rotational dynamic stiffness of the support, the eccentricity is considered to be the consequence of the mass-loading effect of the force transducer. It will be excluded in the support model to predict the reflection and transmission coefficients. Considering the influence of the pipe segment, the mass loading of the force transducer, and the eccentricity, the inertia J'' in Table 4.3 is adjusted by

$$J = J'' + m'' e^2 - m_s L_s^2 / 12 - 0.38 m_a \gamma^2 \tag{4.23}$$

where $L_s = 0.022$ is the length of the pipe segment.

The parameters of the support with the adjusted values are listed in Table 4.4. In the following figures the power reflection and transmission coefficients are predicted by the parametric model given in Section 4.2 based on the directly measured parameters. Also

in the figures are the corresponding power reflection and transmission coefficients estimated by the wave amplitude decomposition method. Here it is assumed that the ends of the pipe are reflecting.

Table 4.4 Modified values of the directly measured parameters of the supports (SI units).

support		K_T, $\times 10^6$	m	K_R, $\times 10^3$	J, $\times 10^{-5}$
aluminium	long	2.595	0.077	1.398	2.840
	short	9.019	0.076	1.840	2.081
steel	long	5.127	0.106	2.713	3.823
	short	14.642	0.091	2.997	2.116

Figures 4.17 and 4.18 show the power reflection and transmission coefficients for the long aluminium support. Corresponding the frequency range 200Hz – 2000Hz, $k_b\Delta$ changes from 0.604 to 1.910. In the frequency range plotted, the measured power coefficients and those predicted by the theoretical model agree very well although slight differences are found in some frequency ranges. This indicates the consistency of the parametric model of the support with the wave-based predictions.

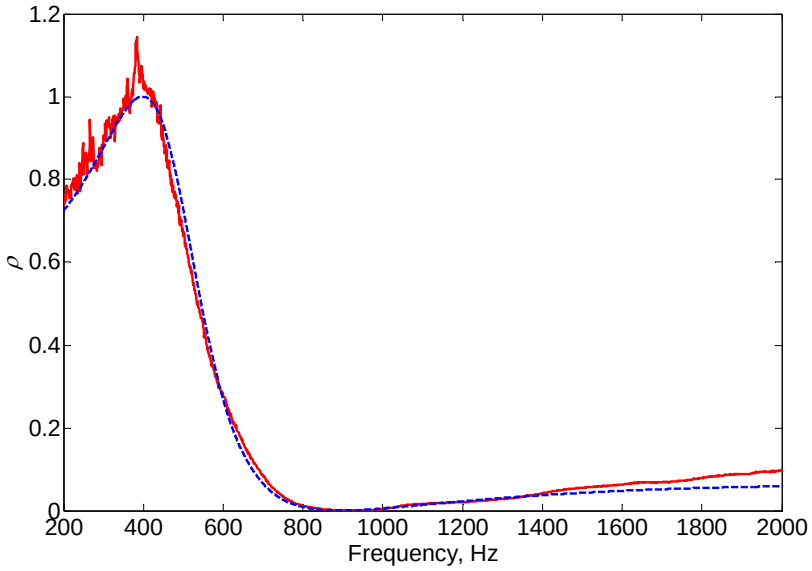

Figure 4.17 Power reflection coefficient of the long aluminium support: ——, measured; -------, predicted based on measured parameters.

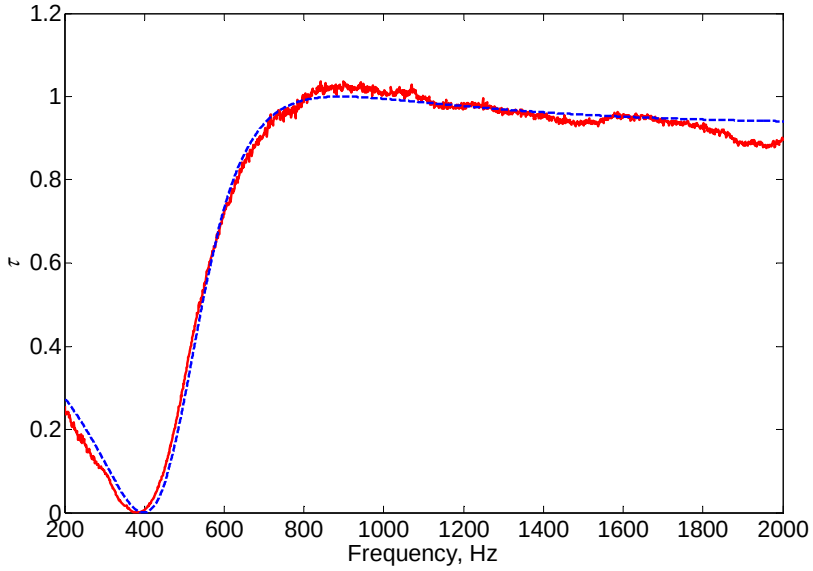

Figure 4.18 Power transmission coefficient of the long aluminium support: ——, measured; - - - - - -, predicted based on measured parameters.

Figure 4.19 shows the sum of the measured power reflection and transmission coefficients for the long aluminium support. In the frequency range plotted, this sum is nearly unity, which indicates that the damping of the structure is negligible.

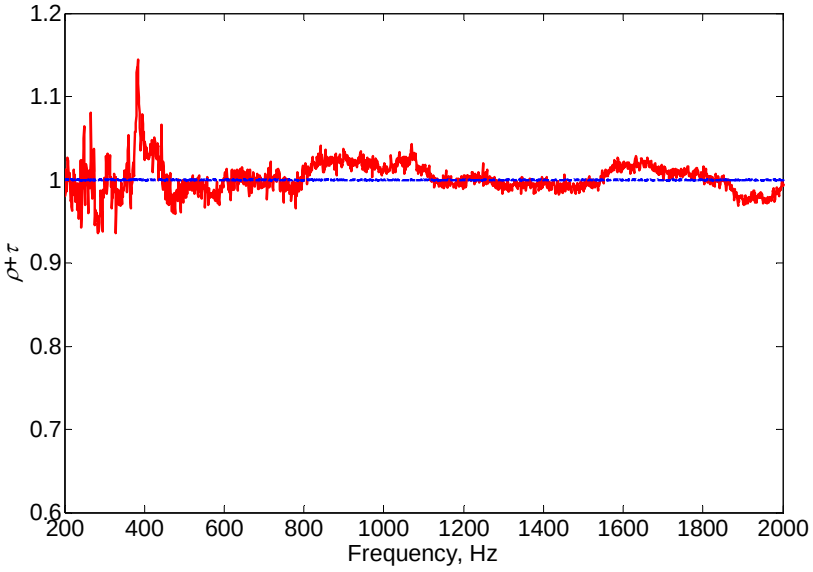

Figure 4.19 Sum of power reflection and transmission coefficients of the long aluminium support: ——, measured; - - - - - -, predicted based on measured parameters.

The power reflection and transmission coefficients for the other three supports are presented in Figures 4.20 to 4.22. Each of the power coefficients predicted from the

parametric model follows the same trends with frequency as the measured results. The results for the long supports are always better than those of the short, which means the parametric model is more appropriate for the long supports. At high frequencies, due to the presence of high order resonances (see the direct measurements of the dynamic stiffnesses in Appendices 6 and 7), the measured power reflection and transmission coefficients correspondingly differ by larger amount. On the whole, the parametric model for the supports agrees well with the measured results. However, if the parameters of the supports are to be estimated accurately from measured reflection and transmission coefficients, appropriate frequency ranges need to be selected. This will be discussed in Chapter 7.

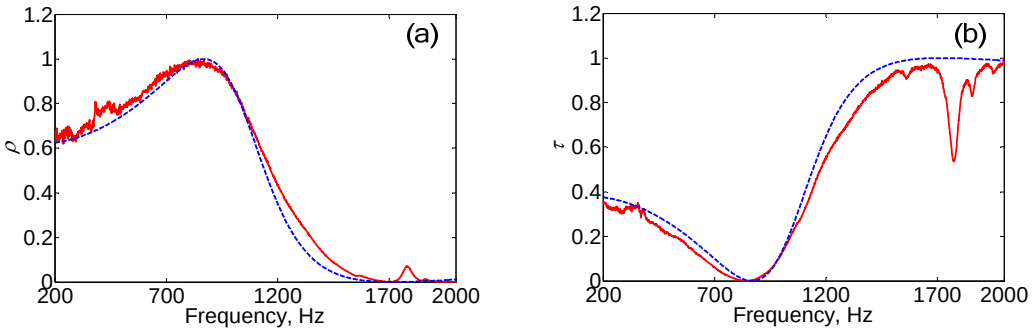

Figure 4.20 Power reflection and transmission coefficients of the short aluminium support: ——, measured; - - - - - -, predicted based based on measured parameters.

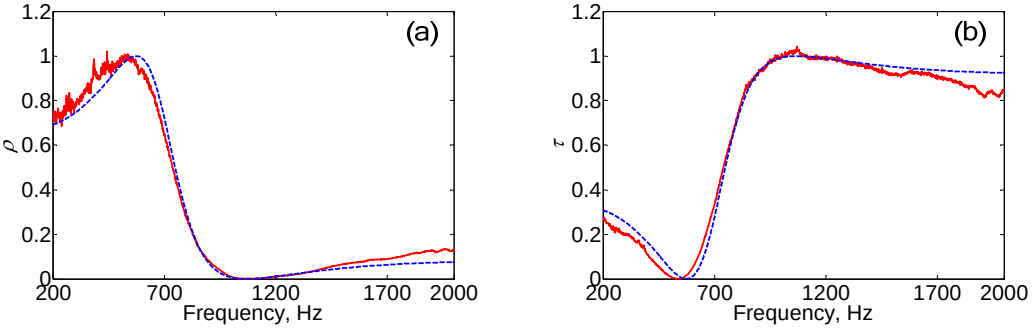

Figure 4.21 Power reflection and transmission coefficients of the long steel support: ——, measured; - - - - - -, predicted based on measured parameters.

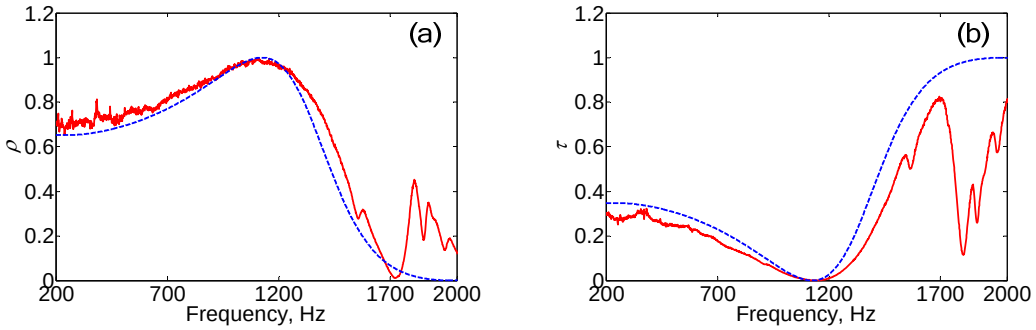

Figure 4.22 Power reflection and transmission coefficients of the short steel support: ——, measured; ------, predicted based on measured parameters.

4.5 Summary

A parametric model was used to represent a pipe support in which the translational and rotational dynamic stiffnesses were considered. The flexural wave reflection and transmission coefficients of the support were derived in terms of the translational and rotational dynamic stiffnesses of the support. The dynamic stiffnesses were further decomposed into mass and stiffness parameters. The pipe was modelled as a waveguide for flexural waves. Therefore the analysis is only valid below the cut-on frequency of the $n = 2$ wave mode. Numerical simulations illustrated the dynamic characteristics of the reflection and transmission coefficients. Damping of the support was also discussed when considering an example of the reflection and transmission coefficients in terms of the mass and stiffness parameters.

The experimental rig features a support holding a pipe. In order to allow for discrepancies between the calculations at the design stage and the measurements, the support was designed to be adjustable so that the translational and rotational dynamic stiffnesses can be altered. Methods were developed to measure the translational and rotational dynamic stiffnesses of the supports directly and the parameters composing the dynamic stiffnesses, such as translational and rotational stiffnesses, mass and moment of inertia were estimated. The flexural wave reflection and transmission coefficients were calculated from the estimated parameters based on the parametric model of the support. Also the reflection and transmission coefficients were measured by the wave amplitude decomposition method. The results from these two approaches agree well,

which indicates that the parametric model is a good model for the reflection and transmission coefficients of the support.

Chapter 5 Wave Reflection and Transmission at Angled Bends

5.1 Introduction

Previous chapters have discussed wave reflection and transmission in straight waveguides with discontinuities. In this chapter attention is focused on a structure with two waveguides jointed at an arbitrary angle.

Wave reflection and transmission in such a structure is more complicated since wave mode conversion occurs. Previous studies have shown much interest in this kind of system: Cremer *et al.* [1] have studied rigidly connected and simply supported right-angled bends. Desmond [67] considered wave propagation at a junction of three bars, which were rigidly connected. Doyle and Kamle [24] discussed the reflection and transmission of flexural waves at an arbitrary T-joint. They considered the joint model as a mass-like discontinuity. Leung and Pinnington [59, 60] investigated a right-angled joint with compliance in all three degrees of freedom. A model for an arbitrary angled bend is considered in this chapter which is characterised by translational and rotational stiffnesses, mass and moment of inertia. The wave reflection and transmission coefficients of the angled bend are investigated by the general approach introduced in Chapter 2.

In the next section, the wave fields in *in-vacuo* piping networks are discussed briefly. Then the reflection and transmission coefficients of an arbitrary angled bend are derived based on a parametric joint model. Power reflection and transmission coefficients associated with the angled bend are discussed. Closed form solutions are given for the special case of a rigid mass-free connection, a mass-like and a spring-like joint, and numerical simulations are performed on these three kinds of joints. For the mass-like and spring-like joints the simulations are given in terms of the impedance ratios.

Damping effects of the joint are also studied by incorporating the damping loss factor as complex stiffnesses. Experiments were performed on a right-angled pipe bend. The decomposed wave amplitudes in the two pipes and the power reflection and transmission coefficients induced by an in-plane flexural wave are presented.

5.2 Wave Fields in Some Joint Networks

Some typical joints, such as L-bends, T-junctions and cross-junctions, etc. shown in Figure 5.1, are widely used in pipe networks. Each pipe can be considered to be a one-dimensional waveguide. The wave modes involved in the branches of the structures depend on the direction of the excitation, boundary conditions and the characteristics of the joint. Figure 5.2 shows an example for two semi-infinite waveguides connected by a joint at a right angle. If waveguide a is excited vertically by an in-plane force, response will be induced not only in waveguide a itself, but also in b through the joint. From the viewpoint of wave propagation in structures, the excitation in waveguide a gives rise to a flexural incident propagating wave and a nearfield wave travelling towards the joint. At the joint the incident waves are partly transmitted to branch b and partly reflected to branch a as well. Owing to the continuity of the structure at the joint, axial

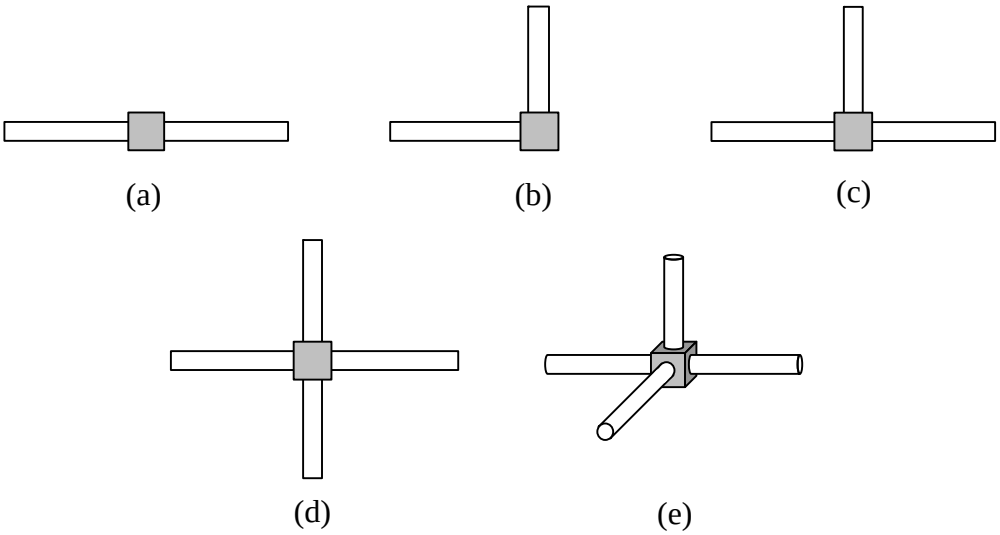

Figure 5.1 Typical structures in pipe networks.

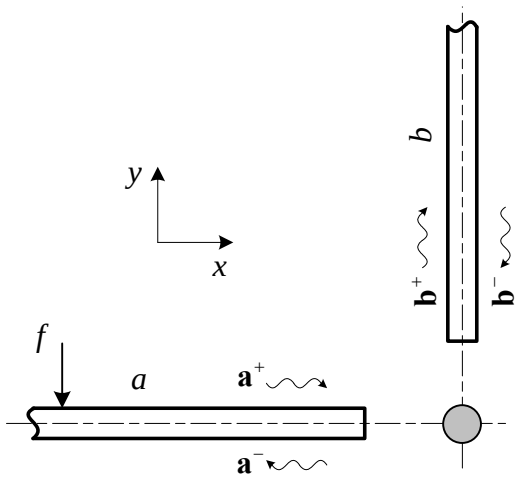

Figure 5.2 Wave fields in a right angled structure.

and flexural waves may be reflected from and transmitted through the joint. The characteristic of the joint is crucial to the reflection and transmission of waves. For example, if the rotational stiffness of the joint is zero, then there will be no transmitted flexural waves in branch b.

5.3 Reflection and Transmission Coefficients in terms of the Parameters of an Angled Bend

In this section, the wave reflection and transmission coefficients at an arbitrary angled bend are derived by using the approach introduced in Chapter 2. For simplicity, only axial and flexural waves in the plane of the bend are assumed to exist in the system. Correspondingly the parameters of the bend are also only defined in this plane.

5.3.1 Reflection and Transmission Coefficient Matrices

The reflection and transmission coefficient matrices for an angled bend are given in this section. Figure 5.3 shows two waveguides connected at an angle ϕ. When a wave (either in-plane flexural or axial) reaches the angled bend, due to the continuity of the joint, the incident wave is reflected and transmitted. As a result, three reflected waves and three transmitted waves are generated: one propagating flexural wave, one nearfield flexural wave and one axial wave. The positive and negative-going wave amplitudes at

any point can be expressed by equation (2.20). The propagation matrix between two points along *x*-axis is given by equation (2.28). The general displacements and forces can be expressed by equations (2.21) and (2.22) respectively. They are related to the wave amplitudes by the displacement and force matrices given respectively in equations (2.25) and (2.26).

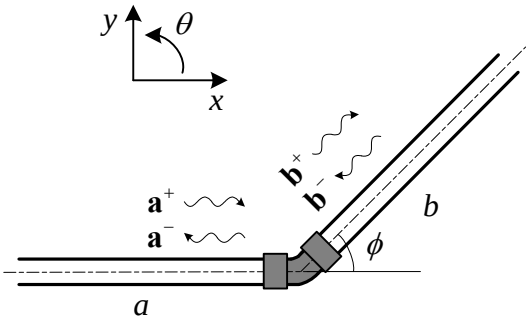

Figure 5.3 Wave amplitudes at an arbitrary-angled bend.

Consider incident waves $\mathbf{a}^+$ and $\mathbf{b}^-$ propagating towards the joint from each side. The wave amplitudes at the joint are related by equation (2.29), which is here

$$\begin{bmatrix} \mathbf{a}_0^- \\ \mathbf{b}_0^+ \end{bmatrix} = \begin{bmatrix} \mathbf{R}_0^{aa} & \mathbf{T}_0^{ba} \\ \mathbf{T}_0^{ab} & \mathbf{R}_0^{bb} \end{bmatrix} \begin{bmatrix} \mathbf{a}_0^+ \\ \mathbf{b}_0^- \end{bmatrix}, \tag{5.1}$$

where $\mathbf{R}$ and $\mathbf{T}$ are the 3×3 reflection and transmission coefficient matrices. If the joint is assumed to be symmetrical, then the matrices can be written as

$$\mathbf{R}_0^{aa} = \mathbf{R}_0^{bb} = \begin{bmatrix} r_{LL} & r_{PL} & r_{NL} \\ r_{LP} & r_{PP} & r_{NP} \\ r_{LN} & r_{PN} & r_{NN} \end{bmatrix}, \ \mathbf{T}_0^{ba} = \mathbf{T}_0^{ab} = \begin{bmatrix} t_{LL} & t_{PL} & t_{NL} \\ t_{LP} & t_{PP} & t_{NP} \\ t_{LN} & t_{PN} & t_{NN} \end{bmatrix}. \tag{5.2}$$

Two subscripts are used for the corresponding reflection and transmission coefficients to signify the incident and the resulting wave modes. Subscripts L, P and N indicate axial, propagating flexural and nearfield flexural wave respectively.

5.3.2 Parametrical Model of the Angled Bend

Various models can be developed for the angled bend. However, here the bend is assumed to incorporate two masses and three springs, as shown in Figure 5.4. Each mass is characterised by a mass m_i and a moment of inertia J_i ($i=1,2$) and is

considered to be rigidly connected to the end of the each waveguide. The three springs which have translational stiffnesses K_x, K_y and angular stiffness K_R respectively connect the two masses together.

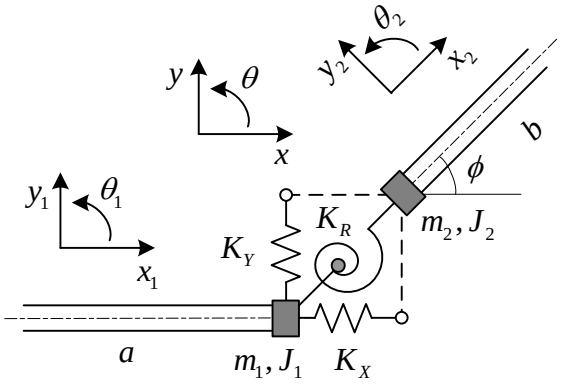

Figure 5.4 Model of an angled bend.

Figure 5.5 shows the free body diagram of each part of the bend. For simplicity, the offset of the system is not considered here. The three parts of the structure can be considered as connected substructures. Such a system can be analysed easily by the transfer matrix method described in Chapter 2. By applying continuity and equilibrium conditions to each of masses 1 and 2, the displacements and forces on the two sides of each mass can be related respectively by

$$\begin{Bmatrix} \mathbf{W}_a \\ \mathbf{F}_a \end{Bmatrix} = \begin{bmatrix} \mathbf{\Omega}_{11}^1 & \mathbf{\Omega}_{12}^1 \\ \mathbf{\Omega}_{21}^1 & \mathbf{\Omega}_{22}^1 \end{bmatrix} \begin{Bmatrix} \mathbf{W}_{a0} \\ \mathbf{F}_{a0} \end{Bmatrix} \text{ and } \begin{Bmatrix} \mathbf{W}_{b0} \\ \mathbf{F}_{b0} \end{Bmatrix} = \begin{bmatrix} \mathbf{\Omega}_{11}^3 & \mathbf{\Omega}_{12}^3 \\ \mathbf{\Omega}_{21}^3 & \mathbf{\Omega}_{22}^3 \end{bmatrix} \begin{Bmatrix} \mathbf{W}_b \\ \mathbf{F}_b \end{Bmatrix}. \tag{5.3}$$

The elements of the transfer matrices are

$$\begin{aligned} &\mathbf{\Omega}_{11}^1 = \mathbf{\Omega}_{11}^3 = \begin{bmatrix} 1 & 0 & 0 \\ 0 & 1 & 0 \\ 0 & 0 & 1 \end{bmatrix}, \quad \mathbf{\Omega}_{12}^1 = \mathbf{\Omega}_{12}^3 = \begin{bmatrix} 0 & 0 & 0 \\ 0 & 0 & 0 \\ 0 & 0 & 0 \end{bmatrix}, \quad \mathbf{\Omega}_{22}^1 = \mathbf{\Omega}_{22}^3 = \begin{bmatrix} 1 & 0 & 0 \\ 0 & 1 & 0 \\ 0 & 0 & 1 \end{bmatrix}, \\ &\mathbf{\Omega}_{21}^1 = \begin{bmatrix} m_1\omega^2 & 0 & 0 \\ 0 & m_1\omega^2 & 0 \\ 0 & 0 & m_1 J^2 \end{bmatrix}, \quad \mathbf{\Omega}_{21}^3 = \begin{bmatrix} m_2\omega^2 & 0 & 0 \\ 0 & m_2\omega^2 & 0 \\ 0 & 0 & m_2 J^2 \end{bmatrix}. \end{aligned} \tag{5.4}$$

The displacements and forces on both sides of the three springs are related by

$$\begin{Bmatrix} \mathbf{W}_{a0} \\ \mathbf{F}_{a0} \end{Bmatrix} = \begin{bmatrix} \mathbf{\Omega}_{11}^2 & \mathbf{\Omega}_{12}^2 \\ \mathbf{\Omega}_{21}^2 & \mathbf{\Omega}_{22}^2 \end{bmatrix} \begin{Bmatrix} \mathbf{W}_{b0} \\ \mathbf{F}_{b0} \end{Bmatrix} \tag{5.5}$$

where

$$\boldsymbol{\Omega}_{11}^{2}=\begin{bmatrix}\cos\phi & -\sin\phi & 0\\ \sin\phi & \cos\phi & 0\\ 0 & 0 & 1\end{bmatrix},\quad \boldsymbol{\Omega}_{12}^{2}=\begin{bmatrix}-\cos\phi/K_X & \sin\phi/K_X & 0\\ -\sin\phi/K_Y & -\cos\phi/K_Y & 0\\ 0 & 0 & -1/K_R\end{bmatrix},$$
$$\boldsymbol{\Omega}_{21}^{2}=\begin{bmatrix}0 & 0 & 0\\ 0 & 0 & 0\\ 0 & 0 & 0\end{bmatrix},\quad \boldsymbol{\Omega}_{22}^{2}=\begin{bmatrix}\cos\phi & -\sin\phi & 0\\ \sin\phi & \cos\phi & 0\\ 0 & 0 & 1\end{bmatrix}. \tag{5.6}$$

It must be noted that when the stiffnesses of the springs are zero, the transfer matrix might be poorly conditioned.

Combining equations (5.3) and (5.5) gives

$$\begin{Bmatrix}\mathbf{W}_a\\ \mathbf{F}_a\end{Bmatrix}=\begin{bmatrix}\boldsymbol{\Omega}_{11} & \boldsymbol{\Omega}_{12}\\ \boldsymbol{\Omega}_{21} & \boldsymbol{\Omega}_{22}\end{bmatrix}\begin{Bmatrix}\mathbf{W}_b\\ \mathbf{F}_b\end{Bmatrix} \tag{5.7}$$

where

$$\begin{bmatrix}\boldsymbol{\Omega}_{11} & \boldsymbol{\Omega}_{12}\\ \boldsymbol{\Omega}_{21} & \boldsymbol{\Omega}_{22}\end{bmatrix}=\begin{bmatrix}\boldsymbol{\Omega}_{11}^{1} & \boldsymbol{\Omega}_{12}^{1}\\ \boldsymbol{\Omega}_{21}^{1} & \boldsymbol{\Omega}_{22}^{1}\end{bmatrix}\begin{bmatrix}\boldsymbol{\Omega}_{11}^{2} & \boldsymbol{\Omega}_{12}^{2}\\ \boldsymbol{\Omega}_{21}^{2} & \boldsymbol{\Omega}_{22}^{2}\end{bmatrix}\begin{bmatrix}\boldsymbol{\Omega}_{11}^{3} & \boldsymbol{\Omega}_{12}^{3}\\ \boldsymbol{\Omega}_{21}^{3} & \boldsymbol{\Omega}_{22}^{3}\end{bmatrix}. \tag{5.8}$$

Thus the displacements and forces on both sides are related by the parameters of the bend.

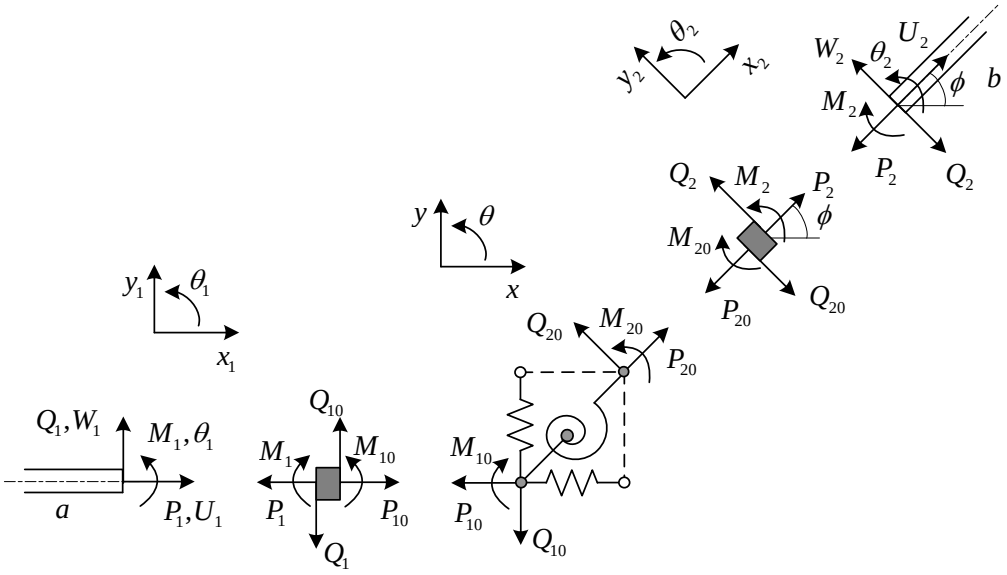

Figure 5.5 Free body diagram of the angled bend and each waveguide.

5.3.3 Reflection and Transmission Coefficients

In this section, the reflection and transmission coefficients of the bend are found using the approach described in Chapter 2. Here it is assumed that the two waveguides in

Figure 5.5 are semi-infinite. By considering only one wave component of the incident waves, the reflection and transmission coefficients induced by this incident wave can be derived by solving equation (2.43). Here as an example, the case with only one incident flexural propagating wave in waveguide a is considered, thus

$$\mathbf{a}^{+}=\begin{Bmatrix}0\\W_P^{+}\\0\end{Bmatrix} \text{ and } \mathbf{b}^{-}=\begin{Bmatrix}0\\0\\0\end{Bmatrix}. \tag{5.9}$$

Substituting equations (2.25), (2.26), (5.2), (5.8) and (5.9) into equation (2.43), after some lengthy manipulations (referring to Appendix 3), yields

$$\begin{bmatrix}
i\gamma_3+i & (i\gamma_6+i\xi_1)\cos\phi & 0 & (-i\gamma_6-i\xi_2)\sin\phi & 0 & (-i\gamma_6+\xi_2)\sin\phi\\
i\sigma_3+i\gamma_3+i & -i\sigma_3\cos\phi & 0 & i\sigma_3\sin\phi & 0 & i\sigma_3\sin\phi\\
0 & (i\gamma_4+i\xi_3)\sin\phi & i\gamma_1+i & (i\gamma_4+i\xi_4)\cos\phi & i\gamma_1-1 & (i\gamma_4-\xi_4)\cos\phi\\
0 & -i\sigma_1\sin\phi & i\sigma_1+i\gamma_1+i & -i\sigma_1\cos\phi & i\sigma_1+i\gamma_1-1 & -i\sigma_1\cos\phi\\
0 & 0 & -\gamma_2-1 & \nu\gamma_5+\frac{\xi_4}{\nu} & i\gamma_2+1 & -i\nu\gamma_5-\frac{\xi_4}{\nu}\\
0 & 0 & -\sigma_2-\gamma_2-1 & -\nu\sigma_2 & i\sigma_2+i\gamma_2+1 & i\sigma_2
\end{bmatrix}
\begin{Bmatrix}r_{HL}\\t_{HL}\\r_{HP}\\t_{HP}\\r_{HN}\\t_{HN}\end{Bmatrix}=
\begin{Bmatrix}0\\0\\-i\gamma_1+i\\-i\sigma_1-i\gamma_1+i\\-\gamma_2+1\\-\sigma_2-\gamma_2+1\end{Bmatrix} \tag{5.10}$$

where

$$\begin{aligned}
&\xi_1=\frac{E_2A_2k_{l2}}{E_1A_1k_{l1}},\quad \xi_2=\frac{E_2I_2k_{b2}^3}{E_1A_1k_{l1}},\quad \xi_3=\frac{E_2A_2k_{l2}}{E_1I_1k_{b1}^3},\\
&\xi_4=\frac{E_2I_2k_{b2}^3}{E_1I_1k_{b1}^3},\quad \nu=\frac{k_{b2}}{k_{b1}},\\
&\sigma_1=-i\frac{K_y}{E_1I_1k_{b1}^3},\quad \sigma_2=-i\frac{K_R}{E_1I_1k_{b1}},\quad \sigma_3=-i\frac{K_x}{E_1A_1k_{l1}},\\
&\gamma_1=\frac{im_1\omega^2}{E_1I_1k_{b1}^3},\quad \gamma_2=\frac{iJ_1\omega^2}{E_1I_1k_{b1}},\quad \gamma_3=\frac{im_1\omega^2}{E_1A_1k_{l1}},\\
&\gamma_4=\frac{im_2\omega^2}{E_1I_1k_{b1}^3},\quad \gamma_5=\frac{iJ_2\omega^2}{E_1I_1k_{b1}},\quad \gamma_6=\frac{im_2\omega^2}{E_1A_1k_{l1}}.
\end{aligned} \tag{5.11}$$

See Appendix 4 for the definition of the above symbols. In equation (5.10), the two waveguides are considered to be of different materials and dimensions. For simplicity, and as is often the case in practice, it is assumed henceforth that the two waveguides are of the same materials and dimensions, such that

$$\xi_1=1,\quad \xi_4=1,\quad \nu=1,\quad \xi_2=\frac{1}{\xi_3}=\xi \tag{5.12}$$

and that the joint is symmetrical, i.e. $K_X=K_Y=K_T$, $m_1=m_2=m/2$ and

$J_1 = J_2 = J/2$, therefore,

$$\begin{aligned} &\sigma_1 = i\frac{\chi}{\xi^3},\ \ \sigma_2 = i\frac{\psi}{\xi},\ \ \sigma_3 = i\frac{\chi}{\xi^2}, \\ &\gamma_1 = \gamma_4 = i\frac{\mu\xi}{2},\ \ \gamma_2 = \gamma_5 = i\frac{\vartheta\xi^3}{2},\ \ \gamma_3 = \gamma_6 = i\frac{\mu\xi^2}{2}. \end{aligned} \tag{5.13}$$

where

$$\chi = \frac{K_T}{EA/\kappa},\ \ \psi = \frac{K_R}{EI/\kappa},\ \ \mu = \frac{m}{\rho A\kappa},\ \ \vartheta = \frac{J}{\rho A\kappa^3},\ \ \xi = \sqrt{\frac{\omega\kappa}{c_l}}. \tag{5.14}$$

$\kappa = \sqrt{I/A}$ is the radius of gyration of the waveguide's cross-section. The parameters in equation (5.14) are non-dimensional and defined in Appendix 4. The physical meanings of the parameters are the same as those defined in Chapters 2 and 4. The first four parameters concern the joint properties relating to the characteristics of the waveguide and are frequency independent. They are the parameters that will be estimated in Chapters 6 and 7.

Substituting the symbols in equations (5.12), (5.13) and (5.14) into equation (5.10) yields

$$\begin{bmatrix} \frac{i\mu\xi^2}{2}+i & \left(\frac{i\mu\xi^2}{2}+i\right)\cos\phi & 0 & -i\left(\frac{\mu\xi^2}{2}+\xi\right)\sin\phi & 0 & \left(-\frac{i\mu\xi^2}{2}+\xi\right)\sin\phi \\ \frac{i\chi}{\xi^2}+i\frac{\mu\xi^2}{2}+i & -\frac{i\chi}{\xi^2}\cos\phi & 0 & \frac{i\chi}{\xi^2}\sin\phi & 0 & \frac{i\chi}{\xi^2}\sin\phi \\ 0 & \left(\frac{i\mu\xi}{2}+\frac{i}{\xi}\right)\sin\phi & \frac{i\mu\xi}{2}+i & \left(\frac{i\mu\xi}{2}+i\right)\cos\phi & \frac{i\mu\xi}{2}-1 & \left(\frac{i\mu\xi}{2}-1\right)\cos\phi \\ 0 & \frac{i\chi}{\xi^3}\sin\phi & \frac{i\chi}{\xi^3}+\frac{i\mu\xi}{2}+i & -\frac{i\chi}{\xi^3}\cos\phi & \frac{i\chi}{\xi^3}+\frac{i\mu\xi}{2}-1 & -\frac{i\chi}{\xi^3}\cos\phi \\ 0 & 0 & -\frac{\vartheta\xi^3}{2}-1 & \frac{\vartheta\xi^3}{2}+1 & i\frac{\vartheta\xi^3}{2}+1 & -i\frac{\vartheta\xi^3}{2}-1 \\ 0 & 0 & -\frac{\psi}{\xi}-\frac{\vartheta\xi^3}{2}-1 & -\frac{\psi}{\xi} & i\frac{\psi}{\xi}+i\frac{\vartheta\xi^3}{2}+1 & i\frac{\psi}{\xi} \end{bmatrix} \begin{Bmatrix} r_{PL} \\ t_{PL} \\ r_{PP} \\ t_{PP} \\ r_{PN} \\ t_{PN} \end{Bmatrix} = \begin{Bmatrix} 0 \\ 0 \\ -i\frac{\mu\xi}{2}+i \\ -i\frac{\chi}{\xi^3}-i\frac{\mu\xi}{2}+i \\ -\frac{\vartheta\xi^3}{2}+1 \\ -\frac{\psi}{\xi}-\frac{\vartheta\xi^3}{2}+1 \end{Bmatrix} \tag{5.15}$$

The six reflection and transmission coefficients can be obtained numerically by solving the above equation.

Equation (5.15) is for the parametric joint model as shown in Figure 5.5, which involves the inertia, stiffness and damping (incorporated into the stiffness) of the joint and angle of the bend. Depending on the situation, one or two properties may dominate the others,

in which case the model can be simplified to a special case, such as rigid connection, mass-like discontinuity or spring-like discontinuity. The corresponding equation for the reflection and transmission coefficients can be obtained by applying appropriate values to the parameters in equation (5.15). Also, the coefficients depend on the joint angle ϕ. If $\phi = 0$, the system becomes a straight waveguide. These cases are discussed in Chapters 2, 3 and 4. In practice, the right-angled bends are used widely. Assuming that $\phi = \pi/2$, equation (5.15) becomes

$$\begin{bmatrix} i\frac{\mu\xi^2}{2}+i & 0 & 0 & -i\frac{\mu\xi^2}{2}-i\xi & 0 & -i\frac{\mu\xi^2}{2}+\xi \\ i\frac{\chi}{\xi^2}-i\frac{\mu\xi^2}{2}+i & 0 & 0 & i\frac{\chi}{\xi^2} & 0 & i\frac{\chi}{\xi^2} \\ 0 & i\frac{\mu\xi}{2}+\frac{i}{\xi} & i\frac{\mu\xi}{2}+i & 0 & i\frac{\mu\xi}{2}-1 & 0 \\ 0 & -i\frac{\chi}{\xi^3} & i\frac{\chi}{\xi^3}+i\frac{\mu\xi}{2}+i & 0 & i\frac{\chi}{\xi^3}+i\frac{\mu\xi}{2}-1 & 0 \\ 0 & 0 & -\frac{\vartheta\xi^3}{2}-1 & \frac{\vartheta\xi^3}{2}+1 & i\frac{\vartheta\xi^3}{2}+1 & -i\frac{\vartheta\xi^3}{2}-1 \\ 0 & 0 & -\frac{\psi}{\xi}-\frac{\vartheta\xi^3}{2}-1 & -\frac{\psi}{\xi} & i\frac{\psi}{\xi}+i\frac{\vartheta\xi^3}{2}+1 & i\frac{\psi}{\xi} \end{bmatrix} \begin{Bmatrix} r_{PL} \\ t_{PL} \\ r_{PP} \\ t_{PP} \\ r_{PN} \\ t_{PN} \end{Bmatrix} = \begin{Bmatrix} 0 \\ 0 \\ -i\frac{\mu\xi}{2}+i \\ -i\frac{\chi}{\xi^3}-i\frac{\mu\xi}{2}+i \\ -\frac{\vartheta\xi^3}{2}+1 \\ -\frac{\psi}{\xi}-\frac{\vartheta\xi^3}{2}+1 \end{Bmatrix}. \quad (5.16)$$

In what follows, attention will be focused on right-angled joints.

5.3.4 Power Reflection and Transmission Coefficients

Since wave mode conversion occurs in an angled bend, the definition of the power reflection and transmission coefficients need to consider the power involved in each wave mode. The power in an axial wave and a flexural wave are given by equation (2.15). Consider V_l and V_b as the axial and flexural wave velocities. They are proportional to the axial and flexural wave displacements, i.e. $|V_l| = \omega|U|$ and $|V_b| = \omega|W|$. Therefore the flexural power reflection coefficient can be expressed as

$$\rho_{PP} = \frac{2\rho A c_b |V_{br}|^2}{2\rho A c_b |V_{bi}|^2} = |r_{bb}|^2 \quad (5.17)$$

where the subscripts *r* and *i* indicate the reflected and incident wave modes respectively. The flexural power transmission coefficient is given by

$$\tau_{PP} = \frac{2\rho A c_b \left|V_{bt}\right|^2}{2\rho A c_b \left|V_{bi}\right|^2} = \left|t_{bb}\right|^2 \tag{5.18}$$

where subscript t indicates the transmitted wave. Similarly the axial power reflection and transmission coefficients are given respectively by

$$\rho_{PL} = \frac{\rho A c_l \left|V_{lr}\right|^2}{2\rho A c_b \left|V_{bi}\right|^2} = \frac{1}{2\xi}\left|r_{PL}\right|^2,\ \tau_{PL} = \frac{\rho A c_l \left|V_{lt}\right|^2}{2\rho A c_b \left|V_{bi}\right|^2} = \frac{1}{2\xi}\left|t_{PL}\right|^2. \tag{5.19}$$

If there is no energy dissipation in the system, then

$$\rho_{PL} + \tau_{PL} + \rho_{PP} + \tau_{PP} = 1. \tag{5.20}$$

In practice the sum of these four coefficients is less than unity owing to the existence of the damping of the system.

5.3.5 Rigid Massless Right-angled Connection

If the joint in Figure 5.5 is considered to be rigidly connected and massless, then $m_1 = m_2 = 0$, $J_1 = J_2 = 0$, $\chi \to \infty$ and $\psi \to \infty$. The propagating reflection and transmission coefficients can be found from equation (5.16) to be

$$\begin{aligned} r_{PL} &= \frac{-2\xi\left(i\xi+1\right)}{\left(\xi+1-i\right)\left(2\xi+1-i\right)},\ t_{PL} = 2\xi\frac{\left(2-i\right)\xi+1-2i}{\left(\xi+1-i\right)\left(2\xi+1-i\right)}, \\ r_{PP} &= \frac{\left(\xi^2-i\xi-1\right)\left(1-i\right)}{\left(\xi+1-i\right)\left(2\xi+1-i\right)},\ t_{PP} = \frac{\left(\xi-i\right)^2\left(1+i\right)}{\left(\xi+1-i\right)\left(2\xi+1-i\right)}. \end{aligned} \tag{5.21}$$

At low frequencies, when the high order terms of ξ can be neglected, the power reflection and transmission coefficients can be approximated respectively by

$$\rho_{PL} = \frac{\xi}{6\xi+2},\ \tau_{PL} = \frac{5\xi}{6\xi+2},\ \rho_{PP} = \frac{1}{6\xi+2},\ \tau_{PP} = \frac{1}{6\xi+2}. \tag{5.22}$$

Equations (5.22) can be considered the asymptotes of the corresponding power reflection and transmission coefficients at low frequencies. From the above equation, at very low frequencies, i.e. $\xi \to 0$, then $\rho_{PL} \to 0$ and $\tau_{PL} \to 0$. This indicates that there is almost no wave mode conversion to axial waves. Conversely, both $\rho_{PP} \to 0.5$ and $t_{PP} \to 0.5$, which means that the flexural incident wave is half transmitted and half reflected in the form of flexural waves.

Figure 5.6 shows the power reflection and transmission coefficients against the non-dimensional frequency, $\xi^2 = \omega\kappa / c_l$. The power reflection and transmission coefficients obtained from equations (5.22) are very close to those obtained from equation (5.21) at low frequencies. With increasing frequency, deviations are found. Since ρ_{PL} and τ_{PL} are relatively small compared with ρ_{PP} and τ_{PP}, only a small proportion of the power is transferred from flexural incident wave to axial waves, especially at low frequencies. τ_{PL} is always about 5 times larger than ρ_{PL}, which means that power in the form of axial waves is mainly carried in waveguide 2. With increasing frequency, the power involved in the axial waves increases, accordingly the power in the flexural waves decreases. In addition, τ_{PP} becomes larger than ρ_{PP}, so a greater proportion of the power in the form of flexural waves is transmitted into waveguide 2.

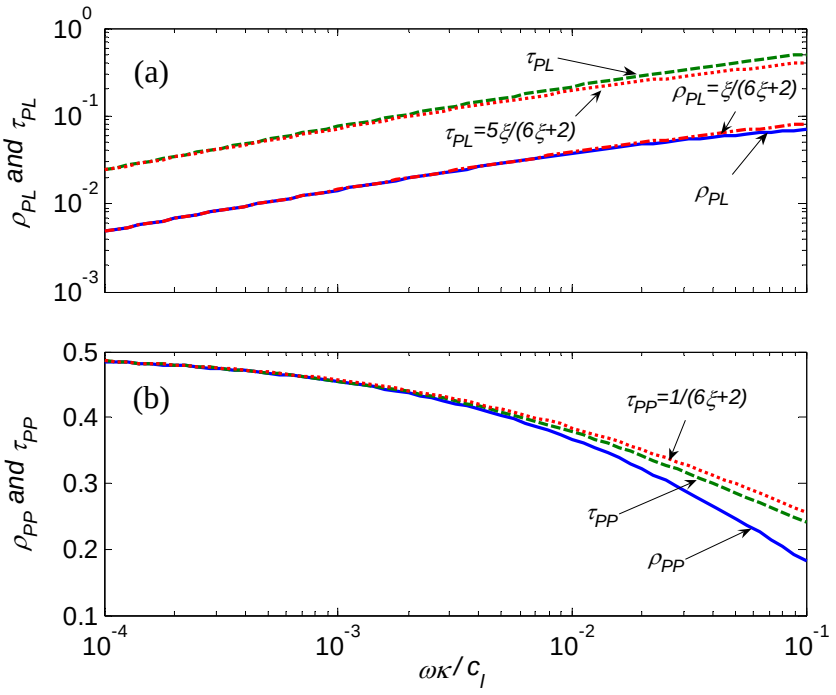

Figure 5.6 Power reflection and transmission coefficients of the rigid massless joint.

5.3.6 Mass-like Joint

Referring to the joint model shown in Figure 5.5, if the connection is rigid and the mass and inertia of the joint play a significant role, it can be considered as a mass-like joint.

In this case, the stiffnesses tend to infinity. The propagating reflection and transmission coefficients are

$$\begin{aligned}
r_{PL} &= \frac{1}{D_m}(2+2i)\xi\left(\mu\xi^2+\xi-i\right),\\
t_{PL} &= \frac{1}{D_m}(2-2i)\xi\left[\left(\mu\xi^2\right)\left(\vartheta\xi^3\right)-(2+i)\mu\xi^2+(\xi-i\xi-i)\vartheta\xi^3-(2-i)\xi-1+2i\right],\\
r_{PP} &= -\frac{1}{D_m}i\left[\begin{array}{l}\left(\mu\xi^2\right)^2\left(\vartheta\xi^3\right)-2\left(\mu\xi^2\right)^2+2(\xi-i)\left(\mu\xi^2\right)\left(\vartheta\xi^3\right)-2(\xi-2i)\left(\mu\xi^2\right)\\ +\left(2\xi^2-2i\xi-1\right)\left(\vartheta\xi^3\right)-2\xi^2+2i\xi+2\end{array}\right],\\
t_{PP} &= \frac{1}{D_m}2\left(\mu\xi^2+\xi-i\right)^2.
\end{aligned} \tag{5.23}$$

where

$$\begin{aligned}
D_m = &\left[\left(\mu\xi^2\right)\left(\vartheta\xi^3\right)-2(1+i)\left(\mu\xi^2\right)+(\xi-i\xi-i)\left(\vartheta\xi^3\right)-2\xi-2+2i\right]\\
&\left[\left(\mu\xi^2\right)+\xi-i\xi-i\right].
\end{aligned}$$

Here, $i\mu\xi^2$ is the ratio of the impedance of the mass to the longitudinal characteristic impedance of the waveguide. Similarly, $i\vartheta\xi^3$ is the ratio of the impedance of the moment of inertia to the rotational characteristic impedance of the waveguide.

Closed form solutions for the power reflection and transmission coefficients are very complicated. However, since the non-dimensional frequency, ξ^2 is very small, the higher order terms in ξ can be neglected. The first order approximations become

$$\begin{aligned}
\rho_{PL} &\approx \frac{4\xi}{\left[\left(\xi^3\vartheta-2\right)^2+4\right]\left(\xi^4\mu^2+1\right)},\quad \tau_{PL} \approx \frac{4\xi\left[\left(\xi^3\vartheta-2\right)^2+1\right]}{\left[\left(\xi^3\vartheta-2\right)^2+4\right]\left(\xi^4\mu^2+1\right)},\\
\rho_{PP} &\approx \frac{\left(\xi^3\vartheta-2\right)^2}{\left(\xi^3\vartheta-2\right)^2+4},\quad \tau_{PP} \approx \frac{4}{\left(\xi^3\vartheta-2\right)^2+4}.
\end{aligned} \tag{5.24}$$

These expressions are only valid when $\xi \ll 1$ and $\mu\xi^2 \gg \xi$. From these approximate expressions, an important frequency where $\xi^3\vartheta = 2$ can be noted. At this frequency the power reflection and transmission coefficients reach their local minima or maxima. This holds both for the exact and simplified expressions. Referring to Equations (5.11) and (5.13), $\vartheta\xi^3 = 2$ means that magnitude of the rotational impedance of the joint is twice that of the rotational characteristic impedance of the waveguide, i.e. the magnitude of

rotational impedance of each added mass (m_1 and m_2) is twice that of rotational characteristic impedance of the waveguide. Once this frequency is found, the joint moment of inertia can be estimated simply by $\vartheta = 2/\xi^3$. Consequently, the mass parameter, μ can be estimated from equation (5.23).

Figure 5.7 shows the power reflection and transmission coefficients as functions of the magnitudes of translational and rotational impedance ratios at the frequency $\xi^2 = 0.0084$. This frequency is equivalent to 500Hz for the pipe in Chapter 4. At the regions where $\xi^3\vartheta = 2$, the power reflection and transmission coefficients reach their local extrema. Large translational impedance or mass of the bend can impede wave mode conversion effectively. Large rotational impedance or inertia of the joint can prevent rotational motion of the bend, and therefore, restrain the energy in the flexural incident waves from transferring to flexural waves in the second waveguide. Consequently, the energy in the reflected axial waves is also reduced. When the mass of the bend is large but the moment of inertia is small, the energy in the flexural incident waves will be half reflected and half transmitted in the form of flexural waves, because in this case the translational motions are prevented but the rotational motions can be transmitted freely. When both of the mass and moment of inertia of the bend are large, both the translational and rotational motions are restrained, so the energy will be totally reflected in the original wave modes.

Figure 5.8 illustrates the power reflection and transmission coefficients as functions of the magnitudes of impedance ratios at the frequency $\xi^2 = 0.0336$, which is equivalent to 2000Hz for the pipe used in the measurements of Chapter 4. The trends of the coefficients are the same as in Figure 5.7 except that the wave mode conversion is larger than that at the low frequency ($\xi^2 = 0.0084$) when the translational impedance of the bend is small.

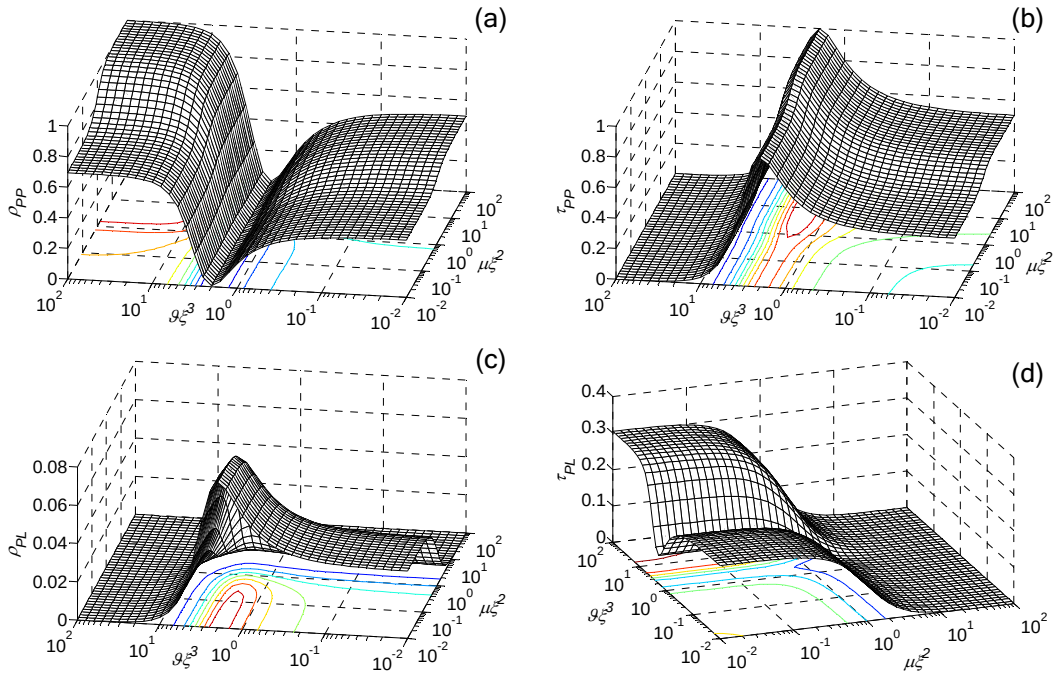

Figure 5.7 Power reflection and transmission coefficients of the mass-like joint: $\xi^2 = 0.0084$.

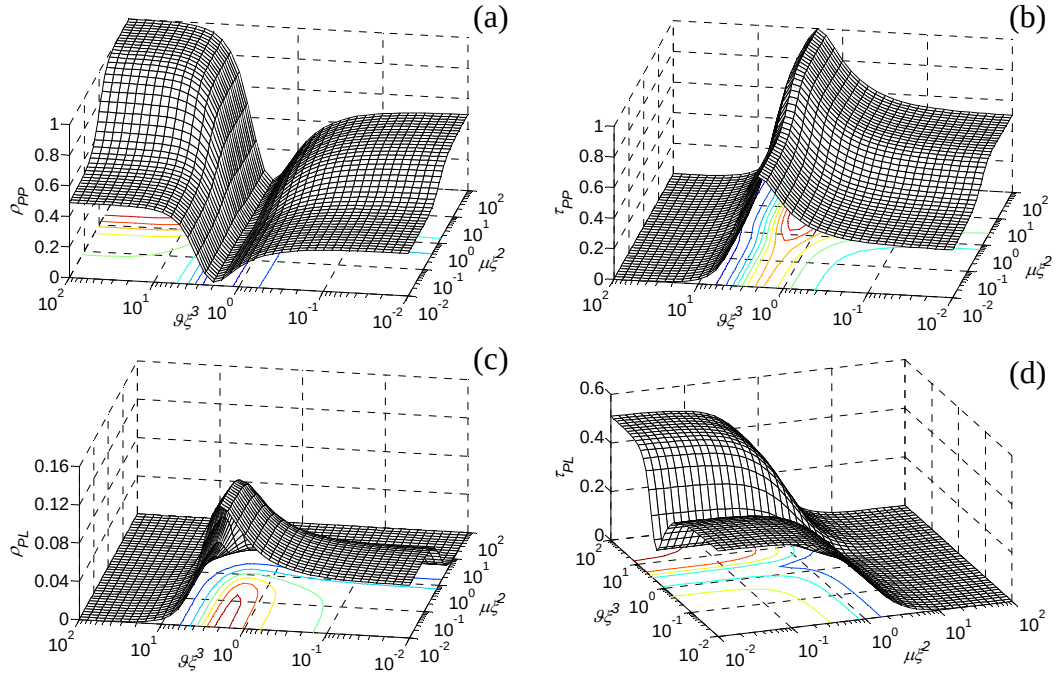

Figure 5.8 Power reflection and transmission coefficients of the mass-like joint: $\xi^2 = 0.0336$.

Figures 5.9 and 5.10 show the first order approximations for the power reflection and transmission coefficients given in equation (5.24) against the magnitudes of impedance

ratios at $\xi^2 = 0.0084$ and $\xi^2 = 0.0336$ respectively. For first order approximations, ρ_{PP} and τ_{PP} are the same for the two values of ξ^2. Therefore, in Figure 5.10, only ρ_{PL} and τ_{PL} are given. The simplified expressions are close to the exact ones shown in Figures 5.7 and 5.8 when the translational impedance of the bend is large. It can also be seen that the first order approximations are more accurate at low frequency. In Figure 5.10(b) $\tau_{PL} > 1$. This is not true since when $\vartheta\xi^3$ is large, the first order approximations are not accurate.

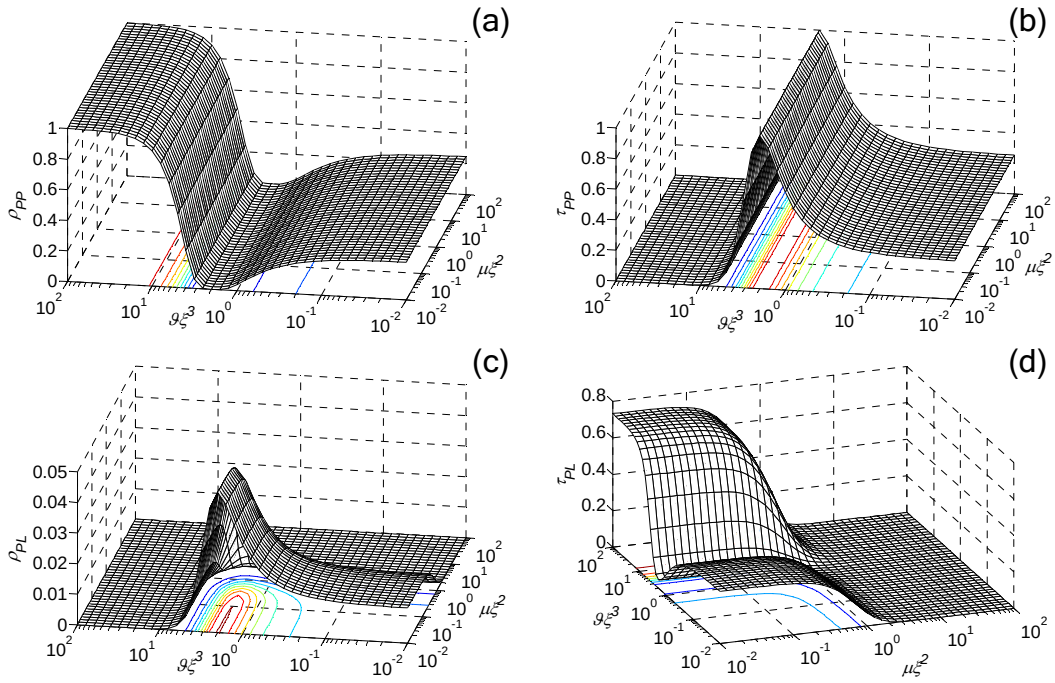

Figure 5.9 First order approximations for the power reflection and transmission coefficients of the mass-like joint: $\xi^2 = 0.0084$.

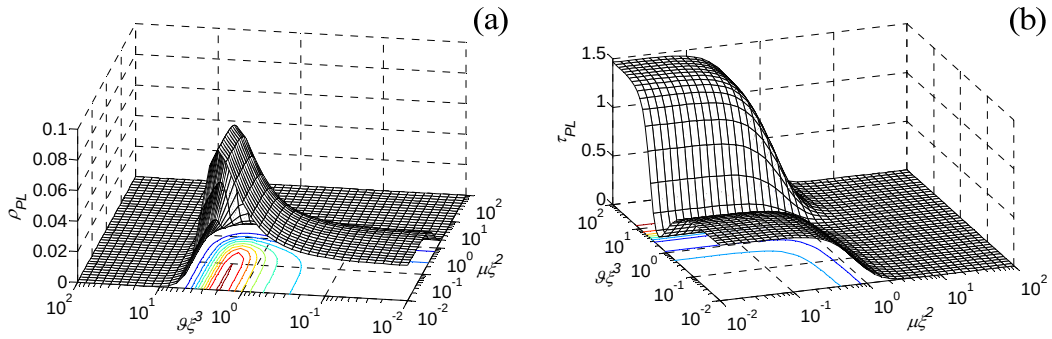

Figure 5.10 First order approximations for the power reflection and transmission coefficients of the mass-like joint: $\xi^2 = 0.0336$.

5.3.7 Spring-like Joint

For the joint model shown in Figure 5.5, if the mass of the bend is relatively small and can be neglected, i.e. $m_1 = m_2 = 0$ and $J_1 = J_2 = 0$, the joint will behave as a spring-like discontinuity. The propagating reflection and transmission coefficients can be found from equation (5.16) to be

$$\begin{aligned}
r_{PL} &= \frac{1}{D_s}(2-2i)\xi\left(\chi/\xi^3\right)(\psi/\xi)\left[(i\xi+1)\left(\chi/\xi^3\right)-1\right],\\
t_{PL} &= \frac{1}{D_s}(2+2i)\xi\left(\chi/\xi^3\right)\begin{bmatrix}(\xi+2i\xi+2+i)\left(\chi/\xi^3\right)(\psi/\xi)\\ +(i\xi+1+i)\left(\chi/\xi^3\right)-(2-i)(\psi/\xi)-1\end{bmatrix},\\
r_{PP} &= \frac{1}{D_s}i\begin{bmatrix}2\left(\xi^2-i\xi-1\right)\left(\chi/\xi^3\right)^2(\psi/\xi)+\left(\xi^2-2i\xi-2\right)\left(\chi/\xi^3\right)^2\\ +2(2i\xi+1)\left(\chi/\xi^3\right)(\psi/\xi)+2(i\xi+1)\left(\chi/\xi^3\right)-2(\psi/\xi)-1\end{bmatrix},\\
t_{PP} &= \frac{1}{D_s}2(\psi/\xi)\left[(i\xi+1)\left(\chi/\xi^3\right)-1\right]^2.
\end{aligned} \tag{5.25}$$

where

$$\begin{aligned}
D_s = &\left[2\left(\xi+i\xi+1\right)\left(\chi/\xi^3\right)(\psi/\xi)+\left(i\xi+i+1\right)\left(\chi/\xi^3\right)-2(1-i)(\psi/\xi)-1\right]\\
&\left[(i\xi+i+1)\left(\chi/\xi^3\right)-1\right].
\end{aligned}$$

Note that $-i\chi/\xi^3$ is the ratio of the impedance of the translational spring to the translational characteristic impedance of the waveguide. Similarly, $-i\psi/\xi$ is the ratio of the impedance of the rotational spring to the rotational characteristic impedance of the waveguide.

In Figure 5.11 the power reflection and transmission coefficients are plotted against parameters χ/ξ^3 and ψ/ξ at frequency $\xi^2 = 0.0084$. Figure 5.11(a) shows that if the magnitudes of impedance ratios are very small, $\rho_{PP} \to 1$. This is as expected because a very soft joint will not transmit energy to the second waveguide, and there would be no wave mode conversion for this case as well. With increasing rotational stiffness, the energy involved in the reflected flexural waves decreases except around regions where $\chi/\xi^3 = 1$. Around these regions, ρ_{PP} is insensitive to the rotational stiffnesses. With soft translational springs, at least half of the energy will be reflected as flexural waves. Figure 5.11(b) shows the energy in the transmitted flexural waves increases with the

rotational stiffness of the bend except at the regions where $\chi/\xi^3=1$. At these regions there is almost no energy transmitted to the flexural waves in the second waveguide. At most half of the total energy can be transmitted to the second waveguide as flexural waves. Figure 5.11(c) indicates that the energy carried by the axial waves in the first waveguide is an order of magnitude smaller than that in the second waveguide. Figure 5.11(d) signifies that the energy in the transmitted axial waves reaches its maximum at the regions where $\chi/\xi^3=1$. τ_{PL} is less sensitive to the rotational stiffness of the bend. In all, the extent of the energy transferred from the incident flexural waves to other waves, as expected, increases with the stiffnesses of the bend. Around the regions where $\chi/\xi^3=1$, wave mode conversion is most noticeable.

Figure 5.12 shows the power reflection and transmission coefficients as functions of parameters χ/ξ^3 and ψ/ξ at frequency $\xi^2=0.0336$. It can be seen that the trend of each coefficient is the same as in Figure 5.11. An obvious phenomenon is that at high frequencies, wave mode conversion increases. More energy is converted into the axial wave modes in the second waveguide at the regions where $\chi/\xi^3=1$.

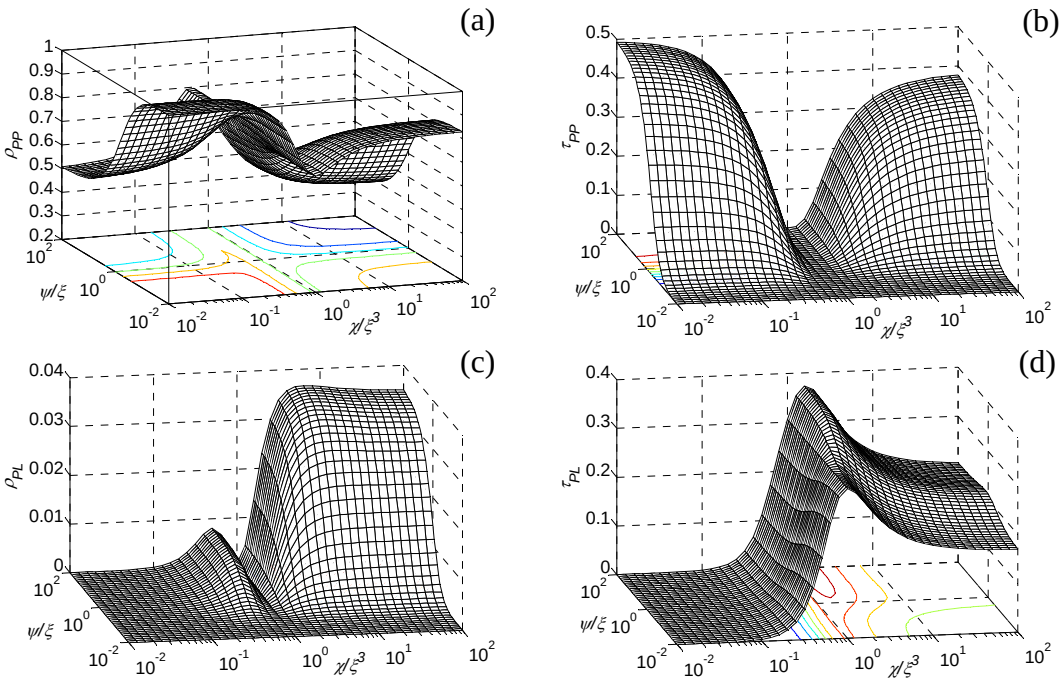

Figure 5.11 Power reflection and transmission coefficients of the spring-like joint: $\xi^2=0.0084$.

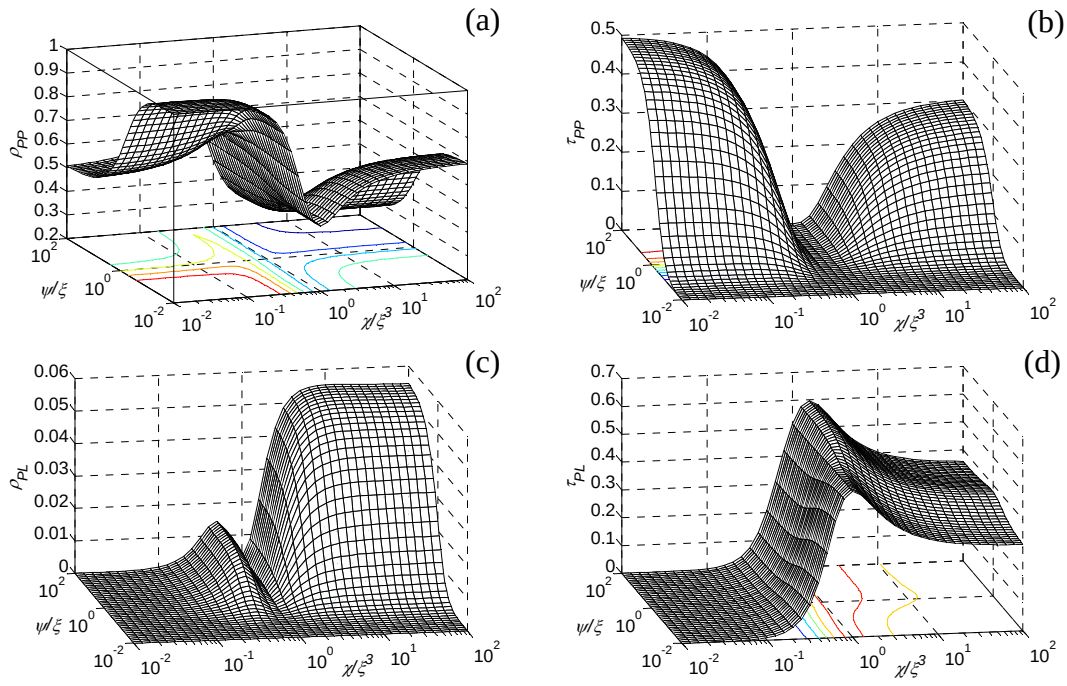

Figure 5.12 Power reflection and transmission coefficients of the spring-like joint: $\xi^2 = 0.0336$.

5.3.8 Damping of the Joint

Damping of the joint is inevitable in practice, therefore it is essential to investigate its effect on the reflection and transmission coefficients. Here a complex stiffness model is incorporated into the stiffness parameters χ and ψ by multiplying them respectively by $(1+i\eta_T)$ and $(1+i\eta_R)$, where η_T and η_R are the damping loss factors in the translational and rotational directions respectively. Figure 5.13 shows the influence of the damping loss factors on the power coefficients ρ_{PP} and τ_{PL} with joint parameters $\chi = 0.01$, $\psi = 0.1$, $\mu = 10$ and $\vartheta = 10$. When the loss factors are small, i.e. $\eta < 0.01$, the effect of the damping is insignificant. The effects of the damping in the translational and rotational springs are different. This is because of the sensitivities of the coefficients to the stiffnesses. For example, τ_{PL} is not sensitive to the rotational stiffness, therefore the damping in the rotational direction has almost no effect on it. When considering the damping in both translational and rotational springs, the effect is the combination of these two cases. The other power reflection and transmission coefficients are similarly affected by damping.

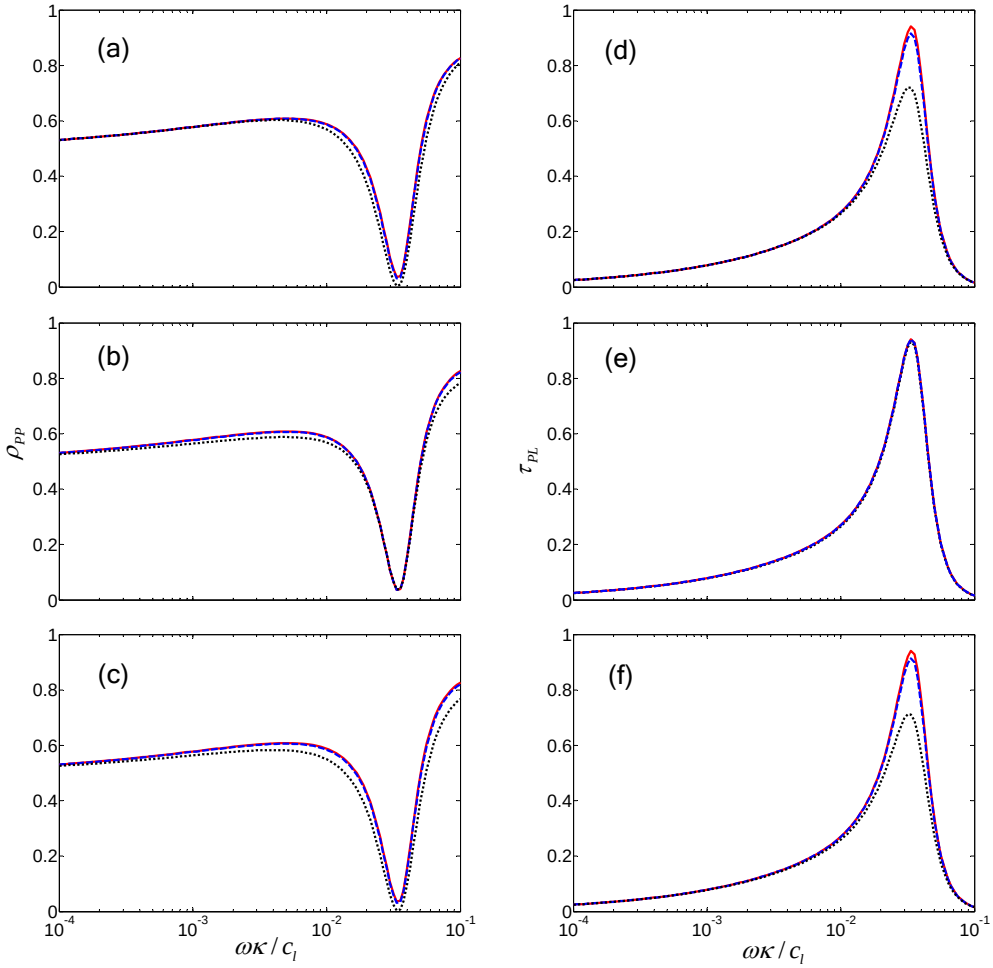

Figure 5.13 Power reflection and transmission coefficients of the right-angled bend: $\chi = 0.01$, $\psi = 0.1$, $\mu = 10$ and $\vartheta = 10$: varying damping loss factors: ——, $\eta = 0$; - - - -, $\eta = 0.01$; ·····, $\eta = 0.1$: (a), (d) damping in translational springs; (b), (e) damping in rotational spring; (c), (f) damping in both translational and rotational springs.

5.4 Reflection and Transmission Coefficients in terms of Wave Amplitudes

A wave amplitude decomposition method has been presented in Chapter 3 to measure reflection and transmission coefficients. This section describes how the reflection and transmission coefficients of the right-angled bend can be measured by such a method. This requires that the reflection and transmission coefficients be derived in terms of the wave amplitudes in the waveguides. The wave field of the system is shown in Figure 5.14. A general excitation in the plane of the bend is assumed to be applied at point 1 of pipe a, which gives rise to waves with amplitudes $\mathbf{c}^+$ and $\mathbf{c}^-$ at this point. The

negative-going waves with amplitudes $\mathbf{c}^-$ will be reflected at the end of pipe *a* (point 4). The reflected waves travel a distance l_3 and superimpose upon the positive-going waves at point 1 to form the positive-going waves on the right-hand side of point 1. At the pipe bend, the waves are reflected and transmitted. Reflections from the end of pipe *b* give rise to negative-going waves. The wave amplitudes at points 2 and 3 are expressed by $\mathbf{a}^{\pm}$ and $\mathbf{b}^{\pm}$ respectively. The waves at the bend are indicated by the subscript 0.

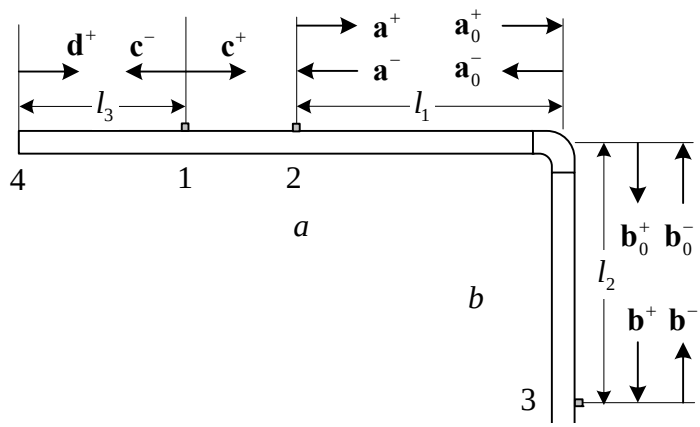

Figure 5.14 Wave field in the right-angled pipes.

The positive- and negative-going waves on both sides of the bend are related by equation (5.1). Symmetry of the structure can reduce the number of unknown reflection and transmission coefficients given by equation (5.2) from 36 to 18. Note that since there are wave mode changes, **R** and **T** are not symmetrical. Neglecting the nearfields, only 8 coefficients are unknown and equation (5.1) becomes

$$\begin{bmatrix} u_{a0}^- \\ w_{a0}^- \\ u_{b0}^+ \\ w_{b0}^+ \end{bmatrix} = \begin{bmatrix} r_{LL} & r_{PL} & t_{LL} & t_{PL} \\ r_{LP} & r_{PP} & t_{LP} & t_{PP} \\ t_{LL} & t_{PL} & r_{LL} & r_{PL} \\ t_{LP} & t_{PP} & r_{LP} & r_{PP} \end{bmatrix} \begin{bmatrix} u_{a0}^+ \\ w_{a0}^+ \\ u_{b0}^- \\ w_{b0}^- \end{bmatrix}. \tag{5.26}$$

Assuming that the pipe ends are axially non-reflecting, for the excitation considered here, $u_{a0}^+ = 0$ and $u_{b0}^- = 0$. The above equation can then be written as

$$\begin{bmatrix} u_{a0}^- & w_{a0}^- \\ u_{b0}^+ & w_{b0}^+ \end{bmatrix} = \begin{bmatrix} w_{a0}^+ & w_{b0}^- \\ w_{b0}^- & w_{a0}^+ \end{bmatrix} \begin{bmatrix} r_{PL} & t_{PL} \\ r_{PP} & t_{PP} \end{bmatrix}. \tag{5.27}$$

The wave amplitudes at points 2 and 3 in Figure 5.14 can be obtained by the wave

amplitude decomposition method discussed in Chapter 3 and then converted to the wave amplitudes at the bend by equation (2.28). Thus the reflection and transmission coefficients can be obtained by solving equation (5.27).

5.5 Experiments on a Right-angled Pipe Bend

This section describes experiments carried out on a right-angled pipe bend. The frequency where the $n = 2$ wave mode cuts on and the wavenumber of the pipe were measured. Then the reflection and transmission coefficients of the bend were measured using the wave amplitude decomposition method. The behaviour of the power reflection and transmission coefficients are analysed below the cut-on frequency of the $n = 2$ ovalling mode.

5.5.1 Experimental Setup

The experimental rig is shown in Figure 5.15. Two copper pipes of length 4m, outer radius 14mm and wall thickness 0.9mm were joined with a soldered right-angled elbow and suspended at two locations by wire. A sandbox with foam wedges was placed at each end of the pipes to approximate anechoic conditions for the flexural waves. A sandwich steel panel was attached perpendicularly to the end of each pipe to minimise axial wave reflections. The approach using a sandwich panel was described previously by Brennan [68], in which the thickness of the panel was chosen to let the characteristic impedance in loading of the panel match the characteristic impedance of the axial wave motion of the pipe, so the energy in the axial waves is transmitted effectively into the panel.

One of the pipes was excited perpendicularly in the plane of the bend by a shaker through a stinger with a force transducer mounted on the pipe. Then below the cut-on frequency for $n = 2$ ovalling mode, only flexural and axial wave modes were generated although torsional waves might exist in practice. A pair of accelerometers was located on each side of the bend, far enough from the pipe ends, the pipe bend and the excitation point, so that the nearfields can be neglected. Flexural and axial motions were

measured separately because the number of available channels on the analyser was limited. The spacings of accelerometers were chosen to be a quarter wavelength at the centre-frequency of interest based on approximate estimates, which were 0.10 m for flexural waves and 0.70 m for axial waves.

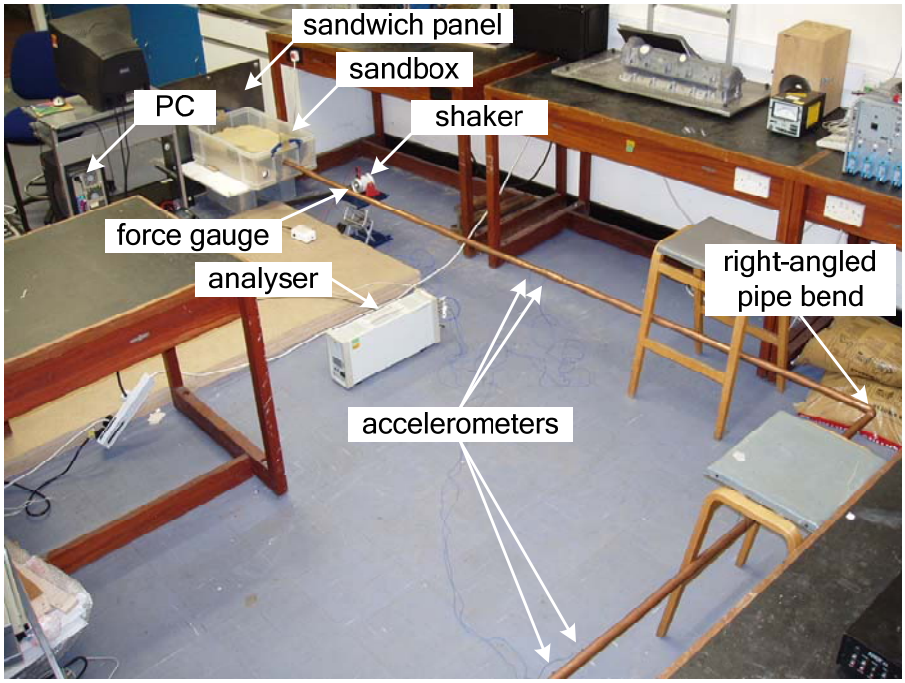

Figure 5.15 Experimental rig for measurements of the reflection and transmission coefficients of a right-angled pipe bend.

5.5.2 Cut-on Frequency for *n* =2 wave mode

Depending on frequency, piping systems can propagate very complicated wave modes. This has been discussed briefly in Chapter 4. When doing measurements on pipes, the wave modes propagating in the frequency range of interest must be known. Since only the in-plane axial and flexural waves are of interest in this thesis, the cut-on frequency for the $n = 2$ wave mode is very important.

Figure 5.16 shows the cross-section of the pipe under test. The pipe was excited in the horizontal direction. Two accelerometers were placed on opposing sides of the pipe cross-section as shown in the figure. The magnitude and phase of the transmissibility between the two accelerometers are shown in Figure 5.17. It can be seen that the magnitude ratio is almost unity and the phase difference between these two

accelerations is π until about 2500Hz. Thus the cut-on frequency for the $n=2$ wave mode for this pipe is about 2500Hz. Measurements on both pipe arms of the bend are very similar. Note that above 2000Hz, the magnitude of the transmissibility begins to deviate from unity. Henceforth the discussion will focus on frequencies below 2000Hz.

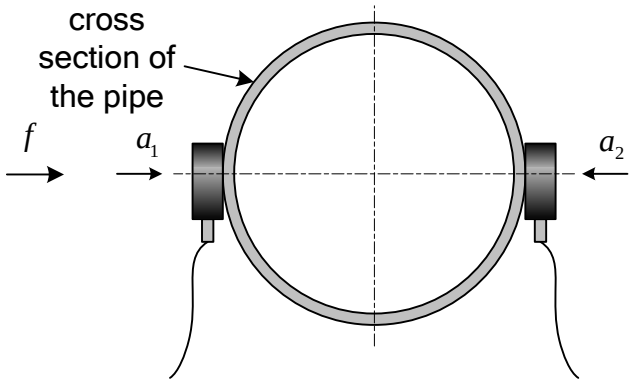

Figure 5.16 Placement of the accelerometers to measure the cut-on frequency for the $n=2$ wave mode.

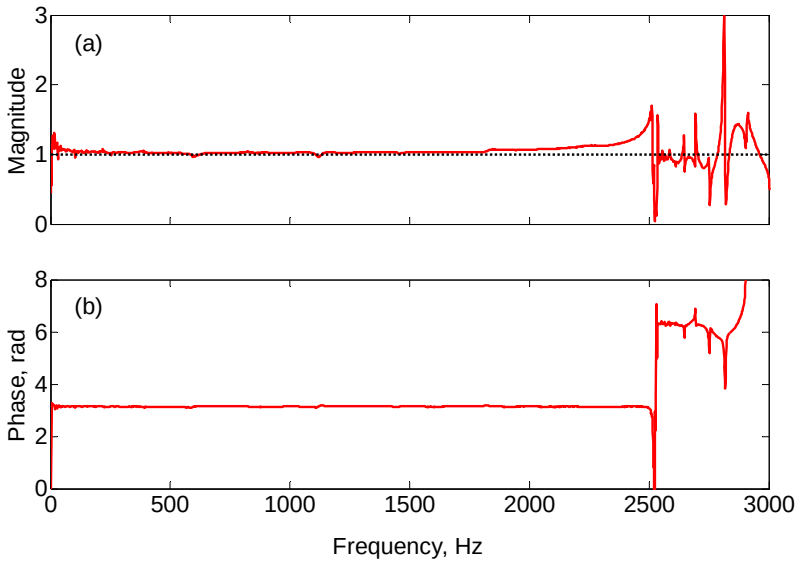

Figure 5.17 Measured transmissibility, a_2/a_1 between the two accelerometers shown in Figure 5.16: (a) Magnitude; (b) Phase.

5.5.3 Wavenumber Measurements

In order to obtain the wave amplitudes and from them the reflection and transmission coefficients, the wavenumbers of the pipes need to be measured. The flexural wavenumber of the pipes was measured over the frequency range of interest by the method described in Chapter 3. A sensor spacing of $\Delta = 0.10\,\text{m}$ was chosen. Figure 5.18

shows the measured real and imaginary parts of the algebraic average of the acceleration ratios, $(a_1 + a_3)/2a_2$ shown in Figure 3.10. The imaginary part is almost equal to zero which means the damping of pipe is very small, therefore the real part is considered to be the value of $(W_1 + W_3)/2W_2$. Figure 5.19 shows the least-squares fit to $\cos k_b\Delta$ in the frequency range 500-2000Hz, which gives $\beta = 0.428$. The errors in β caused by considering it to be a constant are less than 3% in this frequency range.

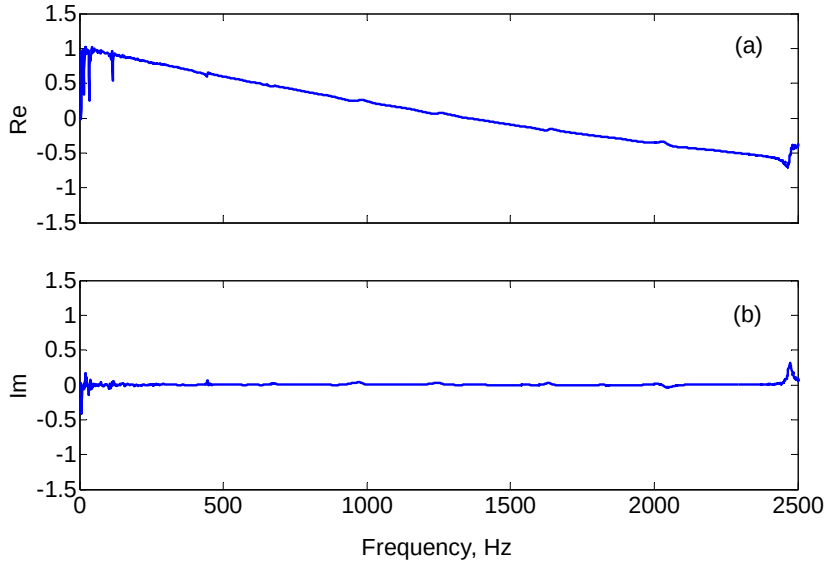

Figure 5.18 Magnitude of $(W_1 + W_3)/2W_2$ for wavenumber measurements of the right-angled pipe: (a) Real part; (b) imaginary part.

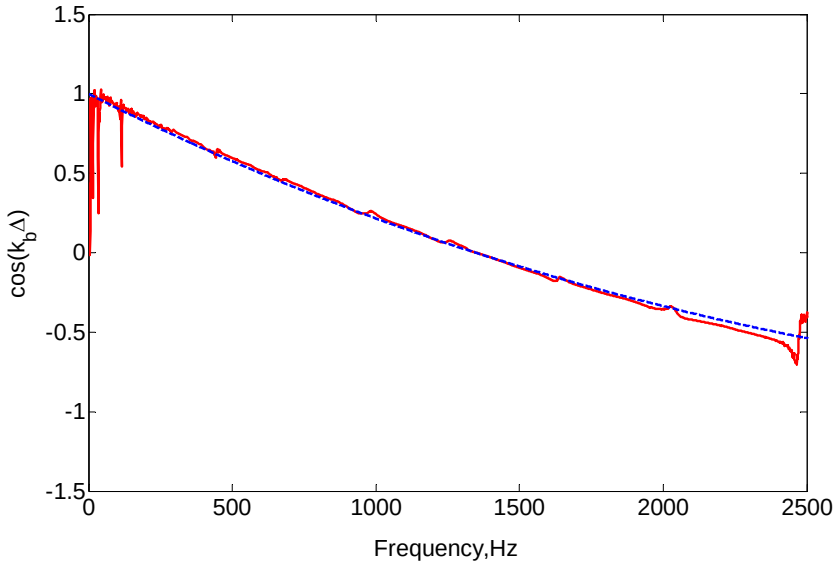

Figure 5.19 $\cos k_b\Delta$ for the pipes: ——, raw data; — —, least-squares fit in 500-2000Hz, $k_b\Delta = \beta\sqrt{f}$ ($\beta = 0.428$).

5.5.4 Measured Reflection and Transmission Coefficients

The measured reflection and transmission coefficients are presented in this section. The axial and flexural wave amplitudes were decomposed independently by the method introduced in Chapter 3. The reflection and transmission coefficients of the right-angled bend were obtained from the decomposed wave amplitudes by application of equation (5.27).

Figure 5.20 shows the method to measure the axial wave motion. The circle is the cross-section of the pipe. One lateral side of the transducer was attached to the pipes to measure the axial motion. Here it is assumed that the difference between the axial motions of the top and bottom of the cross-section is negligible.

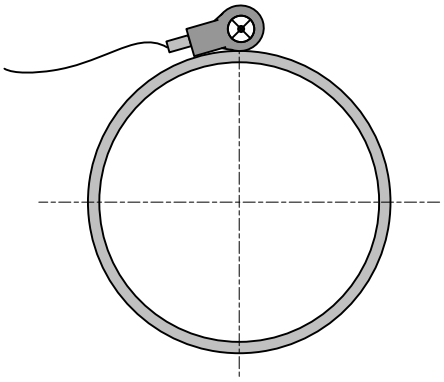

Figure 5.20 Measurement method of the axial wave motion.

Figure 5.21 shows the magnitudes of the outgoing and returning flexural waves in each pipe with in-plane flexural excitation. There are clear resonances below 500Hz. Above this frequency, the differences between the magnitudes of the individual waves in the pipes is very clear: the incident wave is always of the largest magnitude and the amplitude of the end-reflected wave becomes consistently small compared to the amplitudes of the other three waves. However, even with the sandbox, the end-reflection is still not insignificant. This means the end is not anechoic.

Figure 5.22 depicts the magnitudes of the outgoing and returning axial waves in each pipe with flexural excitation. Above 500Hz it is apparent that the waves transmitted

through the bend have the largest magnitudes. There are two large peaks at frequencies 1300Hz and 1800Hz which correspond to the two minima in the magnitudes of the reflected flexural waves in Figure 5.21. At these two frequencies, the energy is mostly converted to the transmitted axial waves. The pipe ends are also not perfectly anechoic for axial waves since the magnitudes of the end-reflected axial waves are not insignificant.

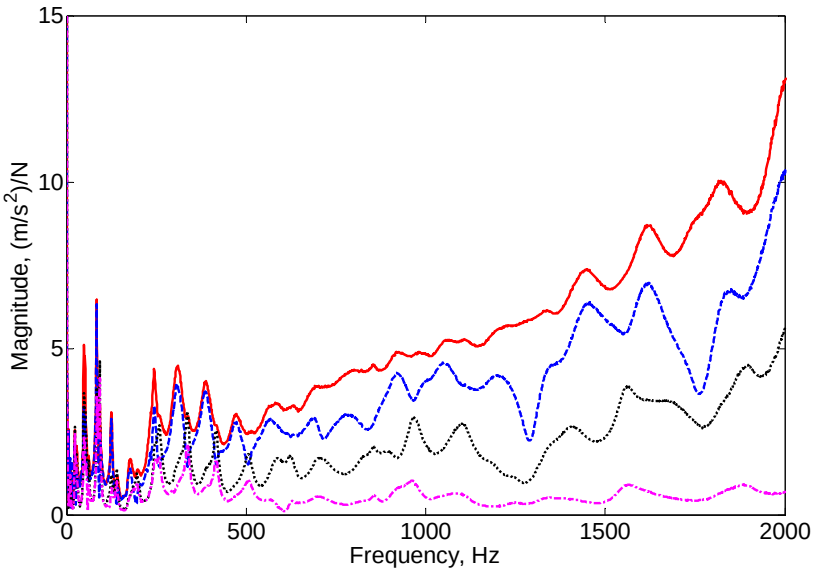

Figure 5.21 Flexural wave amplitudes in each pipe: flexural excitation: ——, incident wave in pipe a; – – – –, reflected wave in pipe a; ·····, transmitted wave in pipe b; –·–·–, end-reflected wave in pipe b.

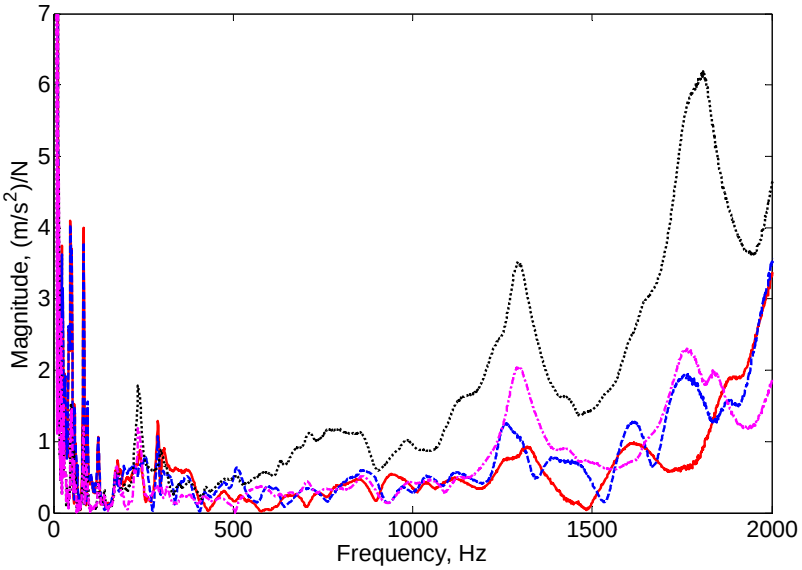

Figure 5.22 Axial wave amplitudes in each pipe: flexural excitation: ——, end-reflected wave in pipe a; – – – –, reflected wave in pipe a; ·····, transmitted wave in pipe b; –·–·–, end-reflected wave in pipe b.

Figure 5.23 shows the power reflection and transmission coefficients of the right-angled bend under the assumption of axially non-reflecting boundaries only and flexurally non-reflecting boundaries only. The reflection and transmission coefficients in these two cases are compared to those of the fully non-reflecting boundary assumption. When the

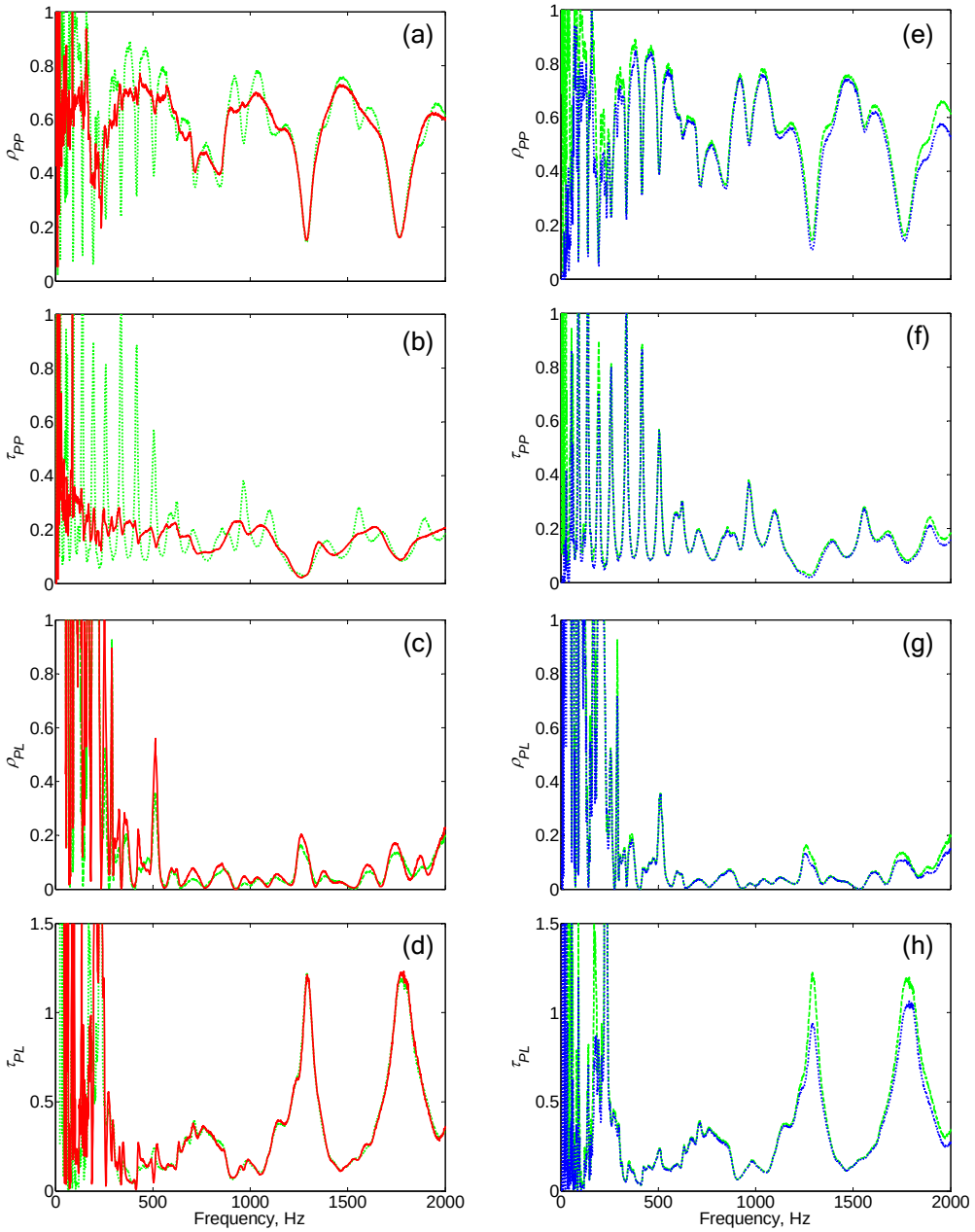

Figure 5.23 Power reflection and transmission coefficients of the pipe bend: - - - -, assuming all boundaries are anechoic; (a),(b),(c) and (d), ——, assuming boundaries are anechoic only for axial waves; (e),(f),(g) and (h), ·····, assuming boundaries are anechoic only for flexural waves.

reflections of the flexural waves from end of pipe *b* (the solid lines in (a) to (d)) only are considered, the rapid oscillations are smoothed dramatically. This means that the reflections of flexural waves from the pipe end are significant. When the reflections of the axial waves from both pipe ends (the dotted lines in (e) to (h)) only are considered, only the two large peaks in frequency range 1000-2000Hz are refined. It can be concluded that the rapid oscillations are caused by neglecting the reflections of the flexural waves from the pipe end and the slow oscillations arise from the assumption of axially non-reflecting boundaries only. It also should be noted that only considering the end reflections of one wave mode does not lessen the oscillations of power coefficients associated with the other wave mode. For example, the oscillations of Figure 5.27(c) are enlarged rather than reduced.

Figures 5.24 to 5.27 show the power reflection and transmission coefficients estimated based on the assumptions of non-reflecting and reflecting boundaries of the pipes. The results from the assumption of non-reflecting pipe ends appear very oscillatory. These oscillations result from the reflections from the pipe ends. This is shown in Figure 5.23. The oscillations can be reduced effectively under the reflecting boundary assumption, especially at high frequencies. This is shown by the solid lines in Figures 5.24 to 5.27. However, the slow oscillations have not been removed totally, i.e. the reflections of axial waves from the pipe ends still have a large influence. A frequency averaging method [63] was adopted to deal with this problem. For each of the power coefficients, the averaging was performed based on a frequency range over which an axial wave has travelled twice the length of one pipe. Since the axial waves are non-dispersive, the averaging bandwidth is then frequency-invariant and it can be calculated based on the wave speed of the axial waves or obtained from Figures 5.24 and 5.27 in which the frequency difference between the two large valleys/peaks can be considered approximately as the averaging bandwidth. Here it is about 480Hz.

In Chapter 7 the parameters of the bend model will be identified from the measured power reflection and transmission coefficients, and then the power reflection and transmission coefficients will be calculated based on the estimated parameters and compared with the measured counterparts. In the limited frequency range considered, the frequency averaged power reflection and transmission coefficients do not change much, which may cause bad conditioning in the parameter identification process.

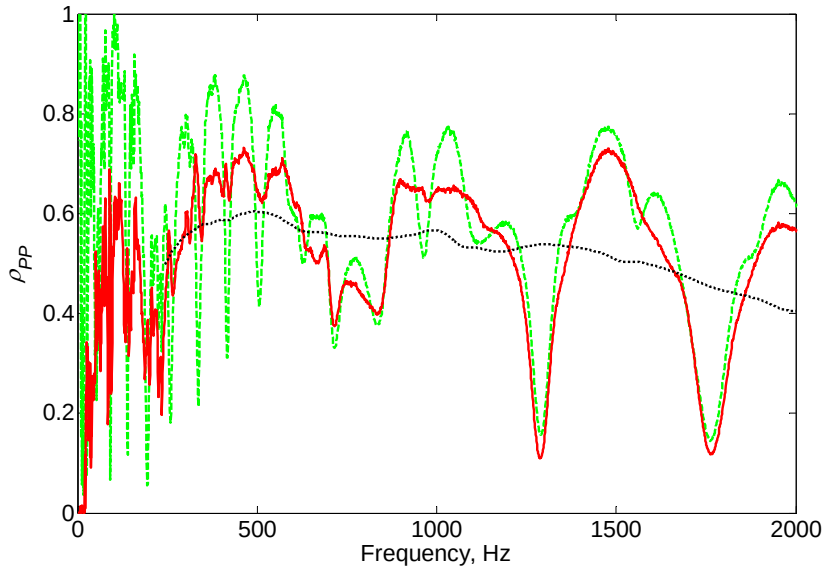

Figure 5.24 Power reflection coefficient ρ_{PP} of the pipe bend: - - - -, non-reflecting boundary assumption; ——, reflecting boundary assumption; ·····, frequency averaged.

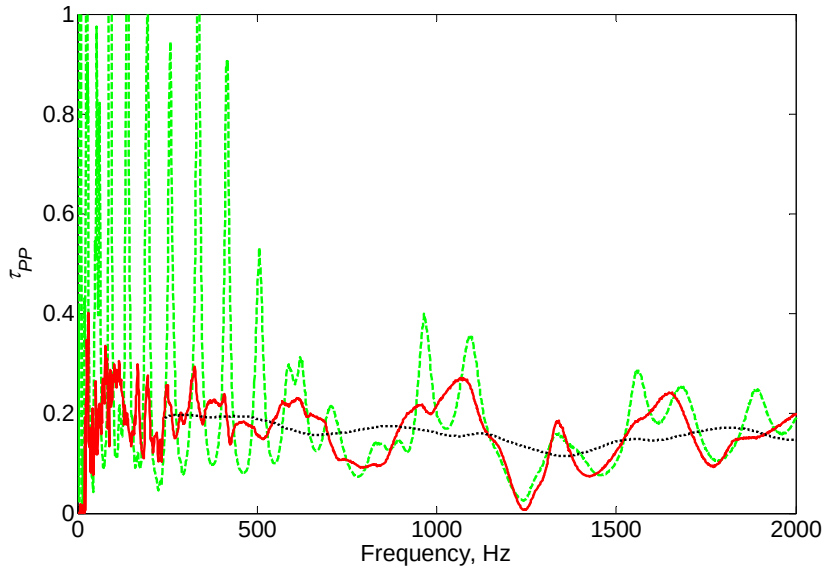

Figure 5.25 Power transmission coefficient τ_{PP} of the pipe bend: - - - -, non-reflecting boundary assumption; ——, reflecting boundary assumption; ·····, frequency averaged.

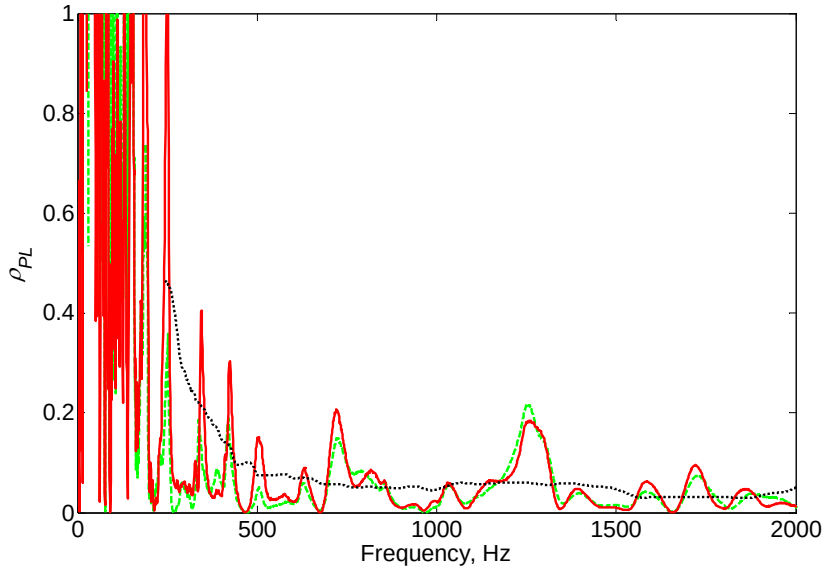

Figure 5.26 Power reflection coefficient ρ_{PL} of the pipe bend: - - - -, non-reflecting boundary assumption; ——, reflecting boundary assumption; ·····, frequency averaged.

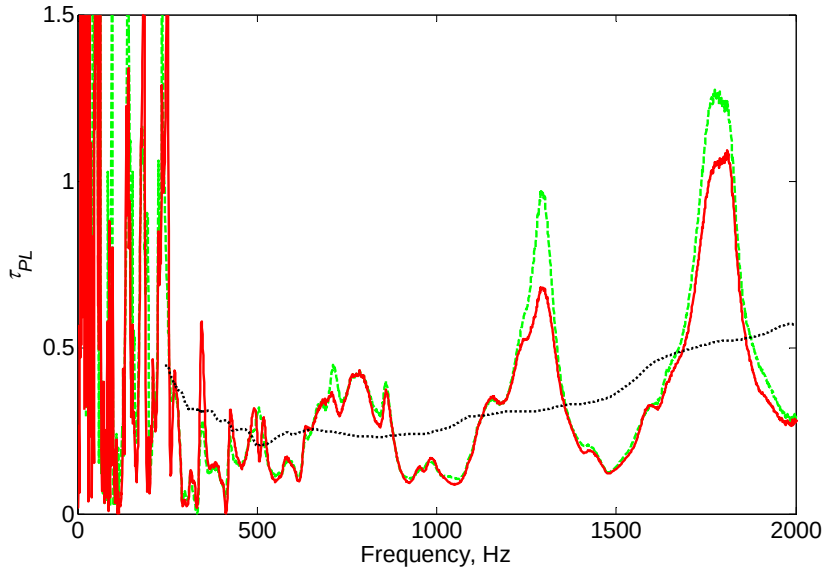

Figure 5.27 Power transmission coefficient τ_{PL} of the pipe bend: - - - -, non-reflecting boundary assumption; ——, reflecting boundary assumption; ·····, frequency averaged.

The sum of the four power reflection and transmission coefficients based on the assumptions of anechoic and echoic boundaries is shown in Figure 5.28. None of the calculations consider damping effects in the structure. In the frequency range of 500-2000Hz, the sum of the frequency averaged reflection and transmission coefficients is close to unity, as expected. Therefore the damping for this case is negligible.

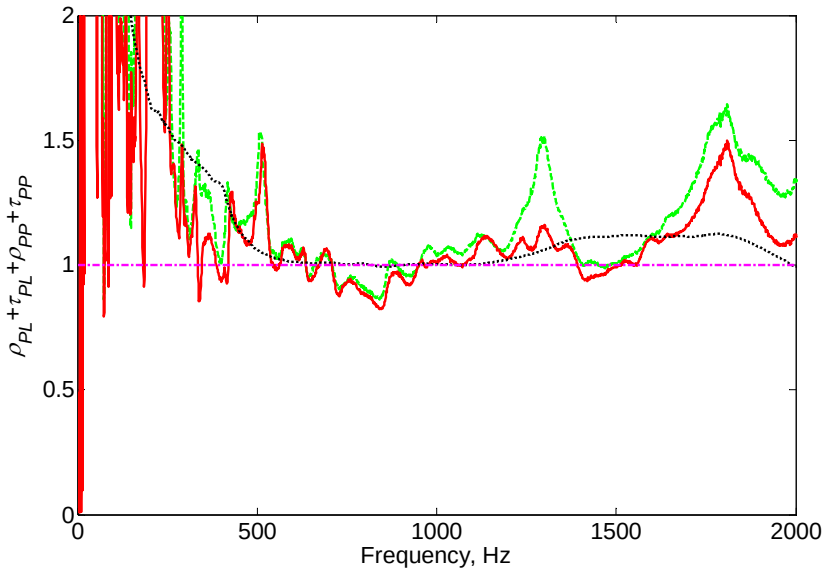

Figure 5.28 Sum of the power reflection and transmission coefficients of the pipe bend: - - - -, anechoic boundary assumption; ——, echoic boundary assumption; ·····, frequency averaged.

5.6 Summary

An arbitrary angled bend connecting two *in-vacuo* pipes was considered to have mass, moment of inertia, and translational and rotational stiffnesses. The general approach introduced in Chapter 2 was employed to derive the reflection and transmission coefficients of the 'mass-spring-mass' model of the arbitrary angled bend. When considering an incident flexural wave in the plane of the bend in one pipe, closed form solutions were given for a massless rigidly connected joint, a mass-like joint and a spring-like joint. The power reflection and transmission coefficients were investigated.

For a rigid massless connection, the power involved in axial waves is much smaller than that in the flexural waves at low frequencies. With increasing frequency, more power is converted from flexural waves to axial waves. The power associated with the axial waves is mainly in the second waveguide. This results from the incident wave being an in-plane flexural wave.

The behaviour of the power reflection and transmission coefficients of the mass-like and spring-like joints can be easily interpreted from the point view of impedance ratios. For

the mass-like joint, at the regions where $\xi^3 \vartheta = 2$, the power reflection and transmission coefficients reach their local extrema. Large mass of the bend can impede wave mode conversion effectively. Large moment of inertia of the joint can prevent rotational motion of the bend, and therefore, restrain the energy in the flexural incident waves from transferring to flexural waves in the second waveguide. For the spring-like joint, the extent of the energy transferred from the incident flexural waves to other waves, as expected, increases with the stiffnesses of the bend. Around the regions where $\chi / \xi^3 = 1$, wave mode conversion is the most dramatic.

For the damping model considered, the effect of the translational and rotational damping of the bend is related to the sensitivity of the power reflection and transmission coefficients to the corresponding stiffnesses. The damping of the pipes measured was considered to be negligible.

For the experiments on the right-angled pipe bend, although sandboxes and sandwich panels were applied for the purpose of removing the wave reflections from the pipe ends, their effect is imperfect. Significant flexural, and especially axial waves were still found to be reflected from the pipe ends. This causes large oscillations in the estimated power reflection and transmission coefficients based on the anechoic boundary assumption. The reflections of flexural waves from the pipe ends are responsible for the rapid oscillations with frequency of the power coefficients and the reflections of the axial waves from pipe ends for the slow oscillations with large amplitude. Including the reflection from the ends in the calculations can reduce the rapid oscillations effectively. The slow oscillations are smoothed by using a frequency averaging method. In the limited frequency range considered, the power reflection and transmission coefficients change only slightly, which may cause bad conditioning for parameter identification process. This will be discussed in Chapter 7.

Chapter 6 Parameter Identification

6.1 Introduction

Waveguides, such as piping systems, comprise joints in the form of flanges, hangers, bolts, valves, pumps and changes in section. These joints contribute to inertia, stiffness and damping and can dramatically alter the dynamic response of the whole system. In many cases these properties are poorly known. A good estimate of the properties of the joints would not only help to predict the dynamic response, but also benefit controlling the vibration level of the waveguides by designing and modifying the joint structures. This chapter discusses approaches by which a parametric joint model is updated from measured wave reflection and transmission coefficients. The experimental implementation of the iterative approach is described in Chapter 7 using the models discussed in Chapters 2, 4 and 5.

A theoretical model for a structure can be updated by experimental measurements. This procedure includes two main steps: the first is to determine an appropriate parametric model for the structure; the second is to estimate the corresponding parameters of the model by experimental observation. Chapters 2, 4 and 5 have developed models for discontinuities in waveguides and derived the reflection and transmission coefficients in terms of the parameters of the discontinuities. Chapter 3 discussed a method to measure the wave amplitude reflection and transmission coefficients. In this chapter, the generic problem concerning parametric joint identification is introduced first. Then approaches concerning the estimation of the joint parameters from measured wave reflection and transmission coefficients are studied. Attention is focused on the Gauss-Newton method in which an objective function is defined that quantifies the discrepancy between measured and predicted reflection and transmission coefficients. Minimisation of this objective function is a non-linear optimisation problem that yields estimates for the parameters of the discontinuities. Problems concerning the choice of the initial values of

the parameters, criteria for terminating the iteration and evaluation of the accuracy of the estimates are also discussed.

6.2 Generic Problem

This section introduces the generic problem concerning joint parameter identification. A joint is usually used to connect two or more substructures. Some typical examples have been shown in Figure 5.1. An example case of coplanar substructures connected by a joint is given in Figure 6.1. When an external excitation is applied to a branch, for example, substructure a, response will arise not only in substructure a itself, but also in b and c through the joint. From the viewpoint of wave propagation in structures, the excitation in waveguide a gives rise to structural waves incident upon the joint, which may be composed of several wave modes, such as longitudinal, flexural, torsional, etc. At the joint the incident waves are partly transmitted to waveguides b and c, and partly reflected to waveguide a as well. If there are more excitations in the system, or if the reflections from ends of the waveguides are considered, more reflected waves and transmitted waves will be generated. Here the properties of the joint play a crucial role. They determine the response of the whole system.

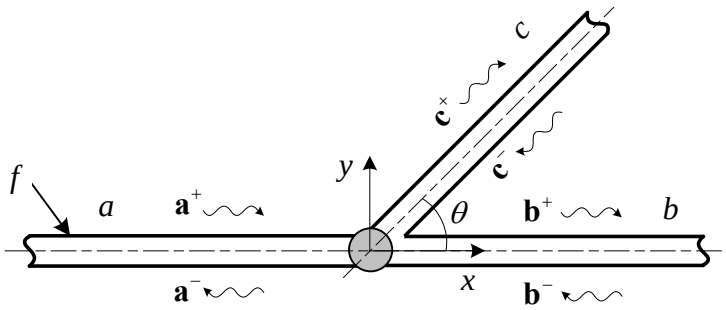

Figure 6.1 Joint with three coplanar waveguides.

The objective is now to investigate the dynamic characteristics of the joint, model it and try to estimate its parameters, such as the inertia, stiffness and damping, from measurements of the responses in waveguides a, b and c. Here the wave amplitude reflection and transmission coefficients of the joint are chosen to be a measure of the dynamic characteristics of the system. The reason is that the reflection and transmission

coefficients depend on the properties of the waveguide and joint. Correspondingly, the scattering coefficients thus can reveal the characteristics of the waveguide and joint. Some parametric models which relate the reflection and transmission coefficients to the properties of the joint have been developed in Chapters 2, 4 and 5. Chapter 3 discussed a method by which the reflection and transmission coefficients corresponding to each wave mode can be estimated from wave amplitude measurements. Now the problem is how to estimate the parameters of the joint model from the measured reflection and transmission coefficients. Questions such as which coefficient or coefficients (reflection or transmission) is to be used, and in which frequency range the measured data is to be chosen to update the parameters will be investigated.

Basically two methods may be employed to estimate the parameters of the joint in this stage:

1) **Direct method**. If the parameters of the joint can be explicitly expressed as functions of the reflection and transmission coefficients, substituting the measured reflection and transmission coefficients into the corresponding expressions gives the parameters directly. This method is simple, but in most cases either such expressions do not exist or the expressions suffer from high sensitivity to measurement errors. Under such situations this method cannot help.

2) **Iterative method**. It is quite usual that differences are found between the measured data and analytical model. An objective function is usually defined as the sum of the squares of the differences between the measured and estimated data. The unknown parameters can be updated by minimising this objective function step by step through an iterative algorithm. If the change in the parameters between successive iterations decreases rapidly enough, then the solution will converge. As far as this thesis is concerned, the objective function will be defined in terms of the power reflection and/or transmission coefficients of the discontinuities.

Both of these methods require an appropriate parametric model of the joint. The second method, the iterative method, is widely used in parameter estimation. The following section introduces these two methods in detail.

6.3 Parameter Estimation Methods

Joint identification, in the sense of parameter estimation, can be considered as an optimisation problem in which the objective is to improve the correlation (determined by an objective function) between the measured and predicted responses by making parametric changes to the analytical model. This often presents a least-squares problem. Many mathematical methods have been applied to such a problem, especially iterative methods [69, 70]. In this section, both the direct method and iterative method concerning parameter identification are introduced.

6.3.1 Direct Method

In some cases, the parameters of the joint model can be expressed in a simple way as

$$\mathbf{AX} = \mathbf{b} \tag{6.1}$$

where q-vector $\mathbf{X}$ represents the unknown parameters, $n \times q$ matrix $\mathbf{A}$ and $n \times 1$ vector $\mathbf{b}$ involve wave reflection and transmission coefficients. Assuming that matrix $\mathbf{A}$ is invertible, the parameters can be estimated by

$$\mathbf{X} = \mathbf{A}^{-1}\mathbf{b}\,. \tag{6.2}$$

Generally, for a given joint model, $\mathbf{A}$ may be singular or nearly singular at some frequencies. In this case, for an overdetermined problem ($n > q$), i.e. the reflection and transmission coefficients are measured at more frequencies than the number of the parameters, the inverse can be defined such that $\|\mathbf{AX} - \mathbf{b}\|$ can be minimised in the least-squares sense in which is

$$\mathbf{A}^{+} = \left(\mathbf{A}^{\mathrm{H}}\mathbf{A}\right)^{-1}\mathbf{A}^{\mathrm{H}}, \tag{6.3}$$

where the superscript H indicates the complex conjugate transpose (the Hermitian). Overdetermining the set of equations can reduce the sensitivity to noise, sensor miscalibration and other measurement errors. However, if the errors are too large, this method is still prone to fail. On the other hand, it is not always possible to find such an explicit expression as equation (6.1).

6.3.2 Iterative Method

If the direct method fails or is not applicable, an iterative algorithm can be used. In this section the nonlinear least-squares problem, usually encountered in parameter identification, is introduced and then an iterative method to solve this kind of problem is reviewed.

6.3.2.1 Nonlinear Least-squares Problem

The general nonlinear least-squares problem is introduced here. In data fitting or parameter identification problems, the objective function is usually defined as the sum of squares of the difference between the measured and predicted outputs, which can be written in the form

$$F(\mathbf{X}) = \frac{1}{2}\mathbf{R}(\mathbf{X})^{\mathrm{T}}\mathbf{R}(\mathbf{X}) \tag{6.4}$$

where the q-vector $\mathbf{X} = \begin{pmatrix} X_1 & X_2 & \cdots & X_q \end{pmatrix}$ represents the unknown parameters to be updated. The n-vector $\mathbf{R}(\mathbf{X}) = \begin{pmatrix} R_1 & R_2 & \cdots & R_n \end{pmatrix}$ is called the residual at $\mathbf{X}$ and can be defined as

$$\mathbf{R}(\mathbf{X}) = \mathbf{Y}_m(\mathbf{X}) - \mathbf{Y}(\mathbf{X}) \tag{6.5}$$

where $\mathbf{Y}_m(\mathbf{X})$ indicates the measured response and $\mathbf{Y}(\mathbf{X})$ represents the predicted output from the theoretical model based on parameters $\mathbf{X}$. For the problem considered in this thesis, $\mathbf{Y}_m(\mathbf{X})$ is the measured reflection and/or transmission coefficient(s) at a number of frequencies and $\mathbf{Y}(\mathbf{X})$ is the predicted counterpart from the parametric joint model. Since the number of frequencies is typically much larger than the number of unknown parameters, the problem here is overdetermined. If the residual $\mathbf{R}(\mathbf{X})$ is a nonlinear function of parameters $\mathbf{X}$, iterative procedures are usually required.

6.3.2.2 Gauss-Newton Method

Many iterative algorithms have been developed for parameter optimisation problems [69, 70]. In this section, the Gauss-Newton method is reviewed. It is an iterative method and requires the calculation of the Jacobean matrix of the objective function.

The Gauss-Newton solution to minimising the objective function in equation (6.4) can be expressed as (see references [69, 70] for detailed procedure)

$$\Delta \mathbf{X}_j = -\left(\mathbf{S}_j^{\mathrm{T}}\mathbf{S}_j\right)^{-1}\mathbf{S}_j^{\mathrm{T}}\mathbf{R}_j \tag{6.6}$$

where $\Delta X_j = X_{j+1} - X_j$, so

$$\mathbf{X}_{j+1} = \mathbf{X}_j - \left(\mathbf{S}_j^{\mathrm{T}}\mathbf{S}_j\right)^{-1}\mathbf{S}_j^{\mathrm{T}}\mathbf{R}_j \tag{6.7}$$

where the subscript j indicates the jth iteration, $\mathbf{X}_{j+1}$ and $\mathbf{X}_j$ are the estimates of the parameters after j+1 and j iterations respectively, $\mathbf{R}_j = \mathbf{Y}_m - \mathbf{Y}_j$, $\mathbf{Y}_j$ is the jth predicted output from the parametric model. $\mathbf{S}_j$ is the Jacobean matrix of $\mathbf{R}_j$ and is defined by

$$\mathbf{S}_j = \begin{bmatrix} \frac{\partial R_1}{\partial X_1} & \frac{\partial R_1}{\partial X_2} & \cdots & \frac{\partial R_1}{\partial X_q} \\ \frac{\partial R_2}{\partial X_1} & \frac{\partial R_2}{\partial X_2} & \cdots & \frac{\partial R_2}{\partial X_q} \\ \vdots & \vdots & \ddots & \vdots \\ \frac{\partial R_n}{\partial X_1} & \frac{\partial R_n}{\partial X_2} & \cdots & \frac{\partial R_n}{\partial X_q} \end{bmatrix}_j . \tag{6.8}$$

Thus the updated parameters may be obtained iteratively from equation (6.6). This approach assumes that each component of the measured data, $\mathbf{Y}_m$ has equal weight. However, in a typical measurement, the responses may have been measured to different accuracy levels or be of different orders of magnitude or different units. In this case, a weighting matrix can be incorporated into the updating algorithm. The objective function then becomes

$$F(\mathbf{X}) = \frac{1}{2}\mathbf{R}(\mathbf{X})^{\mathrm{T}}\mathbf{W}_{RR}\mathbf{R}(\mathbf{X}) \tag{6.9}$$

where the weighting matrix, $\mathbf{W}_{RR}$ is positive definite and usually diagonal. Its elements may be given by, for example, the reciprocals of the variances of the corresponding measurements [6]. The Gauss-Newton method minimising this objective function gives the updated parameters as

$$\mathbf{X}_{j+1} = \mathbf{X}_j - \left(\mathbf{S}_j^{\mathrm{T}}\mathbf{W}_{RR}\mathbf{S}_j\right)^{-1}\mathbf{S}_j^{\mathrm{T}}\mathbf{W}_{RR}\mathbf{R}_j . \tag{6.10}$$

An assumption in equation (6.6) and (6.10) is that $\mathbf{S}_j^{\mathrm{T}}\mathbf{S}_j$ or $\mathbf{S}_j^{\mathrm{T}}\mathbf{W}_{RR}\mathbf{S}_j$ is nonsingular. If matrix $\mathbf{S}_j^{\mathrm{T}}\mathbf{S}_j$ or $\mathbf{S}_j^{\mathrm{T}}\mathbf{W}_{RR}\mathbf{S}_j$ has full rank, the equations may be solved. If they are ill-conditioned or nearly rank-deficient, which may result from incorrectly scaled

parameters, for example, one of the parameters may have little influence on the measurements, or combinations of parameters having similar effects, it is wise to reconsider the choice of parametric model or objective function.

If the model used in data fitting or parameter optimisation is good, $F(\mathbf{X})$ is expected to be small and the minimising process is called a small residual problem. Otherwise one has a large residual problem.

For overdetermined small residual problems with accurate initial data, convergence of the Gauss-Newton method can be expected to be fast. But the method may not converge at all for large residual problems and/or initial data far from the solution [69]. There may be several local minima in a given range, but the global minimum is usually the desired solution. Estimating the initial parameter values prior to iteration is of great importance since an inaccurate choice may lead to a local rather than the global minimum, or even divergence of iteration.

6.4 Application of Parameter Estimation Methods to Joints

Parameter identification of some specific joints from simulated wave reflection and transmission coefficients measurements is investigated in this section. For example, consider a case of a mass-like discontinuity in a straight waveguide, shown in Figure 6.2. The discontinuity is characterised by a mass, m and a moment of inertia, J. The objective is to estimate the joint parameters, m and J from simulated reflection and transmission coefficients measurements for which the true parameter values are known. The parameter identification procedure is shown in Figure 6.3, and includes the following steps:

1) Set up the joint model and assume some initial joint parameter values;
2) Evaluate the reflection and transmission coefficients in terms of the parameters of the discontinuity;
3) Evaluate the displacements (FRFs) at ‘sensor locations’ assumed for simulations for given input;
4) Add noise to the simulated sensor displacements;

5) Estimate wave amplitudes from noisy simulated sensor displacement measurements;
6) Estimate reflection and transmission coefficients from wave amplitudes obtained at step 5;
7) Estimate joint parameters from reflection and transmission coefficients obtained in steps 2 and 6 (for direct method, data from step 6 only are used);
8) Compare updated joint parameters with assumed values at step 1, and compare reflection and transmission coefficients from updated model with simulated measurements.

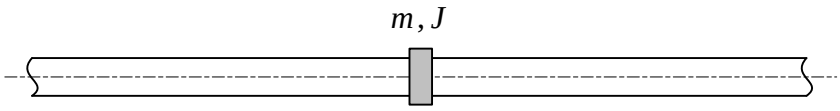

Figure 6.2 A mass-like discontinuity attached to a uniform beam.

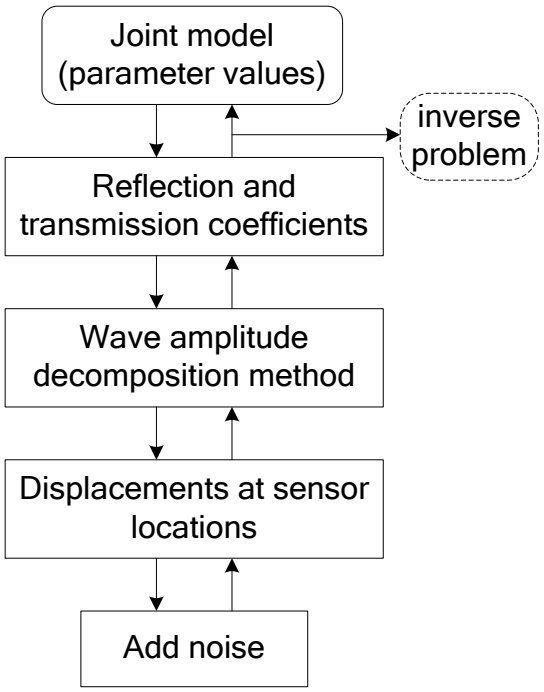

Figure 6.3 Flow chart of joint parameter identification based on simulated response data.

In short, these steps can be merged into two basic processes: one is to generate a simulated data set. This is a forward problem, including steps 1-6. The other, the inverse problem, is to identify joint parameters from the simulated data, step 7 and evaluate the accuracy of the applied approach, step 8. When using practical experimental data to estimate the joint parameters, measured rather than simulated reflection and

transmission coefficients will be employed in the process. This will be discussed in Chapter 7.

Apart from these conventional methods, some particular methods may also be very useful for some special cases. These involve identifying certain frequencies, for example, such as the frequency at which $\vartheta\xi^3 = 2$ occurs in the mass-like right-angled joint and the frequency at which $\chi / \xi^3 = 1$ occurs in the spring-like right-angled joint discussed in Chapter 5. If such a point can be found, the corresponding parameter can be estimated directly. The other parameter (or parameters) can be estimated by the conventional methods, and it will be easier since the number of the parameters to be identified has been reduced.

6.4.1 Direct Method for a Mass-like Discontinuity

Consider flexural wave propagation in an infinite waveguide to which a mass-like discontinuity is attached at $x = 0$ as shown in Figure 6.2. The expressions for the direct method can be derived easily from equation (2.50) as

$$\left[\left(i + r_{PP} + t_{PP}\right)\xi\right]\mu = 2\left(i-1\right)\left(-1 + r_{PP} + t_{PP}\right) \tag{6.11}$$

and

$$\left[\left(i + r_{PP} - t_{PP}\right)\xi^3\right]\vartheta = 2(1-i)\left(1 + r_{PP} - t_{PP}\right) \tag{6.12}$$

where parameters μ and ϑ are the non-dimensional mass and moment of inertia respectively given by equation (2.51). They are the joint parameters to be estimated.

Equations (6.11) and (6.12) are scalar equations and independent of each other. The mass, μ and moment of inertia, ϑ can be estimated from these two equations based on the reflection and transmission coefficients respectively at a single frequency. The results obtained in this way can be highly affected by noise. By considering n frequencies, each equation can be stacked to form a matrix equation in the form of $\mathbf{A}X = \mathbf{b}$, where $\mathbf{A}$ and $\mathbf{b}$ are $n \times 1$ vectors and X is a scalar. Then the parameters can be estimated in a least-squares sense by equation (6.3). This may reduce the effect of noise on data from a single frequency. However, simulations have been performed and results (not presented here) indicate that $\mathbf{A}$ and $\mathbf{b}$ are very sensitive to the phase errors

of the 'measured' reflection and transmission coefficients. This can be explained by inspection of equation (3.12), where the terms involving $k_b a$ and/or $k_b b$ influence the phases of estimated reflection and transmission coefficients. Terms $k_b a$ and $k_b b$ can typically be very large so that the errors in the phases of the reflection and transmission coefficients also become very large, especially at high frequencies. The joint parameters estimated from these reflection and transmission coefficients contaminated by large phase errors are also dramatically affected. Therefore, this direct method, from this point of view, does not give accurate results.

For a spring-like discontinuity in a straight waveguide, similar expressions to equations (6.11) and (6.12) can also be obtained. For more complicated joint models, such as joints in a right-angled bends, it is difficult or impossible to find such explicit expressions for the joint parameters.

6.4.2 Iterative Method for a Mass-like Discontinuity

Since the phases of reflection and transmission coefficients are very sensitive to measurement errors, a method which uses only the moduli of the coefficients is applied to the same case discussed in the above section. For convenience, the squared moduli of the reflection or transmission coefficient, i.e. the power reflection coefficient, $\rho = \left|r_{PP}\right|^2$ or power transmission coefficient, $\tau = \left|t_{PP}\right|^2$ is adopted.

The power reflection coefficient for the joint shown in Figure 6.2 can be derived from equation (2.52) as

$$\rho = \frac{\left[\left(\mu\xi\right)\left(\vartheta\xi^3\right) - 2\mu\xi + 2\vartheta\xi^3\right]^2}{\left(\mu^2\xi^2 + 4\mu\xi + 8\right)\left(\vartheta^2\xi^6 - 4\vartheta\xi^3 + 8\right)} \tag{6.13}$$

where μ and ϑ are the non-dimensional mass and moment of inertia respectively. The residual $\mathbf{R}_j$ in equation (6.6) is defined as

$$\mathbf{R}_j = \boldsymbol{\rho}_m - \boldsymbol{\rho}_j \,. \tag{6.14}$$

In the above expression, $\boldsymbol{\rho}_m = \left(\rho_{m1} \quad \rho_{m2} \quad \cdots \quad \rho_{mn}\right)^{\mathrm{T}}$ where ρ_{mi}, $i = 1, 2, \cdots, n$, is the 'measured' power reflection coefficient at the ith frequency and

$\boldsymbol{\rho}_j = \begin{pmatrix} \rho_{j1} & \rho_{j2} & \cdots & \rho_{jn} \end{pmatrix}^{\mathrm{T}}$ is the analytical counterpart at the *j*th iteration. The *i*th component of $\boldsymbol{\rho}_j$ is given by

$$\rho_{ji} = \frac{\left[\left(\mu_j \xi_i\right)\left(\vartheta_j \xi_i^3\right) - 2\mu_j \xi_i + 2\vartheta_j \xi_i^3\right]^2}{\left(\mu_j^2 \xi_i^2 + 4\mu_j \xi_i + 8\right)\left(\vartheta_j^2 \xi_i^6 - 4\vartheta_j \xi_i^3 + 8\right)}. \tag{6.15}$$

The Jacobean matrix $\mathbf{S}(\mathbf{X})$ at $\mathbf{X}_j$ is

$$\mathbf{S}_j = -\begin{bmatrix} \dfrac{\partial \rho_{j1}}{\partial \mu} & \dfrac{\partial \rho_{j2}}{\partial \mu} & \cdots & \dfrac{\partial \rho_{jn}}{\partial \mu} \\ \dfrac{\partial \rho_{j1}}{\partial \vartheta} & \dfrac{\partial \rho_{j2}}{\partial \vartheta} & \cdots & \dfrac{\partial \rho_{jn}}{\partial \vartheta} \end{bmatrix}^{\mathrm{T}} \tag{6.16}$$

where, by differentiating equation (6.13)

$$\begin{aligned} \frac{\partial \rho_{ji}}{\partial \mu} &= \frac{8\xi_i \left[\left(\mu_j \xi_i\right)\left(\vartheta_j \xi_i^3\right) - 2\mu_j \xi_i + 2\vartheta_j \xi_i^3\right]\left(\vartheta_j \xi_i^3 - \mu_j \xi_i - 4\right)}{\left(\mu_j^2 \xi_i^2 + 4\mu_j \xi_i + 8\right)^2 \left(\vartheta_j^2 \xi_i^6 - 4\vartheta_j \xi_i^3 + 8\right)}, \\ \frac{\partial \rho_{ji}}{\partial \vartheta} &= -\frac{8\xi_i^3 \left[\left(\mu_j \xi_i\right)\left(\vartheta_j \xi_i^3\right) - 2\mu_j \xi_i + 2\vartheta_j \xi_i^3\right]\left(\vartheta_j \xi_i^3 - \mu_j \xi_i - 4\right)}{\left(\mu_j^2 \xi_i^2 + 4\mu_j \xi_i + 8\right)\left(\vartheta_j^2 \xi_i^6 - 4\vartheta_j \xi_i^3 + 8\right)^2}. \end{aligned} \tag{6.17}$$

It should be noted that the non-dimensional mass, μ and moment of inertia, ϑ have different orders of magnitudes and so do the two derivatives in equation (6.17).

If the objective function is insensitive to one or more parameters in a given frequency range, a reasonable value(s) can be assumed for the parameter(s) and only the other parameter(s) is updated. This will simplify the identification process dramatically in some circumstances since the more parameters there are to be updated usually makes the convergence of the iteration method slower and less reliable.

The flow chart for the Gauss-Newton iteration procedure for the mass-like discontinuity on a beam is shown in Figure 6.4.

When using the power transmission coefficient, $\tau = \left|t_{PP}\right|^2$ to update the parameters of the joint, similar expressions can be derived. If there is no energy dissipated, ρ and τ are related by

$$\rho + \tau = 1. \tag{6.18}$$

Therefore

$$\frac{\partial \tau}{\partial \mu} = -\frac{\partial \rho}{\partial \mu} \text{ and } \frac{\partial \tau}{\partial \vartheta} = -\frac{\partial \rho}{\partial \vartheta}. \tag{6.19}$$

The Jacobean matrix is thus the negative of that of the power reflection coefficient. Of course, $\rho_m + \tau_m \neq 1$ due to measurement errors and damping, and one may be more accurate than the other.

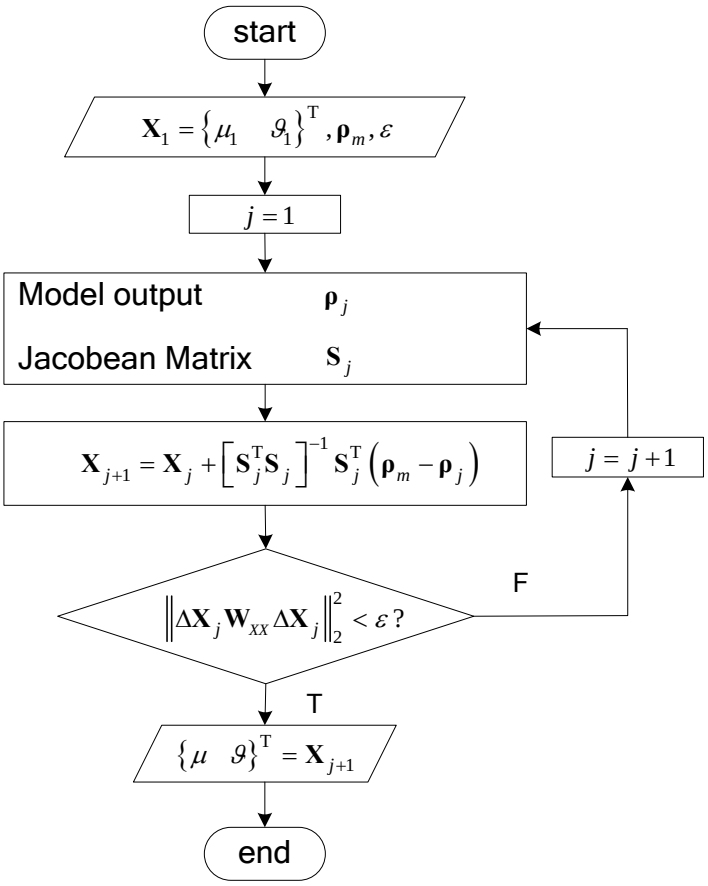

Figure 6.4 Flow chart of Gauss-Newton solution procedure on a simple mass-like discontinuity.

6.4.3 Iterative Method for a Right-angled Joint

In the previous section, the power reflection and transmission coefficients could be expressed explicitly as functions of the joint parameters, as could the objective function. In this section a general method is introduced to obtain the power reflection coefficient or transmission coefficient whether they are expressed explicitly or not.

For the case of the right-angled joint discussed in Chapter 5, Equation (5.16) can be

expressed in the form

$$\mathbf{AC} = \mathbf{b} \tag{6.20}$$

where

$$\mathbf{A} = \begin{bmatrix} -\frac{\mu\xi^2}{2} + i & 0 & 0 & \frac{\mu\xi^2}{2} - i\xi & 0 & \frac{\mu\xi^2}{2} + \xi \\ \frac{\chi}{\xi^2} - \frac{\mu\xi^2}{2} + i & 0 & 0 & \frac{\chi}{\xi^2} & 0 & \frac{\chi}{\xi^2} \\ 0 & -\frac{\mu\xi}{2} + \frac{i}{\xi} & -\frac{\mu\xi}{2} + i & 0 & -\frac{\mu\xi}{2} - 1 & 0 \\ 0 & -\frac{\chi}{\xi^3} & \frac{\chi}{\xi^3} - \frac{\mu\xi}{2} + i & 0 & \frac{\chi}{\xi^3} - \frac{\mu\xi}{2} - 1 & 0 \\ 0 & 0 & -i\frac{\vartheta\xi^3}{2} - 1 & i\frac{\vartheta\xi^3}{2} + 1 & -\frac{\vartheta\xi^3}{2} + 1 & \frac{\vartheta\xi^3}{2} - 1 \\ 0 & 0 & i\frac{\psi}{\xi} - i\frac{\vartheta\xi^3}{2} - 1 & i\frac{\psi}{\xi} & \frac{\psi}{\xi} - \frac{\vartheta\xi^3}{2} + 1 & \frac{\psi}{\xi} \end{bmatrix},$$

$$\mathbf{C} = \begin{Bmatrix} r_{PL} & t_{PL} & r_{PP} & t_{PP} & r_{PN} & t_{PN} \end{Bmatrix}^{\mathrm{T}},$$

$$\mathbf{b} = \begin{Bmatrix} 0 & 0 & \frac{\mu\xi}{2} + i & -\frac{\chi}{\xi^3} + \frac{\mu\xi}{2} + i & -i\frac{\vartheta\xi^3}{2} + 1 & i\frac{\psi}{\xi} - i\frac{\vartheta\xi^3}{2} + 1 \end{Bmatrix}^{\mathrm{T}}.$$

Then the vector of reflection and transmission coefficients can be obtained as

$$\mathbf{C} = \mathbf{A}^{-1}\mathbf{b}. \tag{6.21}$$

If the power reflection coefficient, ρ_{bb} is to be used in the objective function, for example, here a vector $\mathbf{z}$ can be defined as

$$\mathbf{z} = \begin{Bmatrix} 0 & 0 & 1 & 0 & 0 & 0 \end{Bmatrix}^{\mathrm{T}}. \tag{6.22}$$

The vectors for other reflection and transmission coefficients can be deduced by analogy. Then the flexural reflection coefficient is given by

$$r_{PP} = \mathbf{z}^{\mathrm{T}}\mathbf{C}. \tag{6.23}$$

Given the definition of the power reflection coefficient as

$$\rho_{PP} = {r_{PP}}^{\mathrm{H}} r_{PP}, \tag{6.24}$$

substituting Equations (6.21) and (6.23) into (6.24) yields

$$\rho_{PP} = \mathbf{b}^{\mathrm{H}} \left(\mathbf{A}^{-1}\right)^{\mathrm{H}} \mathbf{z}\mathbf{z}^{\mathrm{T}}\mathbf{A}^{-1}\mathbf{b}. \tag{6.25}$$

Correspondingly the derivatives of ρ_{PP} to parameter μ can be obtained by

$$\begin{aligned}\frac{\partial \rho_{PP}}{\partial \mu} = &\frac{\partial \mathbf{b}^{\mathrm{H}}}{\partial \mu}\left(\mathbf{A}^{-1}\right)^{\mathrm{H}}\mathbf{z}\mathbf{z}^{\mathrm{T}}\mathbf{A}^{-1}\mathbf{b} + \mathbf{b}^{\mathrm{H}}\frac{\partial\left(\mathbf{A}^{-1}\right)^{\mathrm{H}}}{\partial \mu}\mathbf{z}\mathbf{z}^{\mathrm{T}}\mathbf{A}^{-1}\mathbf{b} \\ &+\mathbf{b}^{\mathrm{H}}\left(\mathbf{A}^{-1}\right)^{\mathrm{H}}\mathbf{z}\mathbf{z}^{\mathrm{T}}\frac{\partial \mathbf{A}^{-1}}{\partial \mu}\mathbf{b} + \mathbf{b}^{\mathrm{H}}\left(\mathbf{A}^{-1}\right)^{\mathrm{H}}\mathbf{z}\mathbf{z}^{\mathrm{T}}\mathbf{A}^{-1}\frac{\partial \mathbf{b}}{\partial \mu}\end{aligned}. \tag{6.26}$$

See Appendix 10 for the detailed derivation. Other derivatives can be found by analogy. If the four parameters, μ, ϑ, χ and ψ are to be estimated simultaneously, then $\mathbf{X} = \{\mu \quad \vartheta \quad \chi \quad \psi\}^{\mathrm{T}}$. The Jacobean matrix $\mathbf{S}$ at $\mathbf{X}_j$ becomes

$$\mathbf{S}_j = -\begin{bmatrix} \frac{\partial \rho_{PPj1}}{\partial \mu} & \frac{\partial \rho_{PPj1}}{\partial \vartheta} & \frac{\partial \rho_{PPj1}}{\partial \chi} & \frac{\partial \rho_{PPj1}}{\partial \psi} \\ \frac{\partial \rho_{PPj2}}{\partial \mu} & \frac{\partial \rho_{PPj2}}{\partial \vartheta} & \frac{\partial \rho_{PPj2}}{\partial \chi} & \frac{\partial \rho_{PPj2}}{\partial \psi} \\ \vdots & \vdots & \vdots & \vdots \\ \frac{\partial \rho_{PPjn}}{\partial \mu} & \frac{\partial \rho_{PPjn}}{\partial \vartheta} & \frac{\partial \rho_{PPjn}}{\partial \chi} & \frac{\partial \rho_{PPjn}}{\partial \psi} \end{bmatrix} \tag{6.27}$$

where the subscripts ji, $i = 1, 2, \cdots, n$ are the same as those in Equation (6.16).

The method introduced above can also be used in the case of the pipe support model discussed in Chapter 4.

6.5 Some Issues Concerning the Iteration Process

For the iteration process of the Gauss-Newton method, some major issues will be encountered. They are discussed in detail in what follows.

6.5.1 Choice of Objective Function

In theory either the reflection or transmission coefficient can be chosen to establish the objective function. The one with higher sensitivity to the parameters (this is usually frequency dependent) is more preferable. In practice, the accuracy and ease of the measurements of the coefficients should also be considered.

6.5.2 Selection of Frequency Range

The choice of the frequency range for the parameter identification process is usually based on the sensitivity of the objective function to the parameters. High sensitivity of the objective function to the parameters to be updated can improve the goodness of estimation.

6.5.3 Initial Estimate of Parameters

As mentioned at the end of section 6.3.2.2, the initial estimates are of importance to the convergence of the iteration. Good estimates of the initial parameters can lead to a fast convergence while poor estimates might result in slow convergence, converging to other local minima, or even divergence.

Taking the mass-like discontinuity on a beam for example, there are two joint parameters to be updated. One is the non-dimensional mass, μ and the other is the non-dimensional moment of inertia, ϑ. In practice, an initial estimate of the mass can be expected to be more accurately known than that of the moment of inertia. However, an estimate of ϑ can be obtained based on that of μ. Referring to equation (6.13), when

$$(\mu\xi)(\vartheta\xi^3) + 2\vartheta\xi^3 - 2\mu\xi = 0 \tag{6.28}$$

there is no reflection. From the 'measured' power reflection coefficient against non-dimensional frequency ξ^2, the frequency ξ^2 at which $\rho = 0$ might be estimated. From equation (6.28), it yields

$$\vartheta = \frac{2\mu}{\mu\xi^3 + 2\xi^2}. \tag{6.29}$$

The parameter ϑ can be estimated based on an estimate for μ and the value of ξ at this frequency.

A more generally applicable technique for finding good estimates of the initial parameters is possible if a range for each parameter is assumed within which the global minimum is located. Then their ranges can be divided into a coarse grid (Figure 6.5). The initial estimates of the parameters can be chosen as the pair of μ and ϑ where the objective function is lowest. However, it must be noted that this still does not guarantee

good initial parameter estimates since the global minimum may not lie within the ranges chosen.

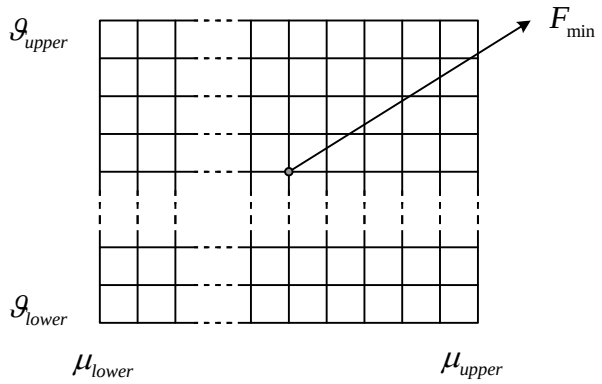

Figure 6.5 Grid of the range of estimated μ and ϑ for the simple mass-like discontinuity.

6.5.4 Termination of Iteration

A theoretical model is always an approximation of the true system. Owing to the existence of measurement noise and inaccuracy of the joint model, the solution at the j th iteration $\mathbf{X}_j$ need never converge to the true value. It may converge to a value close to the true value depending on the noise level and nonsingularity of $\mathbf{S}_j^{\mathrm{T}}\mathbf{W}_{RR}\mathbf{S}_j$ in equation (6.10). Many criteria for terminating the iteration can be defined. Considering the orders of magnitudes of these two parameters and that $\mu_j = 0$ or $\vartheta_j = 0$ is possible, a weighted norm of the difference between the parameter vectors of two successive iterations is used, which is

$$\delta_j = \left\| \Delta\mathbf{X}_j^T \mathbf{W}_{XX} \Delta\mathbf{X}_j \right\|. \tag{6.30}$$

where $\mathbf{W}_{XX}$ is the weighting matrix. When δ_j is small enough, the iteration can be terminated. It should be noted that even if the value of equation (6.30) is very small, it is not sufficient to say that the method has converged. Only when $\sum_{j\to\infty} \delta_j$ tends to a constant, can it be said that the method is converged.

6.5.5 Evaluating the Goodness of the Estimates

When the iteration process is complete, the identification result is obtained. The result needs to be evaluated before drawing any final conclusion. Two ways, graphical and numerical, may be used to measure the goodness of the result. From the plot of the 'measured' and estimated power reflection or transmission coefficient, the result can be viewed easily. A more quantitative way for parametric models is to evaluate the result statistically, among which the sum of squares due to errors (*SSE*), R-square, adjusted R-square and root mean squared error are quite often used. They are discussed in references [71, 72], here only a brief introduction is given.

1) The sum of squares due to errors (*SSE*)

This statistic measures the total deviation from the estimate to the response values and is given by

$$SSE = \sum_{i=1}^{n} w_i \left(y_{mi} - y_i \right)^2 \tag{6.31}$$

where y_{mi} is the *i*th observed or measured response value, y_i is the corresponding response predicted by the model after each iteration, w_i is the *i*th weighting factor ($w_i \neq 0$) and n is the number of response values. A value closer to zero means a better fit of the model. Here the power reflection coefficient ρ or transmission coefficient τ can be the substitute for y.

2) R-square

R-square is the square of the correlation between the measured and predicted response values. It is defined as the ratio of the sum of squares of the regression (*SSR*) and the total sum of squares (*SST*). *SSR* is defined as

$$SSR = \sum_{i=1}^{n} w_i \left(y_i - \bar{y}_m \right)^2 \tag{6.32}$$

where $\bar{y}_m$ is the mean value of the observed response. *SST* is also called the sum of squares about the mean, and is defined as

$$SST = \sum_{i=1}^{n} w_i \left(y_{mi} - \bar{y}_m \right)^2 \tag{6.33}$$

It can be proved that $SST = SSR + SSE$. Therefore, R-square can be expressed as

$$R^2 = \frac{SSR}{SST} = 1 - \frac{SSE}{SST} \tag{6.34}$$

Note that it is possible to get a negative R-square. In this case, R-square cannot be interpreted as the square of a correlation.

3) Adjusted R-square

If the number of estimated parameters in the model is increased, R-square might increase although the estimation may not improve. To avoid this, the degrees of freedom adjusted R-square statistic is used. The adjusted R-square is defined as

$$R_a^2 = 1 - \frac{SSE(n-1)}{SST(n-q)} \tag{6.35}$$

where q is the number of parameters to be estimated. Here the power reflection coefficient ρ or transmission coefficient τ can be the substitute for y. The R-square and adjusted R-square can take on any value less than or equal to 1, with a value closer to 1 indicating a better estimate.

4) Root mean squared error

The root mean square error is defined as

$$RMSE = \sqrt{\frac{SSE}{n-q}}. \tag{6.36}$$

A *RMSE* value closer to zero means a better estimate.

The R-square and the adjusted R-square include both information of *SSE* and *SST*. Only the R-square will be given in what follows.

6.6 Numerical Simulations on a Mass-like Discontinuity

The reflection and transmission coefficients of a mass-like discontinuity in a straight waveguide have been given in terms of the parameters of the discontinuity and waveguide at the end of Chapter 2. In Chapter 3, by introducing a noise model to the transducer array measurements, the reflection and transmission coefficients were obtained from the simulated noisy measurements. In this section, by considering the simulated noisy reflection and transmission coefficients as the 'measured' counterparts, numerical simulations are performed on parameter identification of this discontinuity. The intention is to investigate the robustness of the Gauss-Newton method on joint identification. For simplicity, only the power reflection coefficient is used in the

simulations.

Non-dimensional mass, $\mu_0 = 50$ and non-dimensional moment of inertia, $\vartheta_0 = 10^4$ are chosen as the true values of the parameters of the discontinuity. In Figure 6.6 the noisy power reflection coefficients are plotted against the non-dimensional frequency, $\xi^2 = \omega\kappa / c_l$. The noise level is $\sigma_1 = \sigma_2 = 2\%$ here. The noisy power reflection coefficient is calculated at 1000 values of ξ^2 , which are linearly spaced in the frequency range considered. The dotted line indicates the true value based on the theoretical model. Owing to the randomness of the noise at each point, the simulated 'measured' reflection coefficient is only one particular case. The conclusions drawn here are therefore only limited to this case.

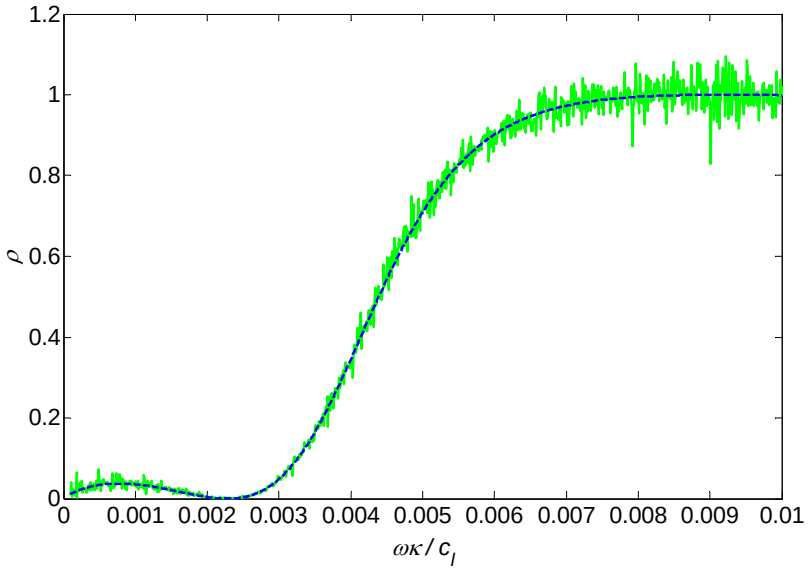

Figure 6.6 Numerical simulations of noisy power reflection coefficient: ——, numerical simulations; - - - -, noise free values based on theoretical model.

6.6.1 Effect of Selected Frequency Range

The objective function is defined over a frequency range. Therefore, the parameters estimated by the Gauss-Newton method are only valid to a particular frequency range. This section examines the influence of frequency range selected for parameter estimation on the identified results. The accuracy of identified results depends on the

sensitivity of the objective function to the unknown parameters. This is also shown in the following analysis.

Four cases of choosing frequency ranges are studied here. Based on the behaviour of the power reflection coefficient over the whole frequency range considered, $\xi^2 \in [0.1,\ \ 3.0]\times 10^{-3}$, $\xi^2 \in [3.1,\ \ 6.0]\times 10^{-3}$ and $\xi^2 \in [6.1,\ \ 9.0]\times 10^{-3}$ are considered as the first three cases. Case 4 includes all the frequencies of the first three cases. In the first range ρ is of small magnitude and the noise is also small. In the third range ρ is getting larger and so does the noise (which is due to the chosen noise model). In the second range, ρ changes rapidly with frequency. In the frequency range above $\xi^2 > 9.0\times 10^{-3}$, ρ is almost independent of frequency which will cause bad conditioning of the estimation process, so it is not considered here.

The dimensionless mass, μ and moment of inertia, ϑ are estimated over the four frequency ranges. Owing to the equal relative noise levels, the weighting matrix of the objective function is taken to be the identity matrix. Figure 6.7 shows the true power reflection coefficient compared with the one estimated from the identified parameters in the third frequency range. The estimated power reflection coefficient is very close to the true one. The estimated results over the four frequency ranges are listed in Table 6.1. The results for the third frequency range are the worst. The next section gives the reason for the different estimation accuracies.

Table 6.1 The estimated values of μ and ϑ in different frequency ranges: noise free values: $\mu_0 = 50$ and $\vartheta_0 = 10\times 10^3$. (Percentages in the brackets are relative errors).

ξ^2 $(\times 10^{-3})$	μ	ϑ $(\times 10^3)$
$[0.1,\ \ 3.1]$	51.38 (2.8%)	10.06 (0.6%)
$[3.1,\ \ 6.0]$	57.30 (14.6%)	10.28 (2.8%)
$[6.0,\ \ 9.0]$	39.26 (-21.5%)	9.33 (-6.7%)
Case 4	51.74 (3.5%)	10.09 (0.9%)

Note: Case 4 includes all the frequencies of the first three cases.

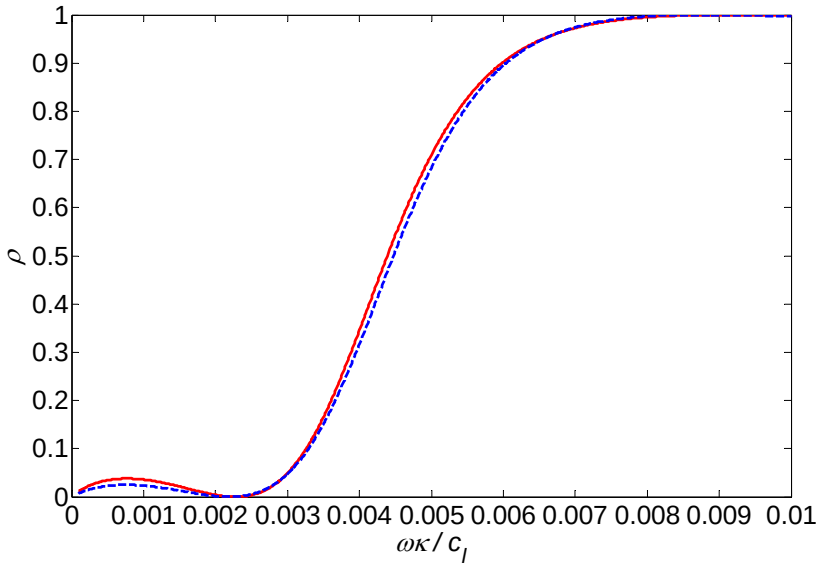

Figure 6.7 Identified power reflection coefficient in the frequency range $\xi^2 \in [6.0,\quad 9.0]\times 10^{-3}$: ——, predicted by true values of μ and ϑ; - - - -, predicted based on identified results of μ and ϑ.

6.6.2 Sensitivity of the Objective Function to Parameters

The accuracy of the estimated parameters is determined by the sensitivity of the objective function to these parameters. In Figure 6.8, the objective functions (equation (6.4)) composed of power reflection coefficient for the four frequency ranges are plotted against the relative mass and inertia parameters, μ/μ_0 and ϑ/ϑ_0. It can be seen that the minimum of the objective function is a valley-like area parallel to the mass μ axis, especially for the cases of 2 and 4. This means that the objective function is less sensitive to the mass parameter, μ than to the moment of inertia, ϑ. That is why the estimated value of μ is relatively poor compared to that of ϑ.

The condition for termination of the iteration process is that the 2-norm of normalised change of the unknown parameter vector of successive steps (see Figure 6.4) is less than 0.1%. Table 6.2 lists the number of total steps of the iteration for each frequency range and the step change of the mass and moment of inertia relative to the true values in the last step of the iteration. The condition number of the Jacobean matrix in the last iteration step is also given. The condition number of the Jacobean matrix corresponds to the accuracy of the identification results. The smaller the condition number, the better

the estimated results. The results of the identified moment of inertia, ϑ are better than those of the mass, μ because the objective function is more sensitive to the moment of inertia (except for the first frequency range for which the objective function is flat around the true values of the parameters). Although the results for the first frequency range are the best, it is not necessarily the best option. In practical measurements the measurement noise might have a large influence on the measured power reflection coefficient at low frequencies. Based on the same noise level in all the frequency ranges, the frequency range of case 4 is a good choice. It includes all the frequency ranges and the condition number of the Jacobean matrix is also relatively small.

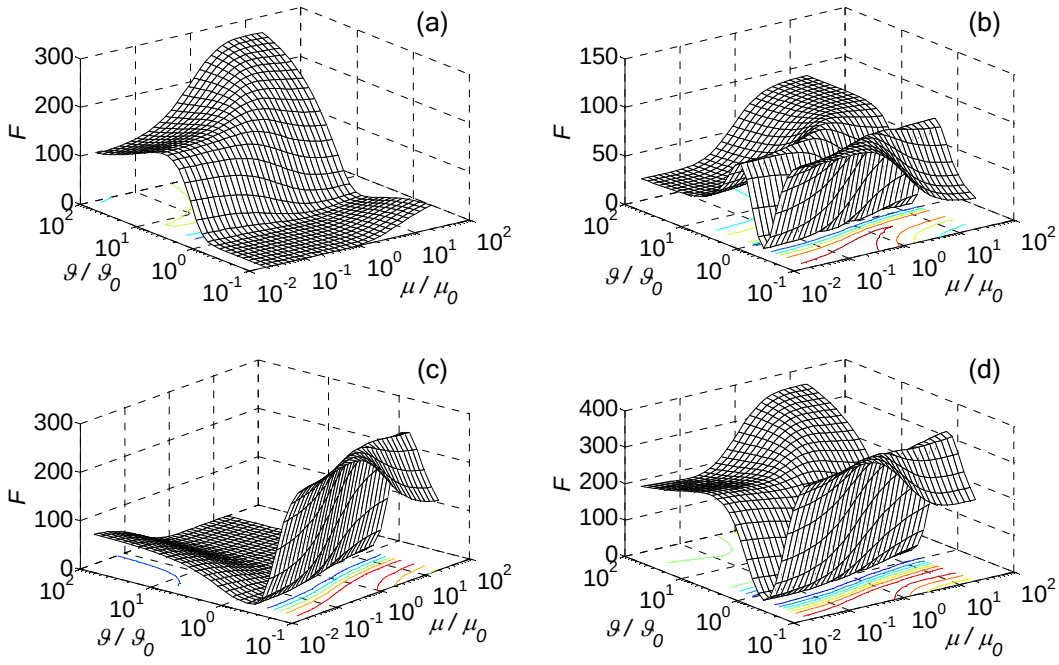

Figure 6.8 Objective function in the four frequency ranges: (a) $\xi^2 \in [0.1,\quad 3.0]\times 10^{-3}$; (b) $\xi^2 \in [3.1,\quad 6.0]\times 10^{-3}$; (c) $\xi^2 \in [6.1,\quad 9.0]\times 10^{-3}$; (d) case 4.

Table 6.2 Step changes of μ and ϑ relative to true values and the condition number of $\mathbf{S}$ in the last iteration. (j is the number of iterations)

ξ^2 ($\times 10^{-3}$)	j	$\Delta\mu_j / \mu_j$	$\Delta\vartheta_j / \vartheta_j$	Condition number of $\mathbf{S}$
$[0.1,\quad 3.1]$	4	0.33×10^{-4}	0.99×10^{-4}	143
$[3.1,\quad 6.0]$	5	-0.29×10^{-4}	-0.05×10^{-4}	355
$[6.0,\quad 9.0]$	7	0.90×10^{-3}	0.23×10^{-3}	498
Case 4	5	-0.42×10^{-4}	-0.08×10^{-4}	144

6.6.3 Effect of Initial Parameter Values

Good estimates of the initial parameters for the iteration process are paramount to avoid convergence to a local minimum rather than the global minimum, since the initial values of the parameters influence the iteration direction. The method for selecting the initial values of the parameters introduced in Section 6.5.3 was used in the above iteration processes. In order to illustrate the effect of the initial values of the parameters, in what follows two sets of initial values of the parameters are chosen. Take the frequency range of Case 4 for example. In Figure 6.8(d) there are several local minima of the objective function. Figures 6.9 and 6.10 show the contour plots of the objective function of Figure 6.8(d). Also shown in these figures are the steps of the iteration process with two different initial parameter pairs. It is obvious that a good estimate of the initial parameters takes fewer steps to reach the final result. A bad choice of the initial values of the parameters takes more steps to reach the global minimum or may fail to converge to the global minimum due to existence of the local minima.

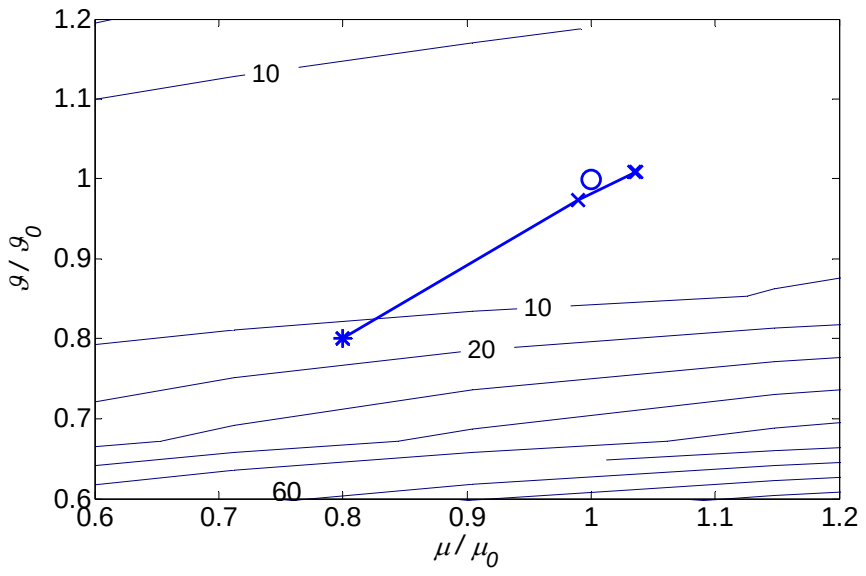

Figure 6.9 Contour plot of the objective function in the frequency range of case 4 with starting parameters, $\mu / \mu_0 = 0.8$ and $\vartheta / \vartheta_0 = 0.8$: *, starting point; ×, iteration steps; O, true values.

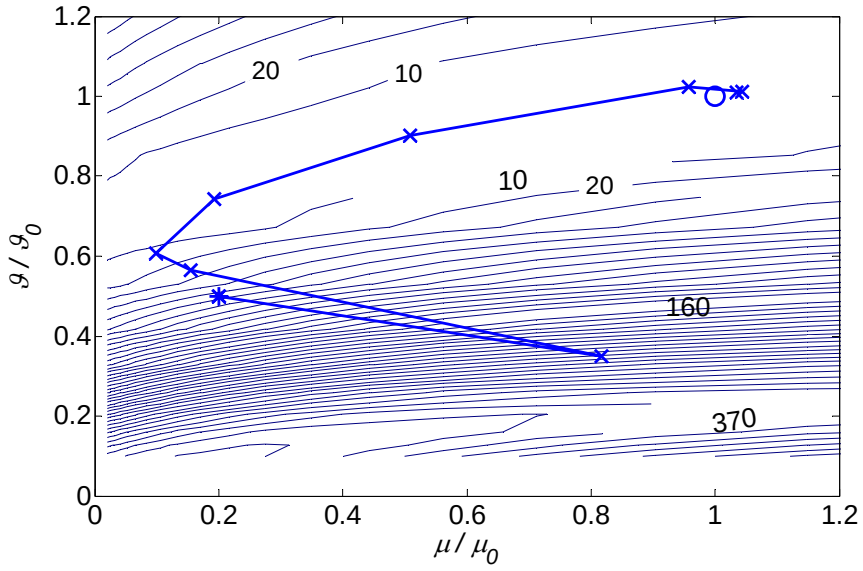

Figure 6.10 Contour plot of the objective function in the frequency range of case 4 with starting parameters: $\mu / \mu_0 = 0.2$ and $\vartheta / \vartheta_0 = 0.5$: *, starting point; ×, iteration steps; O, true values.

6.7 Summary

In this Chapter, two methods, a direct method and an iterative method, have been discussed to estimate the joint parameters from measured reflection or transmission coefficients.

Owing to the high sensitivity of the phases of the reflection and transmission coefficients to the measurement errors, the direct method including the phase information of the reflection and transmission coefficients does not give robust estimates. The emphasis is then put on an iterative method, the Gauss-Newton method, in which only the modulus of the reflection or transmission coefficient is included.

For the iterative method, the initial values of the parameters are of importance since a bad choice may lead the process to a local minimum rather than the global minimum, or divergence. The non-dimensional joint parameters have different orders of magnitude. Therefore, when terminating the iteration, not only the absolute change but also the relative change in each parameter should be considered.

Based on the sensitivities of the objective function to the parameters of the discontinuity, the iteration process can be performed on the power reflection coefficient or transmission coefficient. In practice, the accuracy and ease of the measurements on the corresponding coefficient should also be considered when establishing the objective function.

Owing to the difference of the sensitivity of the objective function to the parameters in a given frequency range, not every parameter is required to be involved in the iteration process. A reasonable value can be assumed for the parameter to which the objective function is much less sensitive. By this way, the identification process can be simplified dramatically and the conditioning of the problem can be improved correspondingly.

To illustrate the applicability of the Gauss-Newton method, numerical simulations have been performed on the parameter identification of a mass/moment of inertia discontinuity in a straight beam. Some issues relating to the iteration process have been investigated.

Chapter 7 Experimental Validation of the Parameter Identification Method

7.1 Introduction

The application of parameter identification methods to reflection and transmission coefficients of joints was introduced and numerical case studies were carried out in Chapter 6. In this chapter, the joint identification technique is validated using experimentally measured reflection and transmission coefficients. These are taken from three types of structures discussed in Chapters 3, 4 and 5, which are mass/moment of inertia discontinuities on a straight beam (Figure 3.12), supported straight pipes (Figure 4.4) and a right-angled pipe bend (Figure 5.4). The parameters estimated by the joint identification method are compared to the directly measured parameters for the mass-like discontinuities in a beam and the pipe supports. Problems concerning the selection of frequency ranges, choice of the objective functions (i.e. reflection or transmission coefficient) are investigated. The feasibility and robustness of the method are examined by these experimental case studies.

7.2 Parameter Identification of the Mass/Moment of Inertia Discontinuity on a Beam

The wave reflection and transmission coefficients of a mass/moment of inertia discontinuity on a straight waveguide were described in Chapter 2 and measurements of the reflection and transmission coefficients of steel blocks attached to a straight beam were presented in Chapter 3. Three mass/moment of inertias were used, which are characterised by long-thin (block 1), short-thin (block 2) and short-thick (block 3) (see Table 3.3). The experimental results showed that estimates of the reflection and

transmission coefficients based on the assumption of reflected beam ends are more accurate than those which assume anechoic boundaries. Therefore, in the iteration process, the measured power reflection and transmission coefficients found using this assumption are used.

7.2.1 Results over Different Frequency Ranges

The objective function is composed of reflection and/or transmission coefficients over a chosen frequency range. This section presents the parameter identification results using different frequency ranges. The iteration process is only performed on the power reflection coefficient in this section. Figure 7.1 shows the measured power reflection coefficient $\hat{\rho}$ for block 1 compared with the predicted values using directly measured mass and inertia. Below 200Hz, the measured results are contaminated by noise and poor numerical conditioning of the Wave Amplitude Decomposition (WAD) method. Above 1500Hz oscillations in the estimates become apparent. In accordance with the above behaviour of the power reflection coefficient, four ways of selecting frequency ranges are considered. They are 500-1500Hz, 1000-2000Hz and 200-3000Hz in which each frequency was selected and Case 4 in which 20 equally spaced frequencies are selected in the range 200-3000Hz. Figures 7.2(a)-(d) show the mesh plots of the objective function against the non-dimensional mass and moment of inertia over the four frequency ranges. The valley-like feature parallel to the mass parameter axis indicates that the objective function is more sensitive to the moment of inertia, therefore in general the estimations of the moment of inertia are more accurate than those of the mass. The flat shape of the objective function in range 500-1500Hz (Figure 7.2(a)) implies that if the initial value of the moment of inertia is far from the true value, bad estimates of the moment of inertia might also be produced.

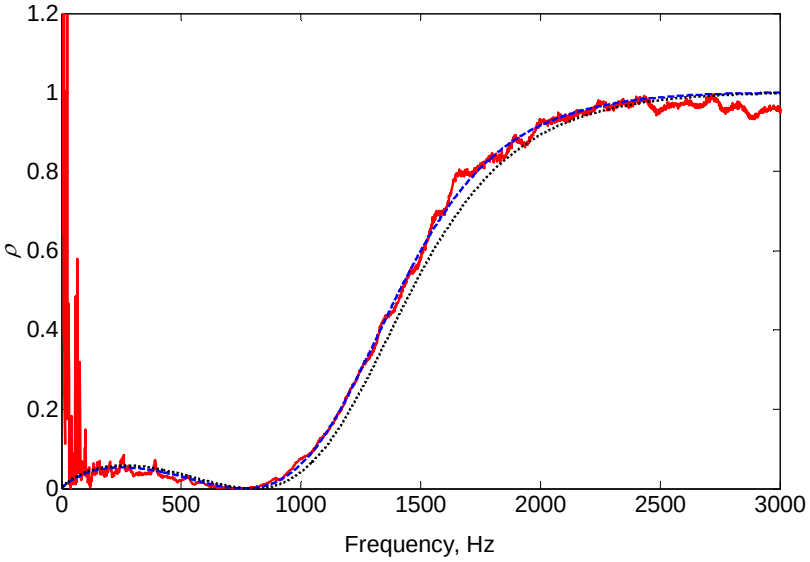

Figure 7.1 Power reflection coefficient of block 1: ——, measured; - - - - - -, estimated based on identified parameters in Case 4; ·····, estimated based on directly measured mass and moment of inertia.

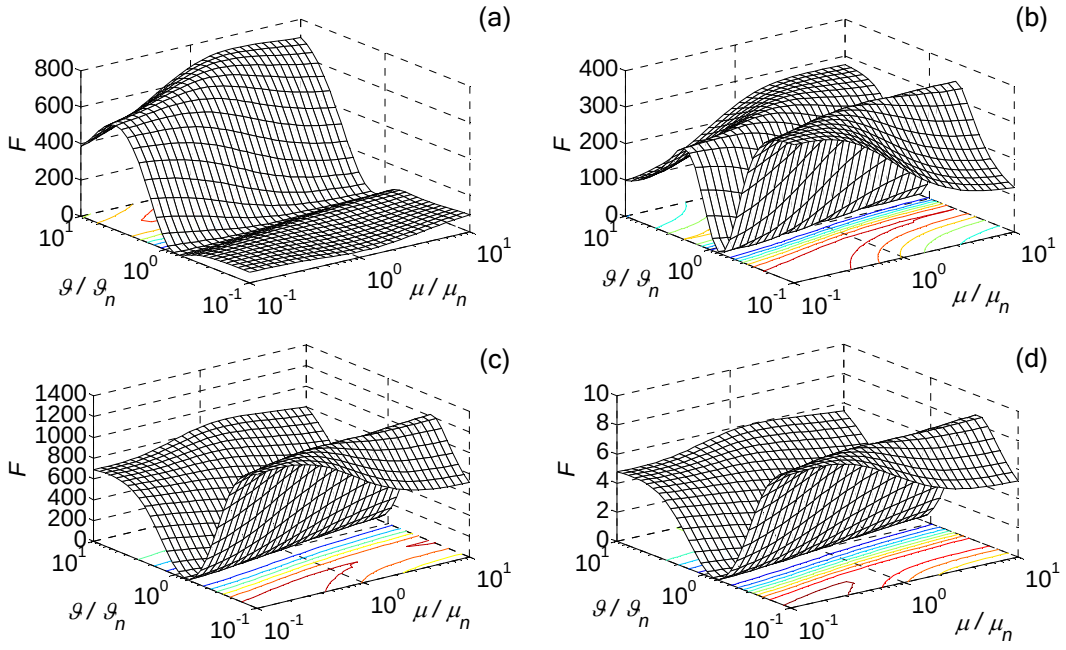

Figure 7.2 Objective function based on power reflection coefficient for block 1: μ_n and ϑ_n are the non-dimensional mass and moment of inertia parameters based on direct measurements: (a) 500-1500Hz; (b) 1000-2000Hz; (c) 200-3000Hz; (d) Case 4.

The non-dimensional mass μ and moment of inertia ϑ of block 1 are estimated for each chosen frequency range and presented in Table 7.1. The results are the best fit to the measured power reflection coefficient in each frequency range. Also given in the

table are the results based on direct measurements. The percentages in the brackets are the relative errors of the identification results with respect to the direct measurements. The directly measured results are only nominal values of the parameters and are not necessarily exact. Due to the connection condition of the mass blocks to the beam and measurement noise, it is normal that differences exist between the direct measurements and estimates from the reflection coefficient. The results from the range 200-3000Hz and Case 4 are very similar. Case 4 actually uses a weighted matrix, which speeds up the iteration process (fewer frequencies), but the random deviations of the measured data are still not removed. As a whole, the percentages shown in the table indicate the parametric model of the mass-like discontinuity is good enough.

Table 7.1 Estimates of the parameters of block 1 from measured power reflection coefficient.

	directly measured	500-1500Hz	1000-2000Hz	200-3000Hz	Case 4
mass, μ	77.0	58.2 (-24%)	71.1(-8%)	74.8 (-3%)	76.7 (-0.4%)
inertia, $\vartheta \times 10^3$	17.0	16.9 (-1%)	17.6 (4%)	17.8 (5%)	17.8 (5%)

Note: Case 4: 20 equally spaced frequencies in the range 200-3000Hz.

Also shown in Figure 7.1 is the predicted power reflection coefficient using parameter values for Case 4. It agrees with the predicted power reflection coefficient based on the directly measured mass and inertia very well except in the middle of the frequency range. The reconstructed power reflection coefficients for other frequency ranges (not shown in the figure) are also very close to the predicted ones based on directly measured mass and moment of inertia. This means the distinctions between the results from different frequency ranges are very small.

7.2.2 Results from Measured Transmission Coefficients

The parameters of the discontinuity can also be estimated from the measured power transmission coefficient. Figure 7.3 shows the measured power transmission coefficient along with the one predicted using the identified parameters in Case 4 and the one based on directly measured mass and moment of inertia. Although larger deviations are found than the power reflection coefficient, the results based on the identified parameters also

mimic the general trend very closely. Table 7.2 shows the mass and moment of inertia identified from the power transmission coefficient. The oscillations on the measured power transmission coefficient are larger than those of the power reflection coefficient, therefore the identified parameters from the transmission coefficient have larger deviations than those obtained from the reflection coefficient. Again the results for the moment of inertia are more accurate than those for the mass, which is due to the high sensitivity of the objective function to the moment of inertia.

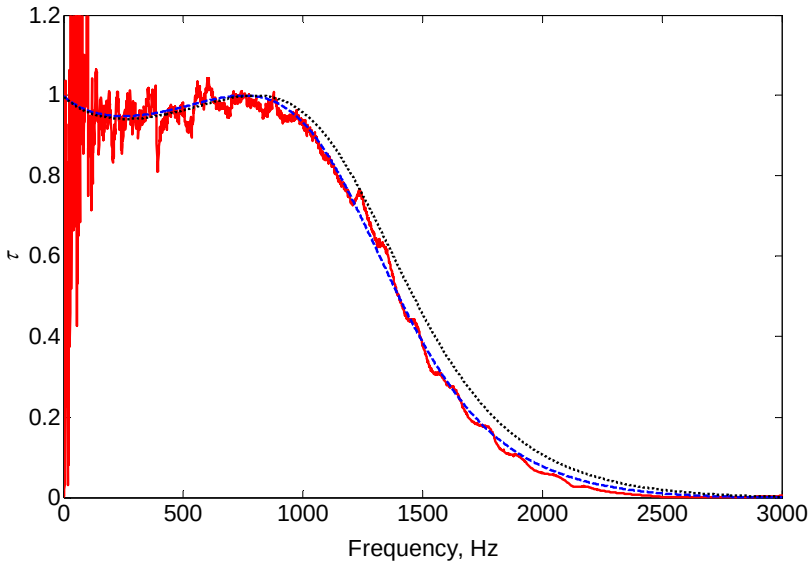

Figure 7.3 Power transmission coefficient of block 1: ——, measured; - - - - - -, predicted from parameters identified in Case 4; ……, predicted based on directly measured mass and inertia.

Table 7.2 Estimation of the parameters of block 1 from measured power transmission coefficient.

	directly predicted	500-1500Hz	1000-2000Hz	200-3000Hz	Case 4
mass, μ	77.0	46.3 (-40%)	43.2(-44%)	68.7 (-11%)	67.6 (-12%)
inertia, $\vartheta \times 10^3$	17.0	16.3 (-4%)	16.2 (-5%)	17.7 (4%)	17.7 (4%)

Note: Case 4: 20 equally spaced frequencies in the range 200-3000Hz.

7.2.3 Results from Normalised Reflection or Transmission Coefficient

If the damping of the system is negligible, the power reflection and transmission coefficients should sum to unity. The sum of the measured power reflection and transmission coefficients for block 1 has large oscillations although it is nearly unity in the frequency range up to 3000Hz (Figure 3.21). The damping is not considered in the beam or in the model of the discontinuity. In order to remedy this, the oscillations in the power reflection and transmission coefficients can be smoothed via normalisation by their sum, i.e. $\hat{\rho}/(\hat{\rho}+\hat{\tau})$ or $\hat{\tau}/(\hat{\rho}+\hat{\tau})$. Thus the normalised power reflection and transmission coefficients sum to unity. Therefore, the parameters estimated from the normalised power reflection coefficient or transmission coefficient are the same. This can be deduced from Equation (6.19). Figures 7.4(a) and (b) show the normalised power reflection and transmission coefficients along with those predicted from the identified and directly measured mass and moment of inertia. The oscillations are reduced dramatically by the normalisation, and the agreement between the measured and predicted data is improved greatly.

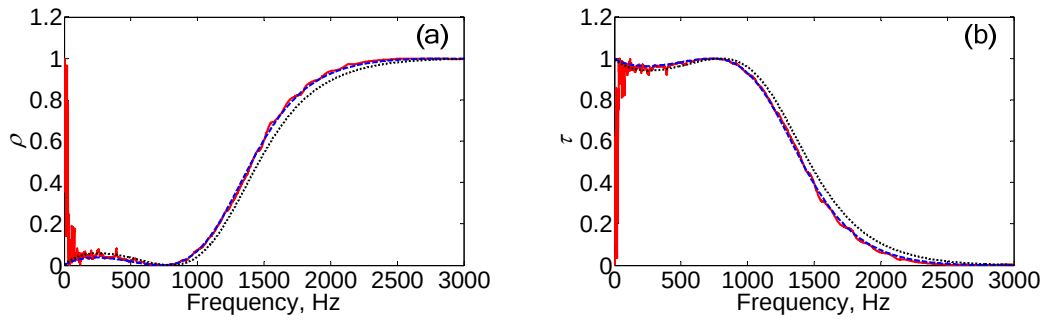

Figure 7.4 Normalised power reflection and transmission coefficients of block 1: ——, measured; - - - - - -, predicted from identified parameters from 200-3000Hz; ·····, predicted based on directly measured parameters.

Table 7.3 lists the estimated mass and moment of inertia from the normalised power reflection or transmission coefficient. The estimated mass and moment of inertia in the four frequency ranges are much more consistent than those using the unnormalised power reflection and transmission coefficients (see Table 7.1). It was mentioned in Section 7.2.1 that the directly measured results are only nominal values of the

parameters and are not necessarily exact. Normalisation of reflection and transmission coefficients can improve the robustness of estimation.

Table 7.3 Estimates of the parameters of block 1 from normalised power reflection or transmission coefficient, $\hat{\rho}/(\hat{\rho}+\hat{\tau})$ or $\hat{\tau}/(\hat{\rho}+\hat{\tau})$.

	directly predicted	500-1500Hz	1000-2000Hz	200-3000Hz	Case 4
mass, μ	77.0	59.9 (-22%)	48.3 (-37%)	59.2(-23%)	61.5 (-20%)
inertia, $\vartheta \times 10^3$	17.0	17.0 (0%)	16.5 (-3%)	17.2 (1%)	17.3 (2%)

Note: Case 4: 20 equally spaced frequencies in the range 200-3000Hz.

7.2.4 Accuracy of the Identified Results

The goodness of the above estimates in terms of R-square (equation (6.34)) is listed in Table 7.4. In all, the R-square values are very close to unity, which means the iteration processes are very successful and the model of the discontinuity accurately predicts the measured data used in the fit. In each frequency range, the estimate based on the power reflection coefficient is marginally better fitted by the theoretical model than the power transmission coefficient. This means that there is more confidence in the estimate using the power reflection coefficient and that the data of the power reflection coefficient are more reliable. After normalisation, the goodness of fit improves again since the errors caused by neglecting the damping of the system are reduced.

Table 7.4 Goodness of the estimation for block 1 in terms of R^2.

	500-1500Hz	1000-2000Hz	200-3000Hz	Case 4
ρ	0.9989	0.9966	0.9979	0.9980
τ	0.9845	0.9964	0.9973	0.9966
$\hat{\rho}/(\hat{\rho}+\hat{\tau})$ or $\hat{\tau}/(\hat{\rho}+\hat{\tau})$	0.9992	0.9985	0.9995	0.9993

Note: Case 4: 20 equally spaced frequencies in the range 200-3000Hz.

7.2.5 Results for Blocks 2 and 3

Figures 7.5(a)-(d) show the measured normalised power reflection and transmission coefficients for block 2 and block 3 together with those predicted from the directly measured mass and moment of inertia. Again, the normalisation smoothes the oscillations on the measured reflection and transmission coefficients, which can be seen from comparison with Figure 3.21. The identified mass and moment of inertia of blocks 2 and 3 from the measured power reflection and transmission coefficients in the frequency range of Case 4 are listed in Table 7.5. The directly measured values of the parameters and the R-square values of the estimation are also given in the table. The estimated parameters are within 16% of the directly measured ones. The values of the R-square are very close to unity. All these indicate that the discontinuity model closely captures the dynamic response of the structure. The robustness of the iterative method is also demonstrated.

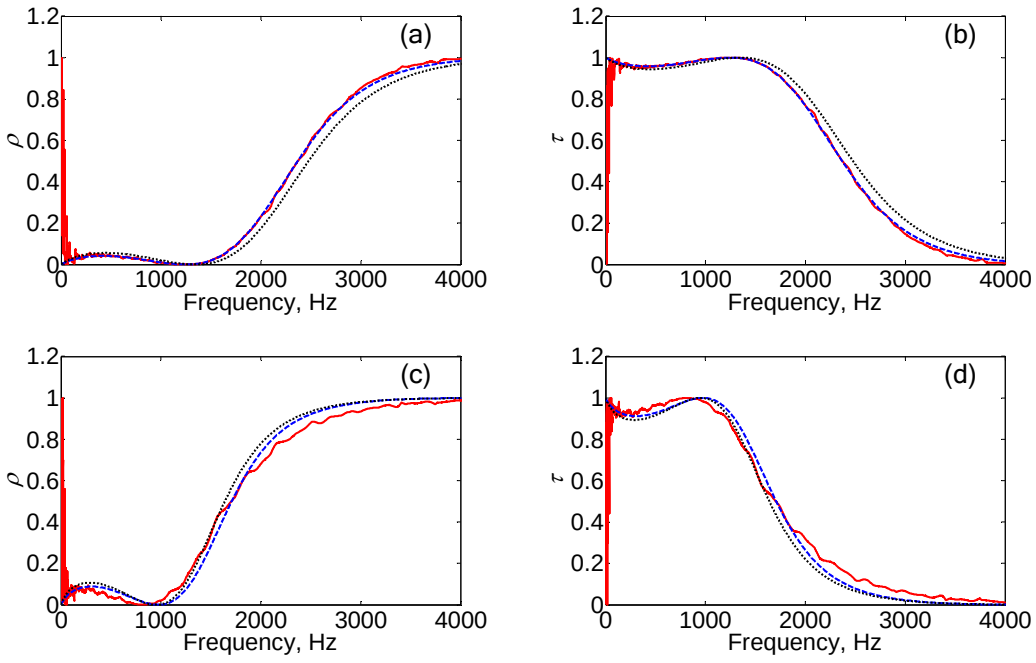

Figure 7.5 Power reflection and transmission coefficients for blocks 2 and 3: ——, measured; - - - - - - -, predicted from identified parameters of Case 4; ……, predicted based on directly measured parameters: (a) block 2: fitting $\rho/(\rho+\tau)$; (b) block 2: fitting $\tau/(\rho+\tau)$; (c) block 3: fitting $\rho/(\rho+\tau)$; (d) block 3: fitting $\tau/(\rho+\tau)$.

Table 7.5 Estimates of the parameters of blocks 2 and 3 from normalised measured reflection and transmission coefficients.

	block 2		block 3	
	directly measured	$\hat{\rho}/(\hat{\rho}+\hat{\tau})$ or $\hat{\tau}/(\hat{\rho}+\hat{\tau})$	directly measured	$\hat{\rho}/(\hat{\rho}+\hat{\tau})$ or $\hat{\tau}/(\hat{\rho}+\hat{\tau})$
mass, μ	57.7	49.2 (-15%)	115	96.5 (-16%)
Moment of inertia, $\vartheta\,(\times 10^3)$	7.68	7.97 (4%)	15.4	14.1 (-8%)
R^2	/	0.9995	/	0.9855

Note: Case 4: 20 equally spaced frequencies in the range 200-3000Hz.

7.3 Parameter Identification of Pipe Supports

In Chapter 4, measurements of the reflection and transmission coefficients of four supports, long and short aluminium, long and short steel (see Figure 4.8 and Tables 4.2 and 4.3), were presented. In this section, the estimated parameters of these pipe supports are investigated. Since the damping in the parameter model of the pipe and supports is neglected, the measured reflection or transmission coefficients normalised by their sum are employed. The power reflection and transmission coefficients predicted from the directly measured parameters are very close to those estimated by the wave amplitude decomposition method. Therefore, these directly measured parameters are used as the initial values for the iteration process (see Table 4.4).

Figures 7.6(a) and (b) show the normalised power reflection and transmission coefficients for the long aluminium support. The four parameters, translational and rotational stiffnesses and mass and moment of inertia of the support, are updated in the range 200-2000Hz. The final results for the four parameters are listed in Table 7.6. The power reflection and transmission coefficients predicted from these parameters are also plotted in the figure, which are the best fit to the normalised measurements and they agree very well. The general trends of the fitted reflection and transmission coefficients also have a good agreement with those predicted using the directly measured parameters.

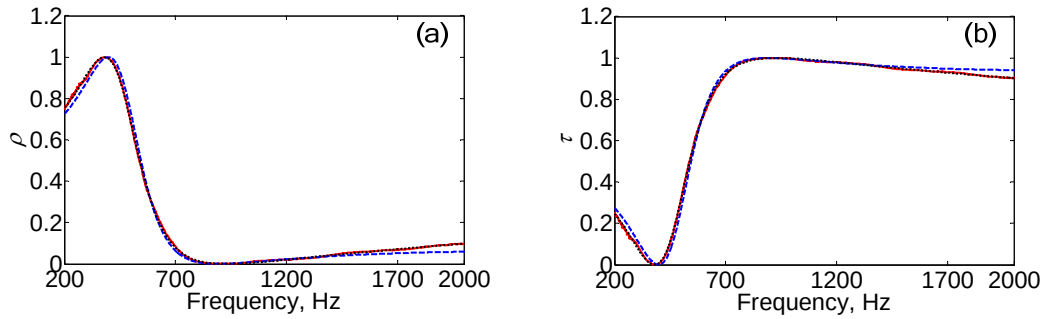

Figure 7.6 Power reflection and transmission coefficients of the long aluminium support: ——, normalised measured; - - - - - -, predicted from directly measured parameters; ·····, predicted from identified parameters using $\hat{\rho}/(\hat{\rho}+\hat{\tau})$ or $\hat{\tau}/(\hat{\rho}+\hat{\tau})$.

The same process is performed for the other three supports. The normalised power reflection and transmission coefficients for each case are plotted in Figures 7.7 to 7.9. The frequency range for the iteration process for each case is selected based on the behaviour of the measured power reflection and transmission coefficients. The data around 350Hz are not used. The power reflection and transmission coefficients predicted from the identified translational and rotational stiffnesses, mass and moment of inertia are also given in the figures. They mimic the general trend of the normalised power reflection and transmission coefficients very well, especially at the middle frequencies. At low and high frequencies, relatively large deviations are found, which are considered as the consequence of the resonances occurring in these frequency ranges. The agreement for the long support of each material (aluminium or steel) is always better than that for the short one. This is consistent with the quality and confidence of the parameters estimated from the direct measurements.

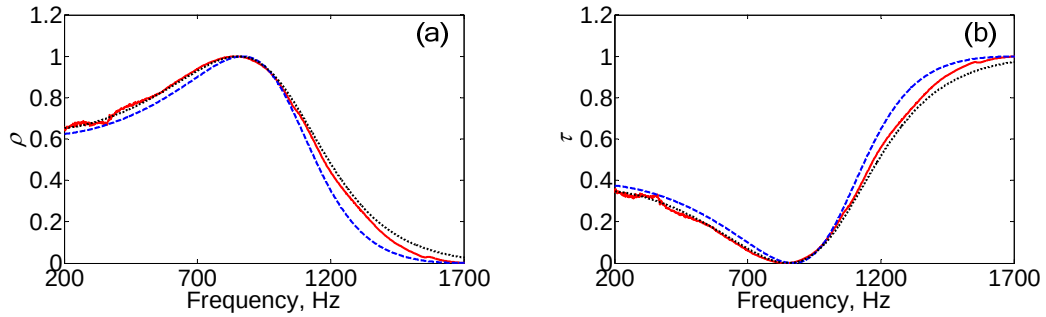

Figure 7.7 Power reflection and transmission coefficients of the short aluminium support: ——, normalised measured; - - - - - -, predicted from directly measured parameters; ·····, predicted from identified parameters using $\hat{\rho}/(\hat{\rho}+\hat{\tau})$ or $\hat{\tau}/(\hat{\rho}+\hat{\tau})$.

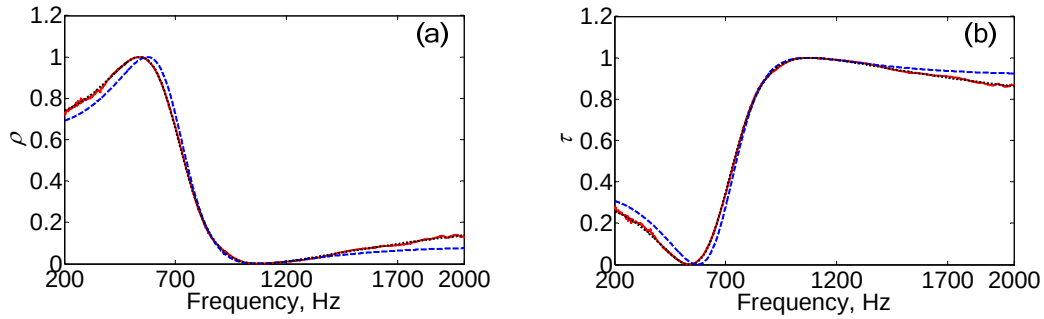

Figure 7.8 Power reflection and transmission coefficients of the long steel support: ——, normalised measured; - - - - - -, predicted from directly measured parameters; ……, predicted from identified parameters using $\hat{\rho}/(\hat{\rho}+\hat{\tau})$ or $\hat{\tau}/(\hat{\rho}+\hat{\tau})$.

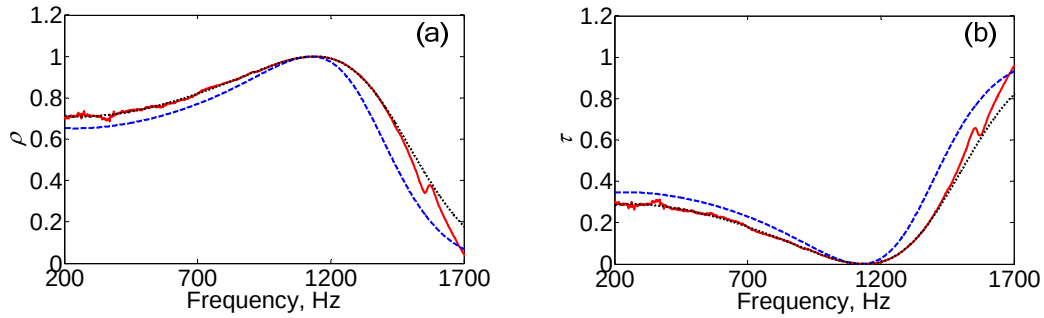

Figure 7.9 Power reflection and transmission coefficients of the short steel support: ——, normalised measured; - - - - - -, predicted from directly measured parameters; ……, predicted from identified parameters using $\hat{\rho}/(\hat{\rho}+\hat{\tau})$ or $\hat{\tau}/(\hat{\rho}+\hat{\tau})$.

The parameters estimated from the normalised power reflection or transmission coefficient for the four supports are listed in Table 7.6. Due to the complex configurations and boundary conditions of the supports, the values in the table are not exactly consistent with those calculated based on the dimensions of the supports and assumptions of simply-supported or clamped boundary conditions. However, the magnitudes of the values are still roughly within the theoretical values given by simply-supported and clamped boundary condition assumptions (see Appendix 11). The percentages in the table indicate the relative deviation of the identified results from those directly measured and given in Table 4.4. The directly measured values of the parameters are only nominal values and not necessarily exact. The translational stiffness has a good consistency. Results for the other three parameters have relatively large discrepancies. This is due to the difference of the sensitivity of the objective function to the updated parameters. Table 7.7 gives the relative changes of the parameters and the condition number of the Jacobean matrix **S** at the last step of iteration. The total

number of iteration steps for each support is also given in the table. The objective function is considered to be less sensitive to the parameter with large relative change. This is consistent with the percentages shown in Table 7.6. The large magnitude of the condition number of $\mathbf{S}$ indicates relatively low confidence of accuracy.

Table 7.6 Estimates of the parameters of the pipe supports from $\hat{\rho}/(\hat{\rho}+\hat{\tau})$. (SI units)

Support		frequency	K_T, $\times 10^6$	m	K_R, $\times 10^3$	J, $\times 10^{-5}$
aluminium	long	200-2000	2.317 (-11%)	0.056 (-30%)	1.572 (12%)	3.276 (15%)
	short	200-1400	7.929 (-12%)	0.046 (-42%)	2.369 (29%)	1.792 (-15%)
steel	long	400-2000	4.465 (-13%)	0.077 (-29%)	3.785 (40%)	3.442 (-10%)
	short	400-1400	14.737 (1%)	0.065 (-31%)	4.716 (57%)	6.474 (204%)

Note: Percentages in the brackets are relative deviations from the directly measured values given in Table 4.4.

Table 7.7 Relative change of parameters and condition number of the Jacobean matrix $\mathbf{S}$ at the last step of iteration for each pipe support.

support		j	$\Delta K_{Tj}/K_{Tj}$ $(\times 10^{-3})$	$\Delta m_j/m_j$ $(\times 10^{-3})$	$\Delta K_{Rj}/K_{Rj}$ $(\times 10^{-3})$	$\Delta J_j/J_j$ $(\times 10^{-3})$	n $(\times 10^6)$
aluminium	long	5	0.0017	0.2382	0.0270	-0.1708	1.4871
	short	5	-0.0017	-0.0071	-0.0530	-0.4307	2.1095
steel	long	5	-0.0005	-0.1078	0.0008	0.0709	1.1359
	short	6	-0.0023	0.0149	-0.0403	-0.2785	2.6010

Note: j, total iteration times; n, condition number of $\mathbf{S}$ at the last step.

7.4 Parameter Identification of a Right-angled Pipe Bend

This section discusses the estimation of the parameter of the right-angled bend of a piping system from measured power reflection and transmission coefficients. The iterative method introduced in Chapter 6 is used to update the joint parameters of the right-angled pipe bend discussed in Chapter 5. The intention is to validate the model of right-angled bend and verify the feasibility of the iterative method of parameter identification.

The measured power reflection and transmission coefficients of the right-angled pipe bend have been given in Chapter 5. A mass-free rigid connected model has previously been compared with the measured results of this structure by other researchers [63]. A more appropriate parametric model is still needed for better agreement. Although a general parametric model was developed in Chapter 5 in which four parameters, the translational and rotational stiffnesses, mass and moment of inertia, were considered, it is not necessarily the best choice for the parameter identification process. In the frequency range measured reliably, each of the power coefficients does not change much. Actually when applying the general bend model (with four parameters to update) to the iteration process over the frequency range 500-2000Hz, the Jacobean matrix is badly conditioned and the iteration does not converge. This means the general model is not appropriate for the iteration process.

The iteration process was then applied to the mass-like and spring-like joint models. By investigating the agreement of the whole trend of each power coefficient and the goodness of the estimation, it is found that the measured results and spring-like model match well. The following discussion only focuses on the spring-like model of the bend. The frequency averaged method reduces the oscillations on the measured power reflection and transmission coefficients effectively (see Chapter 5), and the power reflection and transmission coefficients obtained by this manipulation nearly sum to unity, so are chosen to compose the objective function of the iteration process.

When applying the spring-like model to update the translational and rotational stiffness parameters χ and ψ using ρ_{PP} (can be obtained from equation (5.25)), the iteration process is terminated due to the bad conditioning of the Jacobean matrix $\mathbf{S}$. This is because the objective function is insensitive to the translational stiffness, χ because the joint is effectively rigid. By fixing $\chi = 1$ (very rigid) and only updating the rotational stiffness parameter, finally $\psi = 0.160$ is obtained. This value means that the rotational stiffness of the joint is equal to the bending stiffness of a cantilevered pipe of length 6.25 times the radius of gyration of the cross-section with a moment applied at the end. The predicted power reflection and transmission coefficients based on this result are shown in Figure 7.10. Compared with the massless rigid connected joint model [63],

the general trend of each power coefficient has a much better agreement with the measured one. Relatively large differences are found for ρ_{PL}. This is because, in this case, ρ_{PL} is of small order of magnitude. However, due to the measurement noise, such a small order of magnitude cannot be measured accurately by the equipment and method used here. Usually the axial wave amplitudes are more difficult to measure than the flexural ones. Therefore, the power coefficients involving axial waves are considered to be less reliable. They are presented here only for reference. The iteration process will not be performed through them.

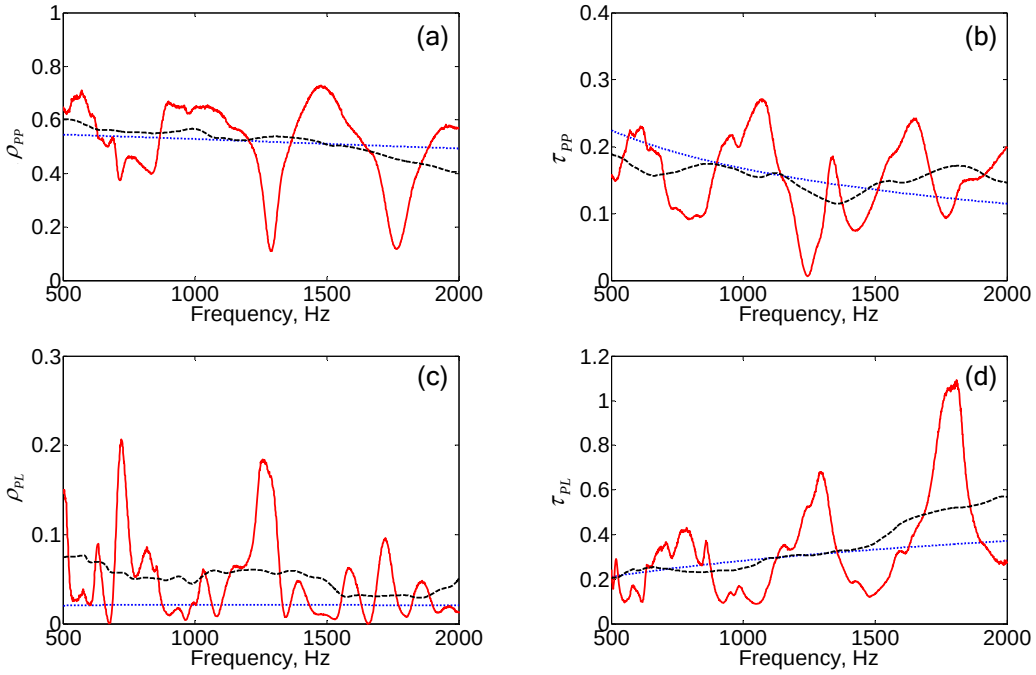

Figure 7.10 Results for the power reflection and transmission coefficients of the right-angled bend when iterating on the rotational stiffness using ρ_{PP}: $\chi = 1$, $\psi = 0.160$: ——, raw measured; – – – –, frequency averaged; ·····, predicted from identified parameters.

Figure 7.11 shows the predicted power reflection and transmission coefficients based on the iteration on the rotational stiffness parameter ψ through τ_{PP} when $\chi = 1$. $\psi = 0.156$ is obtained for this case. It is very close to the result when iterating using ρ_{PP}. It can be concluded that this right-angled bend behaves as a rotational spring-like joint in the frequency range discussed. In the axial direction the joint is considered to be rigidly connected; the rotational stiffness of the bend is about the bending stiffness of a

cantilevered pipe of length 6 times the radius of gyration of the cross-section with a moment applied at the end.

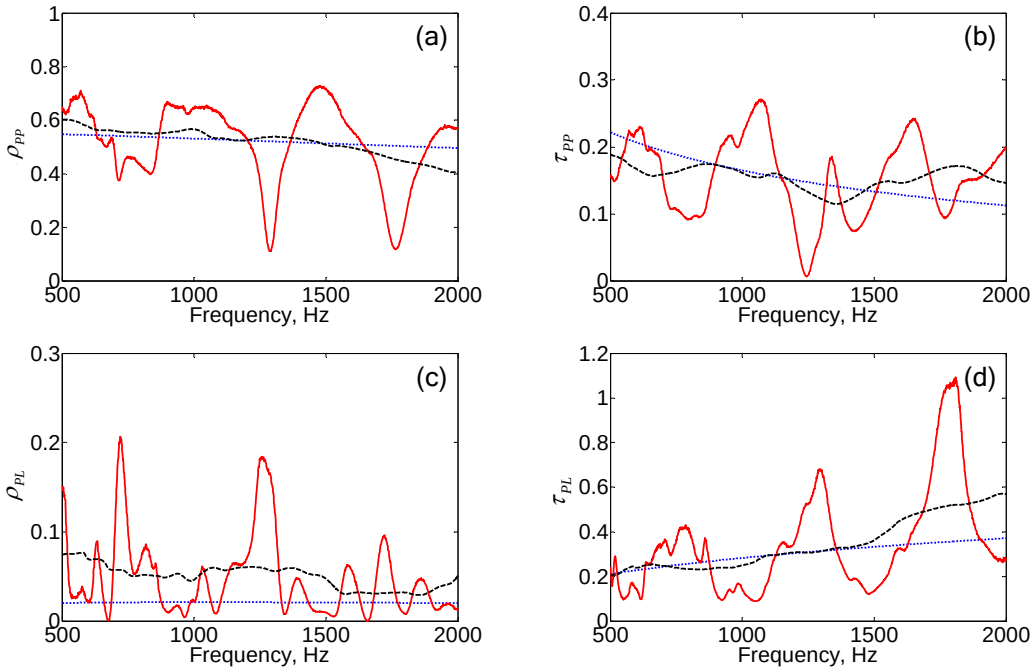

Figure 7.11 Results for the power reflection and transmission coefficients of the right-angled bend when iterating on the rotational stiffness using $\tau_{bb}: \chi = 1,\ \psi = 0.156$: ——, raw measured; – – – –, frequency averaged; ·····, predicted from identified parameters.

The difference between the identified and measured reflection and transmission coefficients originated from the limitations of the experimental data rather than the parameter identification method itself.

7.5 Summary

In this chapter, the joint identification method was applied to three types of structures, mass-like discontinuities on a beam, supported straight pipes and a right-angled pipe bend using measured reflection and transmission coefficients. The parameters of the first two structures estimated in this way were compared to the directly measured ones and good agreement has been achieved. There were problems with the pipe bend mainly because of the limitations in the experimental data rather than the method itself. Some problems concerning the iteration process were discussed, which can be concluded in

what follows.

The selection of the frequency range for the parameter updating process relies on the sensitivity of the objective function to the parameters and the accuracy of the measured data. These two aspects should also be considered when choosing the power reflection or transmission coefficient to compose the objective function. High sensitivity of the objective function to the parameters and good quality of measured data lead to accurate estimates.

The confidence of the estimated parameters is determined by the sensitivity of the objective function. For an insensitive parameter, if an appropriate value can be assumed, then removing this parameter from the iterative process can improve the conditioning of the process and increase the accuracy of the other parameters. If the above effort fails, a more suitable parametric model might be needed for the structure.

In all, the parametric models for the structures are appropriate and can reveal the general trend of the reflection and transmission coefficients. The joint identification method is robust for the parameter identification of the discontinuities from the measured power reflection and transmission coefficients.

Chapter 8 Conclusions

8.1 Introduction

The motivation of this thesis has been to develop an approach by which the parameters of joints in beams and pipes can be estimated from the measured reflection and transmission coefficients. This chapter summarises the contributions that this work has made to the field. Recommendations for future work are given in the light of the conclusions drawn in this research.

8.2 Modelling of Joints and Discontinuities

Dynamic modelling of joints and discontinuities in built-up structures is a challenging task owing to the uncertainty involved in the joints and discontinuities. In most cases, the parameters of joints, such as their damping, stiffness, mass and inertia cannot be accurately modelled due to manufacturing uncertainties and variability of material and dimensions. In this thesis, joint models, such as a mass and moment of inertia discontinuity on a straight beam, a supported straight pipe and a right-angled pipe bend have been examined in Chapters 2, 4 and 5 respectively by using a general wave approach. By using wave approach, the displacements and internal forces can be related to the general wave amplitude vectors in terms of the displacement and internal force matrices respectively. Thus the conventional displacement continuity and force equilibrium equations can then be transformed and expressed by the wave amplitude vectors of the waveguides. This feature of wave approach makes it superior to modal method at solving problems of continuous systems. The parameter identification is based on the premise of the establishment of the joint models. For each joint model, the effect of joint parameters on wave reflection and transmission coefficients has been investigated through closed form solutions and numerical simulations. The experimental

results of the reflection and transmission coefficients of the three types of joints agreed well with the chosen models, which is prerequisite for the parameter identification in later chapters.

8.3 Measurement Considerations

A wave amplitude decomposition method has been reviewed by which the reflection and transmission coefficients of discontinuities in waveguides can be estimated from transducer array measurements. The estimation of reflection and transmission coefficients involves the post processing of measurements in which measurement noise can be amplified. A Gaussian-like noise model has been adopted to represent the measurement noise and a perturbation technique has been used to obtain closed form solutions for the mean and variance of the power reflection and transmission coefficients. These agree well with the Monte Carlo simulations. This has been discussed in Chapter 3. The exercise has given some insight into frequency ranges where reflection and transmission coefficients can be reliably estimated. This helps to determine the frequency ranges to accurately estimate the joint parameters from the measured scattering coefficients.

8.4 Parameter Identification

A parameter identification approach previously applied to FE models has been adapted in Chapter 6 to estimate the parameters of the wave models. Since the phases of measured reflection and transmission coefficients typically change rapidly with the transducer locations and cannot be measured accurately, only the magnitudes of the coefficients have been used. Thus the power reflection coefficient or power transmission coefficient has been chosen to establish the objective function, which is a non-linear function of the parameters of the wave models. The selection of the initial parameters, criteria of terminating the iteration process and evaluation of the accuracy of the estimates have been discussed. The updating approach converges rapidly when the initial parameters are estimated with sufficient accuracy.

8.5 Validation of Parameter Identification Approach

The joint parameter identification technique has been validated through both simulated and experimental case studies. Experimental case studies of mass and moment of inertia discontinuities on a straight beam, pipe supports and a right-angled pipe bend have been implemented in Chapter 7. The parameter identification approach is successful at accurately estimating joint parameters discussed in this thesis, which reaches the final objective of this research. However, some aspects concerning the iteration procedure should be noted:

1) For complex discontinuities, such as the pipe supports and right-angled bend, in order to include all properties of the structures, physical parameters such as stiffness, damping, mass and moment of inertia are all considered in the models. However, for a given structure used in the experiments, it is quite likely that only some particular parameters dominate the dynamic behaviour. In this case, the selection of updating parameters is vital for the iteration process of estimating the properties of the discontinuities. Including parameters to which the objective function is insensitive may result in inaccurate answers. For the structures used in the experiments, appropriate parameters have been chosen for updating and good results have been obtained.
2) The frequency ranges included in the iteration process influence the identification results since in different frequency ranges the sensitivity of the objective function to unknown parameters might be different. Furthermore, measures have been taken to avoid the frequency ranges which have large effect on the measurements.
3) The Jacobean matrix of the objective function becomes ill-conditioned when any two parameters to be updated have similar effects on the output at every measurement, or when the objective function is insensitive to one or more parameters. By adjusting the objective function and reselecting the parameters to update, the conditioning of the updating process can be improved to enable convergence of the update where divergence occurs previously.

8.6 Future Work

The research carried out in this thesis has enhanced the dynamic modelling of discontinuities in waveguides and increased the understanding of estimating stiffness, mass and inertia from measured reflection and transmission coefficients. The following topics warrant some further work.

1) A measurement noise model has been given in Chapter 3 and the influence of the noise on the estimated reflection and transmission coefficients has been discussed. Further research on the noise model would help to understand the nature of measurement noise better. For example, different noise levels could be assumed on different transducers and the statistical distribution characteristics of the estimated reflection and transmission coefficients could be examined further.
2) This thesis has focused on the parameter identification of stiffnesses, mass and inertia. Damping has not been thoroughly investigated. Further identification of the damping of a structure would help to know the energy loss in the system.
3) With the increasing number of parameters to update, the iterative method presented in this research becomes ill-conditioned. More robust methods for parameter identification are still required to accommodate more parameters, such as damping.
4) Only the flexural and longitudinal waves were discussed in this thesis. The reflection and transmission coefficients of other types of waves, such as high order wave modes of pipes, might be more sensitive to the joint parameters. Further research on this topic is worthwhile.

References

1. L. Cremer, M. Heckl and M.M. Ungar 1973 Structure-borne sound. Berlin: Springer Verlag.
2. J.F. Doyle 1997 Wave propagation in structures. 2nd ed., New York: Springer Verlag.
3. F.J. Fahy 1985 Sound and structural vibration: radiation, transmission and response. London: Academic Press Limited.
4. D.J. Mead 1998 Passive vibration control. West Sussex: John Wiley & Sons.
5. R.D. Cook 1989 Concepts and applications of finite element analysis. 3rd ed., New York: Wiley.
6. M.I. Friswell and J.E. Mottershead 1995 Finite element model updating in structural dynamics. Dordrecht: Kluwer academic publishers.
7. M. Petyt 1990 Introduction to finite element vibration analysis. Cambridge: Cambridge University Press.
8. B.R. Mace 1997 Wave coherence, coupling power and statistical energy analysis. Journal of Sound and Vibration **199**: 369-380.
9. M. Liu and R.E. Taylor 2000 Modelling liquid-structure interactions within the framework of statistical energy analysis. Journal of Sound and Vibration **238**: 547-574.
10. B.R. Mace 1993 Statistical energy analysis of two continuous one-dimensional subsystems. Journal of Sound and Vibration **166**(3): 429-461.
11. C. de Jong 1994 Analysis of pulsations and vibrations in fluid-filled pipe systems. PhD thesis: TNO Institute of applied physics.
12. A. Wang 1999 Vibration analysis of fluid filled pipework systems. PhD thesis: University of Southampton.
13. D.M. Lee, M.J. Choi and T.Y. Oh 1996 Transfer matrix modelling for the 3-dimentional vibration analysis of piping system containing fluid flow. KSME Journal **10**: 180-189.
14. E.E. Ungar 1973 The status of engineering knowledge concerning the damping of built-up structures. Journal of Sound and Vibration **26**: 141-154.
15. R.S. Richardson and H. Nolte 1977 Energy dissipation in rotary structural joints. Journal of Sound and Vibration **54**: 577-588.
16. S.L. Folkman, E.A. Roswell and G.D. Ferney 1995 Influence of pinned joints on damping and dynamic behavior of a truss. Journal of Guidance and Control Dynamics **18**: 1398-1403.
17. C.F. Beards and J.L. Williams 1977 The damping of structural vibration by rotating slip in joints. Journal of Sound and Vibration **53**: 333-340.
18. E.H. Dowell 1986 Damping in beams and plates due to slipping at the support boundaries. Journal of Sound and Vibration **105**: 243-253.
19. D.M. Tang and E.H. Dowell 1986 Damping in beams and plates due to slipping at the support boundaries, part 2: numerical and experimental study. Journal of Sound and Vibration **108**: 509-522.

20. D.M. Tang and E.H. Dowell 1986 Random response of beams and plates with slipping at support boundaries. American Institute of Aeronautics and Astronautics Journal **24**: 1354-1361.
21. J. Esteban and C.A. Rogers 2000 Energy dissipation through joints: theory and experiments. Computers and Structures **75**: 347-359.
22. F. Wang and S. Chen 1996 A method to determine the boundary condition of the finite element model of a slender beam using measured modal parameters. American Society of Mechanical Engineers, Journal of Vibration and Acoustics **118**: 474-478.
23. U. Lee and J. Kim 2000 Determination of non-ideal beam boundary conditions: a spectral element approach. American Institute of Aeronautics and Astronautics Journal **38**: 309-316.
24. J.F. Doyle and S. Kamle 1987 An experimental study of the reflection and transmission of flexural waves at an arbitrary T-joint. ASME Journal of Applied Mechanics **54**: 136-140.
25. L.A. Zadeh 1965 Fuzzy sets. Information Control **8**: 338-353.
26. M. Hanss and K. Willner 2000 A fuzzy arithmetical approach to the solution of finite element problems with uncertain parameters. Mechanical Research Communication **29**: 257-272.
27. T.P. Waters 1995 Finite element model updating using frequency response functions. PhD thesis: University of Bristol: Bristol.
28. J. He 1987 Identification of structural dynamic characteristics. PhD thesis: Imperial College of Science, Technology and Medicine.
29. S.Z. Rad 1997 Methods for updating numerical models in structural dynamics. PhD thesis: Imperial College of Science, Technology and Medicine.
30. H. Grafe 1998 Model updating of large structural dynamics models using measured response function. PhD thesis: Imperial College of Science, Technology and Medicine.
31. R.A. Ibrahim and C.L. Pettit 2005 Uncertainties and dynamic problems of bolted joints and other fasteners. Journal of Sound and Vibration **279**: 857-936.
32. J.E. Mottershead and M.I. Friswell 1993 Modal updating in structural dynamics: a survey. Journal of Sound and Vibration **167**(2): 347-375.
33. D.J. Ewins 1984 Modal testing: theory and practice. Letchworth: Research Studies Press.
34. H.G. Natke 1988 Updating computational models in the frequency domain based on measured data: a survey. Probabilistic Engineering Mechanics **3**(1): 28-35.
35. M. Imregun and W.J. Visser 1991 A review of model updating techniques. The Shock and Vibration Digest **23**(1): 9-20.
36. H.G. Natke G. Lallement N. Cottin, et al. 1995 Properties of various residuals within updating of mathematical models. Inverse Problems in Engineering **1**: 329-348.
37. H.G. Natke 1982 Identification of vibrating structures. Berlin: Springer Verlag.
38. A. Berman 1984 System identification of structural dynamic models - theoretical and practical bounds. AIAA conference, 929.
39. A. Berman 1984 Limitations on the identification of discrete structural dynamic models. 2nd International Conference on Recent Advances in Structural Dynmics. Southampton.

40. K.T. Yang and Y.S. Park 1993 Joint structural parameter identification using a subset of frequency response function measurements. Mechanical Systems and Signal Processing **7**: 509-530.
41. J.S. Tsai and Y.F. Chou 1988 The identification of dynamic characteristics of a single bolt joint. Journal of Sound and Vibration **125**(3): 487-502.
42. J.H. Wang and C.M. Liou 1989 Experimental substructure synthesis with linear joints. The International Journal of Analytical and Experimental Modal Analysis, **5**(1): 13-24.
43. Y. Ren and C.F. Beards 1995 Identification of joint properties of a structure using FRF data. Journal of Sound and Vibration **186**: 567-587.
44. J.E. Mottershead and R. Stanway 1986 Identification of structural vibration parameters by using a frequency domain filter. Journal of Sound and Vibration **109**: 495-506.
45. S.W. Hong and C.W. Lee 1991 Identification of linearised joint structural parameters by combined use of measured and computed frequency responses. Mechanical Systems and Signal Processing **5**(4): 267-277.
46. X. Ma, L. Bergman and A. Vakakis 2001 Identification of bolted joints through laser vibrometry. Journal of Sound and Vibration **246**(3): 441-460.
47. Y. Ren and C.F. Beards 1993 An iterative FRF joint identification technique. Proceedings of the 11th International Modal Analysis Conference, 1600-1605.
48. Y. Ren and C.F. Beards 1993 On the importance of weighting on FRF joint identification techniques. Proceedings of the 11th International Modal Analysis Conference, 1606-1611.
49. Y. Ren and C.F. Beards 1993 On the nature of the FRF joint identification techniques. Proceedings of the 11th International Modal Analysis Conference, 1612-1617.
50. H.Y. Hwang 1998 Identification techniques of structure connection parameters using frequency response function. Journal of Sound and Vibration **212**(3): 469-479.
51. Y Rong and H.S. Tzou 1991 Simulation and experiment study on system identifications of elastically jointed structures. ASME Design Engineering Division, Structural Vibration and Acoustics **34**: 119-123.
52. S. Frikha, G. Coffignal and J.L. Trolle 2001 Boundary condition error for parametric updating of in-operation systems - application to operating piping systems. Journal of Acoustical Society of America **241**(3): 373-399.
53. W. Seemann 1996 Transmission and reflection coefficients for longitudinal waces obtained by a combination of refined rod theory and FEM. Journal of Sound and Vibration **197**(5): 571-587.
54. B.R. Mace 1997 Wave analysis of the T-beam. Proceedings of Internoise 97.
55. C.R. Halkyard and B.R. Mace 1998 Energy flow in a T-beam structure: measurement and modelling. Proceedings of Internoise 98.
56. M. Beshara and A.J. Keane 1997 Vibrational energy flows in beam networks with compliant and dissipative joints. Journal of Acoustical Society of America **203**: 321-339.
57. M.S. Ewing and S. Mirsafian 1996 Forced vibration of two beams joined with a non-linear rotational joint: clamped and simply supported end conditions. Journal of Acoustical Society of America **193**: 483-496.
58. C.R. Halkyard and B.R. Mace 1995 Structural intensity in beams - waves, transducer systems and the conditioning problem. Journal of Sound and Vibration **185**(2): 279-298.

59. R.C.N. Leung and R.J. Pinnington 1990 Wave propagation through right-angled joints with compliance-flexural incident wave. Journal of Sound and Vibration **142**(1): 31-46.
60. R.C.N. Leung and R.J. Pinnington 1992 Wave propagation through right-angled joints with compliance-longitudinal incident wave. Journal of Sound and Vibration **153**(2): 223-237.
61. B.R. Mace 1984 wave reflection and transmission in beams. Journal of Sound and Vibration **97**(2): 237-246.
62. J. Linjama 1993 Measurement of bending wave reflection and impedance in a beam by the structural intensity technique. Journal of Acoustical Society of America **161**(2): 317-331.
63. J.M. Muggleton, T.P. Waters and B.R. Mace 2006 Measuring the reflection and transmission coefficients of joints in piping systems. 9th International Conference on Recent Advances in Structural Dynamics. Southampton.
64. N.R. Harland, B.R. Mace and R.W. Jones 2001 Wave propagation, reflection and transmission in tunable fluid-filled beams. Journal of Sound and Vibration **241**(5): 735-754.
65. C.R. Halkyard 2003 Sensor array design for wave decomposition in the presence of coupled motion. Journal of Sound and Vibration **259**: 935-953.
66. J.G. Peatman 1964 Introduction to applied statistics. New York: Harpper & Row Ltd.
67. T.P. Desmond 1981 Theoretical and experimental investigation of stress waves at a junction of three bars. ASME Journal of Applied Mechanics **48**: 148-154.
68. M.J. Brennan, S.J. Elliott and R.J. Pinnington 1997 The dynamic coupling between piezoceramic actuators and a beam. Journal of the Acoustical Society of America **102**: 1931-1942.
69. C.T. Kelley 1999 Iterative methods for optimization. Philadelphia: Society for Industrial and Applied Mathematics.
70. P.E. Gill, W. Murray and M.H. Wright 1993 Practical Optimization London: Academic Press.
71. N.R. Draper and H. Smith 1998 Applied Regression Analysis. 3rd ed., New York: John Wiley & Sons.
72. P.R. Bevington and D.K. Robinson 1992 Data reduction and error analysis for the physical sciences. 2nd ed., Boston: WCB/McGraw-Hill.

Appendix 1 Longitudinal Wave Propagation in Rods

Wave equation	$\frac{\partial^2 u}{\partial t^2} = c_l^2 \frac{\partial^2 u}{\partial x^2}$
Solutions	$u(x,t) = Be^{i(\omega t - k_l x)} + De^{i(\omega t + k_l x)}$
Wave properties	Wave speed $c_l = \sqrt{\frac{E}{\rho}}$, Wave number $k_l = \omega\sqrt{\frac{\rho}{E}}$, $k_l = \frac{\omega}{c_l}$ Group speed $c_g = \frac{\mathrm{d}\omega}{\mathrm{d}k} = \sqrt{\frac{E}{\rho}}$, $c_g = c_l$
Response of a semi-infinite rod excited by a point force at the end	
Case 1	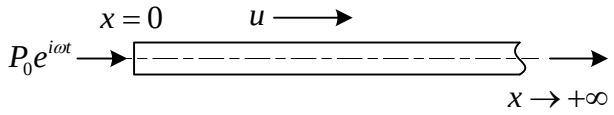
Waves in the rod	$u(x,t) = U_0 e^{i(\omega t - k_l x)}$
Response	Boundary condition: Force balance: $P_0 e^{i\omega t} = EA\left.\frac{\partial u}{\partial x}\right\|_{x=0} \Rightarrow P_0 e^{i\omega t} = EA(-ik_l U_0 e^{i\omega t})$ Solutions: $U_0 = -\frac{P_0}{i\omega Z_0}$, Characteristic impedance $Z_0 = A\sqrt{\rho E} = \rho A c_l = EA/c_l$
Wave reflection at a boundary of a semi-infinite rod with an impedance Z_T attached to the end	
Case 2	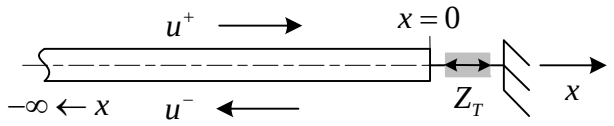
Waves in the rod	Amplitude of incident wave: $u^+(x,t) = U_0 e^{i(\omega t - k_l x)}$, Amplitude of reflected wave: $u^-(x,t) = r_l U_0 e^{i(\omega t + ik_l x)}$, Total amplitude at x: $u(x,t) = u^+(x,t) + u^-(x,t)$
Reflection	Boundary condition: Force balance: $P(0,t) = -Z_T \dot{u}(0,t)$ $\Rightarrow EAU_0(-ik_l + ir_l k_l) = -i\omega Z_T U_0(1 + r_l)$

	Reflection coefficient: $r_l = \dfrac{1 - Z_T / Z_0}{1 + Z_T / Z_0}$,
Mass	$Z_T = i\omega m$ Reflection coefficient: $r_l = \dfrac{1 - i\mu\xi^2}{1 + i\mu\xi^2}$. $\begin{pmatrix} m \to 0 : r_l \to 1; \\ m \to \infty : r_l \to -1 \end{pmatrix}$ $\mu = \dfrac{m}{\rho A \kappa}$, $\xi = \sqrt{\omega \dfrac{\kappa}{c_l}}$
Spring	$Z_T = K_T / i\omega$ Reflection coefficient: $r_l = \dfrac{1 + i\chi / \xi^2}{1 - i\chi / \xi^2}$. $\begin{pmatrix} K_T \to 0 : r_l \to 1; \\ K_T \to \infty : r_l \to -1 \end{pmatrix}$ $\chi = \dfrac{K_T}{EA / \kappa}$
Damper	$Z_T = C_T$ Reflection coefficient: $r_l = \dfrac{1 - \delta}{1 + \delta}$. $\begin{pmatrix} C_T \to 0 : r_l \to 1; \\ C_T \to \infty, r_l \to -1; \\ C_T = Z_0, r_l = 0 \end{pmatrix}$ $\delta = \dfrac{C_T}{\rho A c_l}$
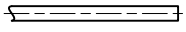 Free end	$r_l = 1$
 Fixed end	$r_l = -1$
Two semi-infinite rods connected by an impedance Z_T	
Case 3	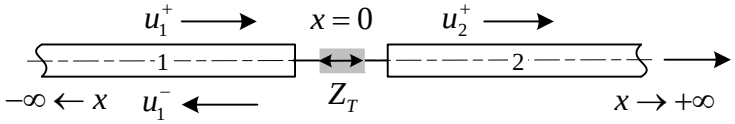
Impedances	$Z_1 = (\rho A c_l)_1 = (EA / c_l)_1$, $Z_2 = (\rho A c_l)_2 = (EA / c_l)_2$
Waves in rods	$u_1^+(x,t) = U_0 e^{i(\omega t - k_{1l} x)}$, $u_1^-(x,t) = r_l U_0 e^{i(\omega t + k_{1l} x)}$, $u_2^+(x,t) = t_l U_0 e^{i(\omega t - k_{2l} x)}$; $u_1(x,t) = u_1^+(x,t) + u_1^-(x,t)$, $u_2(x,t) = u_2^+(x,t)$
Mass	Boundary conditions: $\begin{cases} u_1(0,t) = u_2(0,t) \\ P_2(0,t) - P_1(0,t) = -\omega^2 m u_2(0,t) \end{cases}$ $\Rightarrow \quad \begin{cases} 1 + r_l = t_l \\ Z_2 t_l - Z_1(1 - r_l) = -i\omega m t_l \end{cases}$ Reflection and transmission coefficients:

	$r_l = \dfrac{1-i\mu\xi^2-\xi_1}{1+i\mu\xi^2+\xi_1}, \quad t_l = \dfrac{2}{1+i\mu\xi^2+\xi_1}.$ $\mu = \dfrac{m}{(\rho A\kappa)_1}, \quad \xi = \sqrt{\omega\left(\dfrac{\kappa}{c_l}\right)_1}, \quad \xi_1 = \dfrac{Z_2}{Z_1}$ $\begin{pmatrix} m\to 0: \quad r_l \to \dfrac{1-\xi_1}{1+\xi_1}, \quad t_l \to \dfrac{2}{1+\xi_1}; \\ m\to\infty: \quad r_l \to -1, \quad t_l \to 0 \end{pmatrix}$
Spring	Boundary conditions: $\begin{cases} P_1(0,t) = P_2(0,t) \\ K_T[u_2(0,t)-u_1(0,t)] = P_2(0,t) \end{cases} \Rightarrow \begin{cases} Z_1(1-r_l) = Z_2 t_l \\ K_T(t_l - 1 - r_l) = -i\omega Z_2 t_l \end{cases}$ Reflection and transmission coefficients: $r_l = \dfrac{(1-\xi_1)\chi/\xi^2 + i\xi_1}{(1+\xi_1)\chi/\xi^2 + i\xi_1}, \quad t_l = \dfrac{2\chi/\xi^2}{(1+\xi_1)\chi/\xi^2 + i\xi_1}.$ $\chi = \dfrac{K_T}{(EA/\kappa)_1},$ $\begin{pmatrix} k_T \to 0: \quad r_l \to 1, \quad t_l \to 0; \\ k_T \to \infty: \quad r_l \to \dfrac{1-\xi_1}{1+\xi_1}, \quad t_l \to \dfrac{2}{1+\xi_1} \end{pmatrix}$
Damper	Boundary conditions: $\begin{cases} P_1(0,t) = P_2(0,t) \\ C_T[\dot{u}_2(0,t)-\dot{u}_1(0,t)] = P_2(0,t) \end{cases} \Rightarrow \begin{cases} Z_1(1-r_l) = Z_2 t_l \\ C_T(t_l - 1 - r_l) = -Z_2 t_l \end{cases}$ Reflection and transmission coefficients: $r_l = \dfrac{(1-\xi_1)\delta + \xi_1}{(1+\xi_1)\delta + \xi_1}, \quad t_l = \dfrac{2\delta}{(1+\xi_1)\delta + \xi_1}.$ $\delta = \dfrac{C_T}{(\rho A c_l)_1}$ $\begin{pmatrix} C_T \to 0: \quad r_l \to 1, \quad t_l \to 0; \\ C_T \to \infty: \quad r_l \to \dfrac{1-\xi_1}{1+\xi_1}, \quad t_l \to \dfrac{2}{1+\xi_1} \end{pmatrix}$
 No discontinuity	$r_l = 0, \quad t_l = 1 \qquad (\xi_1 = 1)$
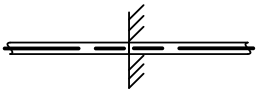 Infinite impedance	$r_l = -1, \quad t_l = 0$

Appendix 2 Bending Wave Propagation in Beams

Wave equation	$EI\dfrac{\partial^4 w(x,t)}{\partial x^4}+\rho A\dfrac{\partial^2 w(x,t)}{\partial t^2}=Q(x,t)$
General solutions	$w(x,t)=(A_1e^{ik_bx}+A_2e^{-ik_bx}+A_3e^{k_bx}+A_4e^{-k_bx})e^{i\omega t}$
Wave properties	Wave speed: $c_b=\omega^{1/2}\left(\dfrac{EI}{\rho A}\right)^{1/4}=\dfrac{\omega}{k_b}$, Wave number: $k_b=\omega^{1/2}\left(\dfrac{\rho A}{EI}\right)^{1/4}$, $k_b=\dfrac{\omega}{c_b}$ Group speed: $c_g=\dfrac{\mathrm{d}\omega}{\mathrm{d}k}=2k_b\left(\dfrac{EI}{\rho A}\right)^{1/2}$, $c_g=2c_b$
Response of a semi-infinite beam excited by a force and a moment at the end	
Case 1	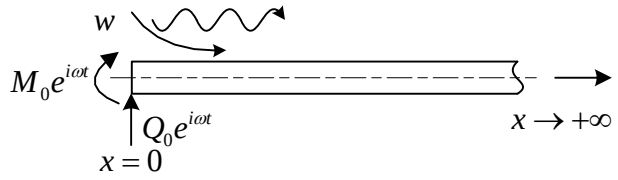
Waves in the beam	$w(x,t)=(W_2e^{-ik_bx}+W_4e^{-k_bx})e^{i\omega t}$
Response	Boundary conditions: Force balance: $\begin{cases}M_0e^{i\omega t}=EIw''(0,t)\\ Q_0e^{i\omega t}=-EIw'''(0,t)\end{cases}$ $\Rightarrow\quad\begin{cases}M_0=EIk_b^2(-W_2+W_4)\\ Q_0=-EIk_b^3(iW_2-W_4)\end{cases}$ Solutions: $W_2=\dfrac{1+i}{2}\left(-\dfrac{M_0}{EIk_b^2}+\dfrac{Q_0}{EIk_b^3}\right)$, $W_4=\dfrac{1-i}{2}\left(\dfrac{M_0}{EIk_b^2}+\dfrac{Q_0}{EIk_b^3}\right)$
Wave reflection at a boundary of a semi-infinite beam with a translational impedance Z_T and a rotational impedance Z_R attached to the end	
Case 2	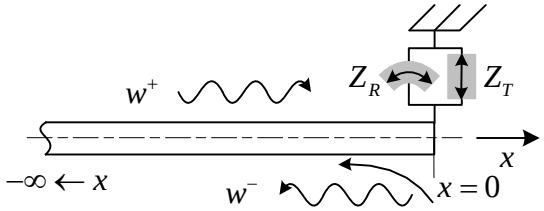
Point impedance	$Z_{T0}=\dfrac{EIk_b^3}{(1-i)\omega}=\dfrac{\rho Ac_b}{1-i}$, $Z_{R0}=\dfrac{EIk_b}{(1+i)\omega}=\dfrac{EI}{(1+i)c_b}$
Characteristic impedance	translational $Z_{T0}^C=\rho Ac_b$, rotational $Z_{R0}^C=EI/c_b$

Waves in the beam	Amplitude of incident wave: $w^+(x,t)=W_0e^{-ik_bx}e^{i\omega t}$ Amplitude of reflected wave: $w^-(x,t)=W_0(r_{\mathrm{p}}e^{ik_bx}+r_{\mathrm{n}}e^{k_bx})e^{i\omega t}$ Total amplitude at x: $w(x,t)=w^+(x,t)+w^-(x,t)$
General impedance	Boundary conditions: Force balance: $\begin{cases}M_z(0,t)=-Z_R\dot{w}'(0,t)\\ Q(0,t)=-Z_T\dot{w}(0,t)\end{cases}$ $\Rightarrow \quad \begin{cases}EIw''(0,t)=-i\omega Z_Rw'(0,t)\\ -EIw'''(0,t)=-i\omega Z_Tw(0,t)\end{cases}$ Reflection coefficients: $r_{\mathrm{p}}=\dfrac{-2iR_TR_R-R_T+R_R-i}{2R_TR_R+R_T+R_R+1}, \quad r_{\mathrm{n}}=\dfrac{(i-1)(2R_TR_R-1)}{2R_TR_R+R_T+R_R+1}.$ $R_T=Z_T/Z_{T0}, \quad R_R=Z_R/Z_{R0}$
Mass $\begin{pmatrix}Z_T=i\omega m,\\ Z_R=i\omega J\end{pmatrix}$	$r_{\mathrm{p}}=\dfrac{-i\mu\vartheta\xi^5+(1+i)\mu\xi^2+(1-i)\vartheta\xi^3+i}{\mu\vartheta\xi^5-(1+i)\mu\xi^2+(1-i)\vartheta\xi^3-1},$ $r_{\mathrm{n}}=\dfrac{(i-1)(\mu\vartheta\xi^5+1)}{\mu\vartheta\xi^5-(1+i)\mu\xi^2+(1-i)\vartheta\xi^3-1}.$ $\mu\xi^2=\dfrac{R_T}{1+i}, \quad \mu=\dfrac{m}{\rho A\kappa}, \quad \xi^2=\dfrac{\omega\kappa}{c_l};$ $\vartheta\xi^3=\dfrac{R_R}{i-1}, \quad \vartheta=\dfrac{J}{\rho A\kappa^3}$ $\begin{pmatrix}m\to 0,J\to 0:(2.1); & m\to 0,J\to\infty:(2.4);\\ m\to\infty,J\to 0:(2.3); & m\to\infty,J\to\infty:(2.2)\end{pmatrix}$
Spring $\begin{pmatrix}Z_T=\dfrac{k_T}{i\omega},\\ Z_R=\dfrac{k_R}{i\omega}\end{pmatrix}$	$r_{\mathrm{p}}=\dfrac{-i\chi\psi/\xi^4-(1+i)\chi/\xi^3+(i-1)\psi/\xi+i}{\chi\psi/\xi^4+(1+i)\chi/\xi^3+(i-1)\psi/\xi-1},$ $r_{\mathrm{n}}=\dfrac{(i-1)(\chi\psi/\xi^4+1)}{\chi\psi/\xi^4+(1+i)\chi/\xi^3+(i-1)\psi/\xi-1}.$ $\dfrac{\chi}{\xi^3}=\dfrac{R_T}{-(1+i)}, \quad \chi=\dfrac{K_T}{EA/\kappa};$ $\dfrac{\psi}{\xi}=\dfrac{R_R}{1-i}, \quad \psi=\dfrac{K_R}{EI/\kappa}$ $\begin{pmatrix}K_T\to 0,K_R\to 0:(2.1); & K_T\to 0,K_R\to\infty:(2.4);\\ K_T\to\infty,K_R\to 0:(2.3); & K_T\to\infty,K_R\to\infty:(2.2)\end{pmatrix}$
Damper $\begin{pmatrix}Z_T=C_T,\\ Z_R=C_R\end{pmatrix}$	$r_{\mathrm{p}}=\dfrac{-i\delta P-(1-i)\delta+(1+i)P-i}{\delta P+(1-i)\delta+(1+i)P+1},$ $r_{\mathrm{n}}=\dfrac{(i-1)(\delta P-1)}{\delta P+(1-i)\delta+(1+i)P+1}.$ $\delta=\dfrac{R_T}{1-i}=\dfrac{C_T}{\rho Ac_b}; \quad P=\dfrac{R_R}{1+i}=\dfrac{C_R}{EI/c_b}$

	$\begin{pmatrix} C_T \to 0, C_R \to 0 : (2.1); & C_T \to 0, C_R \to \infty : (2.4); \\ C_T \to \infty, C_R \to 0 : (2.3); & C_T \to \infty, C_R \to \infty : (2.2) \end{pmatrix}$
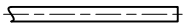 (2.1) Free end	$r_{\mathrm{p}} = -i, \quad r_{\mathrm{n}} = 1 - i$
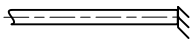 (2.2) Fixed end	$r_{\mathrm{p}} = -i, \quad r_{\mathrm{n}} = i - 1$
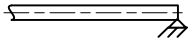 (2.3) Pinned end	$r_{\mathrm{p}} = -1, \quad r_{\mathrm{n}} = 0$
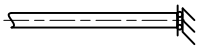 (2.4) Sliding end	$r_{\mathrm{p}} = 1, \quad r_{\mathrm{n}} = 0$
Wave reflection and transmission for two semi-infinite beams connected by impedances Z_T and Z_R	
Case 3	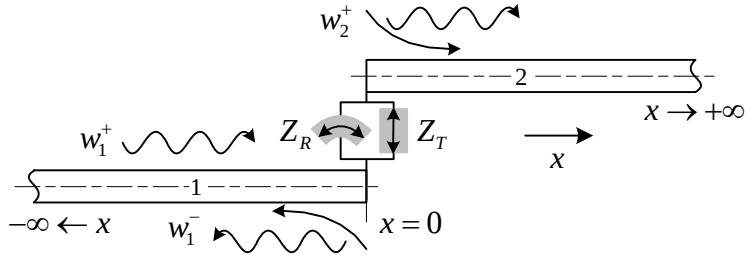 Beam 1 and beam 2 have the same characteristic impedance.
Waves in beams	Amplitude of incident wave: $w_1^+(x,t) = W_0 e^{-ik_b x} e^{i\omega t}$ Amplitude of reflected wave: $w_1^-(x,t) = W_0 (r_{\mathrm{p}} e^{ik_b x} + r_{\mathrm{n}} e^{k_b x}) e^{i\omega t}$ Amplitude of transmitted wave: $w_2^+(x,t) = W_0 (t_{\mathrm{p}} e^{-ik_b x} + t_{\mathrm{n}} e^{-k_b x}) e^{i\omega t}$ Total amplitude in beam 1: $w_1(x,t) = w_1^+(x,t) + w_1^-(x,t)$ Total amplitude in beam 2: $w_2(x,t) = w_2^+(x,t)$
Mass $\begin{pmatrix} Z_T = i\omega m, \\ Z_R = i\omega J \end{pmatrix}$	Boundary conditions: $\begin{cases} \text{continuity of translational displacement}: w_1(0,t) = w_2(0,t) \\ \text{continuity of angular displacement}: w_1'(0,t) = w_2'(0,t) \\ \text{moment balance}: M_{z2}(0,t) - M_{z1}(0,t) = -\omega^2 J w_2'(0,t) \\ \text{force balance}: Q_2(0,t) - Q_1(0,t) = -\omega^2 m w_2(0,t) \end{cases}$ $\Rightarrow \quad \begin{cases} 1 + r_{\mathrm{p}} + r_{\mathrm{n}} = t_{\mathrm{p}} + t_{\mathrm{n}} \\ -i + i r_{\mathrm{p}} + r_{\mathrm{n}} = -i t_{\mathrm{p}} - t_{\mathrm{n}} \\ EIk_b \left[(-t_{\mathrm{p}} + t_{\mathrm{n}}) - (-1 - r_{\mathrm{p}} + r_{\mathrm{n}}) \right] = -\omega^2 J (-i t_{\mathrm{p}} - t_{\mathrm{n}}) \\ -EIk_b^3 \left[(i t_{\mathrm{p}} - t_{\mathrm{n}}) - (i - i r_{\mathrm{p}} + r_{\mathrm{n}}) \right] = -\omega^2 m (t_{\mathrm{p}} + t_{\mathrm{n}}) \end{cases}$ Reflection and transmission coefficients:

	$r_{\mathrm{p}}=-\dfrac{i\xi\left(\mu\vartheta\xi^3+2\vartheta\xi^2-2\mu\right)}{\left(\mu\xi+2-2i\right)\left(\vartheta\xi^3-2-2i\right)}$, $t_{\mathrm{p}}=\dfrac{2\left(\vartheta\xi^3-\mu\xi-4\right)}{\left(\mu\xi+2-2i\right)\left(\vartheta\xi^3-2-2i\right)}$, $r_{\mathrm{n}}=\dfrac{\xi\left[\left(i-1\right)\mu\vartheta\xi^3+2i\vartheta\xi^2+2\mu\right]}{\left(\mu\xi+2-2i\right)\left(\vartheta\xi^3-2-2i\right)}$, $t_{\mathrm{n}}=-\dfrac{2\xi\left(i\vartheta\xi^2-\mu\right)}{\left(\mu\xi+2-2i\right)\left(\vartheta\xi^3-2-2i\right)}$ See Case 2 for μ, ϑ and ξ $\begin{pmatrix} m\to 0, J\to 0:(3.1); & m\to 0, J\to\infty:(3.4); \\ m\to\infty, J\to 0:(3.3); & m\to\infty, J\to\infty:(3.2) \end{pmatrix}$
Spring $\begin{pmatrix} Z_T=\dfrac{K_T}{i\omega}, \\ Z_R=\dfrac{K_R}{i\omega} \end{pmatrix}$	Boundary conditions: $\begin{cases} \text{continuity of moment: } EIw_1''(0,t)=EIw_2''(0,t) \\ \text{continuity of force: } -EIw_1'''(0,t)=-EIw_2'''(0,t) \\ \text{force balance: } k_T\left[w_2(0,t)-w_1(0,t)\right]=-EIw_2'''(0,t) \\ \text{moment balance: } k_R\left[w_2'(0,t)-w_1'(0,t)\right]=EIw_2''(0,t) \end{cases}$ $\Rightarrow \quad \begin{cases} -1-r_{\mathrm{p}}+r_{\mathrm{n}}=-t_{\mathrm{p}}+t_{\mathrm{n}} \\ i-ir_{\mathrm{p}}+r_{\mathrm{n}}=it_{\mathrm{p}}-t_{\mathrm{n}} \\ K_T\left[\left(t_{\mathrm{p}}+t_{\mathrm{n}}\right)-\left(1+r_{\mathrm{p}}+r_{\mathrm{n}}\right)\right]=-EIk_b^3\left(it_{\mathrm{p}}-t_{\mathrm{n}}\right) \\ K_R\left[\left(-it_{\mathrm{p}}-t_{\mathrm{n}}\right)-\left(-i+ir_{\mathrm{p}}+r_{\mathrm{n}}\right)\right]=EIk_b\left(-t_{\mathrm{p}}+t_{\mathrm{n}}\right) \end{cases}$ Reflection and transmission coefficients: $r_{\mathrm{p}}=-\dfrac{2i\left(2\chi/\xi^3-2\psi/\xi-1\right)}{\left(4\chi/\xi^3-1+i\right)\left(4\psi/\xi+1+i\right)}$, $t_{\mathrm{p}}=\dfrac{4\left(4\chi\psi/\xi^4+\chi/\xi^3-\psi/\xi\right)}{\left(4\chi/\xi^3-1+i\right)\left(4\psi/\xi+1+i\right)}$, $r_{\mathrm{n}}=\dfrac{2\left(2\chi/\xi^3+2i\psi/\xi+i-1\right)}{\left(4\chi/\xi^3-1+i\right)\left(4\psi/\xi+1+i\right)}$, $t_{\mathrm{n}}=\dfrac{4\left(\chi/\xi^3-i\psi/\xi\right)}{\left(4\chi/\xi^3-1+i\right)\left(4\psi/\xi+1+i\right)}$ See Case 2 for χ, ψ and ξ $\begin{pmatrix} K_T\to 0, K_R\to 0:(3.5); & K_T\to 0, K_R\to\infty:(3.6); \\ K_T\to\infty, K_R\to 0:(3.7); & K_T\to\infty, K_R\to\infty:(3.1) \end{pmatrix}$
Damper $\begin{pmatrix} Z_T=C_T, \\ Z_R=C_R \end{pmatrix}$	Boundary conditions:

	$\begin{cases}\text{continuity of moment: } EIw_1''(0,t)=EIw_2''(0,t)\\ \text{continuity of shear force: } -EIw_1'''(0,t)=-EIw_2'''(0,t)\\ \text{force balance: } C_T\left[\dot{w}_2(0,t)-\dot{w}_1(0,t)\right]=-EIw_2'''(0,t)\\ \text{moment balance: } C_R\left[\dot{w}_2'(0,t)-\dot{w}_1'(0,t)\right]=EIw_2''(0,t)\end{cases}$ $\Rightarrow \quad \begin{cases}-1-r_{\mathrm{p}}+r_{\mathrm{n}}=-t_{\mathrm{p}}+t_{\mathrm{n}}\\ i-ir_{\mathrm{p}}+r_{\mathrm{n}}=it_{\mathrm{p}}-t_{\mathrm{n}}\\ i\omega C_T\left[(t_{\mathrm{p}}+t_{\mathrm{n}})-(1+r_{\mathrm{p}}+r_{\mathrm{n}})\right]=-EIk_b^3(it_{\mathrm{p}}-t_{\mathrm{n}})\\ i\omega C_R\left[(-it_{\mathrm{p}}-t_{\mathrm{n}})-(-i+ir_{\mathrm{p}}+r_{\mathrm{n}})\right]=EIk_b(-t_{\mathrm{p}}+t_{\mathrm{n}})\end{cases}$ Reflection and transmission coefficients: $r_{\mathrm{p}}=-\dfrac{2\left(2\delta-2P+i\right)}{\left(4\delta+1+i\right)\left(4P+1-i\right)},\quad t_{\mathrm{p}}=\dfrac{4\left(4\delta P-i\delta+iP\right)}{\left(4\delta+1+i\right)\left(4P+1-i\right)},$ $r_{\mathrm{n}}=-\dfrac{2\left(2i\delta-2P+i-1\right)}{\left(4\delta+1+i\right)\left(4P+1-i\right)},\quad t_{\mathrm{n}}=-\dfrac{4\left(i\delta+P\right)}{\left(4\delta+1+i\right)\left(4P+1-i\right)}$ See Case 2 for δ and P $\begin{pmatrix}C_T\to 0,C_R\to 0:(3.5); & C_T\to 0,C_R\to\infty:(3.6);\\ C_T\to\infty,C_R\to 0:(3.7); & C_T\to\infty,C_R\to\infty:(3.1)\end{pmatrix}$
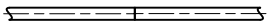 (3.1) No discontinuity	$r_{\mathrm{p}}=0,\ \ r_{\mathrm{n}}=0,\ \ t_{\mathrm{p}}=1,\ \ t_{\mathrm{n}}=0$
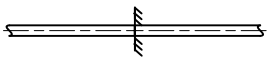 (3.2)Clamped	$r_{\mathrm{p}}=-i,\ \ r_{\mathrm{n}}=i-1,\ \ t_{\mathrm{p}}=0,\ \ t_{\mathrm{n}}=0$
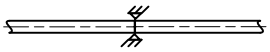 (3.3)Simply supported	$r_{\mathrm{p}}=\dfrac{-1-i}{2},\ \ r_{\mathrm{n}}=\dfrac{-1+i}{2},\ \ t_{\mathrm{p}}=\dfrac{1-i}{2},\ \ t_{\mathrm{n}}=\dfrac{-1+i}{2}$
 (3.4) Sliding support	$r_{\mathrm{p}}=\dfrac{1-i}{2},\ \ r_{\mathrm{n}}=\dfrac{-1+i}{2},\ \ t_{\mathrm{p}}=\dfrac{1+i}{2},\ \ t_{\mathrm{n}}=\dfrac{1-i}{2}$
 (3.5) Separated	$r_{\mathrm{p}}=-i,\ \ r_{\mathrm{n}}=1-i,\ \ t_{\mathrm{p}}=0,\ \ t_{\mathrm{n}}=0$
 (3.6) Double-side sliding	$r_{\mathrm{p}}=\dfrac{1-i}{2},\ \ r_{\mathrm{n}}=\dfrac{1-i}{2},\ \ t_{\mathrm{p}}=\dfrac{1+i}{2},\ \ t_{\mathrm{n}}=\dfrac{-1+i}{2}$
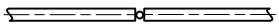 (3.7) Hinge connected	$r_{\mathrm{p}}=\dfrac{-1-i}{2},\ \ r_{\mathrm{n}}=\dfrac{1-i}{2},\ \ t_{\mathrm{p}}=\dfrac{1-i}{2},\ \ t_{\mathrm{n}}=\dfrac{1-i}{2}$
Energy	Power reflection coefficient: $\rho=\dfrac{P_r}{P_i}=\left\lvert r_{\mathrm{p}}\right\rvert^2$ Power transmission coefficient: $\tau=\dfrac{P_t}{P_i}=\dfrac{Z_2}{Z_1}\left\lvert t_{\mathrm{p}}\right\rvert^2$

Appendix 3 Simplification of the general equation for the reflection and transmission coefficients of a mass and moment of inertia discontinuity

The wave vectors are given by equation (2.44) as

$$\mathbf{a}_0^+ = \begin{Bmatrix} W_0 \\ 0 \end{Bmatrix} \text{ and } \mathbf{b}_0^- = \begin{Bmatrix} 0 \\ 0 \end{Bmatrix}. \tag{2.44}$$

Therefore vector

$$\begin{Bmatrix} \mathbf{a}_j^+ \\ \mathbf{b}_j^- \end{Bmatrix} = \begin{Bmatrix} W_0 \\ 0 \\ 0 \\ 0 \end{Bmatrix}. \tag{A3.1}$$

So in the equation (2.43), for the matrix

$$\begin{bmatrix} \boldsymbol{\Psi}_{ja}^- & -\boldsymbol{\Omega}_{11}\boldsymbol{\Psi}_{jb}^+ - \boldsymbol{\Omega}_{12}\boldsymbol{\Phi}_{jb}^+ \\ \boldsymbol{\Phi}_{ja}^- & -\boldsymbol{\Omega}_{21}\boldsymbol{\Psi}_{jb}^+ - \boldsymbol{\Omega}_{22}\boldsymbol{\Phi}_{jb}^+ \end{bmatrix} \begin{bmatrix} \mathbf{R}_j^{aa} & \mathbf{T}_j^{ba} \\ \mathbf{T}_j^{ab} & \mathbf{R}_j^{bb} \end{bmatrix} - \begin{bmatrix} -\boldsymbol{\Psi}_{ja}^+ & \boldsymbol{\Omega}_{11}\boldsymbol{\Psi}_{jb}^- + \boldsymbol{\Omega}_{12}\boldsymbol{\Phi}_{jb}^- \\ -\boldsymbol{\Phi}_{ja}^+ & \boldsymbol{\Omega}_{21}\boldsymbol{\Psi}_{jb}^- + \boldsymbol{\Omega}_{22}\boldsymbol{\Phi}_{jb}^- \end{bmatrix} \tag{A3.2}$$

only the elements in the first column is of interest. And each of them is equal to zero. And the first two columns of the above matrix are given by

$$\begin{bmatrix} \boldsymbol{\Psi}_{ja}^- \mathbf{R}_j^{aa} - \left(\boldsymbol{\Omega}_{11}\boldsymbol{\Psi}_{jb}^+ + \boldsymbol{\Omega}_{12}\boldsymbol{\Phi}_{jb}^+\right)\mathbf{T}_j^{ab} \\ \boldsymbol{\Phi}_{ja}^- \mathbf{R}_j^{aa} - \left(\boldsymbol{\Omega}_{21}\boldsymbol{\Psi}_{jb}^+ + \boldsymbol{\Omega}_{22}\boldsymbol{\Phi}_{jb}^+\right)\mathbf{T}_j^{ab} \end{bmatrix} + \begin{bmatrix} \boldsymbol{\Psi}_{ja}^+ \\ \boldsymbol{\Phi}_{ja}^+ \end{bmatrix} \tag{A3.3}$$

Substituting the equations (2.46) to (2.49) into (A3.3) yields

$$\begin{bmatrix} \begin{bmatrix} 1 & 1 \\ ik_b & k_b \end{bmatrix} \begin{bmatrix} r_{PP} & r_{NP} \\ r_{PN} & r_{NN} \end{bmatrix} - \begin{bmatrix} 1 & 1 \\ -ik_b & -k_b \end{bmatrix} \begin{bmatrix} t_{PP} & t_{NP} \\ t_{PN} & t_{NN} \end{bmatrix} \\ EIk_b^2 \begin{bmatrix} ik_b & -k_b \\ -1 & 1 \end{bmatrix} \begin{bmatrix} r_{PP} & r_{NP} \\ r_{PN} & r_{NN} \end{bmatrix} - \left(\begin{bmatrix} \omega^2 m & \omega^2 m \\ -i\omega^2 Jk_b & -\omega^2 Jk_b \end{bmatrix} + EIk_b^2 \begin{bmatrix} -ik_b & k_b \\ -1 & 1 \end{bmatrix} \right) \begin{bmatrix} t_{PP} & t_{NP} \\ t_{PN} & t_{NN} \end{bmatrix} \end{bmatrix} + \begin{bmatrix} \begin{bmatrix} 1 & 1 \\ -ik_b & -k_b \end{bmatrix} \\ EIk_b^2 \begin{bmatrix} -ik_b & k_b \\ -1 & 1 \end{bmatrix} \end{bmatrix} \tag{A3.4}$$

Since only the first column will be used, then first column of the above matrix is

$$\begin{bmatrix} \begin{bmatrix} r_{PP}+r_{PN} \\ ik_b r_{PP}+k_b r_{PN} \end{bmatrix} - \begin{bmatrix} t_{PP}+t_{PN} \\ -ik_b t_{PP}-k_b t_{PN} \end{bmatrix} \\ EIk_b^2 \begin{bmatrix} ik_b r_{PP}-k_b r_{PN} \\ -r_{PP}+r_{PN} \end{bmatrix} - \begin{bmatrix} \left(\omega^2 m - iEIk_b^3\right) t_{PP} + \left(\omega^2 m + EIk_b^3\right) t_{PN} \\ \left(-i\omega^2 Jk_b - EIk_b^2\right) t_{PP} + \left(-\omega^2 Jk_b + EIk_b^2\right) t_{PN} \end{bmatrix} \end{bmatrix} + \begin{bmatrix} 1 \\ -ik_b \\ -iEIk_b^3 \\ -EIk_b^2 \end{bmatrix} \tag{A3.5}$$

Therefore the final equation becomes

$$\begin{bmatrix} r_{PP}+r_{PN}-t_{PP}-t_{PN} \\ ik_b r_{PP}+k_b r_{PN}+ik_b t_{PP}+k_b t_{PN} \\ iEIk_b^3 r_{PP}-EIk_b^3 r_{PN}-\left(\omega^2 m - iEIk_b^3\right) t_{PP} - \left(\omega^2 m + EIk_b^3\right) t_{PN} \\ -EIk_b^2 r_{PP}+EIk_b^2 r_{PN}+\left(i\omega^2 Jk_b + EIk_b^2\right) t_{PP} + \left(\omega^2 Jk_b - EIk_b^2\right) t_{PN} \end{bmatrix} + \begin{bmatrix} 1 \\ -ik_b \\ -iEIk_b^3 \\ -EIk_b^2 \end{bmatrix} = \begin{bmatrix} 0 \\ 0 \\ 0 \\ 0 \end{bmatrix} \tag{A3.6}$$

This can be written as

$$\begin{bmatrix} 1 & -1 & 1 & -1 \\ ik_b & ik_b & k_b & k_b \\ iEIk_b^3 & -\left(\omega^2 m - iEIk_b^3\right) & -EIk_b^3 & -\left(\omega^2 m + EIk_b^3\right) \\ -EIk_b^2 & \left(i\omega^2 Jk_b + EIk_b^2\right) & EIk_b^2 & \left(\omega^2 Jk_b - EIk_b^2\right) \end{bmatrix} \begin{bmatrix} r_{PP} \\ t_{PP} \\ r_{PN} \\ t_{PN} \end{bmatrix} = \begin{bmatrix} -1 \\ ik_b \\ iEIk_b^3 \\ EIk_b^2 \end{bmatrix} \tag{A3.7}$$

By introducing corresponding symbols the above equation can be expressed as equation (2.50)

Appendix 4 Some definitions of Symbols

Some symbols used in the thesis are derived here and the physical meanings of these symbols are also interpreted.

The longitudinal and flexural wave speeds are given respectively by

$$c_l = \sqrt{\frac{E}{\rho}},\ c_b = \sqrt{\omega}\sqrt[4]{\frac{EI}{\rho A}}. \tag{A4.1}$$

So

$$E = \rho c_l^{\,2},\ EI = \frac{\rho A c_b^{\,4}}{\omega^2}. \tag{A4.2}$$

The longitudinal and flexural wavenumber and the wave speed are related respectively by

$$k_l = \frac{\omega}{c_l},\ k_b = \frac{\omega}{c_b}. \tag{A4.3}$$

Therefore

$$EAk_l = \rho c_l^{\,2} A\frac{\omega}{c_l} = \rho A c_l \omega,\ EIk_b^3 = \frac{\rho A c_b^{\,4}}{\omega^2}\left(\frac{\omega}{c_b}\right)^3 = \rho A c_b \omega. \tag{A4.4}$$

Then

$$\xi_1 = \frac{E_2 A_2 k_{l2}}{E_1 A_1 k_{l1}} = \frac{\rho_2 A_2 c_{l2}}{\rho_1 A_1 c_{l1}},\ \xi_2 = \frac{E_2 I_2 k_{b2}^3}{E_1 A_1 k_{l1}} = \frac{\rho_2 A_2 c_{b2}}{\rho_1 A_1 c_{l1}}. \tag{A4.5}$$

ξ_3 and ξ_4 can be derived in the same way. Here $\rho A c_l$ and $\rho A c_b$ are the longitudinal and translational characteristic impedance of the waveguide. So the meaning of ξ_1 can be explained to be the longitudinal characteristic impedance ratio between the two waveguides.

Similarly

$$\sigma_1 = -i\frac{K_y}{E_1 I_1 k_{b1}^3} = \frac{K_y / i\omega}{\rho_1 A_1 c_{b1}} \tag{A4.6}$$

where $K_y / i\omega$ can be considered the impedance of the spring along *y*-axis. So σ_1 is the ratio of the impedance of the spring along the *y*-axis to the translational characteristic impedance of bending waves in waveguide 1.

Parameter

$$\gamma_2 = i\frac{J_1\omega^2}{E_1 I_1 k_{b1}} = \frac{iJ_1\omega}{E_1 I_1 / c_{b1}} \tag{A4.7}$$

can be explained as the ratio of the impedance of the moment inertia 1 to the rotational characteristic impedance of bending waves in waveguide 1. The rest in equation (3.32) can be interpreted by analogy.

If the material and dimension of the two waveguides are the same, then

$$\xi = \frac{c_b}{c_l} = \frac{\omega\sqrt{\rho/E}}{\sqrt{\omega}\sqrt[4]{\rho A/EI}} = \sqrt{\omega}\sqrt[4]{\frac{\rho I}{EA}} \tag{A4.8}$$

Since that radius of gyration $\kappa = \sqrt{I/A}$ and longitudinal wave speed $c_l = \sqrt{E/\rho}$, then equation (A4.8) becomes

$$\xi = \sqrt{\omega}\sqrt{\kappa/c_l} \tag{A4.9}$$

This can be considered the non-dimensional frequency. Then $\gamma_3 = \xi\gamma_1$ and $\sigma_3 = \xi\sigma_1$. Then

$$\gamma_1 = \frac{im\omega^2}{EIk_b^3} = \frac{im\omega}{\rho A c_b} = \frac{im\xi^2 c_l/\kappa}{\rho A\xi c_l} = i\frac{m}{\rho A\kappa}\xi. \tag{A4.10}$$

Here $\mu = m/\rho A\kappa$ is the ratio between the added mass and the waveguide mass in a length κ. Similarly

$$\gamma_2 = \frac{iJ\omega^2}{EIk_b} = \frac{iJ\omega^3}{\rho A c_b^3} = \frac{iJ\left(\xi^2 c_l/\kappa\right)^3}{\rho A\xi^3 c_l^3} = i\frac{J}{\rho A\kappa^3}\xi^3. \tag{A4.11}$$

Parameter $\vartheta = J/\rho A\kappa^3$ is the ratio between the added moment of inertia and the inertia of the waveguide mass in a length κ with a radius of gyration κ.

As for the stiffness parameter

$$\sigma_1 = -i\frac{K_T}{EIk_b^3} = -i\frac{K_T\xi^3 c_l^3}{EA\kappa^2\left(\xi^2 c_l/\kappa\right)^3} = -i\frac{K_T}{EA/\kappa}\frac{1}{\xi^3}. \tag{A4.12}$$

Parameter $\chi = K_T/\left(EA/\kappa\right)$ is the ratio between the transverse stiffness the spring and the axial stiffness of the waveguide in a length κ.

Parameter

$$\sigma_2 = -i\frac{K_R}{EIk_b} = -i\frac{K_R c_b}{EI\omega} = -i\frac{K_R\xi c_l}{EI\xi^2 c_l/\kappa} = -i\frac{K_R}{EI/\kappa\,\xi}\frac{1}{\xi}. \tag{A4.13}$$

Parameter $\psi = K_R / \left(EI / \kappa \right)$ is the ratio between the rotational stiffness of the spring and the rotational stiffness of a cantilever waveguide in a length κ.

Appendix 5 Mean Values and Variances of Noisy Reflection and Transmission Coefficients

In this appendix, the mean values and the standard deviations of the estimated power reflection and transmission coefficients are derived in detail.

1. The Expectation of the Estimated Power Reflection Coefficient $\hat{\rho}$:

Taking the expected value of both sides of equation (3.18) gives

$$\mu_{\hat{\rho}} \doteq |r|^2 + |r|^2 E\left[2\,\mathrm{Re}\left(\varepsilon_1 - \varepsilon_2 + \varepsilon_2^2 - \varepsilon_1\varepsilon_2 - \varepsilon_1^{\mathrm{H}}\varepsilon_2\right) + \varepsilon_1\varepsilon_1^{\mathrm{H}} + \varepsilon_2\varepsilon_2^{\mathrm{H}}\right] \tag{A5.1}$$

where $E[\bullet]$ denotes taking the expectation. Now each term in the square bracket will be analysed. The expectation of ε_1 is

$$\begin{aligned} E[\varepsilon_1] &= E\left[\frac{e^{2ik_b a}}{2ira_{Pa}^{+}\sin k_b\Delta}\left(-e^{-ik_b\Delta/2}N_1 + e^{ik_b\Delta/2}N_2\right)\right] \\ &= \frac{e^{2ik_b a}}{2ira_{Pa}^{+}\sin k_b\Delta}\left(-e^{-ik_b\Delta/2}E\left[e^{i\phi_1}\right]E[m_1] + e^{ik_b\Delta/2}E\left[e^{i\phi_2}\right]E[m_2]\right) \end{aligned} \tag{A5.2}$$

Since m_1 and m_2 are Gaussian variables with zero mean, $E[m_1]=0$ and $E[m_2]=0$. Then $E[\varepsilon_1]=0$. Similarly, $E[\varepsilon_2]=0$. The expectation of ε_2^2 is given by

$$\begin{aligned} E\left[\varepsilon_2^2\right] &= E\left[\left\{\frac{1}{2ia_{Pa}^{+}\sin k_b\Delta}\left(e^{ik_b\Delta/2}N_1 - e^{-ik_b\Delta/2}N_2\right)\right\}^2\right] \\ &= \frac{-1}{4a_{Pa}^{+2}\sin^2 k_b\Delta}E\left[e^{ik_b\Delta}e^{2i\phi_1}m_1^2 + e^{-ik_b\Delta}e^{2i\phi_2}m_2^2 - 2e^{i\phi_1}e^{i\phi_2}m_1m_2\right] \end{aligned} \tag{A5.3}$$

As mentioned previously, ϕ_1 is uniformly distributed between $-\pi/2$ and $\pi/2$, so

$$E\left[e^{i2\phi_1}\right] = \int_{-\pi/2}^{\pi/2} e^{i2\phi_1}\frac{1}{\pi}d\phi_1 = \frac{1}{\pi}\frac{1}{2i}e^{i2\phi_1}\Big|_{-\pi/2}^{\pi/2} = 0. \tag{A5.4}$$

Similarly, $E\left[e^{i2\phi_2}\right]=0$. Therefore, equation (A5.3) becomes $E\left[\varepsilon_2^2\right]=0$.

The expectation of term $\varepsilon_1\varepsilon_2$ is

$$
\begin{aligned}
E\left[\varepsilon_1\varepsilon_2\right] &= E\left[\frac{e^{2ik_b a}}{2ira_{Pa}^{+}\sin k_b\Delta}\left(-e^{-ik_b\Delta/2}N_1+e^{ik_b\Delta/2}N_2\right)\frac{1}{2ia^{+}\sin k_b\Delta}\left(e^{ik_b\Delta/2}N_1-e^{-ik_b\Delta/2}N_2\right)\right] \\
&= \frac{e^{2ik_b a}}{4ra_{Pa}^{+2}\sin^2 k_b\Delta}E\left[e^{i2\phi_1}m_1^2+e^{i2\phi_2}m_2^2-e^{ik_b\Delta}e^{i\phi_1}e^{i\phi_2}m_1m_2-e^{-ik_b\Delta}e^{i\phi_1}e^{i\phi_2}m_1m_2\right] \qquad \text{(A5.5)} \\
&= 0
\end{aligned}
$$

As for $\varepsilon_1^{\mathrm{H}}\varepsilon_2$,

$$
\begin{aligned}
E\left[\varepsilon_1^{\mathrm{H}}\varepsilon_2\right] &= E\left[\frac{e^{-2ik_b a}}{-2ir^{\mathrm{H}}a_{Pa}^{+\mathrm{H}}\sin k_b\Delta}\left(-e^{-ik_b\Delta/2}N_1+e^{ik_b\Delta/2}N_2\right)^{\mathrm{H}}\frac{1}{2ia_{Pa}^{+}\sin k_b\Delta}\left(e^{ik_b\Delta/2}N_1-e^{-ik_b\Delta/2}N_2\right)\right] \\
&= \frac{-e^{-2ikx_i}}{4r^{\mathrm{H}}\left|a_{Pa}^{+}\right|^2\sin^2 k_b\Delta}E\left[e^{ik_b\Delta}\left|m_1\right|^2+e^{-ik_b\Delta}\left|m_2\right|^2-e^{i\phi_1}e^{-i\phi_2}m_1m_2-e^{-i\phi_1}e^{i\phi_2}m_1m_2\right]
\end{aligned} \qquad \text{(A5.6)}
$$

Since the variance of a variable X can be obtained by $\sigma_X^2 = E\left[X^2\right]-E^2\left[X\right]$, so the expectation of m_1^2 is given by

$$
\begin{aligned}
E\left[m_1^2\right] &= Var\left[m_1\right]+E^2\left[m_1\right] \\
&= Var\left[m_1\right] \\
&= \sigma_1^2\left|a_{Pa}^{+}\right|^2
\end{aligned} \qquad \text{(A5.7)}
$$

where $Var\left[\bullet\right]$ denotes variance. Similarly, $E\left[m_2^2\right]=\sigma_2^2\left|a_{Pa}^{+}\right|^2$. Then equation (A5.6) becomes

$$
E\left[\varepsilon_1^{\mathrm{H}}\varepsilon_2\right] = \frac{-e^{-2ik_b a}}{4r^{\mathrm{H}}\sin^2 k_b\Delta}\left(e^{ik_b\Delta}\sigma_1^2+e^{-ik_b\Delta}\sigma_2^2\right) \qquad \text{(A5.8)}
$$

The expectation of term $\varepsilon_1\varepsilon_1^{\mathrm{H}}$ is

$$
\begin{aligned}
E\left[\varepsilon_1\varepsilon_1^{\mathrm{H}}\right] &= E\left[\left|\varepsilon_1\right|^2\right] \\
&= E\left[\left|\frac{e^{2ik_b a}}{2ira_{Pa}^{+}\sin k_b\Delta}\left(-e^{-ik_b\Delta/2}N_1+e^{ik_b\Delta/2}N_2\right)\right|^2\right] \\
&= \frac{1}{4\left|r\right|^2\left|a_{Pa}^{+}\right|^2\sin^2 k_b\Delta}E\left[\left|m_1\right|^2+\left|m_2\right|^2\right] \\
&= \frac{\sigma_1^2+\sigma_2^2}{4\left|r\right|^2\sin^2 k_b\Delta}
\end{aligned} \qquad \text{(A5.9)}
$$

Similarly the expectation of $\varepsilon_2\varepsilon_2^{\mathrm{H}}$ is

$$
E\left[\varepsilon_2\varepsilon_2^{\mathrm{H}}\right] = E\left[\left|\frac{1}{2ia_{Pa}^{+}\sin k_b\Delta}\left(e^{ik_b\Delta/2}N_1-e^{-ik_b\Delta/2}N_2\right)\right|^2\right] = \frac{\sigma_1^2+\sigma_2^2}{4\sin^2 k_b\Delta} \qquad \text{(A5.10)}
$$

Substituting the above terms into equation (A5.1) and rearranging gives the expectation of $\hat{\rho}$:

$$\mu_{\hat{\rho}} \doteq \rho + \frac{1}{4\sin^2 k_b\Delta}\left\{2\,\mathrm{Re}\left[re^{-2ik_b a}\left(e^{ik_b\Delta}\sigma_1^2 + e^{-ik_b\Delta}\sigma_2^2\right)\right] + (1+\rho)\left(\sigma_1^2+\sigma_2^2\right)\right\} \quad \text{(A5.11)}$$

The maximum and minimum of term $\mathrm{Re}\left[re^{-2ik_b a}\left(e^{ik_b\Delta}\sigma_1^2 + e^{-ik_b\Delta}\sigma_2^2\right)\right]$ are $\pm r\left(\sigma_1^2+\sigma_2^2\right)$ respectively. Therefore, the minimum and maximum of the expectation of $\hat{\rho}$ can be given by

$$\rho + (1-r)^2\frac{\sigma_1^2+\sigma_2^2}{4\sin^2 k_b\Delta} \le \mu_{\hat{\rho}} \le \rho + (1+r)^2\frac{\sigma_1^2+\sigma_2^2}{4\sin^2 k_b\Delta} \quad \text{(A5.12)}$$

Consider further the range of r, the lower and upper bounds of $\mu_{\hat{\rho}}$ can be obtained when $r=1$. These are expressed as

$$\rho \le \mu_{\hat{\rho}} \le \rho + \frac{\sigma_1^2+\sigma_2^2}{\sin^2 k_b\Delta} \quad \text{(A5.13)}$$

So far, the expectation of $\hat{\rho}$ and its lower and upper bounds have been derived. The following section will discuss the standard deviation of $\hat{\rho}$.

2. The variance of the estimated power reflection coefficient $\hat{\rho}$:

This section gives the detailed derivation of the variance of $\hat{\rho}$.

The variance of $\hat{\rho}$ must be acquired before getting its standard deviation. As mentioned previously, the variance of a random variable X can be obtained by $\sigma_X^2 = E\left[X^2\right] - E^2\left[X\right]$. When using this definition to calculate the variance of $\hat{\rho}$, the expectation of $\hat{\rho}^2$ should be obtained first. From equation (3.18),

$$\begin{aligned}
\mu_{\hat{\rho}^2} &= |r|^4 E\left[\left\{1+\left(\varepsilon_1+\varepsilon_1^{\mathrm{H}}\right)-\left(\varepsilon_2+\varepsilon_2^{\mathrm{H}}\right)+\left(\varepsilon_2^2+\varepsilon_2^{2\mathrm{H}}\right)+\varepsilon_1\varepsilon_1^{\mathrm{H}}+\varepsilon_2\varepsilon_2^{\mathrm{H}}-\left(\varepsilon_1\varepsilon_2+\varepsilon_1^{\mathrm{H}}\varepsilon_2^{\mathrm{H}}\right)-\left(\varepsilon_1^{\mathrm{H}}\varepsilon_2+\varepsilon_1\varepsilon_2^{\mathrm{H}}\right)\right\}^2\right] \\
&\doteq |r|^4 E\begin{bmatrix}1+2\left(\varepsilon_1+\varepsilon_1^{\mathrm{H}}\right)-2\left(\varepsilon_2+\varepsilon_2^{\mathrm{H}}\right)+\left(\varepsilon_1^2+\varepsilon_1^{\mathrm{H2}}\right)+3\left(\varepsilon_2^2+\varepsilon_2^{\mathrm{H2}}\right)+4\varepsilon_1\varepsilon_1^{\mathrm{H}}+4\varepsilon_2\varepsilon_2^{\mathrm{H}} \\ -4\left(\varepsilon_1\varepsilon_2+\varepsilon_1^{\mathrm{H}}\varepsilon_2^{\mathrm{H}}\right)-4\left(\varepsilon_1^{\mathrm{H}}\varepsilon_2+\varepsilon_1\varepsilon_2^{\mathrm{H}}\right)\end{bmatrix} \\
&= |r|^4 + 2|r|^4\,\mathrm{Re}\left(E\left[-4\varepsilon_1^{\mathrm{H}}\varepsilon_2\right]\right) + 4|r|^4 E\left[\varepsilon_1\varepsilon_1^{\mathrm{H}}+\varepsilon_2\varepsilon_2^{\mathrm{H}}\right] \\
&= |r|^4 + \frac{|r|^2}{\sin^2 k_b\Delta}\left\{2\,\mathrm{Re}\left[re^{-2ik_b a}\left(e^{ik_b\Delta}\sigma_1^2 + e^{-ik_b\Delta}\sigma_2^2\right)\right] + (1+\rho)\left(\sigma_1^2+\sigma_2^2\right)\right\}
\end{aligned} \quad \text{(A5.14)}$$

In the above deduction, the terms in which the summed indices of ε_1, ε_2, $\varepsilon_1^{\mathrm{H}}$ or $\varepsilon_2^{\mathrm{H}}$ are

higher than second order are neglected. Also the following result is used.

$$E\left[\varepsilon_1^2\right] = E\left[\left\{\frac{e^{2ik_b a}}{2ira_{Pa}^{+}\sin k_b\Delta}\left(-e^{-ik_b\Delta/2}N_1 + e^{ik_b\Delta/2}N_2\right)\right\}^2\right]$$
$$= \frac{-e^{4ik_b a}}{4r^2 a_{Pa}^{+2}\sin^2 k_b\Delta} E\left[e^{-ik_b\Delta}e^{i2\phi_1}m_1^2 + e^{ik_b\Delta}e^{i2\phi_2}m_2^2 - 2e^{i2\phi_1}e^{i2\phi_2}m_1 m_2\right] \quad \text{(A5.15)}$$
$$= 0$$

So the variance of $\hat{\rho}$ can be obtained by

$$\sigma_{\hat{\rho}}^2 = E\left[\hat{\rho}^2\right] - E^2\left[\hat{\rho}\right]$$
$$\doteq \frac{\rho}{2\sin^2 k_b\Delta}\left\{2\,\mathrm{Re}\left[re^{-2ik_b a}\left(e^{ik_b\Delta}\sigma_1^2 + e^{-ik_b\Delta}\sigma_2^2\right)\right] + (1+\rho)\left(\sigma_1^2 + \sigma_2^2\right)\right\} \quad \text{(A5.16)}$$

In equation (A5.16), the terms with second and higher order of σ_1^2 or σ_2^2 are neglected. By a similar way to that of equation (A5.11), the upper bound of the variance of $\hat{\rho}$ can be approximated by

$$\sigma_{\hat{\rho}}^2 \le \frac{2\rho}{\sin^2 k_b\Delta}\left(\sigma_1^2 + \sigma_2^2\right) \quad \text{(A5.17)}$$

3. The expectation of the estimated power transmission coefficient $\hat{\tau}$:

This section gives the deduction of the expected value of estimated power transmission coefficient $\hat{\tau}$.

The expected value of $\hat{\tau}$ can be obtained in a similar way to that of $\hat{\rho}$. Equation (3.25) can also be expressed as

$$\hat{t} = t\left(1+\varepsilon_3\right)\left(1-\varepsilon_2+\varepsilon_2^2+\cdots+\left(-1\right)^n\varepsilon_2^n+\cdots\right). \quad \text{(A5.18)}$$

The estimated power transmission coefficient can be given by

$$\hat{\tau} \approx \tau\begin{bmatrix}1+\varepsilon_3+\varepsilon_3^{\mathrm{H}}-\varepsilon_2-\varepsilon_2^{\mathrm{H}}+\varepsilon_2^2+\varepsilon_2^{\mathrm{H}2}\\ +\varepsilon_2\varepsilon_2^{\mathrm{H}}+\varepsilon_3\varepsilon_3^{\mathrm{H}}-\varepsilon_3\varepsilon_2-\varepsilon_3^{\mathrm{H}}\varepsilon_2^{\mathrm{H}}-\varepsilon_3^{\mathrm{H}}\varepsilon_2-\varepsilon_3\varepsilon_2^{\mathrm{H}}\end{bmatrix}. \quad \text{(A5.19)}$$

Taking the expectation of both sides of the equation gives

$$\mu_{\hat{\tau}} \doteq \tau + |t|^2 E\left[\varepsilon_3+\varepsilon_3^{\mathrm{H}}-\varepsilon_2-\varepsilon_2^{\mathrm{H}}+\varepsilon_2^2+\varepsilon_2^{\mathrm{H}2}+\varepsilon_2\varepsilon_2^{\mathrm{H}}+\varepsilon_3\varepsilon_3^{\mathrm{H}}-\varepsilon_3\varepsilon_2-\varepsilon_3^{\mathrm{H}}\varepsilon_2^{\mathrm{H}}-\varepsilon_3^{\mathrm{H}}\varepsilon_2-\varepsilon_3\varepsilon_2^{\mathrm{H}}\right] \quad \text{(A5.20)}$$

Some of terms in the square bracket have been known. Since N_i are uncorrelated, among the terms with ε_3 or $\varepsilon_3^{\mathrm{H}}$, only the term $\varepsilon_3\varepsilon_3^{\mathrm{H}}$ is non-zero.

The expectation of $\varepsilon_3\varepsilon_3^{\mathrm{H}}$ is obtained by

$$\begin{aligned} E\left[\varepsilon_3\varepsilon_3^{\mathrm{H}}\right] &= E\left[\left|\frac{e^{ik_b(a+b)}}{2ita_{Pa}^{+}\sin k_b\Delta}\left(e^{ik_b\Delta/2}N_3 - e^{-ik_b\Delta/2}N_4\right)\right|^2\right] \\ &= \frac{1}{4|t|^2\left|a_{Pa}^{+}\right|^2\sin^2 k_b\Delta}E\left[|m_3|^2+|m_4|^2\right] \\ &= \frac{\sigma_3^2+\sigma_4^2}{4|t|^2\sin^2 k_b\Delta} \end{aligned} \tag{A5.21}$$

Therefore, equation (A5.20) becomes

$$\begin{aligned} \mu_{\hat{\tau}} &\doteq \tau + |t|^2\left\{E\left[\varepsilon_2\varepsilon_2^{\mathrm{H}}\right]+E\left[\varepsilon_3\varepsilon_3^{\mathrm{H}}\right]\right\} \\ &= \tau + \frac{1}{4\sin^2 k_b\Delta}\left[\tau\left(\sigma_1^2+\sigma_2^2\right)+\sigma_3^2+\sigma_4^2\right] \end{aligned} \tag{A5.22}$$

The above expression is simple enough, so there is no need to calculate its lower and upper bounds.

4. The variance of the estimated power transmission coefficient $\hat{\tau}$:

This section discuss the variance of $\hat{\tau}$. The deduction process is also similar to that of $\hat{\rho}$.

First the expectation of $\hat{\tau}^2$

$$\begin{aligned} \mu_{\hat{\tau}^2} &\doteq |t|^4 E\left[\left(1+\varepsilon_3+\varepsilon_3^{\mathrm{H}}-\varepsilon_2-\varepsilon_2^{\mathrm{H}}+\varepsilon_2^2+\varepsilon_2^{\mathrm{H2}}+\varepsilon_3\varepsilon_3^{\mathrm{H}}+\varepsilon_2\varepsilon_2^{\mathrm{H}}-\varepsilon_3\varepsilon_2-\varepsilon_3^{\mathrm{H}}\varepsilon_2^{\mathrm{H}}-\varepsilon_3^{\mathrm{H}}\varepsilon_2-\varepsilon_3\varepsilon_2^{\mathrm{H}}\right)^2\right] \\ &\doteq |t|^4 E\begin{bmatrix} 1+2\left(\varepsilon_3+\varepsilon_3^{\mathrm{H}}\right)-2\left(\varepsilon_2+\varepsilon_2^{\mathrm{H}}\right)+\left(\varepsilon_3^2+\varepsilon_3^{\mathrm{H2}}\right)+3\left(\varepsilon_2^2+\varepsilon_2^{\mathrm{H2}}\right)+4\varepsilon_3\varepsilon_3^{\mathrm{H}}+4\varepsilon_2\varepsilon_2^{\mathrm{H}} \\ -4\left(\varepsilon_3\varepsilon_2+\varepsilon_3^{\mathrm{H}}\varepsilon_2^{\mathrm{H}}\right)-4\left(\varepsilon_3^{\mathrm{H}}\varepsilon_2+\varepsilon_3\varepsilon_2^{\mathrm{H}}\right) \end{bmatrix} \\ &= |t|^4 E\left[1+4\varepsilon_3\varepsilon_3^{\mathrm{H}}+4\varepsilon_2\varepsilon_2^{\mathrm{H}}\right] \\ &= |t|^4+\frac{|t|^2}{\sin^2 k_b\Delta}\left[|t|^2\left(\sigma_1^2+\sigma_2^2\right)+\sigma_3^2+\sigma_4^2\right] \end{aligned} \tag{A5.23}$$

In the above deduction, the terms in which the summed indices of ε_3, ε_2, $\varepsilon_3^{\mathrm{H}}$ or $\varepsilon_2^{\mathrm{H}}$ are higher than second order are neglected. Also the following result is used.

$$
\begin{aligned}
E\left[\varepsilon_3^2\right] &= E\left[\left(\frac{e^{ik_b(a+b)}}{2it_p a^{+}\sin k_b\Delta}\right)^2\left(e^{ik_b\Delta/2}N_3 - e^{-ik_b\Delta/2}N_4\right)^2\right] \\
&= \frac{-e^{2ik_b(a+b)}}{4t^2 a_{Pa}^{+2}\sin^2 k_b\Delta}E\left[\left(e^{ik_b\Delta/2}e^{i\phi_3}m_3 - e^{-ik_b\Delta/2}e^{i\phi_4}m_4\right)^2\right] \qquad \text{(A5.24)} \\
&= 0
\end{aligned}
$$

The variance of $\hat{\tau}$ is given by

$$
\begin{aligned}
\sigma_{\hat{\tau}}^2 &= \mu_{\hat{\tau}^2} - \left(\mu_{\hat{\tau}}\right)^2 \\
&\doteq \frac{\tau}{2\sin^2 k_b\Delta}\left[\tau\left(\sigma_1^2+\sigma_2^2\right)+\sigma_3^2+\sigma_4^2\right]
\end{aligned} \qquad \text{(A5.25)}
$$

Appendix 6 Conditions for Euler-Bernoulli beam theory and cut-on frequency for *n*=2 wave mode in terms of non-dimensional frequency ξ^2

Euler-Bernoulli beam condition:

The correction terms of the Timoshenko beam equation to Euler-Bernoulli's make less than 10% difference of the wave amplitude when the flexural wavelength satisfies

$$\lambda > 6h \tag{A6.1}$$

where h is the height of the beam.

For a beam with rectangular cross-section $b \times h$:

Radius of gyration

$$\kappa = \sqrt{\frac{I}{A}} = \frac{h}{\sqrt{12}} \tag{A6.2}$$

then $h = \sqrt{12}\kappa$, so $\lambda > 6\sqrt{12}\kappa$. Recalling that

$$\xi = \frac{c_b}{c_l} = \frac{\lambda\omega}{2\pi c_l} \tag{A6.3}$$

then

$$\xi = \frac{\lambda\omega}{2\pi c_l} > \frac{6\sqrt{12}\kappa\omega}{2\pi c_l} = \frac{3\sqrt{12}\xi^2}{\pi} \tag{A6.4}$$

so $\xi < \frac{\pi}{3\sqrt{12}} \approx 0.30$ satisfies the Euler-Bernoulli beam condition.

For a pipe with outside radius A and inside radius a:

$$\kappa = \sqrt{\frac{I}{A}} = \sqrt{\frac{\pi(A^4 - a^4)/4}{\pi(A^2 - a^2)}} = \sqrt{\frac{A^2 + a^2}{4}} \tag{A6.5}$$

If it is a thin pipe, $A \approx a$, then $\kappa = a/\sqrt{2}$. The Euler-Bernoulli pipe condition may be described as $\lambda > 6 \times 2a$. Then $\lambda > 12\sqrt{2}\kappa$, and

$$\xi = \frac{\lambda\omega}{2\pi c_l} > \frac{12\sqrt{2}\kappa\omega}{2\pi c_l} = \frac{6\sqrt{2}\xi^2}{\pi} \tag{A6.6}$$

so $\xi < \frac{\pi}{6\sqrt{2}} \approx 0.37$ satisfies the Euler-Bernoulli beam condition.

Cut-on frequency for $n = 2$ wave mode:

Referring to equation (4.4) the cut-on frequency for the $n = 2$ wave mode is given by

$$\omega_{cut-on} = \omega_r \frac{h}{\sqrt{12}a}\left(2^2 - \frac{3}{2}\right) = \frac{5}{2\sqrt{12}}\frac{hc_l}{a^2} \tag{A6.7}$$

Substituting $\xi_{cut-on} = \sqrt{\omega_{cut-on}}\sqrt{\kappa/c_l}$ into the above equation yields $\xi^2_{cut-on} = \frac{5}{2\sqrt{12}}\frac{h\kappa}{a^2}$.

For cylindrical pipes, $\kappa = a/\sqrt{2}$, so $\xi^2_{cut-on} = \frac{5}{4\sqrt{6}}\frac{h}{a} \approx \frac{h}{a}$.

Appendix 7 Direct Measurements of the Translational Dynamic Stiffnesses of Pipe Supports

The measurements of the translational dynamic stiffness of the short aluminium, long steel and short steel pipe supports are presented in the following figures.

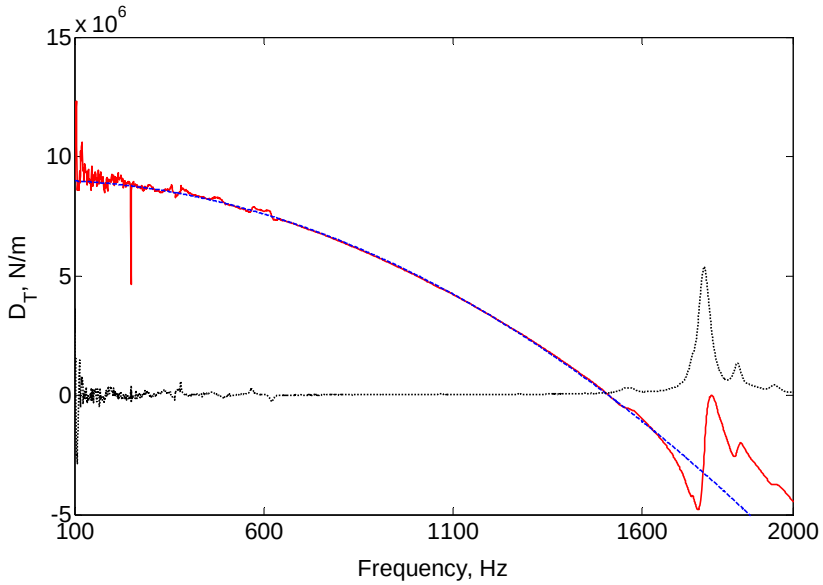

Figure A7.1 Translational dynamic stiffness of the short aluminium support: ——, real part of measured D_T ; - - - - - -, fitted real part of D_T in 400-1400Hz; ·····, imaginary part of measured D_T .

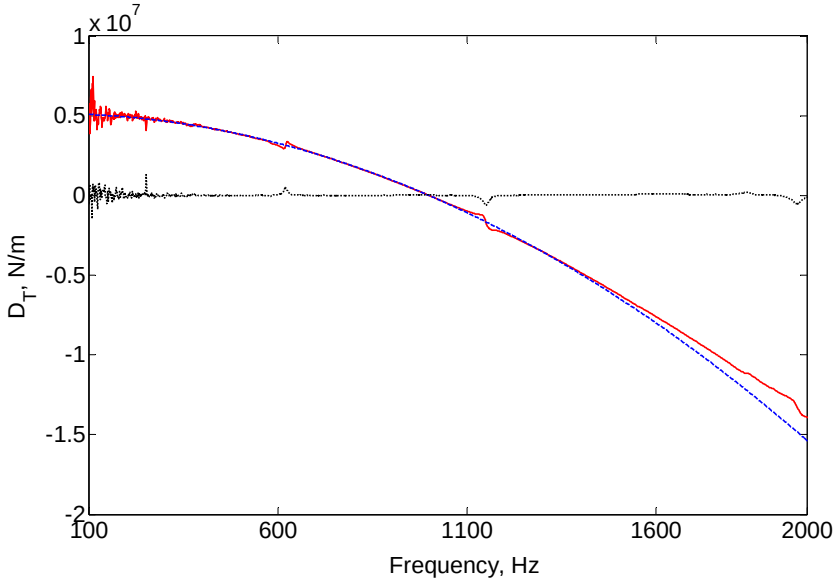

Figure A7.2 Translational dynamic stiffness of the long steel support: ——, real part of measured D_T; - - - - - -, fitted real part of D_T in 200-1400Hz; ...., imaginary part of measured D_T.

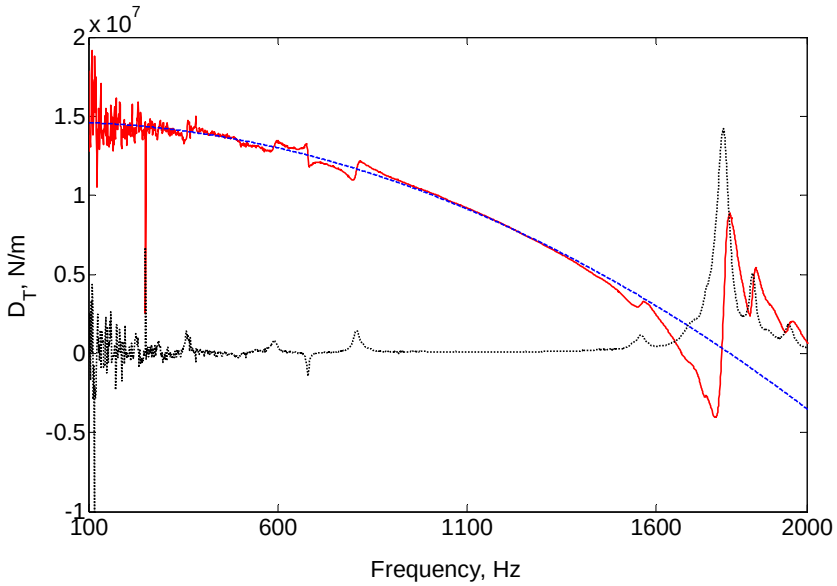

Figure A7.3 Translational dynamic stiffness of the short steel support: ——, real part of measured D_T; - - - - - -, fitted real part of D_T in 400-1400Hz; ...., imaginary part of measured D_T

Appendix 8 Mass-loading Effect of the Force Transducer

Referring to the mass cancellation described in reference [33], the mass-loading effect of the force transducer can be measured in the following way. Figure A8.1 shows the measurement setup. The force transducer was connected to the shaker by a stinger in the vertical direction. A PCB acceleration transducer (with small mass) was attached to the other side of the force transducer. By changing the excitation and/or response point of the force transducer, two types of dynamic masses could be measured. Figure A8.2 shows these two dynamic masses. In the frequency range 1000-2000Hz, the dynamic mass in the standard position is about 0.0090Kg, and when upside down is about 0.0145Kg. So it can be considered the mass-loading of the force transducer is roughly 0.0090Kg when it is in standard position. Compared to the total mass of the force transducer $m_a = 0.0235$ Kg, therefore about 38% of the total mass of the force transducer was added to the support.

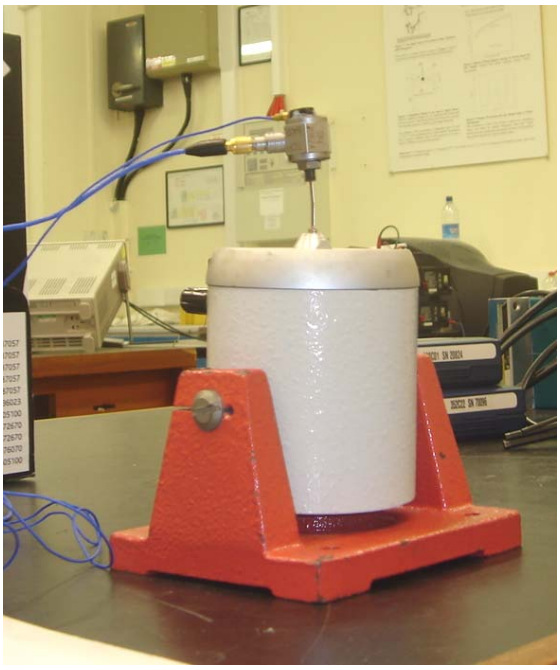

Figure A8.1 Experimental Setup for measuring the mass-loading effect of the force transducer.

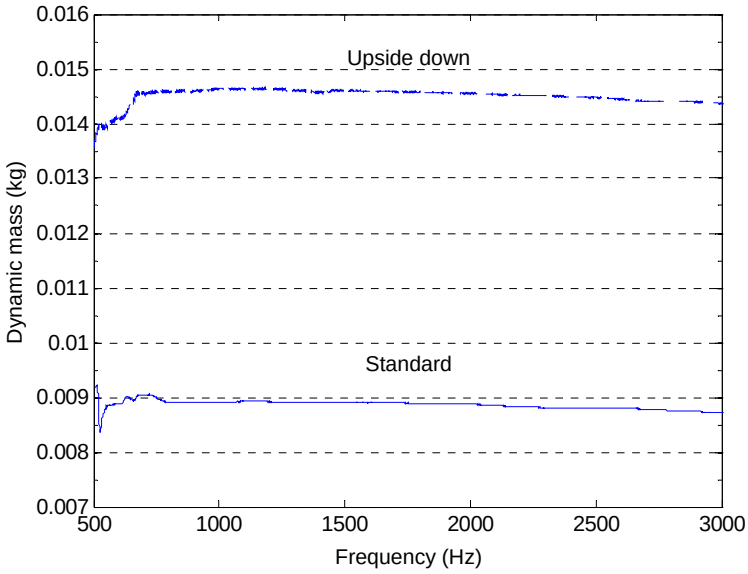

Figure A8.2 Measured dynamic mass of the transducer for the two positions.

Appendix 9 Direct Measurements of the Rotational Dynamic Stiffnesses of Pipe Supports

The measurements of the rotational dynamic stiffness of the short aluminium, long steel and short steel pipe supports are presented in the following figures.

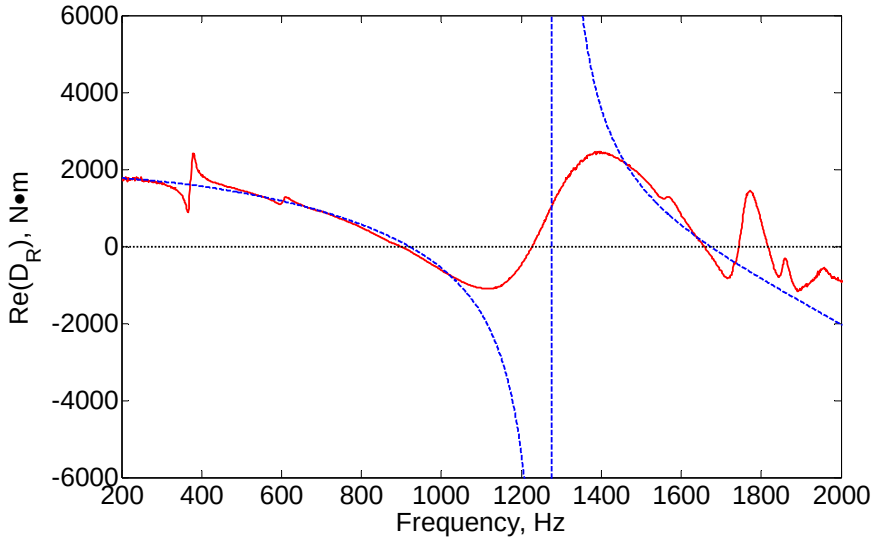

Figure A9.1 Rotational dynamic stiffness of the short aluminium support: ——, real part of measured D_R; - - - - - -, fitted real part of D_R.

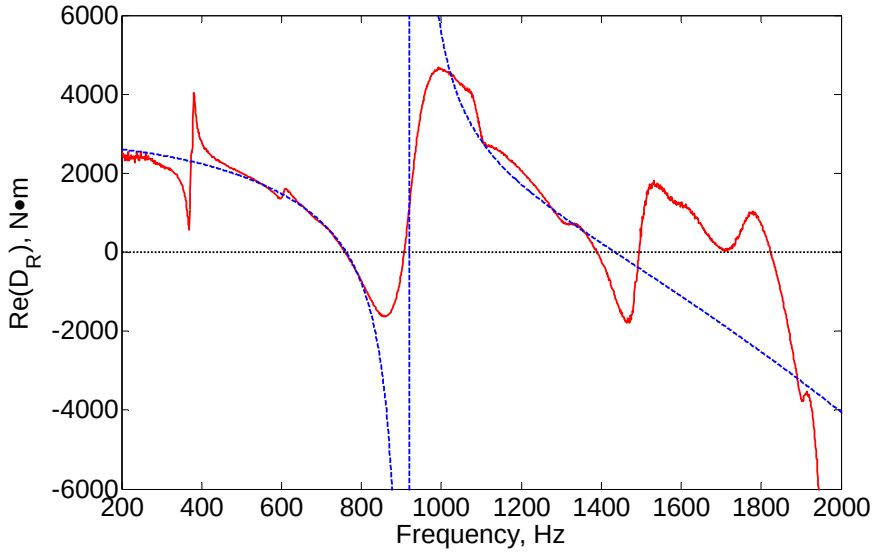

Figure A9.2 Rotational dynamic stiffness of the long steel support: ——, real part of measured D_R; ------, fitted real part of D_R.

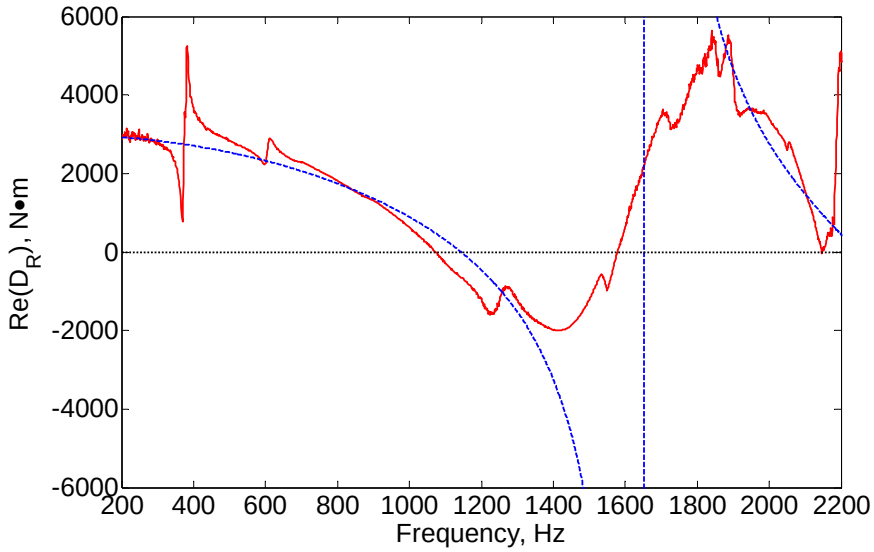

Figure A9.3 Rotational dynamic stiffness of the short steel support: ——, real part of measured D_R; ------, fitted real part of D_R.

Appendix 10 Derivative of a Matrix to a Variable

Derivative of a matrix to a variable can be obtained by the following method:

Since $\mathbf{A}(\mu)^{-1}\mathbf{A}(\mu)=\mathbf{I}$, so

$$\frac{\partial\left(\mathbf{A}^{-1}\mathbf{A}\right)}{\partial\mu}=\frac{\partial\mathbf{A}^{-1}}{\partial\mu}\mathbf{A}+\mathbf{A}^{-1}\frac{\partial\mathbf{A}}{\partial\mu}=0. \tag{A10.1}$$

Then

$$\frac{\partial\mathbf{A}^{-1}}{\partial\mu}=-\mathbf{A}^{-1}\frac{\partial\mathbf{A}}{\partial\mu}\mathbf{A}^{-1}. \tag{A10.2}$$

Since $\left[\mathbf{A}(\mu)^{-1}\mathbf{A}(\mu)\right]^{\mathrm{H}}=\mathbf{I}$, so

$$\frac{\partial\left(\mathbf{A}^{-1}\mathbf{A}\right)^{\mathrm{H}}}{\partial\mu}=\frac{\partial\left(\mathbf{A}^{\mathrm{H}}\left(\mathbf{A}^{-1}\right)^{\mathrm{H}}\right)}{\partial\mu}=\frac{\partial\mathbf{A}^{\mathrm{H}}}{\partial\mu}\left(\mathbf{A}^{-1}\right)^{\mathrm{H}}+\mathbf{A}^{\mathrm{H}}\frac{\partial\left(\mathbf{A}^{-1}\right)^{\mathrm{H}}}{\partial\mu}=0. \tag{A10.3}$$

Then

$$\frac{\partial\left(\mathbf{A}^{-1}\right)^{\mathrm{H}}}{\partial\mu}=-\left(\mathbf{A}^{\mathrm{H}}\right)^{-1}\frac{\partial\mathbf{A}^{\mathrm{H}}}{\partial\mu}\left(\mathbf{A}^{-1}\right)^{\mathrm{H}}. \tag{A10.4}$$

Therefore

$$\begin{aligned}\frac{\partial\rho_{bb}}{\partial\mu}=&\frac{\partial\mathbf{b}^{\mathrm{H}}}{\partial\mu}\left(\mathbf{A}^{-1}\right)^{\mathrm{H}}\mathbf{z}\mathbf{z}^{\mathrm{T}}\mathbf{A}^{-1}\mathbf{b}-\mathbf{b}^{\mathrm{H}}\left(\mathbf{A}^{\mathrm{H}}\right)^{-1}\frac{\partial\mathbf{A}^{\mathrm{H}}}{\partial\mu}\left(\mathbf{A}^{-1}\right)^{\mathrm{H}}\mathbf{z}\mathbf{z}^{\mathrm{T}}\mathbf{A}^{-1}\mathbf{b}\\&-\mathbf{b}^{\mathrm{H}}\left(\mathbf{A}^{-1}\right)^{\mathrm{H}}\mathbf{z}\mathbf{z}^{\mathrm{T}}\mathbf{A}^{-1}\frac{\partial\mathbf{A}}{\partial\mu}\mathbf{A}^{-1}\mathbf{b}+\mathbf{b}^{\mathrm{H}}\left(\mathbf{A}^{-1}\right)^{\mathrm{H}}\mathbf{z}\mathbf{z}^{\mathrm{T}}\mathbf{A}^{-1}\frac{\partial\mathbf{b}}{\partial\mu}\end{aligned}. \tag{A10.5}$$

Appendix 11 Stiffnesses of Several Pipe Support Models

This appendix gives the stiffnesses of several pipe supports described in Chapters 4 and 7 based on simply-supported and clamped boundary conditions.

Figure A11.1 shows a support model which combines two bars with one end clamped and the other free. The stiffness of the model can be considered as the sum of the translational stiffness at the end of the bar. D is the outside diameter of the copper pipe discussed in Chapters 4 and 7. The combined stiffness can be obtained by

$$K_T = 2\frac{3EI}{\left(l/2 - D/2\right)^3} \tag{A11.1}$$

where E is the young's modulus of the supporting bar, I is the second moment of the area and l is the span of the whole support.

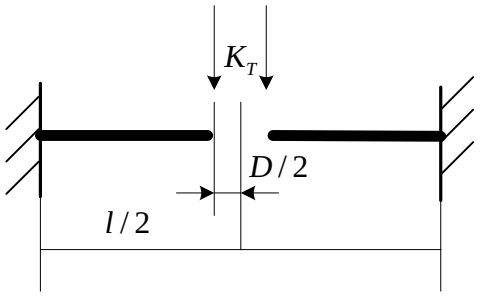

Figure A11.1 Translational stiffness of two clamped parallel bars: Model A11.1.

Figure A11.2 shows bar with simply-supported ends. The translational stiffness at the middle point of the bar is

$$K_T = \frac{48EI}{l^3}. \tag{A11.2}$$

The dimension of the copper pipe is also neglected here.

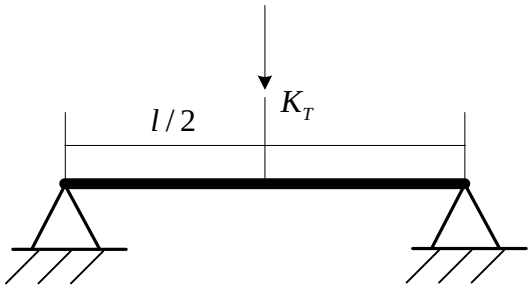

Figure A11.2 Translational stiffness at the middle point of a bar with simply-supported ends: Model A11.2.

Figure A11.3 shows bar with clamped ends. The translational stiffness at the middle point of the bar is

$$K_T = \frac{192EI}{l^3}. \tag{A11.3}$$

The dimension of the copper pipe is also neglected here.

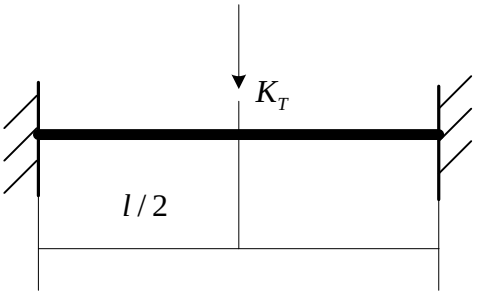

Figure A11.3 Translational stiffness at the middle point of a bar with clamped ends: Model A11.3.

Figure A11.4 shows bar with clamped ends. The torsional stiffness at the middle point of the bar is

$$K_R = \frac{\pi G d^4}{16l} \tag{A11.4}$$

where G is the shear modulus and d is the diameter of the supporting bar. The dimension of the copper pipe is also neglected here. This can be considered as the rotational stiffness of the pipe support discusses in Chapters 4 and 7.

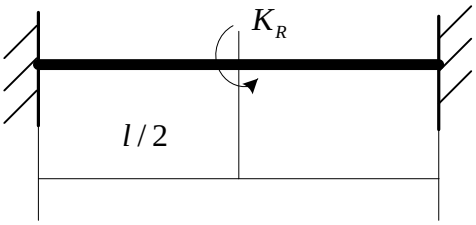

Figure A11.4 Torsional stiffness at the middle point of a bar with clamped ends: Model A11.4

Table A11.1 gives the translational and rotational stiffnesses for the pipe supports based on the above discussed boundary conditions. Compared to those values listed in Table 7.6, for the aluminium supports, the estimated values of the translational stiffness from measurements are close to the model with clamped ends; for the steel supports, the estimated values of the translational stiffness are close to the model with simply-supported ends. The values of estimated rotational stiffness agree well with the model A11.4.

Table A11.1 Stiffnesses of pipe supports based on several boundary condition assumptions. (SI units)

support		K_T, $\times 10^6$			K_R, $\times 10^3$
		Model A11.1	Model A11.2	Model A11.3	Model A11.4
aluminium	long	1.126	0.688	2.753	1.472
	short	4.775	2.231	8.925	2.179
steel	long	3.285	2.008	8.030	4.199
	short	13.927	6.508	26.031	6.214

Note: 1. $d = 0.01266$;
2. $l = 0.185$ for long supports and $l = 0.165$ for short supports;
3. $E = 7.2\times10^{10}$ and $G = 2.7\times10^{10}$ for aluminium supports, and $E = 2.1\times10^{11}$ and $G = 7.7\times10^{10}$ for steel supports.